

**A Study of Large Transverse Momentum Direct Photon  
plus Away-Side Jet Production using 500 GeV/c proton  
and  $\pi^-$  Beams Incident on a Beryllium Target**

by

**P. D. D. S. Weerasundara**

B.Sc., University of Colombo, 1984

M.S., University of Pittsburgh, 1987

Submitted to the Graduate Faculty of  
Arts and Sciences in partial fulfillment  
of the requirements for the degree of  
Doctor of Philosophy

**FERMILAB  
LIBRARY**

University of Pittsburgh

1993



To my parents  
for their love and encouragement



## ABSTRACT

# A Study of Large Transverse Momentum Direct Photon plus Away-Side Jet Production using 500 GeV/c proton and $\pi^-$ Beams Incident on a Beryllium Target

P. D. D. S. Weerasundara, Ph.D.

University of Pittsburgh, January 1993

This thesis presents the results from a study of the production of large transverse momentum direct photons and their away-side jets using 500 GeV/c proton and  $\pi^-$  beams incident on a Be target. The data used in this analysis were taken during the 1987-88 fixed target run using the E706 spectrometer at Fermilab. The spectrometer, which triggered on a high transverse momentum electromagnetic deposition, consists of a finely segmented large acceptance liquid argon calorimeter and a large acceptance charged particle spectrometer.

An algorithm has been developed to reconstruct the recoil jets associated with high transverse momentum direct photons and  $\pi^0$  mesons. The structure of the events containing a high transverse momentum direct photon has been investigated and the results are compared with the predictions of ISAJET and PYTHIA Monte Carlo simulations. The differential cross sections for the production of direct photons plus their away-side jets have been measured as a function of the direct photon  $P_T$  as well as a function of the recoil jet pseudorapidity. The beam dependence of the cross section has been investigated. The cross section results are compared with the predictions of leading log and next-to-leading log QCD calculations.



## ACKNOWLEDGEMENTS

The success of a high energy physics experiment is inevitably the result of a great deal of hard work by a large number of people. There are many individuals who contributed to the success of the experiment E706 and I wish to take this opportunity to thank them all. Eventhough it is very difficult to thank every one individually, there are several people who deserve special thanks for helping me to realize the end result; the completion of my thesis. With great pleasure, I take this opportunity to thank those individuals.

First of all I would like to thank Paul Shepard, my thesis advisor and Gene Engels for their guidance and the continued support throughout this thesis project over the past six years. I am grateful for the encouragement and the friendship that Paul and Gene have given me through out. I thank Paul for initiating me in to this thesis project. I am greatly indebted to Gene for the invaluable guidance he gave me towards the completion of this thesis. Without Gene's help, the completion of this thesis would have been very difficult.

I would like to express my very special thanks to Sudhindra Mani for the guidance and the friendship he has given to me throughout. I have learnt a great deal of physics and experimental skills from Mani. Gene Engels, Paul Shepard and Sudhindra Mani have greatly influenced in shaping me as an experimental physicist.

Many thanks to Sajan Easo, Phil Gutierrez, Sudhindra Mani and Jim Dunlea for taking an intial interest in Jet Physics. Many aspects of this analysis stemmed from the early efforts of those individuals.

Many thanks to George Ginther for his advice and encouragement on countless occasions. Thank you George for encouraging me to give a talk at DPF-92. I greatly value the immense guidance I received from Marek Zielinski during the final stage of this analysis. Mani and Marek are largely responsible for my understanding of the

theoretical aspect of this analysis. Thank you Marek for the crash course in LaTeX on SGI. Thanks also to Dane Skow, John Mansour, Brajesh Choudhary, David Brown and WooHyun Chung for their help in completing this analysis.

I also thank Jeff Owens of Florida State University for providing us with the QCD Monte Carlo code and I thank Joye Huston and John Mansour for making that code accessible to me.

I would like to thank all the first run graduate students and postdoctoral fellows for their unparalleled contribution to this experiment. Many thanks to G. Balocchi, R. Benson, D. Brown, B. Choudhary, W. Desoi, J. Dunlea, S. Easo, G. Fanourakis, G. Ginther, P. Gutierrez, K. Hartman, V. Kapoor, I. Kourbanis, A. Lanaro, C. Lirakis, P. Lukens, S. Mani, J. Mansour, D. Orris, E. Perbys, A. Sinanidis, D. Skow, G. Wu, T. Yasuda, C. Yosef and M. Zielinski. I also thank all the senior faculty members of the E706 collaboration for their fine effort in making E706 a successful experiment. Special thanks goes to our spokesman Paul Slattery for providing an excellent leadership to the experiment. Tom Ferbel and Carl Bromberg deserve special mention for their helpful comments and suggestions on this analysis. Thanks a lot Tom for taking a personal interest in helping me to secure a postdoc position. It has been a pleasure working with all these folks and I wish them well in their future endeavors.

Many thanks to my longtime roommate and good friend Steve Blusk for his company and the tireless effort he took in assembling the silicon detectors for the last two runs of E706. Thanks to Tim Stone for keeping those nano latches in good shape. I also wish to acknowledge the technical support I received from Jim Tweed.

Many thanks to my longtime friends Upul Sonnadara and Kithsiri Jayananda of the University of Pittsburgh for their friendship and the help they have given me in overcoming numerous bureaucratic obstacles while I was at Fermilab. Many thanks to our graduate secretary Ms. Mariem Green of the University of Pittsburgh

for the assistance she provided me over the past several years in handling many administrative matters.

My heartfelt thanks go to Rohana Liyanage, Athula Yapa, Ruwansiri Apa, Kanthi and Dharmaratne, Steve Blusk, WooHyun Chung, Rob Roser, Brajesh Choudhary and Sudhindra Mani for making the life in mid-west very enjoyable.

Thanks a lot to Bimali Padmaperuma and my wife Shanika Daluwatta for proof reading the early chapters of this manuscript and making helpful comments.

Last but not least, I wish to thank my parents for their love and the support given to me over the years.

Fermilab

Batavia, Illinois.

January 27, 1993.



# TABLE OF CONTENTS

List of Figures	xi
List of Tables	xv
<b>1 Introduction</b>	<b>1</b>
1.1 Parton Model and QCD	1
1.1.1 Kinematic Variables and Notations	3
1.2 QCD and High $P_T$ Hadronic Interactions	5
1.2.1 Scaling Violation	6
1.2.2 Running Coupling Constant $\alpha_S(Q^2)$	7
1.3 Direct Photon Physics	9
1.3.1 Direct Photons	10
1.3.2 Direct Photons plus Away-Side Jets	12
1.4 Goals of the Thesis	13
<b>2 The E706 Spectrometer</b>	<b>15</b>
2.1 Meson-West Beam Line and Cherenkov Detector	16
2.2 Target	18
2.3 The Tracking System	20
2.3.1 The Silicon Strip Detector System	20
2.3.2 The MW9AN Analysis Magnet	27
2.3.3 Proportional Wire Chambers	28
2.4 Liquid Argon Calorimeter	30

2.4.1	Electromagnetic Calorimeter . . . . .	32
2.4.2	Hadron Calorimeter . . . . .	35
2.5	Forward Calorimeter . . . . .	38
<b>3</b>	<b>Trigger and Data Acquisition System</b>	<b>40</b>
3.1	Experimental Trigger . . . . .	40
3.1.1	General Description . . . . .	40
3.1.2	Trigger Logic . . . . .	41
3.2	Data Acquisition System . . . . .	45
<b>4</b>	<b>Event Reconstruction</b>	<b>49</b>
4.1	Charge Particle Reconstruction . . . . .	50
4.1.1	Beam Tracking . . . . .	51
4.1.2	Upstream Tracking . . . . .	51
4.1.3	Downstream Tracking . . . . .	52
4.2	Determination of Momentum and Charge of Tracks . . . . .	52
4.3	Primary Vertex Reconstruction . . . . .	58
4.3.1	View Vertex Fitting . . . . .	60
4.3.2	Matched Vertex Fitting . . . . .	61
4.3.3	Vertex Resolution and Reconstruction Efficiency . . . . .	63
4.4	Electromagnetic Shower Reconstruction . . . . .	66
4.4.1	Reconstruction of Photon Energy and Position . . . . .	67
4.4.2	Photon Arrival Time . . . . .	68
<b>5</b>	<b>Data Selection</b>	<b>69</b>
5.1	Event Selection . . . . .	70
5.1.1	Muon Background . . . . .	71
5.1.2	Hadron and Electron Rejection . . . . .	74

5.1.3	$\pi^0$ and $\eta$ Definition . . . . .	78
5.1.4	Single Photon Definition . . . . .	82
5.2	Shower and Track Selection . . . . .	82
5.3	Monte Carlo Calculation of Direct Photon Background . . . . .	86
<b>6</b>	<b>Jet Analysis</b>	<b>89</b>
6.1	Experimental Evidence for Away-Side Jets . . . . .	90
6.1.1	Azimuthal Correlation . . . . .	90
6.1.2	Rapidity Correlation . . . . .	94
6.2	Jet Reconstruction . . . . .	96
6.3	Monte Carlo Study of Jet Reconstruction . . . . .	98
6.3.1	Jet Monte Carlo Event Generation . . . . .	100
6.3.2	Particle Misassignment . . . . .	103
6.3.3	Jet Reconstruction Efficiency and Jet Axis Resolution . . . . .	106
6.4	Parton Momentum Fractions . . . . .	107
6.5	Properties of Recoil Jets . . . . .	112
6.5.1	Charged Multiplicity . . . . .	112
6.5.2	Transverse Momentum and Jet Width . . . . .	116
6.5.3	Longitudinal Fragmentation . . . . .	119
<b>7</b>	<b>Cross Sections</b>	<b>128</b>
7.1	Overview . . . . .	128
7.1.1	Energy Scale . . . . .	129
7.1.2	Reconstruction Efficiency and EMLAC Acceptance . . . . .	129
7.1.3	Trigger Corrections . . . . .	131
7.1.4	Correction for the Vertex Reconstruction Efficiency . . . . .	131
7.1.5	Correction for the veto wall cut . . . . .	132
7.1.6	Beam Count . . . . .	132

7.1.7	Recoil Jet Pseudorapidity Correction . . . . .	133
7.2	$\pi^0 + Jet$ Cross Section . . . . .	134
7.3	$\gamma + Jet$ Cross Section . . . . .	136
7.4	Background subtraction for the $\gamma + jet$ cross section . . . . .	142
<b>8</b>	<b>Results and Conclusions</b>	<b>145</b>
8.1	Direct Photon plus Away-Side Jet Cross Sections . . . . .	145
8.2	Beam Dependence of the Cross Sections . . . . .	147
8.3	Comparison with QCD Predictions . . . . .	150
8.3.1	Comparison with Leading Log QCD Predictions . . . . .	150
8.3.2	Comparison with Next-to-Leading Log QCD Predictions . . . . .	152
8.4	Conclusions . . . . .	158
	<b>APPENDIX A</b>	<b>164</b>
	<b>REFERENCES</b>	<b>169</b>

## LIST OF FIGURES

1.1	Schematic illustration of high $P_T$ hadronic interaction . . . . .	6
1.2	Higher order corrections to $2 \rightarrow 2$ direct photon subprocess due to soft gluon emission from partons. . . . .	8
1.3	Loop diagrams contributing to higher order corrections . . . . .	8
1.4	QCD diagrams contributing to the direct photon production to first order in $\alpha_s$ . . . . .	11
1.5	Results on inclusive jet production and inclusive direct photon production from UA1 and UA2 experiments . . . . .	12
2.1	Plan view of the MWEST spectrometer. . . . .	16
2.2	Plan view of the SSD's and the target region . . . . .	21
2.3	PIN diode as a particle detector . . . . .	22
2.4	A Micro-strip version of PIN diodes . . . . .	22
2.5	The readout system for the SSD's . . . . .	26
2.6	Cathode-Anode arrangement in a single PWC module . . . . .	29
2.7	LAC cryostat and gantry . . . . .	33
2.8	A cross-sectional view of a single cell of the EMLAC . . . . .	34
2.9	Electromagnetic calorimeter . . . . .	36
2.10	Exploded view of a single cookie . . . . .	37
2.11	Forward calorimeter . . . . .	38
3.1	Layout of the trigger system scintillating counters . . . . .	41
3.2	Schematic diagram of the Data Acquisition System . . . . .	47

4.1	Fraction of three and four hit tracks/event per event in the SSD X and Y view. . . . .	53
4.2	$\chi^2$ distribution of PWC space tracks. . . . .	54
4.3	PWC space track hit multiplicity. . . . .	55
4.4	Track projection differences at the center of the magnet. . . . .	57
4.5	$\pi^+\pi^-$ mass distribution. . . . .	59
4.6	$\mu^+\mu^-$ mass distribution. . . . .	59
4.7	X and Y view impact parameters of vertex tracks. . . . .	62
4.8	Longitudinal and transverse resolution of primary vertex position. . .	64
4.9	Reconstructed primary vertex Z-position. . . . .	65
5.1	TVC distributions for muon induced events and non-muon events. . .	73
5.2	Illustration of the concept of photon "directionality" . . . . .	75
5.3	Photon $P_T$ vs directionality. . . . .	76
5.4	Photon directionality vs TVC time. . . . .	77
5.5	$E_{Front}/E_{Total}$ distributions . . . . .	79
5.6	$\Delta R$ distribution for track-shower matching . . . . .	80
5.7	$\gamma\gamma$ mass distribution. . . . .	83
5.8	$\pi^0$ energy asymmetry distribution. . . . .	84
5.9	Comparison between data and Monte Carlo. . . . .	88
6.1	$\Delta\phi$ distributions for $\pi^0$ events. . . . .	91
6.2	$\Delta\phi$ distributions for $\gamma$ events. . . . .	92
6.3	$\Delta\phi$ distributions for $\pi^0$ and $\gamma$ events. . . . .	93
6.4	Rapidity correlation between the two highest $P_T$ away side charged particles. . . . .	95
6.5	Quantities relevant to the reconstruction of recoil jets. . . . .	99
6.6	Monte Carlo comparison of $\chi^2/DF$ for PWC tracks. . . . .	101

6.7	Monte Carlo comparison of “number of hits” per PWC track . . . . .	102
6.8	Pseudorapidity distributions of charged tracks in CM frame. . . . .	104
6.9	$P_T(B \rightarrow R)/P_T(R \rightarrow R)$ as a function of the leading particle pseudo- rapidity. . . . .	105
6.10	Pseudorapidity smearing of the reconstructed recoil jet . . . . .	108
6.11	$\langle \text{Recoil jet pseudorapidity } \eta \rangle$ vs generated recoil jet pseudorapidity $\eta$ . . . . .	109
6.12	Recoil jet reconstruction efficiency as a function of recoil jet pseudo- rapidity. . . . .	110
6.13	Recoil jet axis resolution. . . . .	111
6.14	Parton momentum fractions $x_a$ and $x_b$ for $\pi^0 + jet$ and $\gamma + jet$ events. . . . .	113
6.15	$(x_a - x_b)$ for $\pi^0 + jet$ and $\gamma + jet$ events. . . . .	114
6.16	Distributions of charged particles in recoil jets. . . . .	115
6.17	Jet width $\langle q_T \rangle$ vs $z$ . . . . .	117
6.18	Transverse fragmentation distributions for recoil jets. . . . .	118
6.19	Unsubtracted $dn_{ch}/dz$ distributions for $\gamma + jet$ events. . . . .	121
6.20	Misassignment in and efficiency correction for the fragmentation func- tions . . . . .	123
6.21	Unscaled fragmentation functions . . . . .	124
6.22	Scaled fragmentation functions . . . . .	125
6.23	Parametrization of the $\gamma + jet$ fragmentation functions. . . . .	126
7.1	E/P ratio for electrons . . . . .	130
7.2	$\gamma e^+ e^-$ mass distribution . . . . .	130
7.3	Sideband subtracted $\pi^0 + jet$ cross section per nucleon as a function of $P_T$ . . . . .	137

7.4	$\pi^0 + jet$ cross section per nucleon as a function of recoil jet pseudorapidity $\eta_2$ . . . . .	139
7.5	$\gamma + jet$ cross section per nucleon as a function of $P_T$ (unsubtracted) . . . . .	141
7.6	$\gamma + jet$ cross section as a function of recoil jet pseudorapidity $\eta_2$ (unsubtracted) . . . . .	142
7.7	The ratios of $(\gamma + jet)/(\pi^0 + jet)$ . . . . .	143
8.1	Background subtracted direct photon + jet cross sections . . . . .	146
8.2	Background subtracted $(\gamma + jet)/(\pi^0 + jet)$ ratios. . . . .	148
8.3	$\sigma_{\pi^- Be \rightarrow \gamma + jet + X} / \sigma_{p Be \rightarrow \gamma + jet + X}$ as a function of $P_T$ . . . . .	149
8.4	$\sigma_{\pi^- Be \rightarrow \gamma + jet + X} / \sigma_{p Be \rightarrow \gamma + jet + X}$ as a function of recoil jet pseudorapidity. . . . .	151
8.5	$\gamma + jet$ cross section as a function of $P_T$ compared with leading log QCD predictions. . . . .	153
8.6	$\gamma + jet$ cross section as a function of $P_T$ compared with next-to-leading log QCD predictions. . . . .	155
8.7	$\gamma + jet$ cross section as a function of $\eta_2$ compared with next-to-leading log QCD predictions. . . . .	156
8.8	Average $P_T$ as a function of $\eta_2$ and the ratios of data to next-to-leading log QCD predictions. . . . .	157
8.9	$\gamma + jet$ cross section as a function of $\eta_2$ compared with next-to-leading log QCD predictions. . . . .	159
8.10	$\sigma_{\pi^- Be \rightarrow \gamma + jet + X} / \sigma_{p Be \rightarrow \gamma + jet + X}$ as a function of $P_T$ compared with next-to-leading log QCD predictions. . . . .	160
8.11	$\sigma_{\pi^- Be \rightarrow \gamma + jet + X} / \sigma_{p Be \rightarrow \gamma + jet + X}$ as a function of $\eta_2$ compared with next-to-leading log QCD predictions. . . . .	161

## LIST OF TABLES

1.1	Additive quantum numbers for quarks . . . . .	2
2.1	Beam composition . . . . .	17
2.2	Properties of the nuclear targets . . . . .	19
2.3	1987-88 Run summary . . . . .	20
2.4	SSD wafer parameters . . . . .	24
2.5	PWC geometrical parameters . . . . .	31
3.1	Trigger threshold settings . . . . .	44
5.1	Summary of the data sample which survives the successive event level cuts. . . . .	70
5.2	Number of direct photon candidates available to the analysis . . . . .	85
7.1	Process dependent corrections for beam count . . . . .	133
7.2	Averaged corrections for the cuts applied in $\pi^0$ event selection . . . . .	138
7.3	Averaged corrections for the cuts applied in direct $\gamma$ event selection . . . . .	140
A.1	$\gamma + jet$ differential cross sections as a function of $P_T$ . . . . .	164
A.2	$\gamma + jet$ differential cross sections as a function of recoil jet pseudorapidity ( $\eta_2$ ). . . . .	165
A.3	$\sigma_{\gamma+jet}/\sigma_{\pi^0+jet}$ as a function of $P_T$ . . . . .	166
A.4	$\sigma_{\gamma+jet}/\sigma_{\pi^0+jet}$ as a function of recoil jet pseudorapidity ( $\eta_2$ ). . . . .	167
A.5	$\sigma_{\pi^-Be\rightarrow\gamma+jet+X}/\sigma_{pBe\rightarrow\gamma+jet+X}$ as a function of $P_T$ . . . . .	168

A.6	$\sigma_{\pi^-Be \rightarrow \gamma + jet + X} / \sigma_{pBe \rightarrow \gamma + jet + X}$ as a function of recoil jet pseudorapidity	
	( $\eta_2$ )	168

# CHAPTER 1

## Introduction

This thesis presents the results from a study of the production of large transverse momentum direct photons plus their away side jets using 500 GeV/c proton and  $\pi^-$  beams incident on a Be target. The data used in this analysis were taken using the Fermilab E706 spectrometer. E706 is a second generation fixed target experiment designed to study the characteristics of high transverse momentum ( $P_T$ ) direct photon production and its associated event structure. The experiment employs a finely segmented lead and liquid argon calorimeter to detect direct photons and a large acceptance charged particle spectrometer to study the associated event structure.

In the following sections we will briefly introduce the reader to some of the phenomenological concepts which lay the theoretical foundation and motivation that lead to the analysis presented in this thesis.

### 1.1 Parton Model and QCD

The early deep inelastic scattering experiments[1] have revealed that the nucleon consists of point like constituents which are called *partons*. In the 'naive' parton model these point like constituents were identified with *Quarks*, ruling out the possibility that quarks are a mere abstract mathematical entity[2]. These 'quarks' come in six different flavors, namely, u,d,s,c,b and t and are spin 1/2 particles (fermions). They carry fractional electric charges;  $\frac{2}{3}|e|$  and  $-\frac{1}{3}|e|$ . Table 1.1 summarizes the additive quantum numbers of quarks.

Table 1.1: Additive quantum numbers for quarks. Electric charge  $Q$ , Isospin third component  $I_z$ , Strangeness  $S$ , Charm  $C$ , Bottom  $B$ , Top  $T$ .

Quantum Number	Quark Flavors					
	d	u	s	c	b	t
$Q$	-1/3	2/3	-1/3	2/3	-1/3	2/3
$I_z$	-1/2	1/2	0	0	0	0
$S$	0	0	-1	0	0	0
$C$	0	0	0	1	0	0
$B$	0	0	0	0	-1	0
$T$	0	0	0	0	0	1

All the known *baryons* (combination of three quarks) and *mesons* (quark and anti-quark pair) can be interpreted as some combination of these quarks. With the quantum numbers shown in the table 1.1, it wasn't possible to form a hadron wave function which satisfies the Pauli Principle. This resulted in the postulation of a new quantum number called *color* which facilitated the anti-symmetrization of hadron wave functions. The color quantum number has three degrees of freedom which are traditionally called "red", "blue" and "green". Since the early 70's it was found that the quarks alone do not carry the total momentum of the proton. This led to the suggestion that there are some neutral (no electromagnetic or weak coupling) constituents of the nucleon which perhaps bound the ensemble of quarks together inside hadrons. This is the origin of the term *Gluon*. These *Quarks* and *Gluons*, collectively called partons, form today's *Parton Model*. The gauge theory that describes the strong interaction between quarks mediated by the gauge boson 'gluon' is

called Quantum ChromoDynamics (QCD). QCD fundamentally differs from Quantum ElectroDynamics(QED)<sup>1</sup> primarily in two ways; first, in the strength of the coupling constant and in the behaviour of the interactions as a function of distance. As we shall see later in this chapter, the QCD coupling strength  $\alpha$ , decreases with the increasing  $Q^2$  where  $Q$  is the 4-momentum transfer in some parton interaction. This weakening of the coupling constant at high  $Q^2$  (*i.e.* at short distances) is called the property of *Asymptotic Freedom*[3, 4] and was a necessary ingredient in the success of QCD. This feature of asymptotic freedom allows the application of well known perturbative techniques to the problem of obtaining predictions for the processes that are dominated by short distance interactions. As we shall discuss in section 1.2, it is for this reason that large momentum transfer processes have played an important role in testing QCD. Secondly, the gluon has a net color (unlike the neutrally charged gauge photon in QED). The gluons exist in eight different superpositions of color and anti-color states. Because of this net colour quantum number, the gluons can couple to other gluons. This possibility is not available in QED as photons do not have electric charge and hence couldn't couple to other photons. This coupling is essentially a result of the *non-Abelian* nature of the QCD lagrangian[5].

In section 1.2 we will briefly introduce some fundamental concepts from QCD in relation to the investigation of large  $P_T$  phenomena.

### 1.1.1 Kinematic Variables and Notations

Before we go into detail, a few definitions of some of the kinematic variables and notations are in order for describing large  $P_T$  phenomena. Upper case letters will be used to designate hadrons participating in the interaction and the lower case letters will be used when referring to the hadron constituent (partons) undergoing the hard scatter.

---

<sup>1</sup>QED describes the interaction between electrically charged fermions and photons.

When discussing the kinematics for the single particle inclusive reaction

$$A + B \rightarrow C + X \quad (1.1)$$

where A and B are the initial-state hadrons, C is the final-state hadron and X refers to any object produced in association with C. The four momenta of hadrons A, B and C are denoted by  $p_A$ ,  $p_B$  and  $p_C$ , respectively. Then the Mandelstam variables are defined as

$$s = (p_A + p_B)^2, \quad t = (p_A - p_C)^2, \quad u = (p_B - p_C)^2 \quad (1.2)$$

where  $s$  is the square of the center-of-mass energy and  $t$  and  $u$  are the squares of the four momentum transfer from particles A to C and B to C respectively.

A similar set of variables  $\hat{s}$ ,  $\hat{t}$  and  $\hat{u}$  are defined for the parton scattering subprocess  $a + b \rightarrow c + d$ . The energy and momentum conservation require that

$$s + t + u = \sum_i m_i^2 \quad (1.3)$$

where  $\sum_i m_i^2$  is the sum of the square of the masses of the initial and final state particles. For massless partons this becomes

$$\hat{s} + \hat{t} + \hat{u} = 0 \quad (1.4)$$

Another variable that will extensively be used throughout this thesis is the rapidity  $y$  which is defined as

$$y = \frac{1}{2} \ln \frac{E + p_z}{E - p_z} \quad (1.5)$$

where  $E$  is the total energy of the particle and  $p_z$  is the longitudinal momentum component along the beam direction. When the mass of the particle is negligible compared to its transverse momentum, Eq. 1.5 becomes  $y = \ln \cot \theta/2 = \eta$  where  $\eta$  is called the *pseudorapidity* and  $\theta$  is the scattering angle. Pseudorapidity coincides with rapidity in the limit  $m \rightarrow 0$ . For the sake of completeness, we shall introduce

the variables  $x_a$  and  $x_b$ , defined as the fraction of the momenta carried by parton  $a$  inside hadron A and by parton  $b$  inside hadron B in the initial state. A complete set of relationships among the aforementioned variables can be found in the appendix of reference [6].

## 1.2 QCD and High $P_T$ Hadronic Interactions

Over the last two decades, QCD has become a well established gauge theory of strong interactions. In QCD, the hard scattering process between two hadrons is described as the interaction between quarks and gluons which are the constituent of the incoming hadrons. Figure 1.1 shows a schematic picture of a high  $P_T$  inclusive hadronic interaction corresponding to Eq. 1.1. In order to derive an expression for the cross section for this inclusive reaction, we must know the momentum distribution of partons inside the colliding hadrons as well as the probability of obtaining final state hadrons from the outgoing partons. These distributions are not perturbatively calculated and have to be determined experimentally.

In the parton model the hard scattering is described by the lowest-order subprocesses, which for high  $P_T$  particle production, corresponds to two body scattering. Assuming the initial and final partons are collinear with the initial and final state hadrons, the inclusive cross section for the large  $P_T$  reaction corresponding to figure 1.1 is then given by

$$E_C \frac{d\sigma}{d^3p_C}(AB \rightarrow C + X) = \sum_{abcd} \int dx_a dx_b dz_c G_{a/A}(x_a) G_{b/B}(x_b) D_{C/c}(z_c) \frac{\hat{s}}{z_c^2 \pi} \frac{d\sigma}{d\hat{t}}(ab \rightarrow cd) \delta(\hat{s} + \hat{t} + \hat{u}) \quad (1.6)$$

where  $x_a$  and  $x_b$  are the fraction of longitudinal momentum carried by parton  $a$  in hadron A and parton  $b$  in hadron B, respectively and  $z$  is the fraction of momentum of parton  $c$  carried by hadron C. The distribution function  $G_{a/A}(x_a)$  is the probability of finding a parton  $a$  in hadron A with a momentum fraction lying between  $x_a$  and

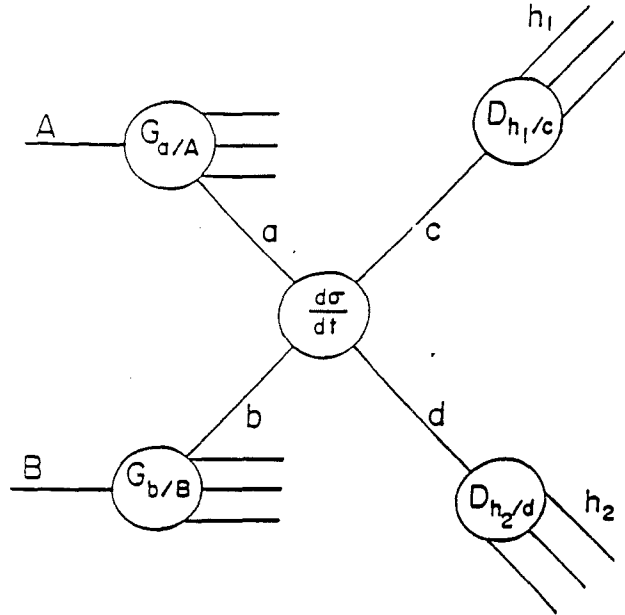


Figure 1.1: Schematic illustration of high  $P_T$  hadronic interaction.

$x_a + dx_a$  and a similar definition exists for  $G_{b/B}(x_b)$ . The fragmentation function  $D_{C/c}(z_c)$  is the probability of finding hadron  $C$  with a momentum fraction between  $z_c$  and  $z_c + dz_c$  from a parton  $c$ .

### 1.2.1 Scaling Violation

The scale invariance of the above distribution and fragmentation functions is a result of the lowest order perturbation calculation of the hard scattering cross section  $d\sigma/d\hat{t}$  (*i.e.* only the QCD processes that involve only two partons in the initial and in the final states are considered)[7]) within the standard parton model. In order to carry out the perturbation calculation to higher order, more complicated QCD diagrams must be considered. When higher order sub-processes are considered, one encounters a variety of singularities that must be treated with care in order to obtain finite results.

The singularities arising due to the radiative corrections, *i.e.* the corrections for soft gluon emission from incoming and outgoing partons (figure 1.2), are handled with the *factorization procedure* as discussed in references [6, 8, 9]. This gives rise to momentum dependent distribution and fragmentation functions (*i.e.*  $G(x_a) \rightarrow G(x_a, Q^2)$  and  $D(z_c) \rightarrow D(z_c, Q^2)$ ). This dependence on the momentum transfer  $Q^2$  is referred to as the *scaling violation*. Although, the distribution and fragmentation functions cannot be calculated from the first principles using perturbative calculations, their  $Q^2$  dependence is completely predicted by the Altarelli-Parisi equations[10]. These functions are first determined at some reference scale  $Q_0^2$  and evolve to a desired  $Q^2$  using these equations. This *factorization procedure* is applied only up to some arbitrary mass scale  $M$  which sets the limit on the validity of the perturbative approach.

### 1.2.2 Running Coupling Constant $\alpha_S(Q^2)$

The singularities associated with the loops appearing in the graphs in figure 1.3 are taken care of by introducing a momentum dependent strong coupling (or running coupling) constant  $\alpha_S$  in the *renormalization group equation*. This introduces a second arbitrary mass scale  $\mu$  to be included in the theory. To loop order one[3] and in the leading logarithm approximation, the running coupling constant  $\alpha_S(Q^2)$  has the form

$$\alpha_S(Q^2) = \frac{12\pi}{(11n - 2f) \ln(Q^2/\Lambda^2)} \quad (1.7)$$

where  $n$  is the number of colors and  $f$  is the number of flavors allowed within the accessible phase phase.  $\Lambda$  is a free parameter, which determines the scale at which  $\alpha_S$  becomes large, and hopefully results in the confinement of quarks within hadrons. Embodied in Eq. 1.7 is the property of *Asymptotic Freedom*, where the coupling constant becomes weak with increasing  $Q^2$ , which lead to the possibility of successful application of perturbative QCD to large  $P_T$  phenomena.

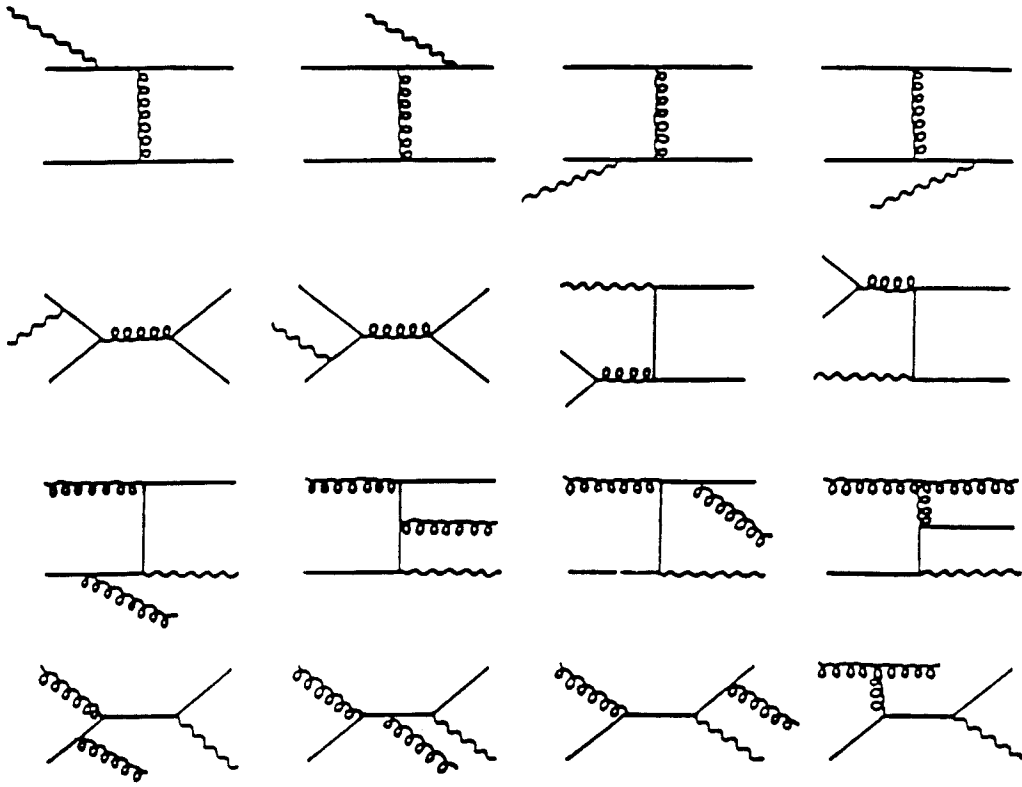


Figure 1.2: Higher order corrections to  $2 \rightarrow 2$  direct photon subprocess due to soft gluon emission from partons.

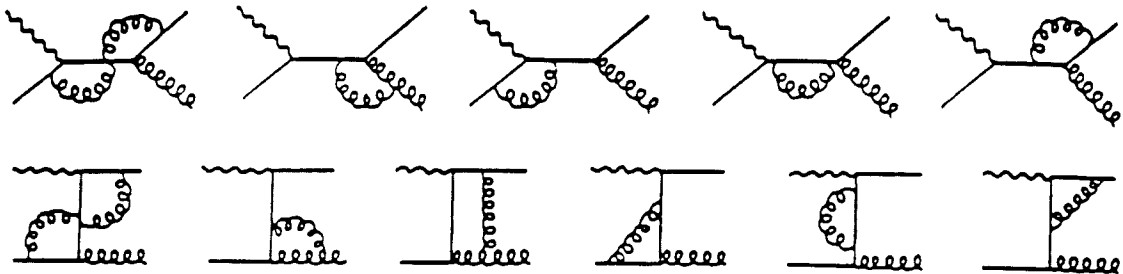


Figure 1.3: Loop diagrams contributing to higher order corrections.

### 1.3 Direct Photon Physics

The hadronic production of large  $P_T$  hadrons has provided considerable insight into the understanding of the hard scattering of partons. Since the final state hadrons are fragments of outgoing partons, high  $P_T$  hadrons provide an indirect probe of the hard scattering process. The hadronic production of large transverse momentum jets<sup>2</sup> has proven to be an excellent test of QCD predictions for the absolute production cross sections which includes a description of short-distance interactions. These final state jets emerge as a result of the hadronization of the outgoing partons. The 4-momentum of the jet is closely related to the parent parton and provides a better probe for studying the interactions at the parton level. Nevertheless, the *Inclusive Jet Physics* at fixed target energies is a difficult enterprise, in that there are experimental difficulties in correctly identifying the jets. QCD predicts the emergence of four jets in hard scattering, with two high  $P_T$  jets resulting from the fragmentation of the hard scattered partons and two additional jets resulting from the fragmentation of the spectator partons. At energies available to fixed target experiments, these jets tend to overlap, making it is very difficult to assign final state hadrons to the appropriate jet. Besides the experimental difficulties in jet identification, one has to disentangle a large number of subprocesses to calculate the inclusive jet cross section, due to the *non-abelian* nature of QCD. Therefore, it would be interesting to study high  $P_T$  hadronic interactions where one could directly constrain the parton level kinematics with a relatively small number of hard scattering subprocesses. Large transverse momentum direct photon production is a viable candidate for such a reaction and has been recognized as an excellent process for studying the dynamics of the hard scattering processes[6, 11] which provides a stringent test of QCD.

---

<sup>2</sup>The term *jet* refers to a collimated collection of hadrons emerging from the hard-scattering reaction

### 1.3.1 Direct Photons

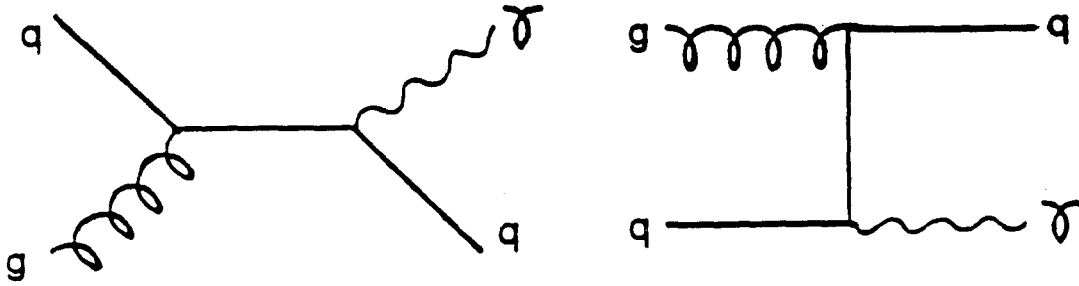
*Direct Photons* are the photons which emerge directly from the hard scattering interaction rather than as a result of an electromagnetic decay of hadrons. Since the photons carry no electrical charge, they do not interact with other photons, greatly reducing the number of subprocesses that would contribute to hadronic production of direct photons. To first order in  $\alpha_S$  (*i.e.*  $O(\alpha\alpha_S)$ ), there are only two subprocesses that contribute to direct photon production; namely the *Compton diagram* ( $qg \rightarrow \gamma q$ ) and the *annihilation diagram* ( $q\bar{q} \rightarrow \gamma g$ ), as shown in figure 1.4. To first order, direct photons unaccompanied by additional hadrons probe the large momentum transfer subprocess without the complication of an unknown fragmentation function. The well understood pointlike nature of the electromagnetic coupling of quark-photon vertex makes the higher order QCD calculations relatively simple. Experimentally, the four-momentum of a photon is easier to reconstruct than that of a jet, and hence gives a direct handle in probing the hard scattering process.

Unfortunately, the rate of direct photon production is relatively lower compared to inclusive jet production by a factor of the order of the electromagnetic coupling constant  $\alpha$  ( $\approx 1/137$ ). This is an over estimate, since there are more diagrams contributing to the inclusive jet production. This is clearly demonstrated using the results from UA1 and UA2 experiments, as shown in figure 1.5[12]. However, the experiments have shown that direct photons are produced at a rate comparable to that of single hadrons in  $P_T$  ranges accessible to fixed target experiments, making it possible to perform high statistics measurements.

Neglecting Fermi motion of partons, the invariant inclusive cross section for the hadronic production of direct photons, to first order in  $\alpha_S$ , is given by

$$E_C \frac{d\sigma}{d^3p_C}(AB \rightarrow \gamma + X) = \sum_{ab} \int dx_a dx_b G_{a/A}(x_a, Q^2) G_{b/B}(x_b, Q^2) \times \frac{\hat{s}}{\pi} \frac{d\sigma}{dt}(ab \rightarrow \gamma d) \delta(\hat{s} + \hat{t} + \hat{u}) \quad (1.8)$$

## Compton Diagrams



## Annihilation Diagrams

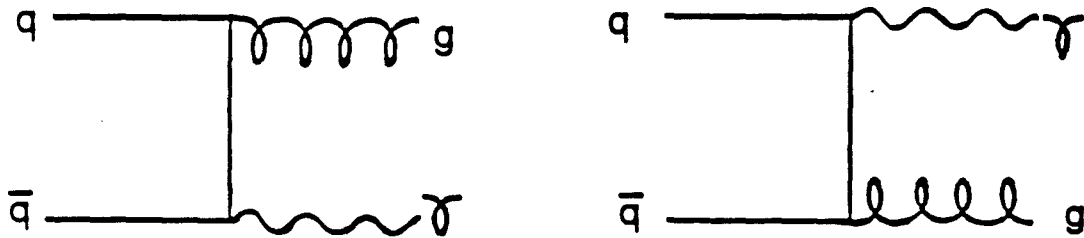


Figure 1.4: QCD diagrams contributing to the direct photon production to first order in  $\alpha_s$ . Top: Compton diagram ( $qg \rightarrow \gamma q$ ). Bottom: annihilation diagram ( $q\bar{q} \rightarrow \gamma g$ ).

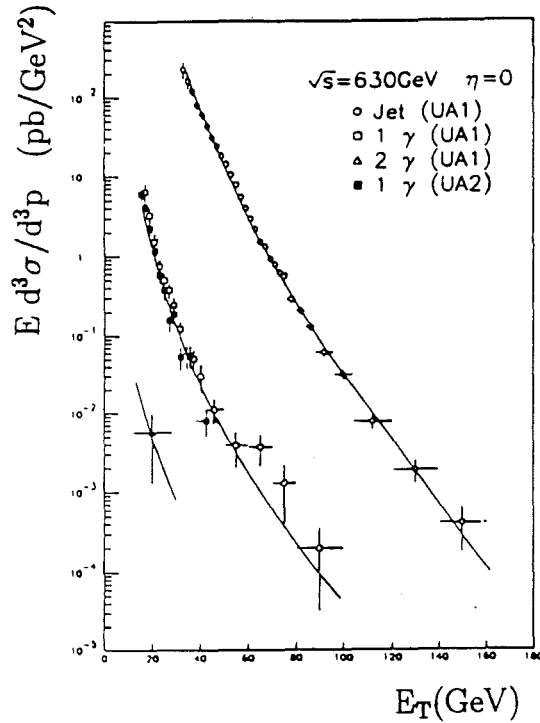


Figure 1.5: Results on inclusive jet production and inclusive direct photon production from UA1 and UA2 experiments.

where the subprocess cross section  $d\sigma/d\hat{t}$  for the Compton and annihilation diagrams are given by

$$\frac{d\sigma}{d\hat{t}}(qg \rightarrow \gamma q) = -\frac{\pi\alpha\alpha_s}{3\hat{s}^2} e_i^2 \frac{\hat{u}^2 + \hat{s}^2}{\hat{s}\hat{u}} \quad (1.9)$$

$$\frac{d\sigma}{d\hat{t}}(q\bar{q} \rightarrow \gamma g) = \frac{8\pi\alpha\alpha_s}{9\hat{s}^2} e_i^2 \frac{\hat{u}^2 + \hat{t}^2}{\hat{t}\hat{u}} \quad (1.10)$$

where  $e_i$  is the fractional charge of the  $i^{\text{th}}$  quark.

### 1.3.2 Direct Photons plus Away-Side Jets

The existing results[11] on the measurements of inclusive production of direct photons have shown a good agreement with the QCD predictions in leading-log approximation[6] as well as with the recently available next-to-leading log QCD calculations[13] over a wide kinematic range. These measurements have led to the extraction of parton distributions for nucleons, in particular, the gluon distributions

in nucleons. However, the calculation of the inclusive cross section in Eq. 1.8 involves an integration over the parton distributions weakening its sensitivity to the gluon distribution in the nucleon. It has long been realized that the simultaneous measurement of the 4-momenta of the direct photon and its away-side jet could provide more precise information on the gluon distribution in nucleon[14]. As shown in the appendix in reference [6], in the leading log approximation, the arguments for both parton distributions would be fixed by the kinematics of the measured direct photon and its away-side jet. In the approximation that the parton  $k_T$  effects ( *i.e.* the transverse component of the parton momentum) can be neglected, the differential cross section for producing a jet opposite a direct photon is given by:

$$\frac{d\sigma(AB \rightarrow \gamma + jet + X)}{d\eta_1 d\eta_2 dP_T^2} = \sum_{ab} x_a x_b G_{a/A}(x_a, Q^2) G_{b/B}(x_b, Q^2) \times \frac{d\sigma}{dt}(ab \rightarrow \gamma + jet) \quad (1.11)$$

where  $P_T$  is the transverse momentum of the direct photon and  $\eta_1$  and  $\eta_2$  are the pseudorapidities of the direct photon and the away-side jet. Eq. 1.11 emphasizes the fact that the  $\gamma + jet$  cross section is more sensitive to the gluon distribution than the inclusive cross section given in Eq. 1.8.

## 1.4 Goals of the Thesis

It is the goal of this thesis to report a measurement of the cross section for the production of direct photons plus their away-side jets in the collision of proton and  $\pi^-$  beams on a Be target. As part of the analysis we investigate the structure of the events containing a direct photon and compare the results with the predictions of ISAJET and PYTHIA Monte Carlo programs as well as with WA70[15] results. Finally we compare the measured cross sections for  $\gamma + jet$  production with the predictions of leading-log and next-to-leading log QCD calculations.

In the chapters to follow, we describe the MWEST spectrometer, the experimental trigger, the event reconstruction and analysis procedure, the event structure and finally the comparison of the cross section results with theoretical predictions based upon QCD calculations.

## CHAPTER 2

### The E706 Spectrometer

In this chapter, the necessary details of all the subsystems of the E706 spectrometer will be discussed. As the front part of the MWEST spectrometer, the E706 spectrometer was designed to study the high transverse momentum ( $P_T$ ) electromagnetic phenomena and associated charged and neutral particle production. To achieve this goal, the E706 spectrometer utilizes a charged particle spectrometer, a liquid argon calorimeter and a steel/scintillator forward calorimeter. The subsystems were designed and developed by the collaborating institutions of the experiment E706. All of the subsystems of the spectrometer were designed to handle high interaction rate which was necessary in order to collect sufficient data and to extract useful information about the relatively small direct photon production cross-section. Figure 2.1 shows a plan view of the MWEST spectrometer configuration for the 1987-88 fixed target run.

The E706 spectrometer consists of

- A Silicon Strip Detector (SSD) system
- A dipole analysis magnet
- A Proportional Wire Chamber (PWC) system
- A Liquid Argon Calorimeter (LAC), consisting of both electromagnetic and hadronic sections
- A Forward Calorimeter (FCAL)

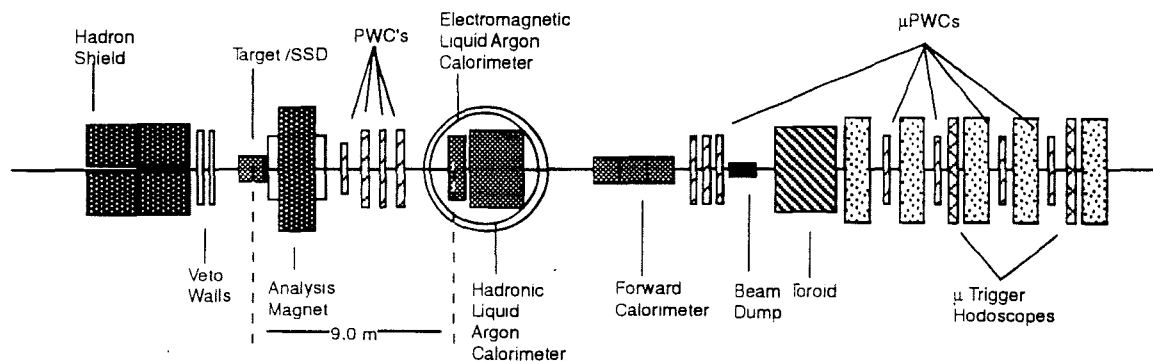


Figure 2.1: Plan view of the MWest spectrometer. Detector elements from hadron shield down to and including the forward calorimeter comprises the E706 spectrometer.

Downstream of the forward calorimeter is the experiment E672 spectrometer which ran concurrently with the E706 spectrometer. The E672 spectrometer will not be discussed in this thesis, since E672 data has no relevance to the analysis discussed below.

The charged particle spectrometer (SSD's, analysis magnet and PWC's) was utilized to determine the interaction vertices and momenta of all charged particles in an event<sup>1</sup>, while the electromagnetic calorimeter measured the energy and position of all the electromagnetic showers. The hadron calorimeter measured the energy and position of charged and neutral hadrons. The forward calorimeter was designed to measure the total energy and the  $P_T$  of the forward beam jet, which was not detected by the LAC.

## 2.1 Meson-West Beam Line and Cherenkov Detector

The E706 spectrometer is located in the MW9 experimental hall at the downstream end of the Meson-West (MWest) beam line. The MWest beam line is designed to transport a secondary beam of energy up to 800 GeV. The secondary beam is gen-

<sup>1</sup>See chapter 3 for the definition of an event.

erated by the collision of the primary beam<sup>2</sup> on an aluminum target<sup>3</sup> consisting of one interaction length.

The protons in the primary beam arrived in a very narrow time bucket ( $\sim 1$  ns wide) during a 23 seconds long spill and the buckets are separated by 19.7 ns<sup>4</sup>. During the 1987-88 fixed target run, the E706 experiment collected data using both positive and negative 500 GeV/c secondary beams. The positive beam consisted primarily of protons ( $\sim 90\%$ ) with  $\sim 7\%$   $\pi^+$  and  $\sim 2\%$   $K^+$ . A typical secondary beam intensity was about  $6.5 \times 10^7$  particles/spill for the positive running. For the negative beam, the maximum intensity achieved was  $6.5 \times 10^7$  particles/spill and the negative beam consisted primarily of  $\pi^-$ . Table 2.1 summarizes the beam constituents for both the positive and negative running modes.

Table 2.1: Beam composition.

Positive Beam			Negative Beam		
$\pi^+$ (%)	$K^+$ (%)	$p$ (%)	$\pi^-$ (%)	$K^-$ (%)	$\bar{p}$ (%)
$7.2 \pm 0.1$	$1.7 \pm 0.1$	$91.2 \pm 0.1$	$96.9 \pm 0.2$	$2.9 \pm 0.2$	$0.2 \pm 0.01$

The secondary beam particles were tagged with a 42 meters long differential Cherenkov counter. The Cherenkov counter was located in the 67 meters long parallel section of the MWest beam line, 216 meters downstream of the primary target and 98 meters upstream of the experimental target. It used Helium gas as the radiator and the counter was operated at a pressure between 4-7 psi, during the 87-88 run. A 32.4 meter focal length mirror was used to focus the Cherenkov light and two

<sup>2</sup>The primary beam is the 800 GeV Fermilab Tevatron proton beam.

<sup>3</sup>The aluminum target will be referred to as the primary target here after.

<sup>4</sup>1 ns =  $1 \times 10^{-9}$  seconds

different rings of six photomultiplier tubes each were used to collect the light. The inner ring of photo tubes (called the coincidence channel) has a radius of 10.19 cm and the outer ring (anti-coincidence or veto channel) has a radius of 19.3 cm. Two scintillating counters with dimensions 10.16 cm  $\times$  10.16 cm, were placed at the two ends of the Cherenkov counter to ensure that the counted beam has passed through the entire counter. During the negative running mode, the counter was used to tag  $K^-$  with an efficiency of  $\sim 50\%$  and with less than a 5% contamination due to  $\pi^-$ . In this running mode, any particle that wasn't tagged as  $K^-$  was called a  $\pi^-$ . For the positive run,  $\pi^+$  were tagged with an efficiency of  $\sim 78\%$  with about 8% contamination due to  $K^+$ . A detailed description of the secondary particle production and of the Cherenkov counter can found in reference [16].

The halo muon flux along the beam was reduced by several large spoiler magnets placed in the beam line. Located downstream of the Cherenkov counter is a large hadron shield which removed the hadrons travelling parallel to the beam.

Immediately downstream of the hadron shield were two veto walls consisting of two overlapping scintillation counters used to reject muons which were not swept out by upstream spoiler magnets. High energy muons can produce bremsstrahlung photons far from the beam line axis which mimic a high  $P_T$  signal in the electromagnetic calorimeter. A signal indicating a coincidence between the counters in the two veto walls was used to veto these muon events at the trigger selection level (see chapter 3).

## 2.2 Target

The experiment employed two nuclear targets Be and Cu. The choice of two nuclei enable us to study the nuclear effects in the direct photon and neutral meson ( $\pi^0, \eta$ ) production. Table 2.2 shows the properties of the nuclear targets used in the

Table 2.2: Properties of the nuclear targets.

Parameters	Be	Cu
Length (cm)	4.00	0.16
Atomic Number	9.01	63.54
Density ( $g/cm^3$ )	1.85	8.96
Radiation Length (%)	11.33	11.19
$\pi$ interaction Length (%)	6.90	0.83
$p$ interaction Length (%)	9.24	1.03
$K$ interaction Length (%)	6.25	0.77

experiment during the 87-88 run.

The data taken during the '87-'88 run were divided into several sets, delimited by changes in the beam sign, target type, etc. Table 2.3 summarizes the breakdown of the run sets. Data taken without LAC triggers are not included in table 2.3.

The experiment used a segmented target to help localize photon conversions and secondary interactions. The segmented target consisted of twenty slices of 2 mm thick Be, with cross-sectional area of 2 cm  $\times$  12 cm and the slices were separated by 1.6 mm air gaps. The two 0.8 mm thick Cu foils with the same cross-sectional area were placed 3.2 mm upstream of the first Be piece and were separated by a 1.6 mm air gaps. Figure 2.2 shows the SSD's and the target configuration.

Table 2.3: 1987-88 Run Summary.

Run Set	Beam	Target	Run Number Interval	Number of Events
A	Negative	Cu+Be	2852-3036	786K
B	Positive	Cu+Be	2588-2670	440K
C	Positive	Cu+Be	2387-2586	1225K
D	Negative	Be	2062-2382	1247K
E	Positive	Be	1782-2007	1508K
F	Positive	Be	1672-1719	161K

## 2.3 The Tracking System

The E706 tracking system consisted of a set of silicon strip detectors, a dipole magnet and a set of proportional wire chambers. The tracking system was used primarily to determine the beam particle trajectory, the primary interaction vertex and the momenta of all charged tracks within the acceptance of the tracking system. In addition, the charged particle tracks reconstructed<sup>5</sup> in the PWC's (in conjunction with the electromagnetic showers in the LAC) were used to identify electrons.

### 2.3.1 The Silicon Strip Detector System

A silicon strip detector (SSD) is an array of independent PIN diodes fabricated on a single piece of silicon crystal as shown in figure 2.4 [17]. Under reverse voltage bias, the p-n-p structure of two adjacent strips ensures a high impedance between them

<sup>5</sup>see Chapter 4 for the reconstruction of charge particle trajectories.

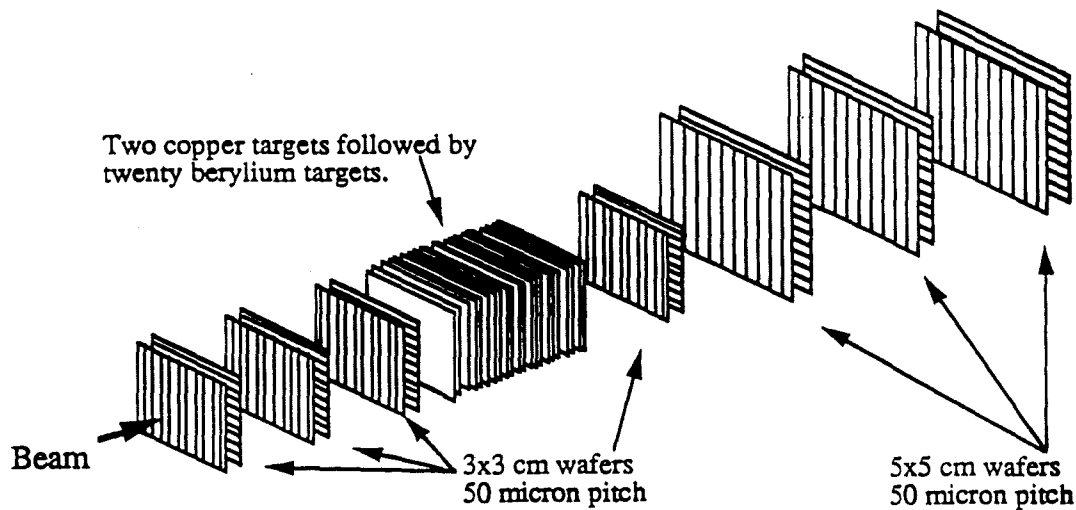


Figure 2.2: Plan view of the SSD's and the target region.

and maintains them as independent detectors. The PIN diodes, a semiconductor detector (see figure 2.3), have a long and important history, well over two decades, in the field of nuclear physics. What is unique about silicon detectors in the field of high precision electronic detectors is the fact that they are based on highly developed planar technology [18]. Silicon detectors based on this technology can have a very high precision in spatial position and energy measurements and are very radiation hard.

A charged particle passing through a semiconductor detector deposits ionization energy, thus creating electron-hole pairs in the semiconductor. These e-h pairs can be separated by the presence of an electric field. The charge collected at the electrodes give a signal proportional to the deposited energy.

The choice of silicon microstrip detectors for the E706 was their small size, good spatial resolution, large signal/noise potential and rapid response time.

A minimum ionizing particle (MIP) passing through a SSD shown in figure 2.4 will produce about 25,000 e-h pairs. The collection time for the total charge depends

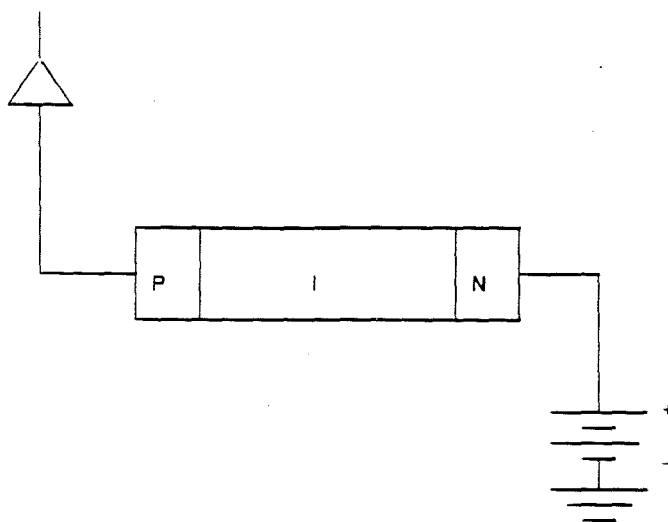


Figure 2.3: PIN diode as a particle detector. The diode is reverse voltage biased.

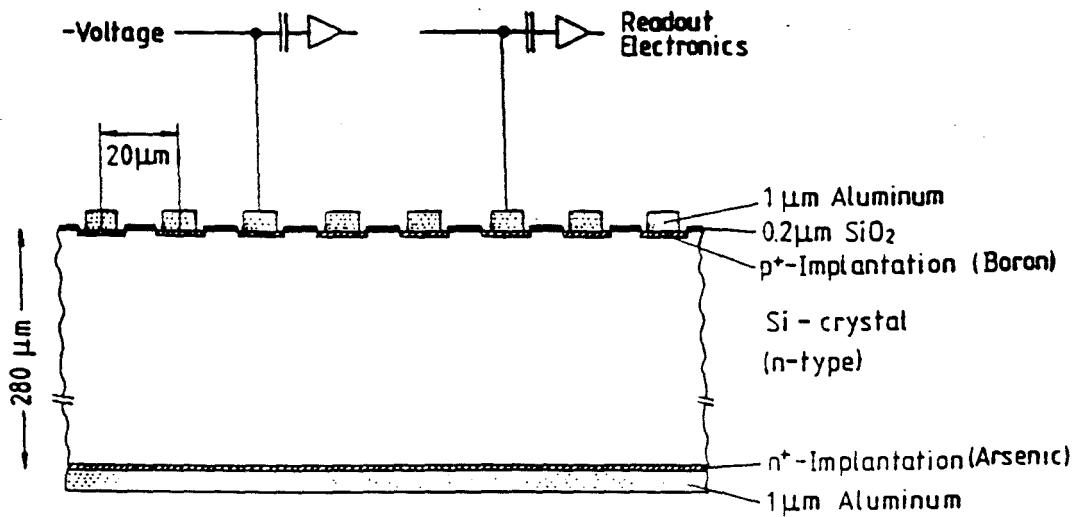


Figure 2.4: A Micro-strip version of PIN diodes.

on the electric field strength, the mobility of charge carriers, and the thickness of the SSD. For the SSD's employed in the E706 spectrometer, the charge collection time is  $\sim 25$  ns[19].

#### 2.4.1.1 Detector Configuration

The SSD's serves as the front end of the E706 spectrometer. The SSD wafers are placed in pairs with the micro-strips in one wafer orthogonal to those in the other wafer, to make an X-Y module. An X-plane has its strips vertical and a Y-plane has its strips horizontal. During the 87-88 run we employed seven X-Y modules (14 SSD planes). The layout of the SSD's is shown in figure 2.2. The three modules upstream of the target operated as beam chambers and the four modules downstream of the target operated as the upstream component of the charged particle spectrometer. All the beam chambers and the first module immediately downstream of the target consisted of  $3\text{cm} \times 3\text{cm}$  silicon wafers and the rest of the modules consisted of  $5\text{cm} \times 5\text{cm}$  wafers. All the silicon planes have  $50\ \mu\text{m}$  strip pitch and a thickness of  $\sim 300\ \mu\text{m}$ . There are 10800 strips available for instrumentation out of which only 7120 channels were instrumented during the '87-'88 run, defining the active region (and the acceptance) of the SSD's. Table 2.4 lists the number of instrumented channels, active region and the Z-coordinates of the SSD planes.

#### 2.4.1.2 Read Out Electronics

The readout system for the SSD's was designed to operate at a 1 MHz interaction rate. The read out system provided the digital information on the lines illuminated by MIPs passing through the SSD's. The charge produced by a MIP is amplified by a Rel-Lab IO 323-C charge sensitive (pre) amplifier before it is fed into a commercially available amplifier-discriminator circuit to produce a logic signal for storage as digital data. The details on the design and the development of

Table 2.4: SSD wafer parameters. Beam chambers are denoted by B and the vertex chambers are denoted by V.

Plane Number	View	Type	Instrumented number of strips	Active region (cm)	Z Position (cm)
1	X	B	256	1.28	-129.001
2	Y	B	256	1.28	-128.114
3	X	B	256	1.28	-32.872
4	Y	B	256	1.28	-31.961
5	X	B	256	1.28	-15.413
6	Y	B	256	1.28	-14.498
7	X	V	384	1.92	-2.384
8	Y	V	384	1.92	-1.470
9	X	V	640	3.20	3.067
10	Y	V	640	3.20	3.981
11	X	V	768	4.84	8.645
12	Y	V	768	4.84	9.560
13	X	V	1000	5.00	14.086
14	Y	V	1000	5.00	15.001

the pre-amplifiers are described in reference [19]. Beyond the pre-amplification stage, the SSD's and PWC's have an identical readout system manufactured by Nanometric System Inc. [20].

The Nanometric read out system consists of 16 channel *N-277* amplifier and discriminator modules, 32 channel *N-278* latch modules, *N-280* dedicated crate controllers and *N-281* CAMAC interface modules. Figure 2.5 shows a schematic diagram of the readout system for the SSD system[21].

The outputs of the pre-amplifiers are fed into *N-277* modules. Each channel of *N-277* (330  $\Omega$  input impedance) consists of a wide-band differential amplifier followed by a discriminator. Each *N-277* card requires +5.0 volts at 0.4 amperes and -5.2 volts at 0.68 amperes. The *N-277* cards are housed in commercially available vector crates which can accommodate up to 20 cards in one crate.

The output of the pre-amplifier produced an analog signal with a peak current of  $\sim 11.5\mu\text{A}$  which is well within the dynamic range (0.5 - 20  $\mu\text{A}$ ) of the *N-277* amplifier (the *N-277* amplifier is sensitive to  $1/2\mu\text{A}$ ). The threshold level for the discriminator was set by an external DC voltage source.

The *N-277* produced an ECL output signal (with a maximum width of  $\sim 45$  ns ) which was transmitted to an *N-278* along a  $\sim 50$  ft long twisted flat ribbon cable. The *N-278* latches are capable of internally delaying each input signal by a pre-determined delay value. The delay values range from 350 to 650 ns. When the leading edge of the delayed input signal falls within the 100 ns 'load' pulse (generated by the trigger logic), the signals are latched and loaded into a 32-bit buffer. The latched data are readout by *N-280* crate controllers once the controllers receive the read pulse again provided by the trigger logic. The 32-channels in the *N-278* are readout as two 16-bit words and only the non-zero words were readout. The maximum readout time of the data from the latches to the controllers is 5  $\mu\text{s}$ . Each *N-278* channel was assigned a wire address, corresponding to a micro-strip in

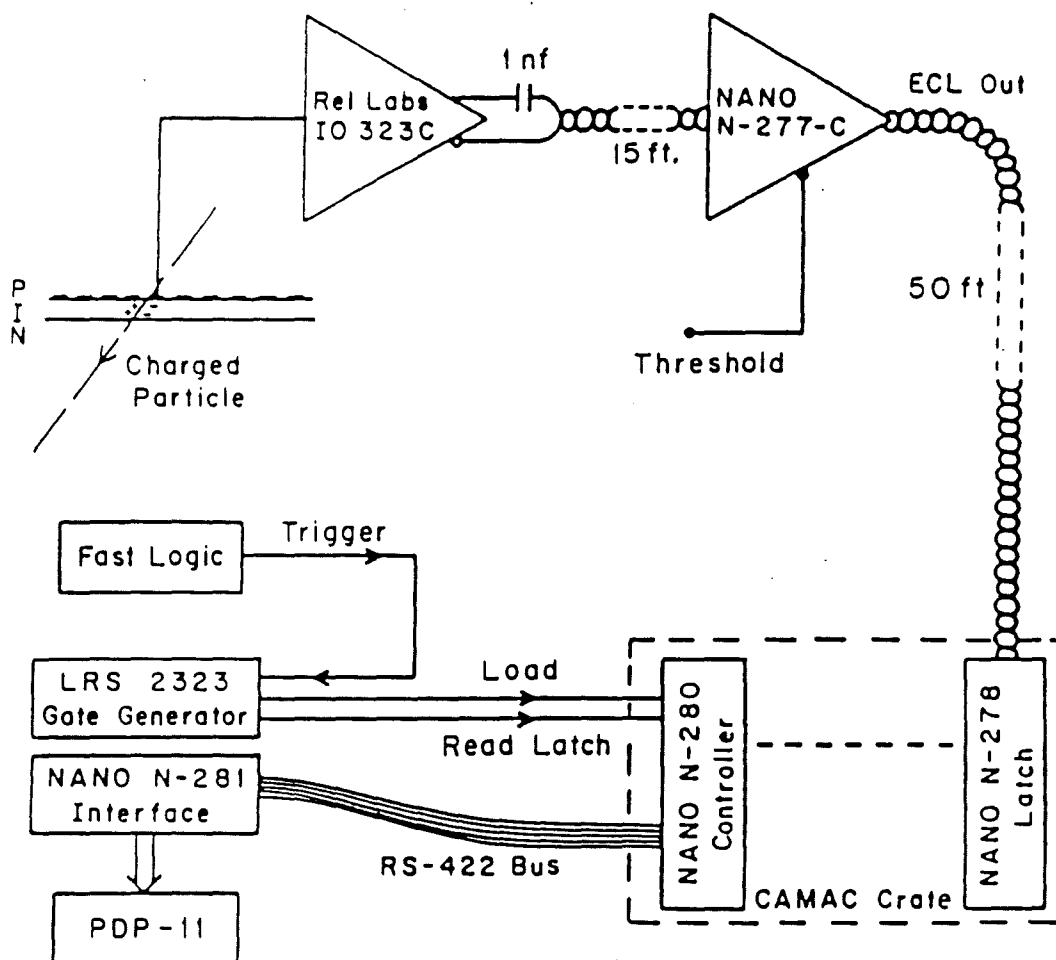


Figure 2.5: The readout system for the SSD's.

the SSD's. The wire-address map was pre-loaded into the *N-280* controllers by a software program. All the latched data were decoded via this wire map to assign hits in a data word to a wire address.

All of the *N-280* create controllers were serially connected to an *N-281* CAMAC interface module. The data from the *N-280*'s were transmitted to *N-281* interface along an RS-422 data bus (see figure 2.5). The data from *N-281* interface were, directly transferred to the memory of a PDP-11 micro-computer. The SSD and PWC systems had, one CAMAC interface each, connected to the same PDP-11. The data read in to the memory of the PDP-11 were sent to a micro-vax computer for concatenation with the data from the other sub-systems of the spectrometer (see Chapter 3).

Once the data were readout into a PDP-11, a 'reset' signal generated by the trigger logic clears out the data in the latches and prepare the *N-278*'s and *N-280*'s, to read the next event.

### 2.3.2 The MW9AN Analysis Magnet

The dipole analysis magnet located between the SSD's and PWC's enables us to determine the momenta of charged particles within its geometrical acceptance. During the 87-88 run, the magnet was operated at a current of 1050 amperes, corresponding to a vertical magnetic field strength of 6.24 kG. At this operating current, the transverse momentum impulse imparted to a charged particle is  $\sim 450$  MeV/c.

The 20 cm thick mirror plates installed on both ends of the magnet reduce the fringe field, making the vertical field a nearly uniform magnetic field. The fringe field measured at the last SSD plane and the first PWC plane, was found to be less than 1 % of its maximum field strength. In the parametrization of the magnetic field, the effect of the fringe field was taken into account[22].

The geometrical acceptance of the dipole magnet was defined by the hole dimensions of the two mirror plates. The upstream mirror plate hole is 35.56 cm  $\times$  25.4 cm and that of the downstream mirror plate is 127.0 cm  $\times$  91.4 cm. The Z-position of the front face of the upstream mirror plate was at 44.4 cm and the back face of the downstream mirror plate was at 354.2 cm. The effective length of the magnet is 328 cm and the center of the magnet was at  $\sim$  2 m downstream of the target<sup>6</sup>. The magnetic field was mapped using the ZIPTRACK system (developed at Fermilab) [24] at currents 700, 1400 and 2100 amperes. A polyethylene bag filled with Helium gas was installed in the central region of the magnet to reduce the effects of the Coulomb scattering of those charged particles produced in the target.

### 2.3.3 Proportional Wire Chambers

The proportional wire chambers (PWC), the downstream component of the charge particle spectrometer, were located downstream of the dipole magnet (figure 2.1). The PWC system consists of four independent, but similar modules. Each module contains a set of four anode planes (X, Y U and V) with sense wires oriented at -90, 0, 37 and -53 degrees, with respect to the vertical direction.

For each anode plane in each module, there is a pair of cathode planes, one on either side of the anode plane. The cathode planes were constructed of graphite coated 1.0 mil<sup>7</sup> thick mylar sheets. These cathode planes were segmented into three regions, namely the central beam region, diffractive region and the main region. Figure 2.6 shows the structure of the segmentation of the cathode planes. This segmentation allows one to set the high voltage independently in different regions, there by reducing the sensitivity of the anode wires in the central beam region.

---

<sup>6</sup>The longitudinal coordinate of the magnet center was determined using electrons from photon conversions[23].

<sup>7</sup>1 mil =  $10^{-3}$  inches

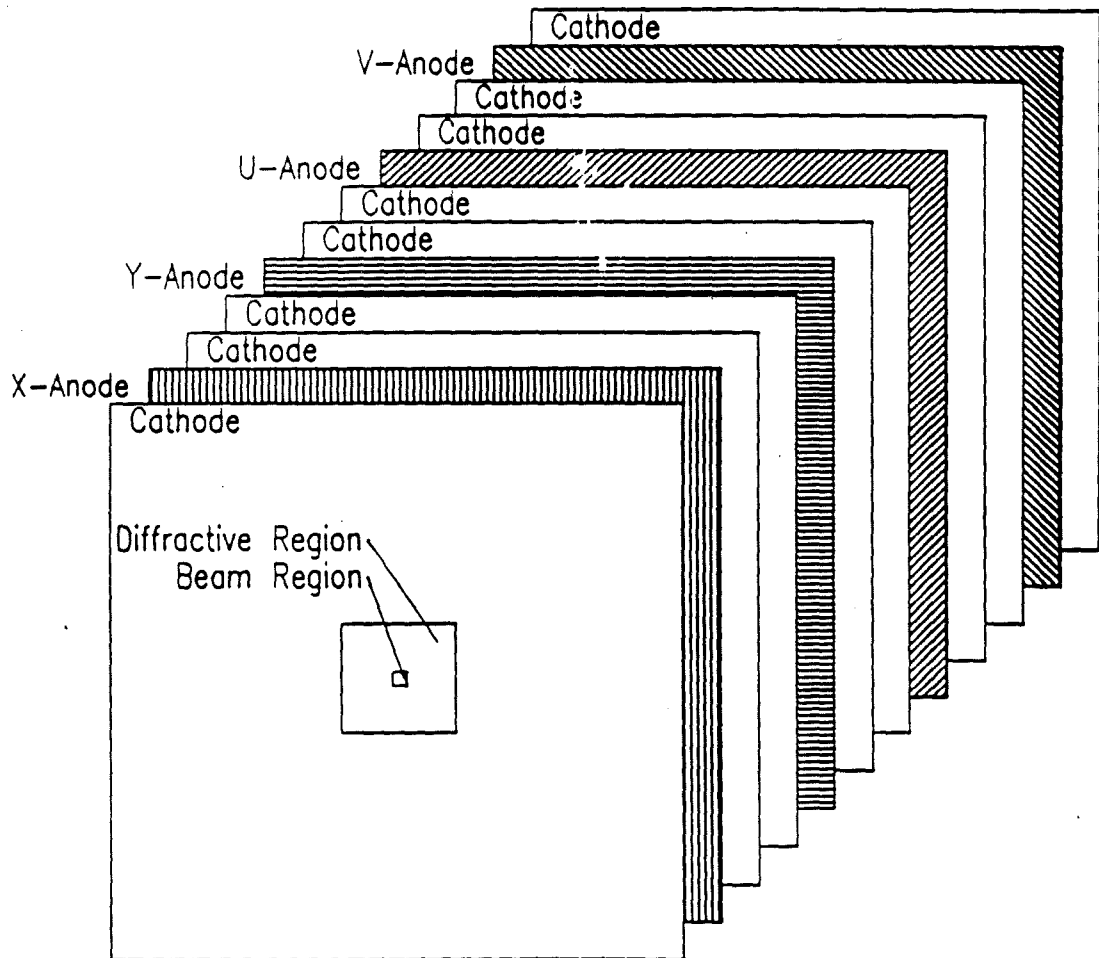


Figure 2.6: Cathode-Anode arrangement in a single PWC module.

The anode planes were made of gold plated tungsten wires with a diameter of 0.8 mils. The anode wires were spaced 0.1 inch apart and the distance between an anode plane and a cathode plane was 0.226 inch.

The gas composition in the PWC system was 18% isobutane, 1.1% isopropyl alcohol, 0.1% freon and 79.7% argon, where argon provided most of the electrons produced from ionization.

Even though, all four PWC modules are similar, they differ in dimensions to maintain an approximately constant solid angle acceptance. The dimensions of the first module are 1.63 m  $\times$  1.22 m and that of the second and third modules are 2.03 m  $\times$  2.03 m. The fourth module has the dimension of 2.44 m  $\times$  2.44 m.

The PWC system has a total of 13,440 channels read out via the Nanometric readout system described in section 2.4.1.2. Table 2.5 shows the number of wires, the orientation angle and the Z coordinate of the PWC planes. For a detail description of the PWC system, see the reference[23].

## 2.4 Liquid Argon Calorimeter

The primary component of the E706 spectrometer is the Liquid Argon calorimeter (LAC)[25], situated downstream of the PWC system (see figure 2.1). The LAC consists of an electromagnetic section (EMLAC) and a hadronic section (HALAC). Both the sampling calorimeters have an absorbing material interleaved with an active sampling medium. Argon was used as the active medium in both calorimeters. In order to distinguish between electromagnetic and hadronic showers, the absorbing material in the EMLAC should have a small radiation length ( $X_0$ ) and a large nuclear interaction length ( $\lambda_I$ ). The EMLAC used lead sheets as the absorbing material and the HALAC used steel plates for its absorbing material. The LAC was used to measure the energy and position of electrons, photons and hadrons. Both the

Table 2.5: PWC geometrical parameters.

Module	Number of Wires	Angle (degrees)	Z Position (cm)
1 X	640	-90.0	380.02
1 Y	480	0.0	381.77
1 U	704	-53.1	383.52
1 V	672	36.9	385.27
2 X	800	-90.0	473.30
2 Y	800	0.0	475.05
2 U	896	-53.1	476.80
2 V	896	36.9	478.55
3 X	800	-90.0	567.75
3 Y	800	0.0	569.50
3 U	896	-53.1	571.25
3 V	896	36.9	573.00
4 X	960	-90.0	660.29
4 Y	960	0.0	662.05
4 U	1120	-53.1	663.81
4 V	1120	36.9	665.57

calorimeters were housed in a  $\sim 5\text{m}$  diameter,  $\sim 9\text{m}$  high cylindrical cryostat as shown in figure 2.7.

A detailed discussion on the design criteria, the construction and the performance of the LAC can be found in reference[26].

### 2.4.1 Electromagnetic Calorimeter

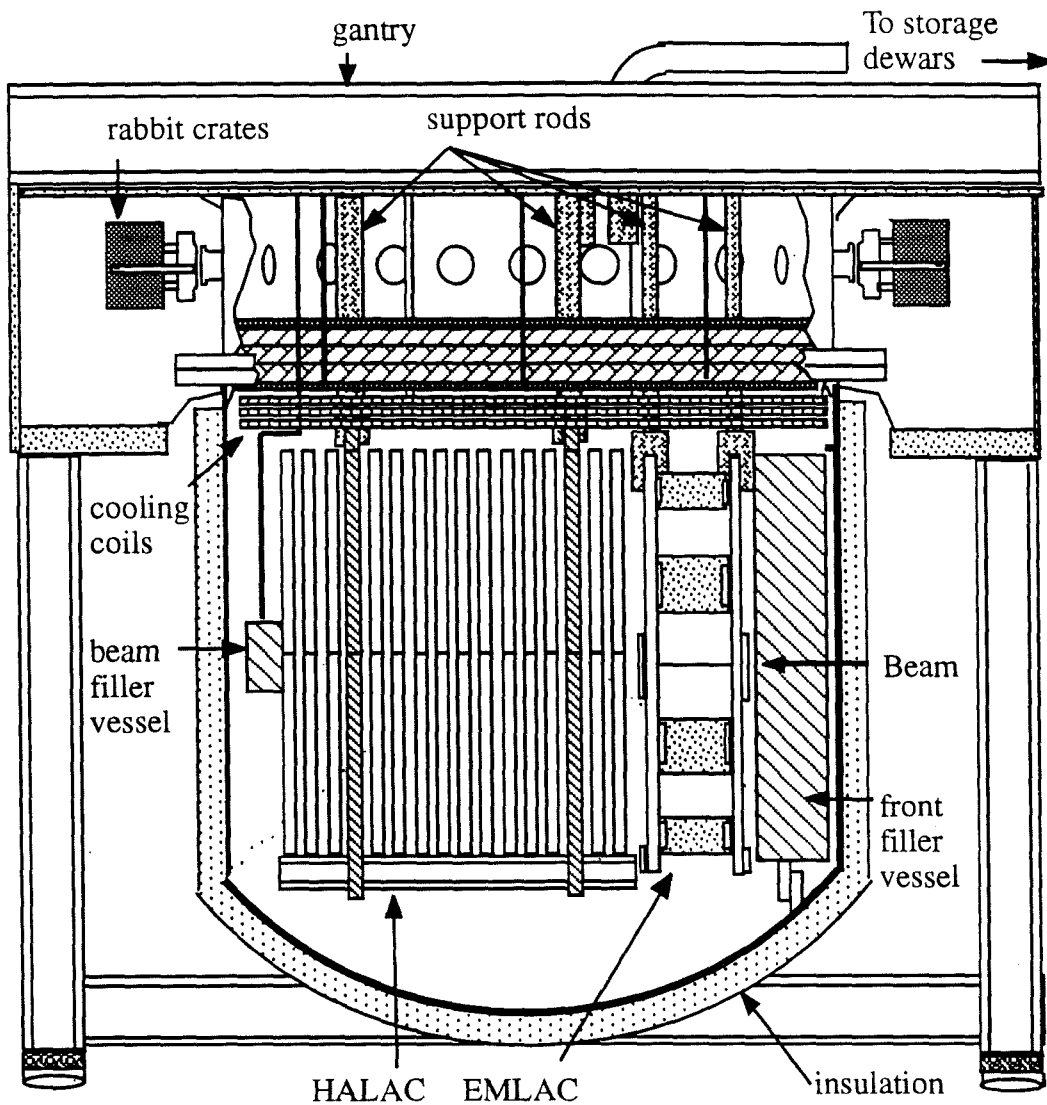
The  $\sim 3\text{m}$  diameter and  $\sim 0.75\text{m}$  long electromagnetic calorimeter (EMLAC) consists of mechanically independent but functionally equivalent, quadrants held together by an overall support structure. The active region of the EMLAC with inner radius of  $\sim 20\text{cm}$  and an outer radius of  $\sim 150\text{ cm}$  corresponds to an approximate angular coverage of  $22 \leq \theta \leq 176$  milliradians in the laboratory coordinate system.

Each quadrant is longitudinally divided into 33 cells (figure 2.8). A single cell consists of two lead sheets, each 2 mm thick and two copper-clad G-10<sup>8</sup> boards, each 1.6 mm thick. The lead sheets and the G-10 boards were separated by 2.5 mm liquid argon gaps, as shown in figure 2.8. The lead plates are of quadrant size and the readout G-10 boards are of octant size. Lead sheets serve as the absorber and as the high voltage cathodes. The EMLAC was designed to operate at 2.5 kV applied to each of the cathode plates.

The readout G-10 anode boards have a radial (R) and azimuthal ( $\phi$ ) geometry as shown in figure 2.9. The first anode plate in each cell has R-strips etched on both sides of the G-10, and the second anode plate has  $\phi$ -strips, again, etched on both sides. The R-view boards have 254 concentric strips. All the R-strips were focused on the target,  $\sim 9\text{ m}$  upstream from the front face of the LAC, in such a way that a particle originating at the target, would pass through the same sequential R-strips in each successive cell. The widths of the R-strips in the first anode board are 0.5446 cm and the widths of the R-strips on anode boards in successive cells increased

---

<sup>8</sup>G-10 is a form of epoxy-fiberglass material



Cut View of the LAC

Figure 2.7: LAC cryostat and gantry. Suspended in the Cryostat are the EMLAC and the HALAC.

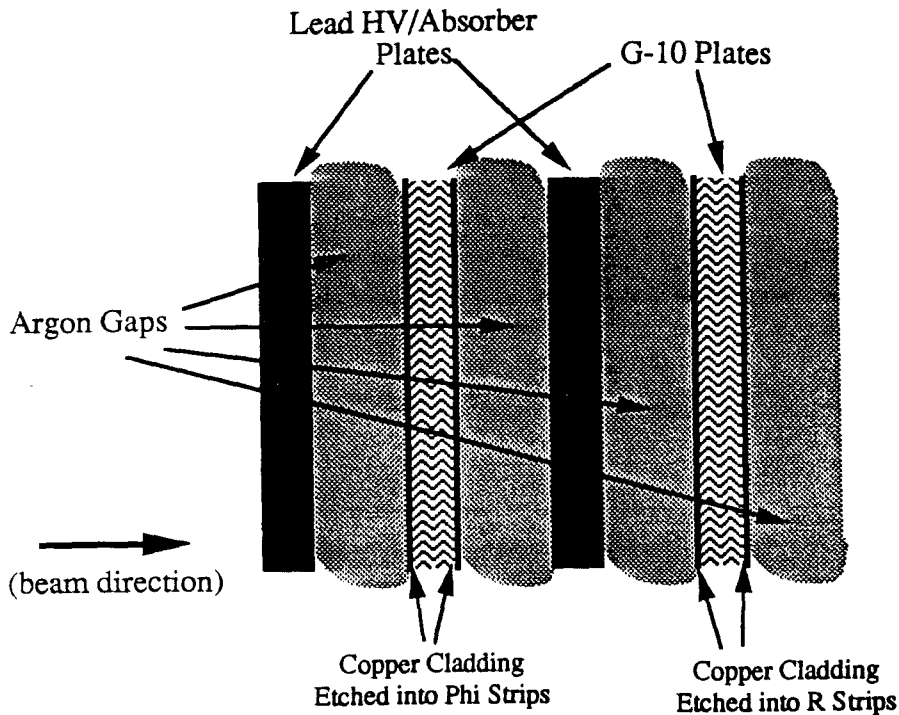


Figure 2.8: A cross-sectional view of a single cell of the EMLAC.

with the distance from the target to the anode board[27].

The  $\phi$ -view anode boards are divided into an inner  $\phi$  and an outer  $\phi$  region. The inner  $\phi$  region has 96 strips, each strip subtending 16.36 milliradians in azimuth and the outer  $\phi$  region has 192 strips, each subtending 8.18 milliradians in azimuth. The inner/outer  $\phi$  boundary in the first  $\phi$  board was at a radius of 40 cm from the beam center of the EMLAC and was also focused on the target just as the R-strips.

For readout purposes, the EMLAC is longitudinally divided into two sections, with the front section containing 11 cells and the back section containing 22 cells. The longitudinal segmentation is very useful in discriminating between electromagnetic and hadronic showers and also in improving the ability to resolve very closely situated di-photons[28].

The octant size of the anode boards resulted in each quadrant having two R-boards and two  $\phi$ -boards. For readout purposes these are labeled as (1) left-R,

(2) right-R, (3) inner- $\phi$  and (4) outer- $\phi$ . The front and back sections of the EMLAC are read out separately. The EMLAC has a total of 6264 channels readout via an electronic readout system developed at Fermilab [29]. Figure 2.9 shows a perspective view of the fully assembled EMLAC.

## 2.4.2 Hadron Calorimeter

The Hadron Calorimeter (HALAC) designed to measure the energy and position of charged and neutral hadrons, was located downstream of the EMLAC in the liquid argon dewar (see figure 2.7).

The HALAC, which is 8 interaction lengths in depth, consists of 52 steel absorber plates, each of 2.54 cm thickness, interleaved with readout cells called "cookies". Figure 2.10 shows an exploded view of a single cookie. The read out boards are separated from the absorber plates by a 0.32 cm argon gap. An extra readout module was placed in front of the first absorber plate to provide a total of 53 cookies. The two anode planes inside a cookie are made of single sided copper-clad G-10 boards and these anode plane were placed in the cookie, with the copper side facing away from each other. Equilateral triangular readout pads were cut into the anode boards and the size of the pads were determined in such a way that 93% of the hadronic shower energy could be contained in a hexagon formed by six pads. The size of the pads increases with the distance from target, in order to maintain the focusing of pads on the target (as with the R-strips in EMLAC). The pad size increases from 10.9 cm in the first cell to 13.3 in last cell, in height.

As with the EMLAC, the HALAC is longitudinally divided in to two sections, with front section containing 14 cookies and 13 steel plates and the back section containing the rest of the cookies and absorber plates. The front and back sections are readout separately. The corresponding pads from the front section of the HALAC are connected together for readout purposes as are the pads of the back section. For

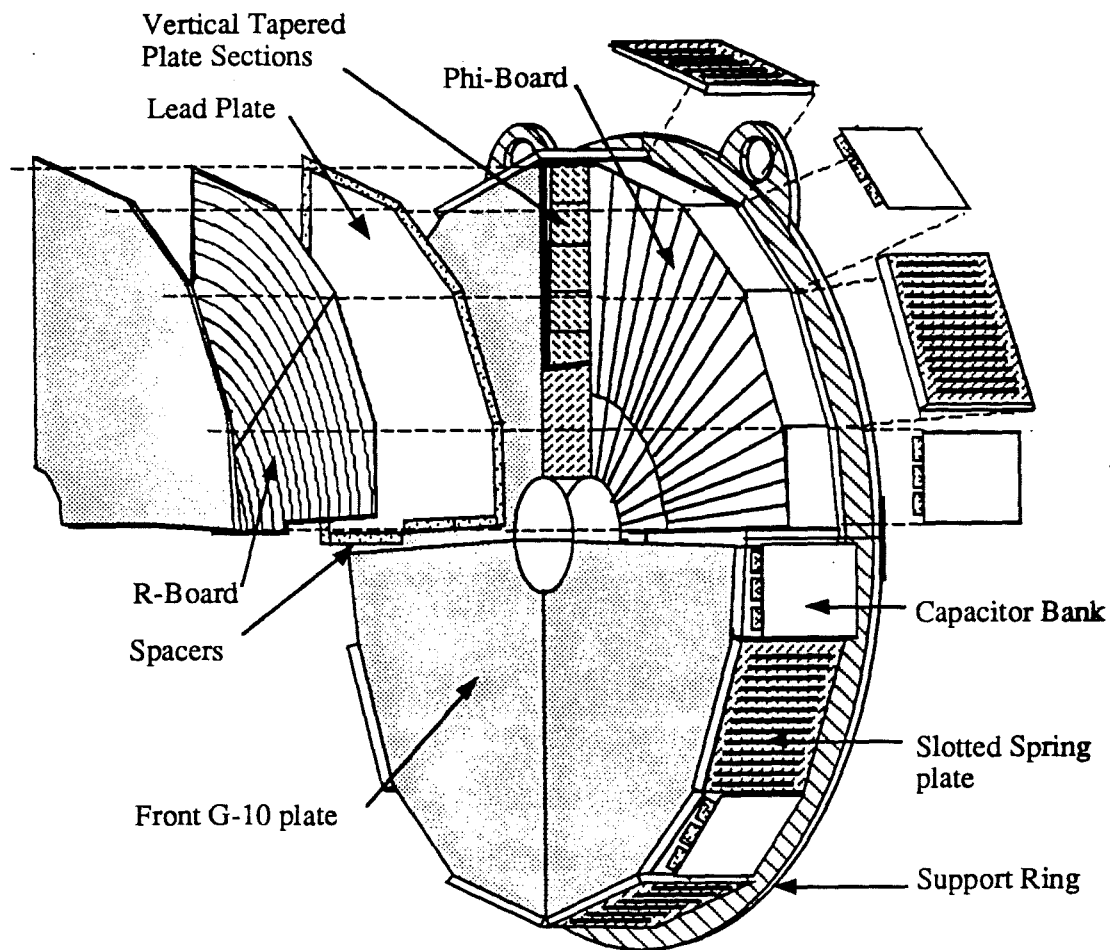
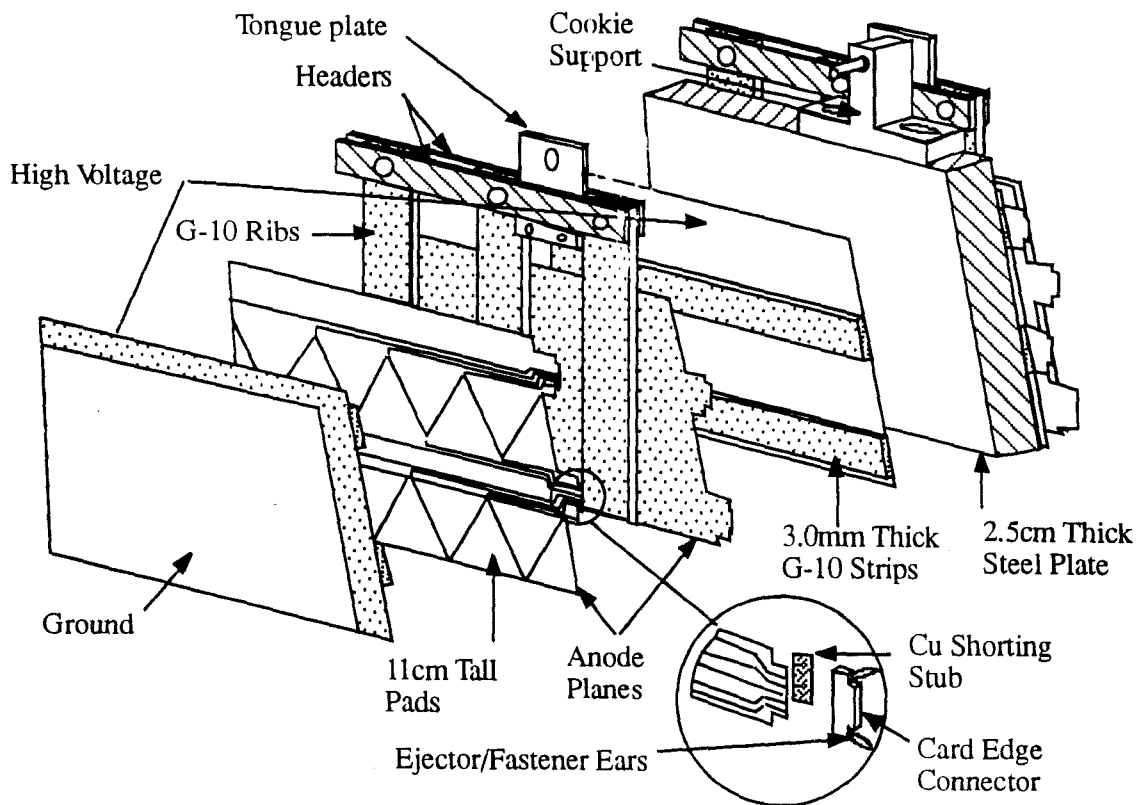


Figure 2.9: Electromagnetic calorimeter. All the primary elements of EMLAC are shown here.



Exploded View of a HALAC Cell

Figure 2.10: Exploded view of a single Cookie.

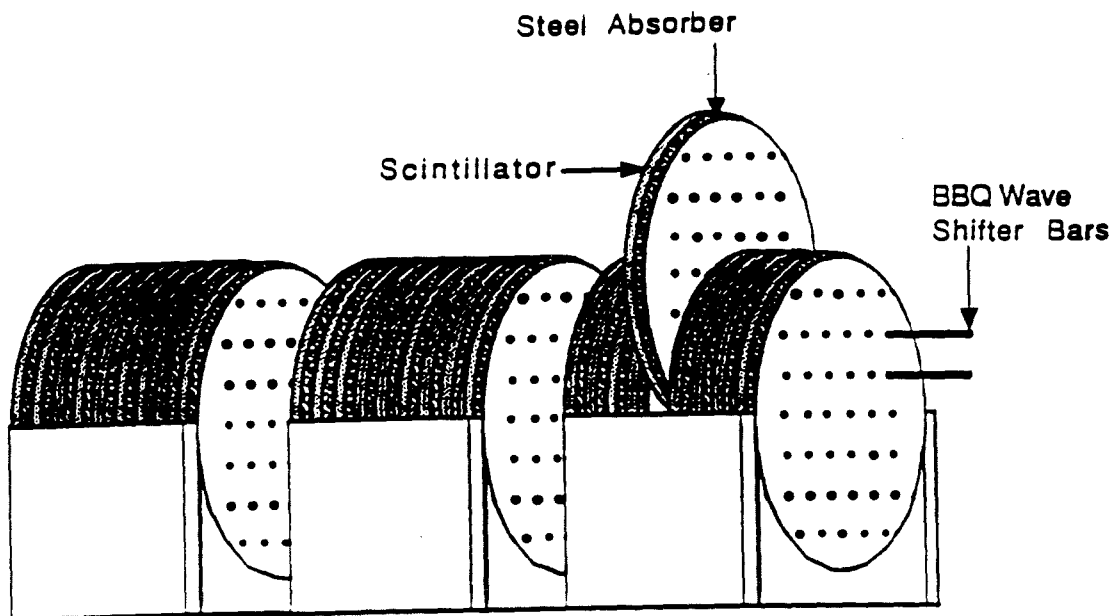


Figure 2.11: Forward Calorimeter.

a detailed description of the HALAC and its readout system, the reader is referred elsewhere [30].

## 2.5 Forward Calorimeter

The Forward Calorimeter (FCAL) consists of three identical modules (see figure 2.11), and is located downstream of the LAC at  $\sim 17$  m from the experimental target. FCAL was designed to intercept the forward beam jet region which is not covered by the LAC. It is capable of operating at 10 MHz interaction rates. The FCAL provided measurements of the total energy and the  $P_T$  of the beam jet produced by the fragmentation of beam particles.

Each of the FCAL modules has 28 circular steel absorber plates. Each absorber plate has a 114 cm diameter and a 1.9 cm thickness. The absorber plates are spaced 0.69 cm apart. Sandwiched between the steel plates, and on either end of each

module are 29 sheets of acrylic scintillator of 4.6 mm thickness. A 3.18 cm diameter hole was drilled through the center of each module, along the length of it, for the purpose of transmitting the non-interacting beam through FCAL.

A total of 76 holes (each  $\sim 1$  cm in diameter) are drilled through the entire stack of plates on an 11.5 cm grid to accommodate 86.4 cm long wave-shifter rods. These rods are doped with BBQ, an organic dye, which shifts the light from the blue to green end of the spectrum. The rods contain an ultraviolet absorbing agent to absorb any Cherenkov light produced by the hadrons which pass through. One end of each wave-shifter rod is silvered and the other end is connected to a photomultiplier tube. The phototubes are readout via flash ADC system. The total signal from the FCAL is proportional to the energy deposited in the FCAL and from these signals one can determine the total energy and the  $P_T$  of the beam jet. A detail discussion on the characteristics of the forward energy production can be found in the reference [31].

## CHAPTER 3

# Trigger and Data Acquisition System

In this chapter we will present a brief description of the trigger and the data acquisition (DA) system of E706, implemented during the 1987-88 fixed target run. The experimental trigger and the DA system is central to collecting the data from the various parts of the spectrometer and recording it on a storage medium (magnetic tapes). A discussion on various components of the trigger logic followed by a description of the DA system will be presented in the next two sections.

### 3.1 Experimental Trigger

#### 3.1.1 General Description

E706 implements a trigger system designed to run at a maximum of  $10^6$  interactions/second and to select events with high- $P_T$  ( $P_T > 3$  GeV/c) electromagnetic showers in the EMLAC. The energy in each radial strip of a given shower is weighted according to its radial distance from the beam line and are summed together to determine the total  $P_T$  of an EM shower. The  $P_T$  of a photon or a neutral meson which deposits total energy  $E$  in the EMLAC, can be represented by

$$P_T = E \sin(\theta) \tag{3.1}$$

where  $\theta$  is the production angle (i.e. the angle between the beam line and the line from the target to the centroid of the energy deposition).

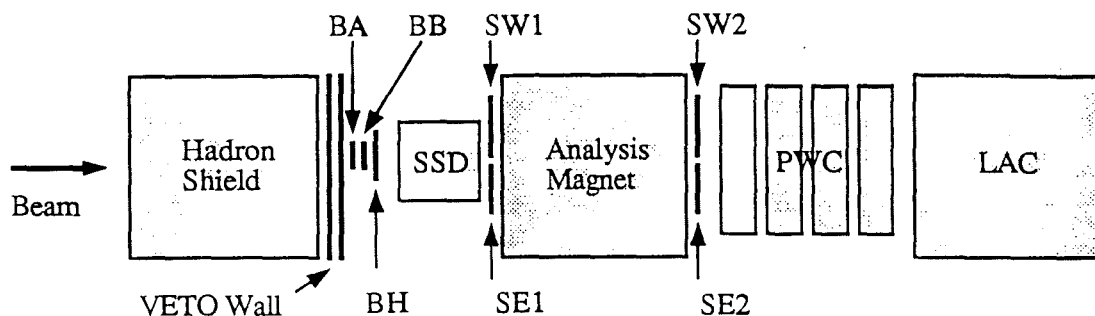


Figure 3.1: Layout of the trigger system scintillating counters. The size of the counters has been exaggerated compared to the surrounding components of the spectrometer.

### 3.1.2 Trigger Logic

In this section we discuss the basic trigger logic (or components), which together formed the E706 trigger. No attempt will be made to discuss the hardware implementation of the trigger. A detailed description of the trigger implementation and its performance can be found in reference [32].

The E706 triggering process takes place in three basic steps:

- Beam and Interaction definition
- Pre-Trigger definition (pre-selection of an event)
- Trigger definition (final selection of an event)

The beam and interaction definition of the trigger are governed by the signals from several scintillating counters located at various places in the spectrometer as shown in figure 3.1.

The incident beam particle is defined by the signals from the two scintillating counters **BA** and **BB**, located upstream of the target (see figure 3.1). The two

counters (with dimensions 2.54 cm  $\times$  2.54 cm) completely overlap each other. The signals from the two counters were put in coincidence with the `RF_CLOCK`<sup>1</sup>, to define the beam signal

$$BEAM \equiv BA \bullet BB \bullet RF\_CLOCK.$$

The logical OR of the discriminated signals from the four scintillating counters (SE1, SW1, SE2 and SW2, located on either side of the dipole magnet), put in coincidence with the beam signal defined as interaction trigger signal. SE1 and SW1 are located  $\sim$  35 cm down stream of the target and SE2 and SW2 are located  $\sim$  367 cm downstream of the target. The four counters cover the full acceptance of the spectrometer. In addition to firing any of the interaction counters, in time with the beam, it is additionally required that there be no other interactions occurred within  $\pm 60$  ns of the present interaction, in order to prevent overlapping of events. It is further required that the interaction not be initiated by a beam halo particle. This is done by taking the interaction signal in anti-coincidence with the signal from the hole counter BH (see figure 3.1). When the interaction signal, defined as

$$INT \equiv BEAM \bullet (SE1 + SW1 + SE2 + SW2) \bullet \overline{BH}$$

satisfy the above conditions, an interaction strobe is then generated to be used in the pre-trigger definition.

Once the interaction strobe is generated, the final trigger decision is made based on the energy deposition in the EMLAC. Each octant is treated independently for triggering purpose, and a octant pre-trigger is generated for each octant which satisfies the following two conditions[32].

- total  $P_T$  deposition within the innermost 96 R-strips or the next 128 R-strips is at least  $\sim 1.7$  GeV/c and the  $P_T$  signal is in time with the interaction trigger.

---

<sup>1</sup>The `RF_CLOCK` is the reference Radio Frequency signal ( $\sim 53$  MHz and  $\sim 10$  ns wide) provided by the accelerator, which was synchronized with the arrival of beam buckets.

- total amount of  $P_T$  deposited in the octant within the 300 ns time interval preceding the present interaction trigger is less than  $\sim 1.5$  GeV/c.

The logic OR of the octant pre-triggers are put in coincidence with the interaction strobe and in anti-coincidence with the SCRKILL<sup>2</sup> and the AND of the two veto-wall signals<sup>3</sup>. If an octant pre-trigger is generated in the absence of the SCRKILL and the two veto-wall signals, a LAC PRETRIGGER is generated. This PRETRIGGER is used to latch the data from the various parts of the spectrometer. It is used as the LOAD signal to latch the data from the tracking system and the FCAL, and as the EVENT signal to the Before/After Time modules (BATs) for the LAC. It is also used in the formation of LAC triggers that are described below. If no PRETRIGGER is formed, the process is carried out for the next interaction.

Once a PRETRIGGER is generated, the final trigger decision is made based on the local and global<sup>4</sup>  $P_T$  deposition in the octant(s). Since a global  $P_T$  signal can be formed due to the presence of coherent noise and/or low  $P_T$  multi-photons in an octant, a local  $P_T$  requirement is introduced, taking advantage of the fine granularity of the EMLAC, to suppress triggering on low- $P_T$  events. This local  $P_T$  condition requires that a substantial fraction of the octant global  $P_T$  be deposited within 16 consecutive R-strips (approximately the width of one photon shower) in one octant. The local and global  $P_T$  signals are discriminated using two different nominal threshold levels, called low and high threshold. These threshold levels were changed several times during the 1987-88 run, as shown in the table 3.1.

During the 1987-88 run, four LAC triggers were implemented using these two  $P_T$  signals and the two  $P_T$  thresholds, and they are defined as follows:

---

<sup>2</sup>SCRKILL is a 30  $\mu$ sec wide signal generated to suppress the impact of coherent noise produced by the 400 Hz power supply used for LAC electronics.

<sup>3</sup>Rejecting the events based on the veto-wall signals is aimed at reducing muon induced high  $P_T$  triggers.

<sup>4</sup>In the context of the trigger, *local* refers to a collection of 16 contiguous R-strips in an octant and *global* refers to the physical boundaries defining an octant.

Table 3.1: Trigger threshold settings

Trigger threshold settings (GeV/c)				
GLB $P_T$ HI	GLB $P_T$ LO	LOC $P_T$ HI	LOC $P_T$ LO	Date
5.0				04-NOV-1987
	3.0			14-NOV-1987
		1.6	1.2	01-DEC-1987
4.0	2.5	4.2		08-JAN-1988
3.6		3.6		23-JAN-1988
			3.0	11-FEB-1988

**LOCAL•GLOBAL HIGH (LGHI)** trigger is formed when at least one octant satisfies the local- $P_T$  low threshold and global- $P_T$  high threshold.

**LOCAL•GLOBAL LOW (LGLO)** trigger is formed when at least one octant satisfies the local- $P_T$  low threshold and global- $P_T$  low threshold.

**SINGLE LOCAL (SLOC)** trigger is formed when at least one octant satisfies the local- $P_T$  high threshold.

**TWO GAMMA (TWOOG)** trigger is formed when at least one octant satisfies the local- $P_T$  low threshold and any one of the three geometrically opposite octants also satisfied the local- $P_T$  low threshold.

The LAC triggers LGHI, LGLO and SLOC could be satisfied by a single octant, whereas TWOOG required at least two octants. SLOC was implemented to study single photon,  $\pi^0$  and  $\eta$  production and TWOOG was designed to study massive two-photon decays. The LGLO trigger was primarily implemented to study lower  $P_T$

phenomena but also provides the opportunity to study the efficiency of the LGHI. Due to the higher occurrence of low- $P_T$  events, the LGLO trigger was pre-scaled by a factor of  $ten$  to avoid its dominance in the event selection. Only the SLOC triggered events are used in the analysis performed in this thesis.

Any of the above defined LAC triggers in coincidence with the PRETRIGGER produced the final trigger for the interaction (it should be noted that more than one LAC trigger could be generated for a given interaction). Once the final trigger has been generated, an INTERRUPT signal is sent to the computers, instructing them to readout the event<sup>5</sup>. After the data in all the subsystems is readout, a computer RESET signal is sent out to the trigger system to generate CLEAR signals to 'reset' all of the readout electronics of the subsystems and preparing the spectrometer to readout the next event. If no LAC trigger follows the generation of a PRETRIGGER, a 'reset' signal is sent to the tracking system, FCAL and BAT's and the trigger system waits  $\sim 5\mu\text{sec}$  before processing the next event.

## 3.2 Data Acquisition System

The E706 data acquisition (DA) system for the 1987–88 run consisted of a Digital Equipment Corporation (DEC) Microvax II ( $\mu\text{VAX}$ ) series computer, four DEC PDP-11 series mini-computers and two 6250 bpi (nine track magnetic) tape drives. The DA system was configured in a multilayered computer network that allowed communication among them. Microvax II was the central control unit of the DA system. The four PDP-11's referred to as the front-end of the DA system, were one level below the  $\mu\text{VAX}$  in the DA chain. Each of the four PDP-11's readout a separate subsystem of the MWEST spectrometer. Three PDP-11's were used by E706 and the fourth one was used by the E672 experiment. The four PDP-11's, named

---

<sup>5</sup>The generic term 'EVENT' collectively refers to all the data from the spectrometer corresponding to a final trigger.

as 'NEU', 'ROCH', 'MX' and 'MU', acquired data from the PLANES (SSD's and PWC's), FCAL, LAC (EM and HADRON) and the E672 Muon system, respectively. In addition to the planes, NEU also readout Cherenkov data and trigger logic as well. Figure 3.2 shows a schematic diagram of the DA system. The PDP-11/34's NEU, ROCH and MU read data through serial and parallel CAMAC links, and the LAC data acquisition used the RABBIT system[29], whose tasks were controlled by the MX (PDP-11/45).

The software package, generally referred to as *VAXONLINE*[33] that controlled the E706 data acquisition, was developed by the Data Acquisition software development group at the Fermilab computing department. The *VAXONLINE*, a multilevel program that ran on the  $\mu$ VAX, involves four major processes:

*GLOBAL\_MENU* a menu driven program, directs the user to the other attached processes.

*RUN\_CONTROL* is the user interface to the system. It ran on the  $\mu$ VAX as well as on all the PDP-11's and controlled and coordinated the data taking process.

*EVENT\_BUILDER* concatenated appropriate sub-events from each of the PDP-11's into one complete event on the  $\mu$ VAX.

*OUTPUT* controls and spools the output (the concatenated events) to magnetic tapes or disk.

For the concatenation of events by the *EVENT\_BUILDER*, it is necessary to have some scheme to match the appropriate sub-events (corresponding to the same interaction), from the different sub-systems of the spectrometer. A device called a "Hydra Scaler" is used for this purpose. Hydra Scaler stored a common 'event number' to the sub-event from each of the PDP-11's. This number is initiated by

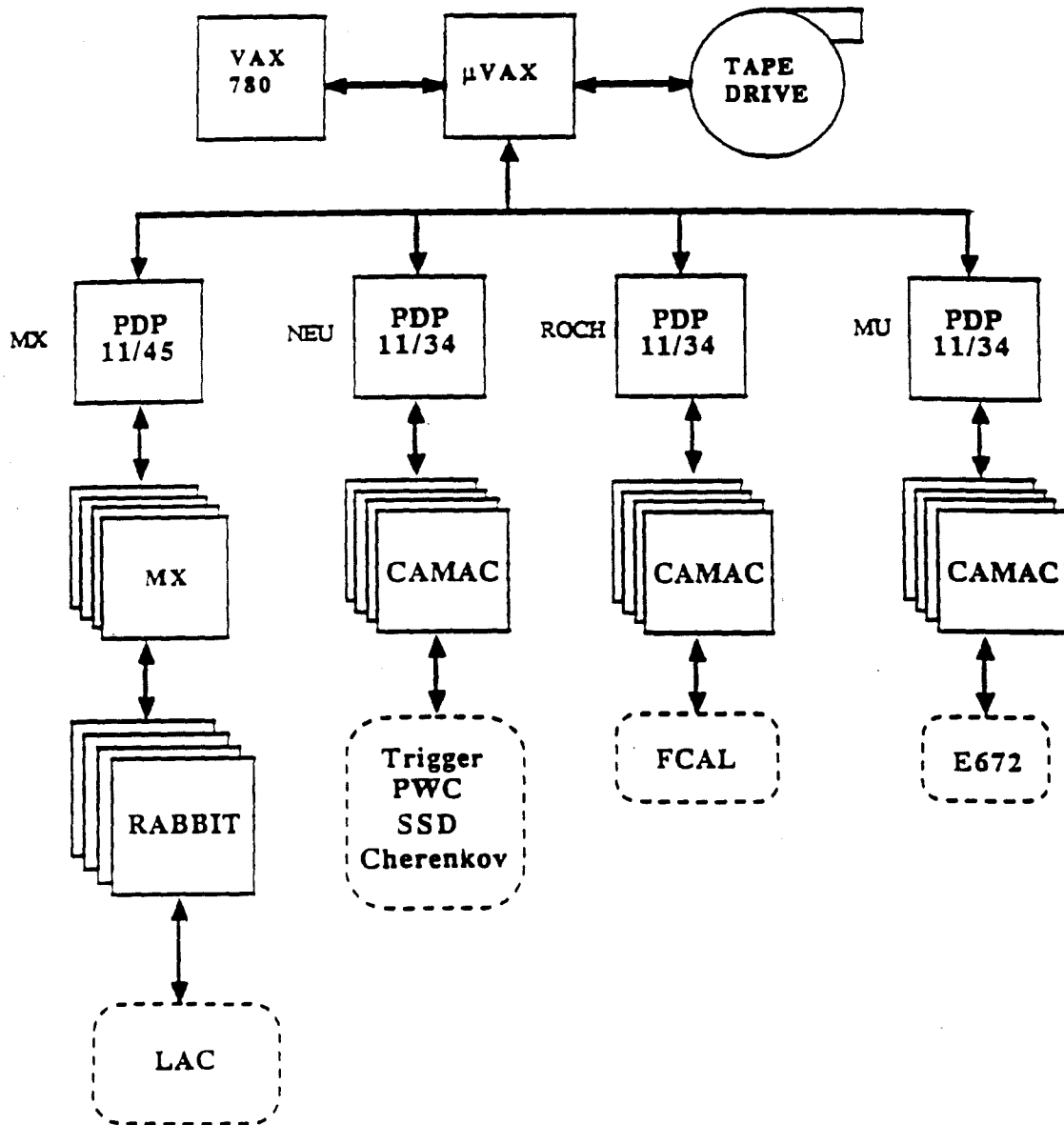


Figure 3.2: Schematic diagram of the data acquisition system.

NEU and is incremented by one for each successive trigger. *EVENT\_BUILDER* uses this number to match data for concatenation.

A fraction of the data were sent to a DEC VAX 780 computer, where a number of CONSUMER<sup>6</sup> programs ran to monitor the quality of the data. The plane monitor, displayed the hit multiplicity and the hit profile for all the SSD's and PWC's. The trigger monitor displayed the reconstructed trigger from CAMAC data. The scaler monitor displayed all the scaler readouts between spills. The status monitor displayed the run number, event number, the size of the PDP-11 sub events in data words. The E706 color graphics event display was also ran through out the data taking as another online monitor and have proved to be very useful tool in monitoring almost all the subsystems of the spectrometer.

The data taking process was segmented in to "runs" where the term "run" referred to a collection of data, during which the operating conditions of the spectrometer remained essentially unchanged. Each 'run' was assigned a unique run number through the *RUN\_CONTROL*. The upper limit on the length of a 'run' was determined by the amount of the data that can be written on to a 6250 bpi magnetic tape. Under normal operating conditions,  $\sim 12,000$  events were written (in  $\approx 20$  minutes) on to one tape defining one 'run'. The OUTPUT was configured to handle two tape drives, minimizing the dead time due to tape handling (mounting and dismounting of the tapes), at the beginning and end of each run.

---

<sup>6</sup>CONSUMER program as part of VAXONLINE, provides a frame work with in which the user can write monitoring programs.

## CHAPTER 4

### Event Reconstruction

The first level of offline analysis is the reconstruction of the entire event. In this chapter we will describe the aspects of event reconstruction relevant to the analysis presented in this thesis; namely, the charge particle reconstruction and the electromagnetic shower reconstruction.

The driver code MAGIC [34], written primarily in FORTRAN-77, controls the reconstruction of data from individual detector elements of the E706 spectrometer. MAGIC is a multi-tasks controller program. In the sequence of an event reconstruction, MAGIC will read in the raw data<sup>1</sup>, unpack the raw data and reconstruct the event. A set of user-supplied control cards determine the specific action(s) that MAGIC will execute and controls the number of events to be processed. In addition to the event reconstruction, MAGIC writes out the reconstructed data on to the Data Summary Tapes (DST's).

MAGIC uses a code-management system called PATCHY developed at CERN<sup>2</sup>. PATCHY [35] provides a method for managing the development of machine independent code which can be run on many different computers, such as VAX, AMDAHL and ACP<sup>3</sup> [36]. The event reconstruction of the data presented in this thesis was done on the Fermilab ACP system. MAGIC also employed the CERN developed memory management system called ZEBRA [37]. Unlike the standard FORTRAN-77, ZEBRA provides a dynamic memory (data banks) structure for the storage of

---

<sup>1</sup>Electronic data that were written on to magnetic tapes during the data taking of the experiment.

<sup>2</sup>European Center for Nuclear Research, Geneva, Switzerland.

<sup>3</sup>ACP is a parallel computer processor developed by the Fermilab Computer Department.

raw and reconstructed data. With ZEBRA, the memory was divided in to several divisions, namely the input division, intermediate division(s) and the output division. Each division contains a specific set of data banks. The ZEBRA data banks in the output division<sup>4</sup> were written onto the tapes, and the data on these output tapes was divided into several different streams by a program called SPLITTER<sup>5</sup>, for higher level PHYSICS analysis.

## 4.1 Charge Particle Reconstruction

In the context of charge particle (track) reconstruction, the tracking system is viewed as consisting of Beam tracking, SSD tracking and PWC tracking. In the following discussion of track reconstruction, the SSD tracks are referred to as “upstream” tracks and the PWC tracks are referred to as “downstream” tracks. The software package (PLREC) that does the track reconstruction is well modularized to handle each section of the tracking system independently[38]. Besides reconstructing the trajectories of charge particles, PLREC also determines the momentum and charge of the reconstructed tracks and reconstructs the primary interaction vertex. Nevertheless, the discussion in this section will be restricted to track reconstruction only. The determination of charge and momentum of tracks and the primary vertex reconstruction will be discussed in the subsequent sections.

Before any track reconstruction takes place, PLUNP<sup>6</sup> routine which is the the raw data unpacker, converts the electronic data into spatial hit coordinates, corrected for any alignment offsets for all the planes. It is this corrected hit coordinate information, that are used in track reconstruction.

---

<sup>4</sup>The ZEBRA output is available in machine independent format.

<sup>5</sup>see chapter 5.

<sup>6</sup>Although PLUNP is part of PLREC, it is called from the driving program MAGIC.

### 4.1.1 Beam Tracking

The beam track reconstruction was done independently in the two orthogonal views X and Y. Each view has three beam chambers. First, all the three-hit tracks in a given view are reconstructed by looping over all possible pairs of hits from two seed planes and searching for a hit in the third plane within a 1.5 strip spacing of the road defined by the two seed hits. When a third hit is found, a least-square fit is made to the three hits and the slope and intercept of the track and the  $\chi^2$  of the fit are calculated. Once all the possible three-hit tracks are found, the two-hit view tracks are made from the hits that are not used in the three-hit track fitting. Beam tracks with  $\chi^2 > 2.0$  and/or a slope  $> 0.01$  radians are rejected. It is further required that the lateral projections of beam tracks lie within  $\pm 0.7$ cm when projected to the beam hodoscope and within  $\pm 1.0$ cm when projected to the experimental target. Beam tracks that did not satisfy these conditions are rejected.

### 4.1.2 Upstream Tracking

The upstream tracking in the SSD's is also done independently in the two orthogonal views X and Y, where each view has four planes. PLREC is designed to optimize the reconstruction of three and four hit view tracks only. No attempt is made to reconstruct two-hit tracks in the SSD's due to the complications arising from the charge sharing and the presence of noise hits, which would lead to the formation of large number of fake two hit tracks. Even at the level of three hit track reconstruction, the charge sharing and noise hits present a great deal of confusion in the pattern recognition, leading to the reconstruction of a substantial fraction of fake three hit view tracks in the SSD's.

The upstream view track reconstruction is very similar to that in the PWC system and the same track fitting code is used in both cases. A detailed description of the

view track fitting algorithm can be found in [38]. Figure 4.1 shows the distributions of fraction of three and four hit SSD tracks per event in the X and Y view.

### 4.1.3 Downstream Tracking

The algorithm for PWC view track fitting is the same as that for upstream view track fitting [38]. Unlike the SSD system, the PWC system consists of four views (X,Y,U and V), enabling the reconstruction of *space* tracks. First, the view tracks are formed in the four views and then X and Y view track pairs are correlated with pairs of U and V view tracks. When an XY pair matched with a UV pair, a *space* track is formed. Again, a detail description of the downstream view and space track fitting algorithms can be found in reference [38].

Each accepted space track is required to have at least thirteen hits. The 16, 15 and 14 hit space tracks have a  $\chi^2/DOF$  cut off at 3.0 and for the 13 hit space tracks, the  $\chi^2/DOF$  cut is set at 1.5. Figure 4.2 shows the  $\chi^2$  distribution for the 13, 14, 15 and 16 hit space tracks. It is further required that no two space tracks share more than *six* hits. If two space tracks shared six hits, the one with the lowest number of hits is dropped. If they have the same number of hits, then the one with the higher  $\chi^2$  is deleted. Any space track with nine or more un-shared hits was retained. Figure 4.3 shows the relative fraction of the 13, 14, 15 and 16 hit tracks per event.

## 4.2 Determination of Momentum and Charge of Tracks

To determine the charge and momentum of the reconstructed tracks, it is necessary to know the bending angles of the tracks in the dipole magnetic field. This bending angle can be determined by identifying the correct pair of upstream and downstream tracks that represents the trajectory of a charge particle through the tracking system. This pairing of the upstream and downstream tracks is called the

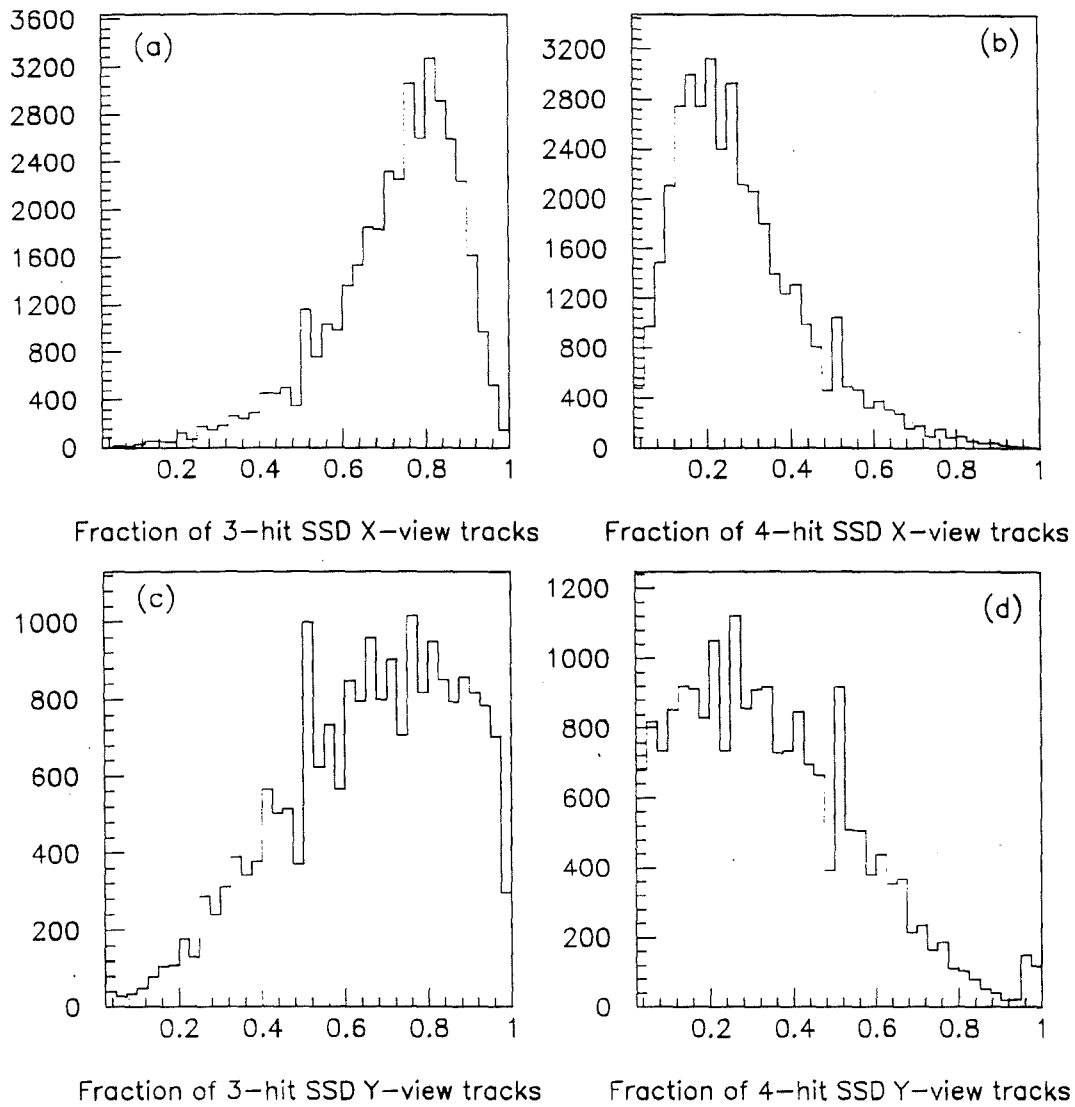


Figure 4.1: (a)–(d) Fraction of three and four hit tracks per event in the SSD X and Y view.

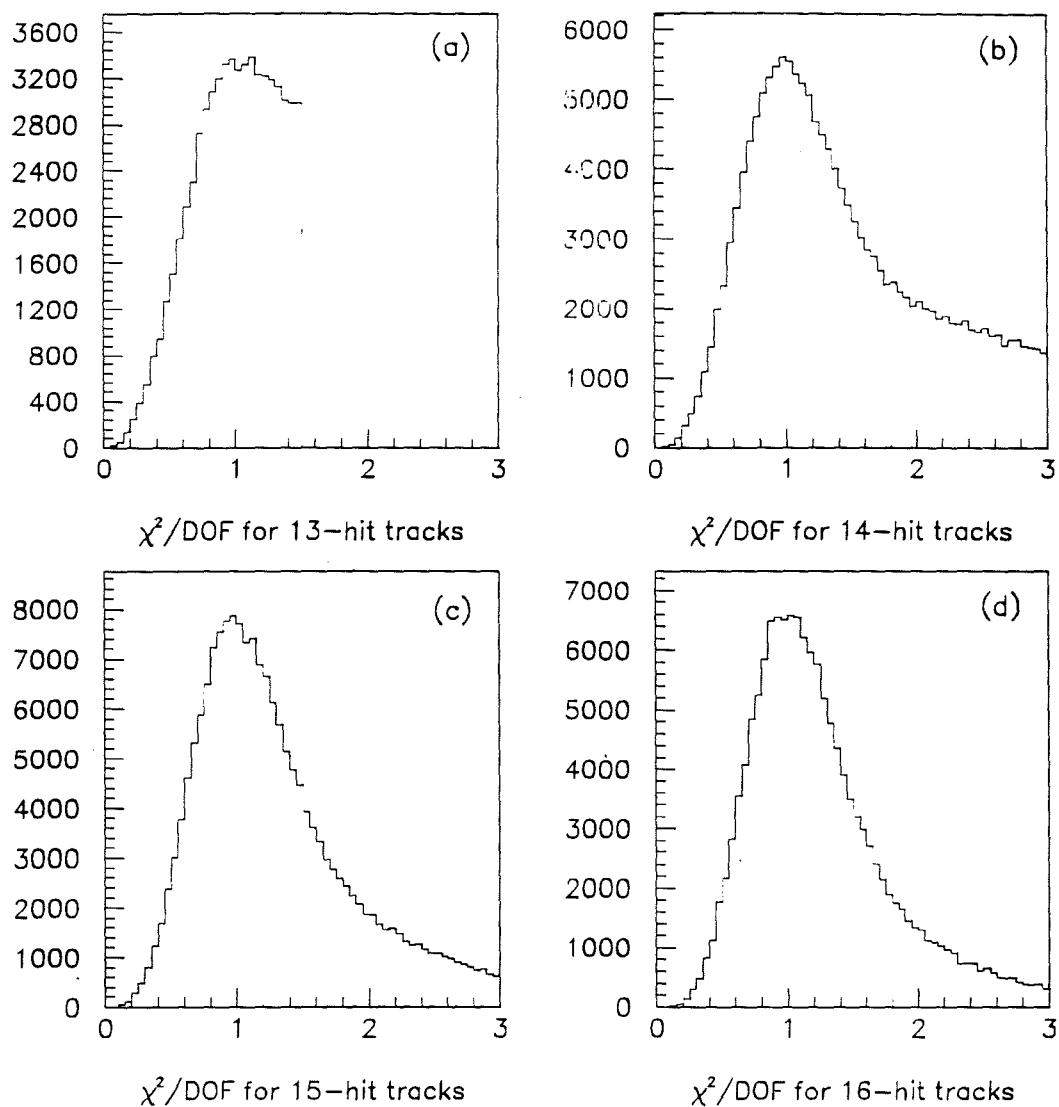


Figure 4.2:  $\chi^2/DOF$  for PWC space tracks (a) 13 hit space tracks (b) 14 hit space tracks (c) 15 hit space tracks (d) 16 hit space tracks.

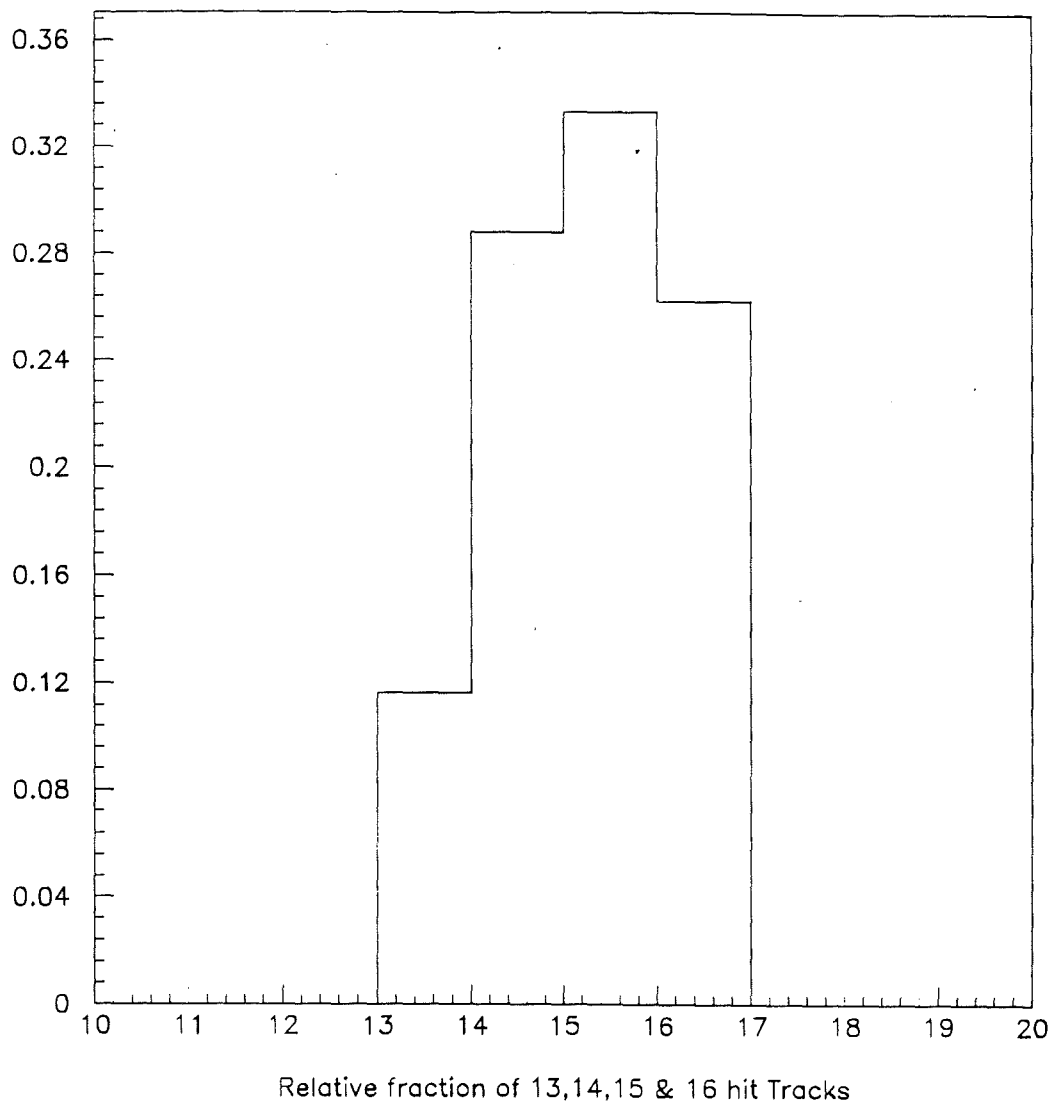


Figure 4.3: Relative fraction of the 13, 14, 15 and 16 hit PWC space tracks per event.

*linking* at the magnet. The procedure for linking tracks is very briefly outlined here. A detailed discussion of linking tracks can be found in reference [38].

In the *linker*, each PWC *space* track was matched with the SSD view tracks, by projecting the tracks to the *effective* center of the magnet. The upstream view track projections<sup>7</sup> at the center of the magnet should be within  $\pm 0.7\text{cm}$  to that of a PWC space track for the view tracks to link with a space track. Since the tracks bend primarily in the XZ plane, an additional cut of  $2.5\text{ mrad}$  was imposed on the Y-slope difference between the upstream and downstream tracks. These cuts were determined by plotting the X and Y view projection differences and the Y-slope difference. Figure 4.4 shows the  $\Delta X$  and  $\Delta Y$  at the center of the magnet for the linked tracks. Due to the ambiguities of the track projections and the limited constraints on the upstream view tracks, more than one upstream view track can frequently link to a PWC space track. In that case, for each space track, up to four links (in each view) are stored in Zebra banks, in ascending order of the projection difference, with the first link being the closest one and often referred to as the *best link*. Once the primary interaction vertex was reconstructed these four links are re-arranged, giving preference to the linked view tracks coming from the primary vertex, and re-defining the best link. For a given downstream track, if there is no upstream X-view track within the linking window, a straight line was drawn from the projected point at the magnet center to the primary vertex point, to determine the bending angle. If the primary vertex wasn't found, a line was drawn to the center of the target.

Once the bending angle was determined using the *best link*, the momentum and the charge of a track can be calculated as follows.

---

<sup>7</sup>Track projections at the center of the magnet were corrected for the effective magnetic field approximation.

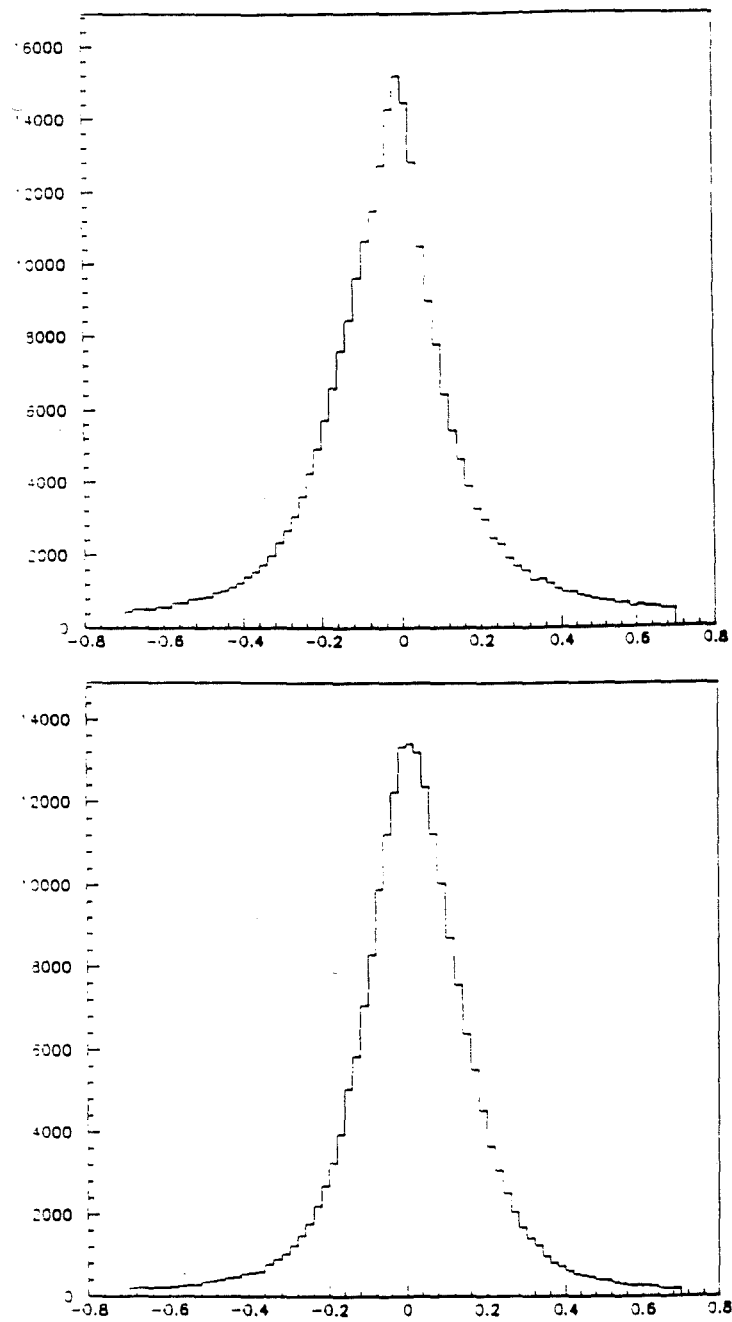


Figure 4.4: Track projection differences at the center of the magnet. Top:  $\Delta X$  and Bottom:  $\Delta Y$ .

The sign of the charge of a track is given by Eq. 4.1.

$$q = \text{sign}(\theta_1 - \theta_2) \cdot \text{sign}(B_0) \quad (4.1)$$

and the  $P_T^{\text{kick}}$  is given by Eq. 4.2

$$P_T^{\text{kick}} = qB_0L_0 \quad (4.2)$$

where  $B_0$  is the magnitude of the effective magnetic field and  $L_0$  is the effective length of the magnet, in the thin lens approximation.

The momentum ( $P$ ) of a track can be determined from the following equations.

$$\sqrt{p_x^2 + p_z^2} = \frac{P_T^{\text{kick}}}{\sin(\theta_2) - \sin(\theta_1)} \quad (4.3)$$

$$\frac{p_x}{p_z} = \tan(\theta_x) \quad (4.4)$$

$$\frac{p_y}{p_z} = \tan(\theta_y) \quad (4.5)$$

where  $p_x, p_y$  and  $p_z$  are the three components of the the momentum and  $\theta_1$  and  $\theta_2$  are the entrance and exit angles of the track into and out of the magnet, respectively, in the XZ plane.  $\tan(\theta_x)$  and  $\tan(\theta_y)$  are the upstream X and Y view track slopes, respectively.

The momentum scale in the tracking system was calibrated using the decays of  $K_S^0 \rightarrow \pi^+\pi^-$  and  $J/\psi \rightarrow \mu^+\mu^-$ . See figures 4.5 and 4.6[39]. Based on a Monte Carlo study, the momentum resolution of the tracking system was found to be  $\sigma_P/P \simeq 0.09\% \times P$  [23].

### 4.3 Primary Vertex Reconstruction

As part of PLREC, the piece of code that does the primary vertex reconstruction was developed over a period of two years by several collaborators on the experiment. Since this author was responsible for developing the code into its final form for the

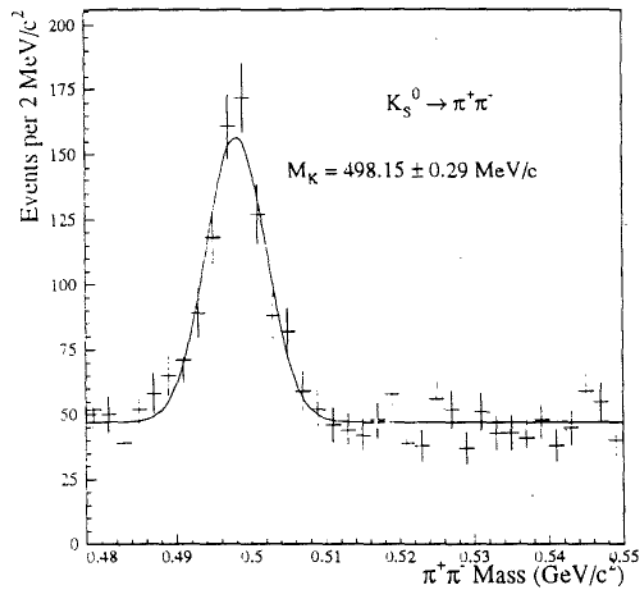


Figure 4.5:  $\pi^+\pi^-$  mass distribution with corrected momentum scale.

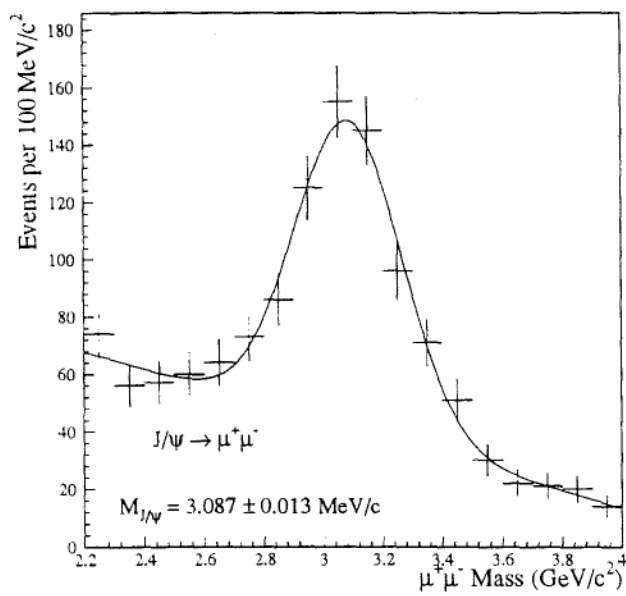


Figure 4.6:  $\mu^+\mu^-$  mass distribution with corrected momentum scale.

1989 ACP pass, the vertex reconstruction algorithm and its performance will be discussed in a little more detail.

The general philosophy of the vertex reconstruction is to first determine the X and Y view vertices using the SSD view tracks and then match the two view vertices to get the final primary vertex position.

### 4.3.1 View Vertex Fitting

The view vertex reconstruction procedure is the same for both X and Y views. In the view vertex reconstruction, the vertex fitting algorithm first selects four-hit linked SSD view tracks that come from the fiducial target region. If there are four or more such tracks selected, the fitting algorithm proceeds to fit a view vertex as described below. If there aren't enough tracks, the algorithm also looks for un-linked four hit view tracks coming from the fiducial target region. If the algorithm selects at least four 4-hit view tracks, it proceeds to fit a view vertex. Otherwise it will also search for three-hit linked view tracks coming from the fiducial target region. If there aren't sufficient tracks selected, the view vertex fitting is not performed.

Once a set of SSD view tracks are selected, the algorithm does an iterative process to fit a view vertex by minimizing a  $\chi^2$  as defined in equation 4.6 below. For example, for X-view vertex fitting, the  $\chi^2$  is minimized with respect to the X and Z coordinates of the vertex to be determined.

$$\chi^2 = \sum_k (\chi_k^2(a_k, b_k) - \chi_k^2(a'_k, b'_k)) \quad (4.6)$$

where  $\chi_k^2(a_k, b_k)$  is defined as

$$\chi_k^2(a_k, b_k) = \sum_j \frac{[x_j - (a_k z_j + b_k)]^2}{\sigma_j^2} \quad (4.7)$$

and  $\chi_k^2(a'_k, b'_k)$  is defined as

$$\chi_k^2(a'_k, b'_k) = \sum_j \frac{[x_j - (a'_k z_j + b'_k)]^2}{\sigma_j^2} \quad (4.8)$$

and  $a_k$  and  $b_k$  are the slopes and intercepts of the fitted SSD upstream view tracks as described in section 4.1.2.  $a'_k$  and  $b'_k$  are the slopes and intercepts of hypothetical tracks that pass through the primary view vertex.  $(x_j, z_j)$  is a point on the view track in the X-Z plane.  $\sigma_j$  is the position resolution of the SSD's. The summation in equation 4.6 is over all selected view tracks and the summation in equations 4.7 and 4.8 is over the total number of SSD planes used in fitting that track.

Expanding equation 4.7 about  $(a'_k, b'_k)$  and setting  $b'_k$  equal to  $b_k$  and minimizing equation 4.6 with respect to X and Z, one can solve for the X-view vertex position.

After a candidate view vertex is found, the impact parameter<sup>8</sup> to the vertex is calculated for all the selected tracks. Figure 4.7 shows the X and Y view impact parameter of the tracks used in vertex fitting. At the end of each iteration, the track with the largest impact parameter is removed from the selected track sample, and a view vertex is fitted with the reduced set of selected tracks. The iterative procedure is stopped when the largest impact parameter of the tracks associated with the vertex is less than  $50\mu\text{m}$  or the average impact parameter of all the tracks associated with the view vertex is less than  $20\mu\text{m}$  or one is left with only two tracks associated with the view vertex. Once a view vertex is found, all the tracks in that view with an impact parameter less  $50\mu\text{m}$  are assigned to the vertex. The beam track associated with the view vertex is defined as the one with the smallest impact parameter ( $< 50\mu\text{m}$ ) to that view vertex. This procedure is repeated for the Y-view too. The algorithm is optimized to find the primary vertex position in each view.

### 4.3.2 Matched Vertex Fitting

Once the view vertices are found, a re-fitting is done using the tracks in one view and the Z-position of the view vertex found in the other view, to obtain the best

---

<sup>8</sup>Impact parameter of a track to a vertex is defined as the shortest distance between the track and the vertex.

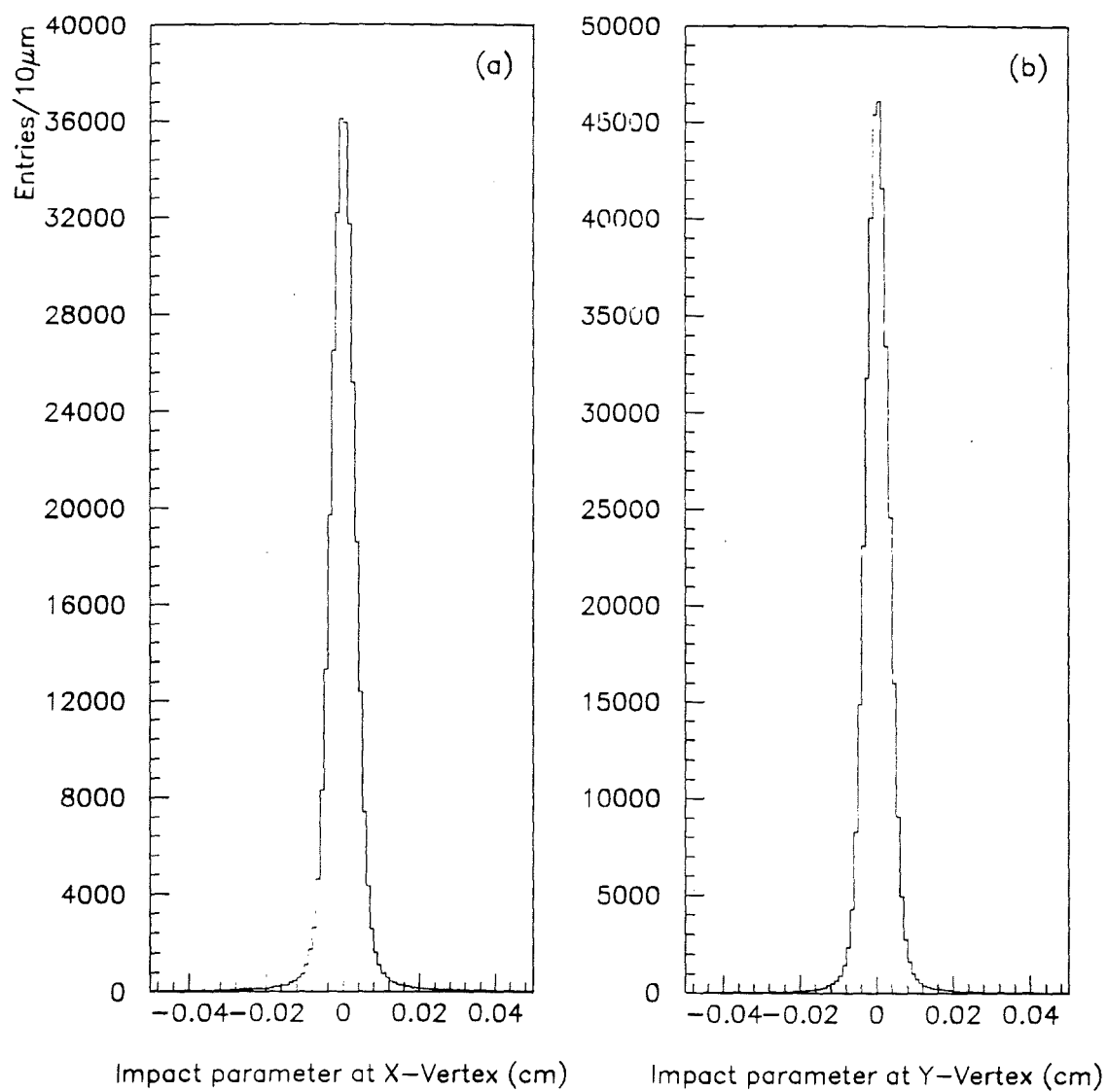


Figure 4.7: X and Y view impact parameter of tracks associated with the view vertices.

possible primary vertex location. The tracks selected for the re-fitting in one view should come from the fiducial target region in that view and should intersect with each other within 1 cm of the Z-position of the other view vertex. The re-fitting is done for both X and Y views. At the end of re-fitting, one is left with a minimum of a single pair of view vertices or a maximum of four pairs of view vertices. In the case of a single pair, if the difference of the Z-position of the two view vertices is less than 1 cm, the pair is called a matched vertex and the weighted average of the Z coordinates of the two view vertices is calculated to determine the Z-position of the final primary vertex. In the case of more than one pair of view vertices, the upstream one with the smallest Z-difference (with Z-difference less than 1 cm) is called the matched vertex and the weighted average of the Z-position is calculated. In both cases, the X and Y positions of the two view vertices are used as the two transverse coordinates of the final primary vertex.

### 4.3.3 Vertex Resolution and Reconstruction Efficiency

Figure 4.8 a) shows the difference in the Z-position of the two view vertices and figure 4.8 b) shows the spatial impact parameter of the associated beam track at the vertex. These two plots provide a measure of the longitudinal and the transverse position resolution of the primary vertex. The resolution along the beam direction is about  $700 \mu\text{m}$  and the transverse resolution is about  $20 \mu\text{m}$ . These numbers are in agreement with calculations that include the instrumental resolution as well as the multiple scattering of the secondary particles associated with the primary vertex [19][21]. Figure 4.9 a) shows the reconstructed vertex Z-position where the segmented target structure is clearly visible. The two small double-peaks at either end are due to vertices produced at the two SSD planes immediately before and after the target. Figure 4.9 b) shows the longitudinal vertex position resolution as a function of the Z-coordinate of the primary vertex. It is obvious from these two

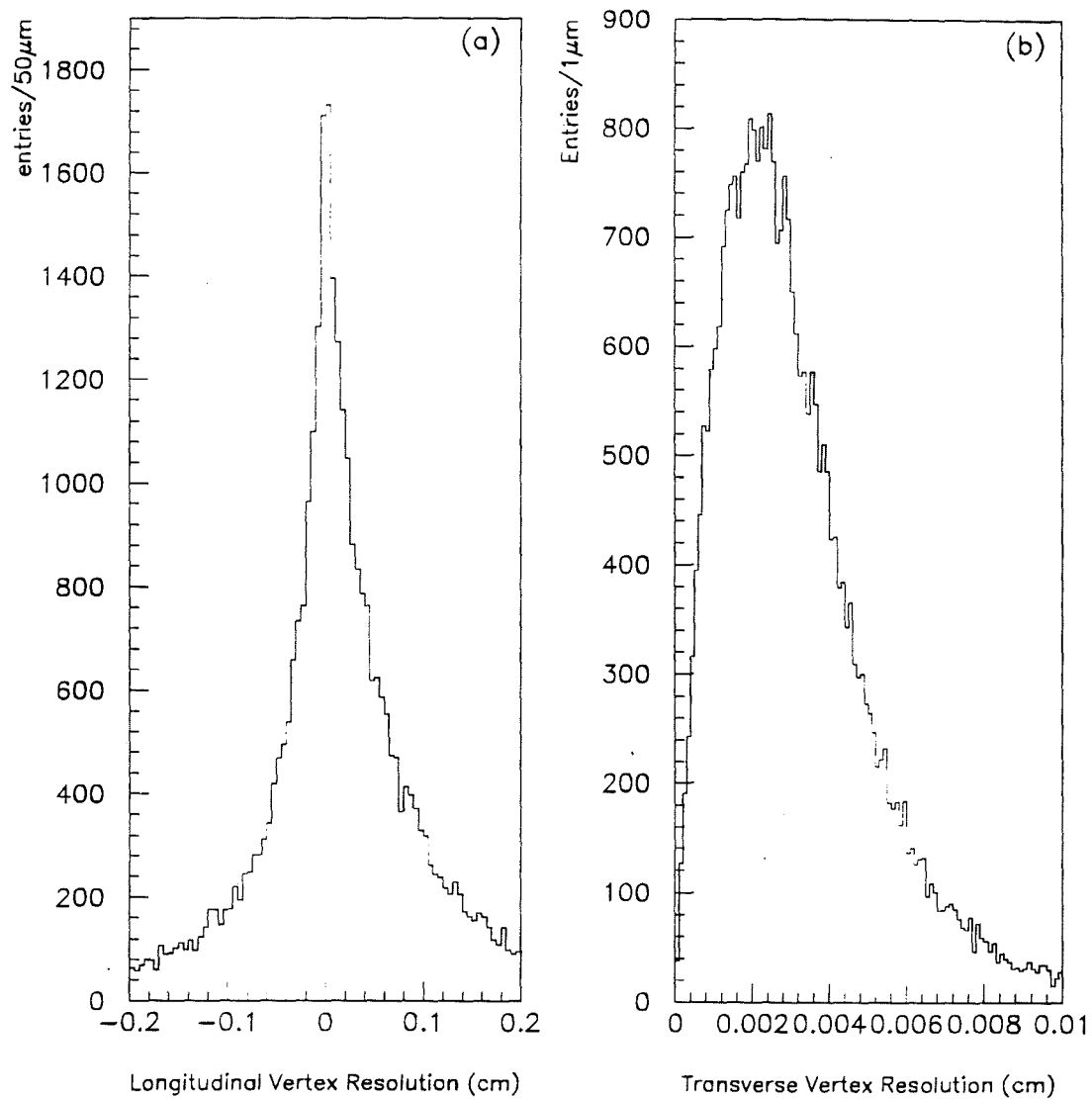


Figure 4.8: a) Z-position difference of the two view vertices. b) Spatial impact parameter of the beam track assigned to the primary vertex.

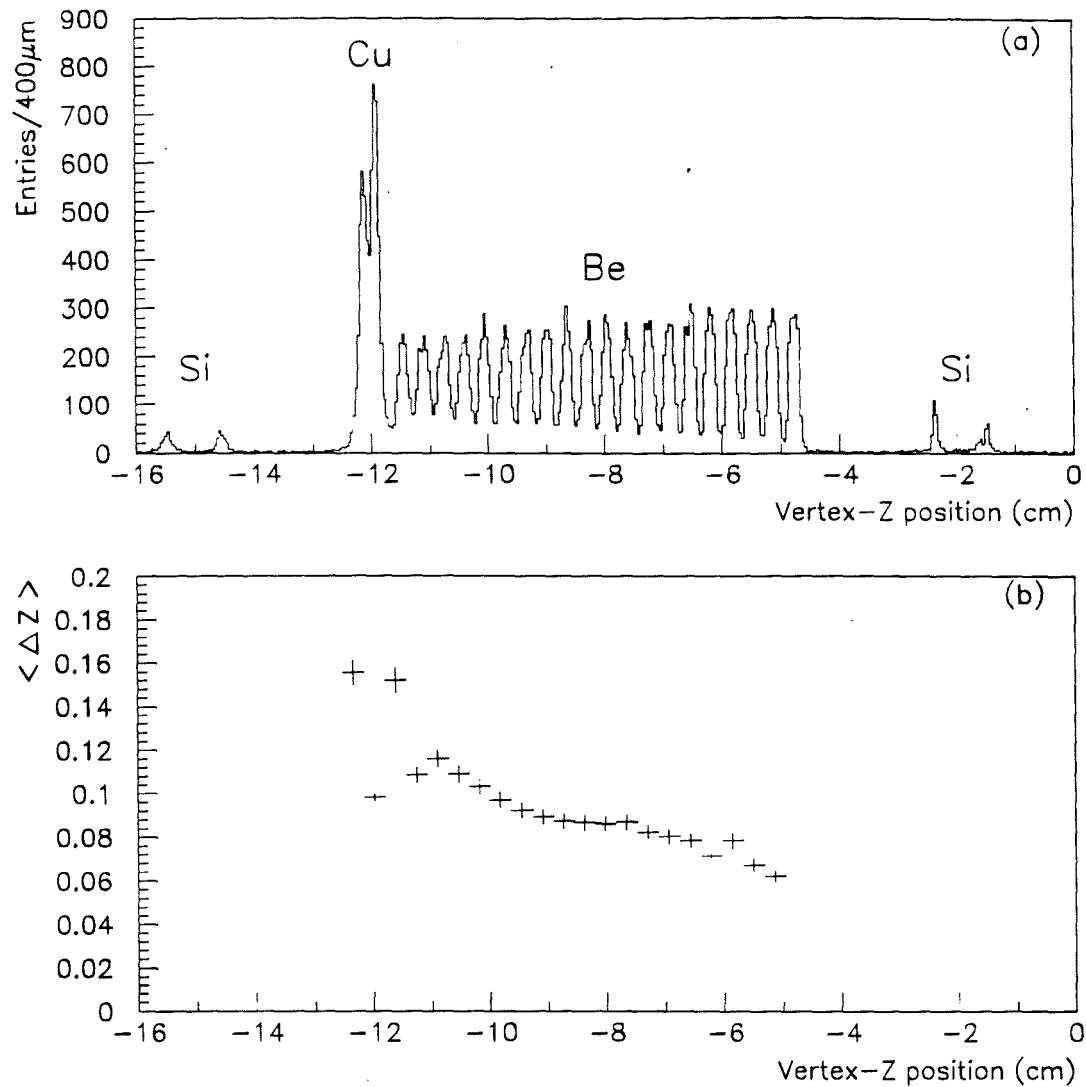


Figure 4.9: a) Z-position of the reconstructed primary vertices. The segmented target structure is clearly visible. b) Average Z-position difference of two view vertices as a function of Z.

plots, that the downstream vertices have a better Z-position resolution compared to the vertices further upstream in the experimental target. This difference is primarily due to multiple Coulomb scattering of secondary particles produced in the upstream interactions and the increased lever arm between the upstream interactions and the downstream SSD modules.

To account for the vertex reconstruction inefficiencies, a careful study<sup>9</sup> was performed on a pre-selected sample of events which contained high  $P_T$  photons, in which the reconstruction program failed to find a primary interaction vertex. Based on this study, a correction factor was calculated as a function of the vertex Z-position (see chapter 7). The average vertex reconstruction efficiency was found to be  $\sim 93\%$ .

#### 4.4 Electromagnetic Shower Reconstruction

The electromagnetic shower reconstruction program EMREC reconstructed the energy and position of the incident photons and electrons that shower in the EMLAC. The electromagnetic shower reconstruction has been addressed in detailed in the reference [27]. For the sake of completeness, in the next two subsections, we will present a brief description of the reconstruction of energy and position of the photons and the timing information on the EMLAC pulse height.

The EMREC program uses the energy deposition ( $E_i$ ) on each channel, in reconstructing the electromagnetic showers. The strip energy  $E_i$  is determined from the formula,

$$E_i = A_{EM} G_i (N_i - N_i^0) \quad (4.9)$$

where  $N_i$  is the digitized value of the pulse height in the channel,  $N_i^0$  is the pedestal for the channel<sup>10</sup>,  $G_i$  is the relative value of the channel gain and  $A_{EM}$  is the nominal normalization factor of the EMLAC, which was roughly determined from the electron

---

<sup>9</sup>Including a visual scan of the events.

<sup>10</sup>PEDESTAL for a channel is the digitized pulse height observed in the absence of a true signal.

beam calibration data to be 3.1 MeV per ADC count.

For reconstruction purposes, the corresponding strip energies from the front and back section of the EMLAC were added together to form a "software summed" section. Except where otherwise noted, the pattern recognition code operated on these summed signals.

#### 4.4.1 Reconstruction of Photon Energy and Position

The reconstructor first finds *groups* within each of the four views ((1) left-R, (2) right-R, (3) inner- $\phi$  and (4) outer- $\phi$ ). A group is defined as a cluster of at least three consecutive strips in the views 1-3 or at least two consecutive strips in the fourth view with a total cluster energy greater than 750 MeV. It was further required that the average energy per strip in the cluster be greater than 150 MeV and the maximum strip energy be more than 300 MeV. Once a group is found, the information is stored in a designated ZEBRA bank.

Once the groups are found, the code then searches for the *peaks* in each of the groups. A peak in a cluster is defined as the point where the derivative of the energy distribution changes from positive to negative. For each found peak, there are two *valleys* located at either side of the peak. A *valley* is defined as either the strip with lowest deposited energy between two peaks or the end strip in the group if the peak is first, last or the only peak in the group. To recover the low energy peaks lost due to the addition of front and back energies, the peak finding algorithm is applied to the front section again, searching for peaks between any two valleys already found in the summed section. For each peak found in the front section R-view, the front radial position and the corresponding back peak radial position were determined.

In the next stage of the shower reconstruction, single-view photons ("gammas") were reconstructed using the already determined groups and peaks, in each view. For single-peak groups, a parametrized shower shape was fitted to determine the

energy and position of the “gamma”. For multi-peak groups, first the group was split into separate showers and then the energy and position were calculated on the corrected pulse distribution [27].

The last step in the shower reconstruction is to correlate the “gammas” in R and  $\phi$  views to form the final photons. Since the radial and azimuthal view readout boards were alternated in the EMLAC, the longitudinal energy profile of showers would be roughly the same in both views. This means that the total energy and the ratio of front and back energies would be very close in the two views. These two conditions have been used as the primary matching criteria in correlating “gammas”. The problems arising due to matching “gammas” near view boundaries were handled appropriately [27]. After all “gammas” were correlated, the  $\phi$  view “gammas” were reconstructed again, using the radial information obtained during the correlation procedure. This yielded a more accurate energy. After the  $\phi$  “gammas” were refitted, the “gammas” were re-correlated and the final photon energy and position were determined.

#### 4.4.2 Photon Arrival Time

The arrival time associated with each final photon is calculated using the TVC<sup>11</sup> information [28]. This timing information is used in the analysis to reject photons that were “out-of-time” with the event interaction.

---

<sup>11</sup>Time to Voltage Converter (TVC) is a timing circuitry inside the LAC amplifier modules.

## CHAPTER 5

### Data Selection

The table 2.3 summarizes the full data sample collected with a LAC trigger in the 1987/88 run. The data are divided in to 6 sets, defined by target type, beam polarity etc. The sets were labeled A through F in reverse chronological order. Out of this full data sample, only the sets A, C, D and E are used in the analysis presented in this thesis. Set B is omitted due to a malfunction of one of the tracking chambers and set F is not used because the data for this set were collected before the *Single-Local* trigger was implemented.

The data in the selected sets also contain uninteresting events, such as the events with no reconstructed primary vertex, events triggered by halo muons, etc., that are not relevant to this analysis. All such events were removed from the data sample by applying suitable event level cuts which we will describe later in this chapter. Table 5.1 summarizes the data sample remaining in each selected set after applying the cuts. In this chapter we will describe the selection of events containing a large transverse momentum  $\gamma$ ,  $\pi^0$  or  $\eta$  from the compressed binary DST's. We also will describe the cuts applied in selecting charged tracks and photons, to be included in the reconstruction of jets. The subject of the calculation of meson induced background to direct photon signal is introduced at the end of this chapter. The actual  $\pi^0$  background estimation is described in chapter 7.

## 5.1 Event Selection

Only the events which satisfied the *Single-Local* trigger were analyzed for two reasons. First, in the  $P_T$  range of interest, this trigger was very efficient for the detection of  $\pi^0$ 's and  $\gamma$ 's. Second, the *Single-Local* trigger is the only trigger which is understood and for which a reliable set of corrections exists. To ensure the quality of the data and to select a rich sample of enhanced high  $P_T$  events with a non-muon induced LAC trigger, each reconstructed event has been subjected to the following list of cuts.

- Neither veto wall shadowing the triggering quadrant registers a hit.
- The event has a reconstructed primary vertex in the fiducial target region.
- The maximum uncorrelated energy in the triggering quadrant is less than 10 GeV.
- The event contains reconstructed physics tracks and reconstructed showers.

Table 5.1: Summary of the data sample which survives the successive event level cuts described in the text above.

Run Set	Veto Wall cut	Vertex cut	Uncorrelated energy cut	Final No. Events
A	188,632	147,230	142,730	142,730
C	47,084	37,735	36,557	36,557
D	57,399	46,492	44,778	44,778
E	38,863	26,728	25,954	25,954

Two of the potential major sources of background to the direct photon signal are from the bremsstrahlung of beam halo muons in the outer regions of the EMLAC and from the electromagnetic decay of  $\pi^0$  and  $\eta$  mesons[27, 39]. The veto wall cut in the event selection was imposed, mainly, to reject halo muon induced high  $P_T$  triggered events from the data sample. Muon rejection will be discussed in section 5.1.1 and the background due to the electromagnetic decay of  $\pi^0$ 's and  $\eta$ 's will be discussed in section 5.3. The vertex cut helped not only to reject muon induced events but also to insure that the event interaction occurred in the fiducial target region. The reconstructed longitudinal vertex position helped select events originating from different nuclear targets.

The uncorrelated energy cut was imposed to reject events where the energy and the location of photons were not properly established.

### 5.1.1 Muon Background

The in-flight decays of pion beam particles resulted in a large number of muons travelling more-or-less parallel to the beam axis but frequently several feet away from it. These muons produce photons through bremsstrahlung and at large radius satisfy the high  $P_T$  trigger. The *on-line* veto wall requirement in the formation of the LAC pre-trigger vetoed the muon-induced high  $P_T$  events at the trigger level[32]. It is required that the section of the two veto walls corresponding to the triggering quadrant have no signal within  $\sim -20$  ns to 120 ns of the interaction time.

The *off-line* veto wall cut is necessary due to; a) the inefficiency of the two veto walls, b) the gaps between the scintillating counters in the veto wall coincidence and c) the fact that the online veto wall signal time window was not centered with respect to the octant pre-trigger signal. Evidence for these "out-of-time" muon induced events is illustrated in figure 5.1(b).

Besides the *off-line* veto wall cut, the photon timing information, its longitudinal profile development and its directionality can all be used to reject muon induced events.

Associated with each reconstructed photon is its arrival time at the LAC with respect to the time at which the event's interaction occurred. This timing information is calculated in EMREC for each reconstructed photon using the timing information provided by the TVC's. Figure 5.1 show the timing distributions for single photons (a) with *off-line* veto wall cut and (b) without *off-line* veto wall cut. The distribution is sharply peaked at zero, when there is no hit in the veto walls shadowing the triggering quadrant. The distribution with a veto wall hit is broadly peaked at -40ns. This shows that the trigger was sensitive to muons occurring more than 20ns, before the interaction, and hence not vetoed at the trigger level. The broadness of this peak compared to that in (a) indicates the fact that the muons are not correlated with the event's interaction. The relatively small peak at zero and the large positive tail in figure 5.1(b) reflects the inefficiency in the *on-line* veto wall requirement. All the single photons occurring more than 15ns before or 40ns after the nominal zero time were rejected from the single photon data sample.

Another quantity that was used to reject muon induced showers is the directionality of the photons. The directionality, which is a measure of the photon's trajectory in the EMLAC, is defined as;

$$\delta_r = R_f - \frac{Z_f}{Z_b} R_b \quad (5.1)$$

where  $R_f$  and  $R_b$  are the radial positions of the reconstructed photons at the front and back section of the LAC. The quantities

$$Z_f = 900 \text{ cm} \quad (5.2)$$

$$Z_b = 918.5 \text{ cm}$$

are the longitudinal positions of the beginning of the front and back sections of the

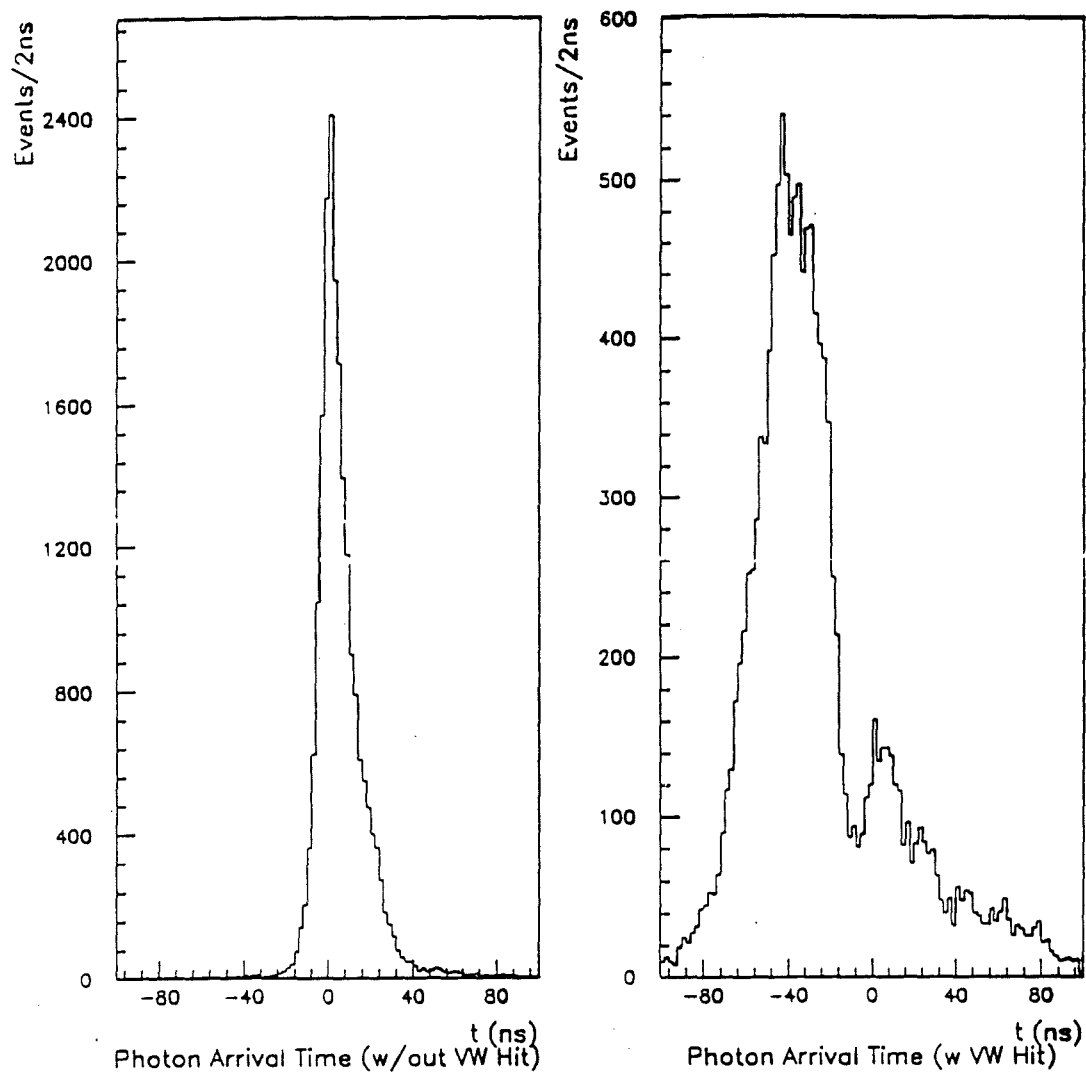


Figure 5.1: TVC distributions for (a) non- $\mu$  events and (b)  $\mu$  induced events.

LAC relative to the target center. Particles which travel parallel to the beamline, *eg.* muons, will tend to have larger values of  $\delta_r$  at all radii than those which came from the target. In fact, particles coming from the target are expected to have directionalities distributed about zero. This effect is illustrated in Figure 5.2.

A scatter plot of directionality versus  $P_T$  for single photons is shown in figure 5.3(a) for events with a hit in either of the veto wall quadrants shadowing the triggering quadrant. The large enhancement in the positive high directionality ( $> 0.4$ ) band for the entire high  $P_T$  range indicates a large contamination of muon induced events in this data sample. Figure 5.3(b) shows the effect of the *off-line* veto wall cut in rejecting muon induced high  $P_T$  events. The remaining band which is nearly symmetric about zero, corresponds to the photons originating from the target.

Figure 5.4 shows the correlation of the photon timing and its directionality for events (a) with and (b) without a hit in the veto wall quadrant corresponding to the triggering quadrant. It is clear from the top figure that the showers with high directionality are generally out-of-time with the event interaction. The dotted lines in figure 5.4(a) shows the *off-line* cuts used to select the direct photon candidate events.

### 5.1.2 Hadron and Electron Rejection

The photons that survived the muon rejection cuts were subjected to more cuts to remove the background to the direct photon sample due to charged and neutral hadrons and due to electrons and positrons.

The fact that the electromagnetic and hadronic showers have a different longitudinal profile development was used to discriminate between hadronic and electromagnetic showers. Hadrons deposit much of their energy in the back section of the EMLAC and deposit relatively small amount of energy in the front section of

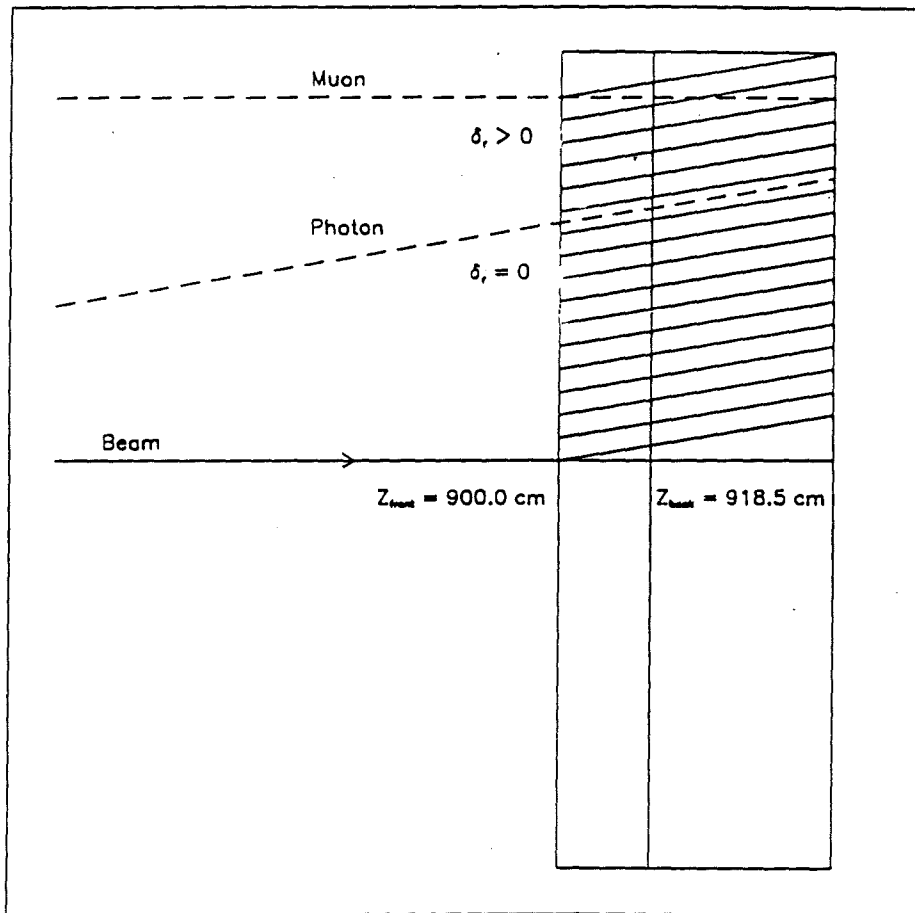


Figure 5.2: Illustration of the concept of photon “directionality”. Showers generated by particles from the target tend to have directionalities near zero. Showers generated by particles incident parallel to the beam line have larger positive directionalities.

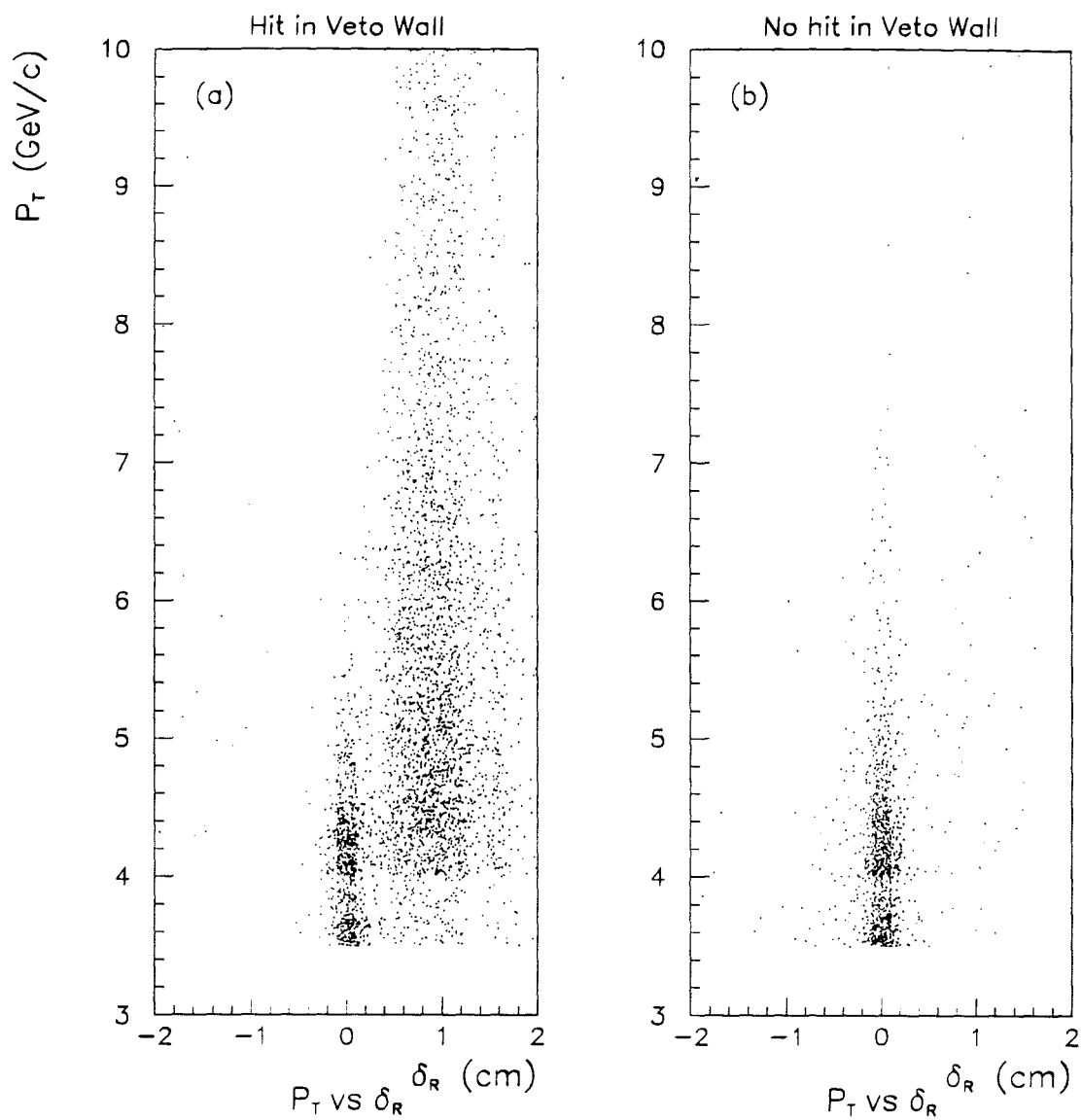


Figure 5.3: Photon  $P_T$  vs directionality. (a) A hit in either veto wall section shadowing the triggering quadrant, and (b) No hit in the veto wall.

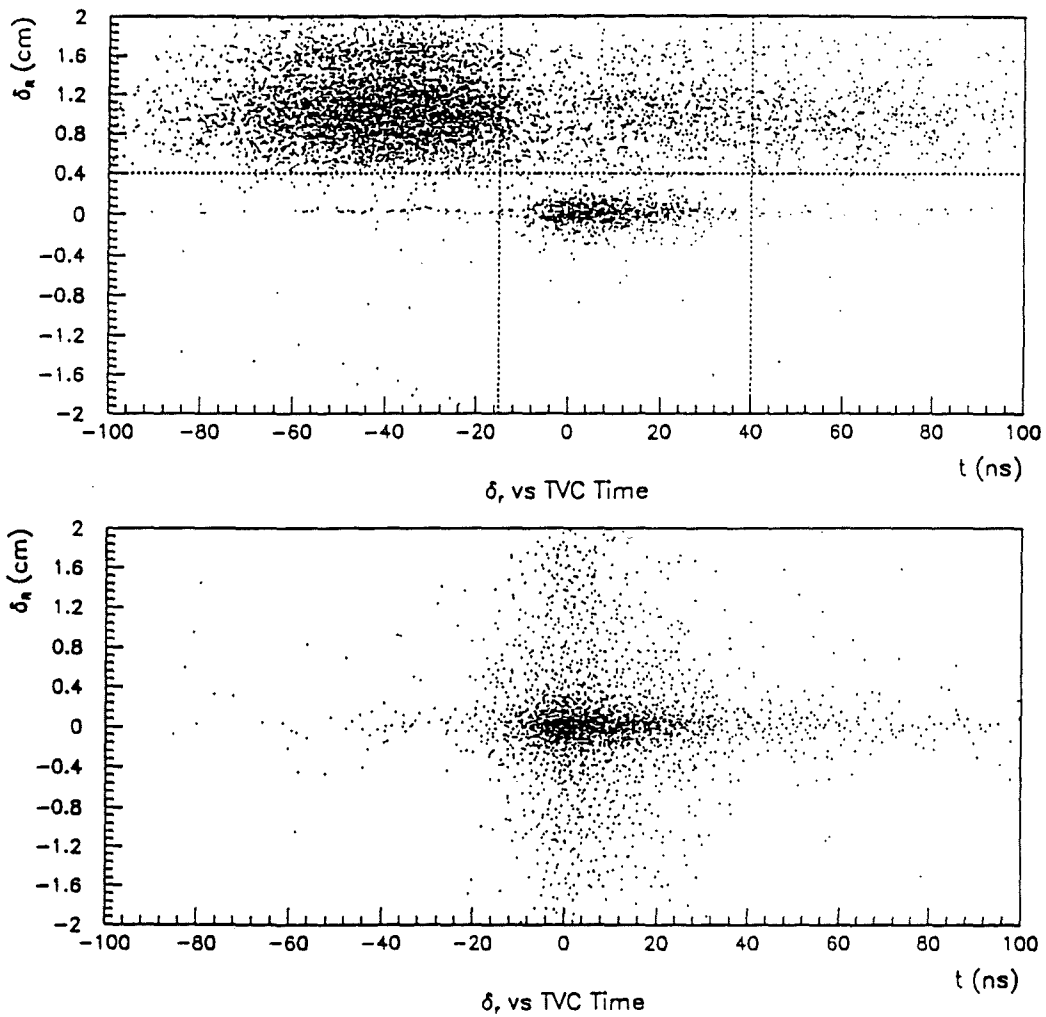


Figure 5.4: Photon directionality *vs* TVC time (a) A hit in either veto wall section shadowing the triggering quadrant, and (b) No hit in the veto wall section shadowing the triggering quadrant.

the EMLAC due to its small interaction length. Thus the distribution of the ratio “ $E_{Front}/E_{Total}$ ” for hadrons tends to peak at a value much less than 1.0 whereas for the electromagnetic showers this distribution tends to peak near one. Figure 5.5 shows the  $E_{Front}/E_{Total}$  distributions for electromagnetic and hadronic showers. All the showers with  $E_{Front}/E_{Total} < 0.2$  were excluded from the direct photon sample.

Another source of background to the direct photon signal are the electrons and positrons produced by pair-conversion of photons from  $\pi^0$  decay in the target. These conversion electrons and positrons are called ZMP (Zero Mass Pairs)[23]. This contamination is reduced by using the tracking information from the PWC system. Figure 5.6 shows the radial distance between these converted pairs and the nearest shower at the front face of the EMLAC[23, 40]. It is clear that the tracks and showers corresponding to ZMP’s match quite well within 1cm of radial distance between them. This fact was used to reject electromagnetic showers due to ZMP’s, and all showers that match with a charged track at the front face of the EMLAC with  $\Delta R < 1$  cm are rejected from the direct photon sample.

Finally fiducial cuts are applied to reject photons which fell close to detector boundaries. The reconstruction of these photons was not very reliable. It is required that the reconstructed radial position (  $R$  ) of the photons fall in the region  $24 \text{ cm} < R < 138 \text{ cm}$  and the  $\phi$  position be 2 cm away from the EMLAC octant boundary and 3 strips away from the quadrant boundary.

### 5.1.3 $\pi^0$ and $\eta$ Definition

The understanding of the reconstruction of  $\pi^0$  and  $\eta$  signals is vital to the understanding of the direct photon signal since the electromagnetic decay of these two neutral mesons produces a potential source of background to the direct photon signal.

Figure 5.7 shows the two photon invariant mass spectrum for the  $\gamma\gamma$  pairs, with both  $\gamma$ ’s in the same triggering octant and with the vector sum  $P_T$  of the two photon

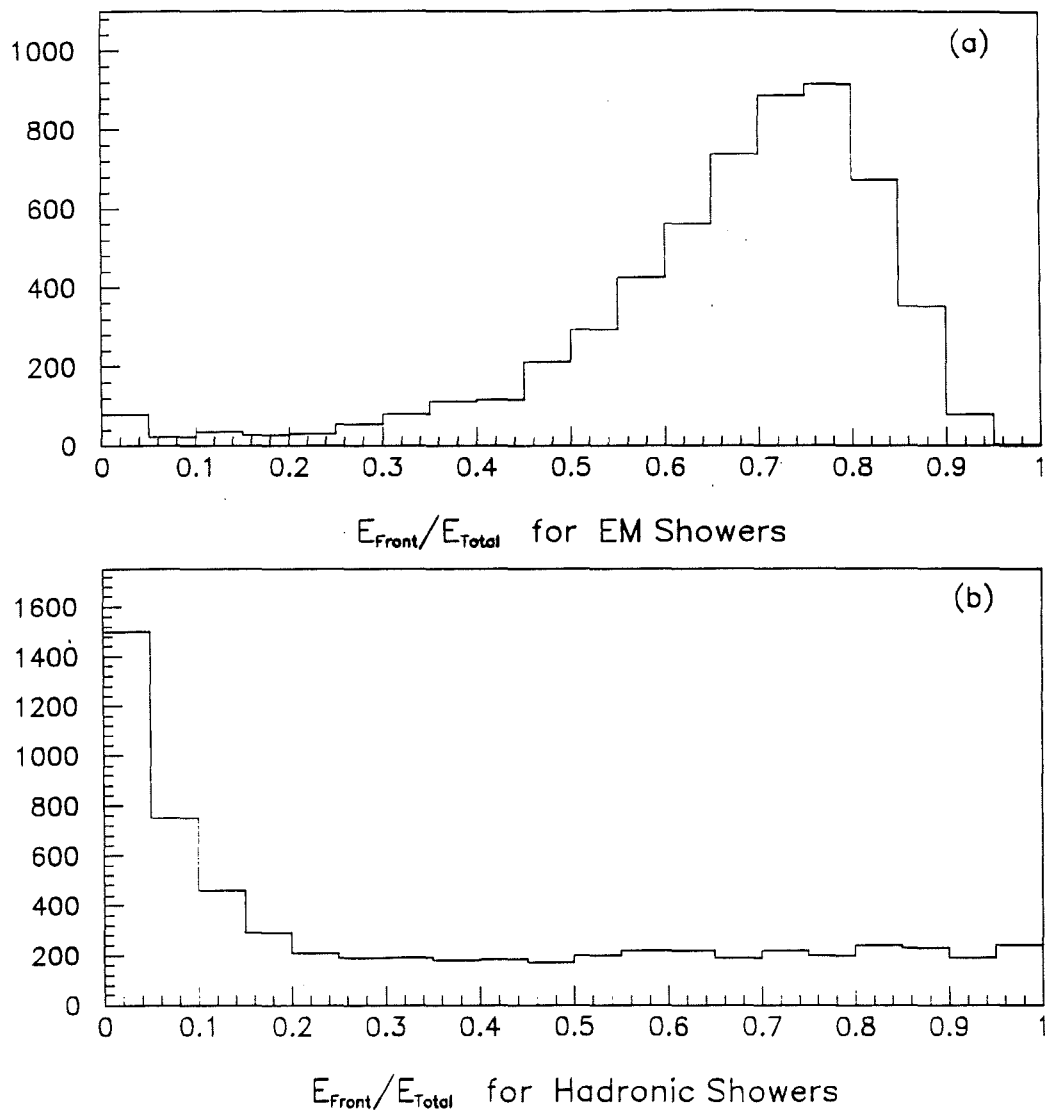


Figure 5.5:  $E_{Front}/E_{Total}$  distributions for (a) Electromagnetic and (b) hadronic showers.

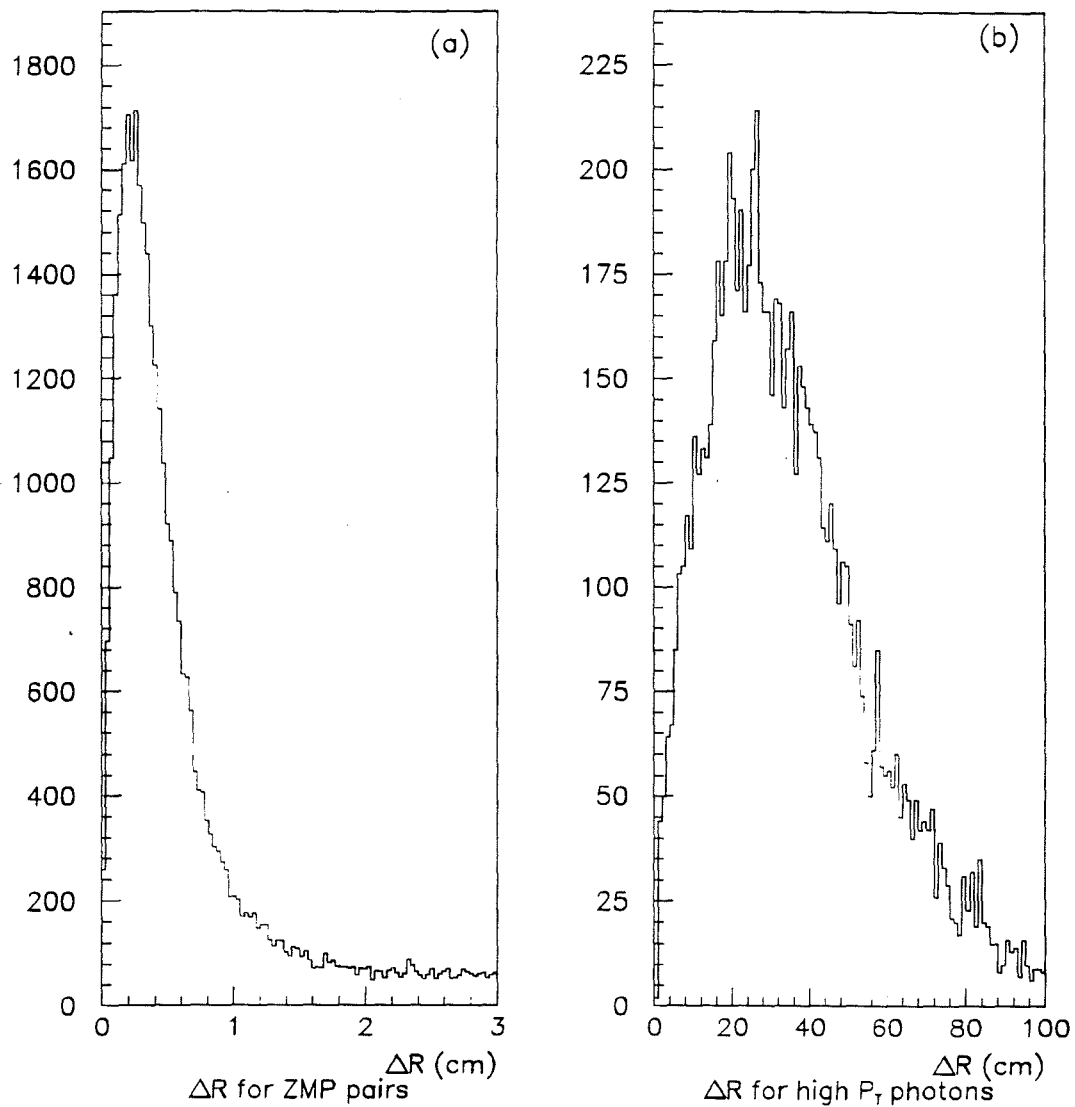


Figure 5.6:  $\Delta R$  distribution for track-shower matching.  $\Delta R$  for (a) ZMP pairs, and (b) High  $P_T$  photon and the nearest track.

pairs  $> 3.5 \text{ GeV}/c$ . It is further required that the pseudorapidity ( $y_{cm}$ ) of the two photon pair be in the range  $-0.7 < y_{cm} < 0.7$  (which corresponds to the active region of the EMLAC). Here the photons are subjected to the fiducial cuts and  $P_T$  cuts only.

The  $\pi^0$  and  $\eta$  peaks are clearly visible at  $\sim 135 \text{ MeV}/c^2$  and  $\sim 550 \text{ MeV}/c^2$ , respectively. For the purpose of the study of  $\pi^0$  and  $\eta$  production, the mass range  $110 \text{ MeV}/c^2 < M_{\gamma\gamma} < 160 \text{ MeV}/c^2$  was defined as the  $\pi^0$  mass band and the mass range  $450 \text{ MeV}/c^2 < M_{\gamma\gamma} < 650 \text{ MeV}/c^2$  was defined as the  $\eta$  mass band. To account for the combinatorial background under the  $\pi^0$  and  $\eta$  peaks, sidebands with equivalent mass range were defined for each signal. The mass regions  $75\text{-}100 \text{ MeV}/c^2$  and  $170\text{-}195 \text{ MeV}/c^2$  were designated as  $\pi^0$  sidebands and the  $\eta$  sidebands were defined to be the mass ranges  $340\text{-}440 \text{ MeV}/c^2$  and  $660\text{-}760 \text{ MeV}/c^2$ . For any distribution made for the  $\pi^0$  or  $\eta$  signals corresponding distributions were made for sidebands too. These sideband distributions were subtracted from the distributions within the  $\pi^0$  or  $\eta$  peak, to yield the background subtracted distributions for  $\pi^0$ 's and  $\eta$ 's.

Figure 5.8 shows the (a)unsubtracted and (b)sideband subtracted energy asymmetry distributions for the  $\pi^0$  mass band, where the asymmetry ( $A$ ) is defined as:

$$A = \frac{|E_1 - E_2|}{E_1 + E_2} \quad (5.3)$$

and  $E_1$  and  $E_2$  are the energies of each photon in the di-photon pair. Since the  $\pi^0$  is a pseudo scalar particle, it decays isotropically into two photons in the rest frame of the  $\pi^0$  with the two photons emerging back-to-back. Thus one would expect a flat distribution for the asymmetry. However, a departure from this flatness is seen at high asymmetry (*i.e.*  $A > 0.75$ ). Highly asymmetric decays of  $\pi^0$ 's produce photons with very low energy and at large angle relative to the  $\pi^0$  in its rest frame. The limited acceptance of the EMLAC and the reconstruction inefficiency at low energies ( $< 10\text{GeV}$ ), result in a substantial loss of  $\pi^0$ 's with asymmetry  $> 0.75$ . For

the study of inclusive  $\pi^0$  and  $\pi^0 + jet$  production, a 0.75 cut was imposed on the asymmetry to select a clean sample of  $\pi^0$ 's. The dotted line in Figure 5.7 show the effect of the asymmetry cut of 0.75 on the  $\gamma\gamma$  mass spectrum.

#### 5.1.4 Single Photon Definition

A high  $P_T$  photon ( $P_T > 3.5$  GeV/c), in any of the triggering octants that did not combine with any other photon to form a  $\pi^0$  or an  $\eta$  signal with an  $A < 0.75$  is accepted as a direct photon candidate, if it satisfied the following additional cuts.

- All of the events cuts are satisfied.
- There is no charged track within 1.0cm radially from the photon at the front face of the EMLAC.
- The directionality of the photon  $< 0.4$ .
- $E_{Front}/E_{Total} > 0.2$ .
- The TVC timing for the photon satisfies the condition  $-15$  ns  $<$  TVC  $<$  40 ns.
- The photon is in the fiducial region of the EMLAC.

Table 5.2 summarizes the total number of direct photon candidate events available to the analysis before the subtraction of the meson-induced background is done.

## 5.2 Shower and Track Selection

For the purpose of the jet analysis which is the subject of the next chapter, several cuts are made to select candidate photons and charged tracks for inclusion in the jet reconstruction. It is required that the candidate particles satisfy the following cuts.

- candidate particles must have  $P_T > 250$  MeV/c.

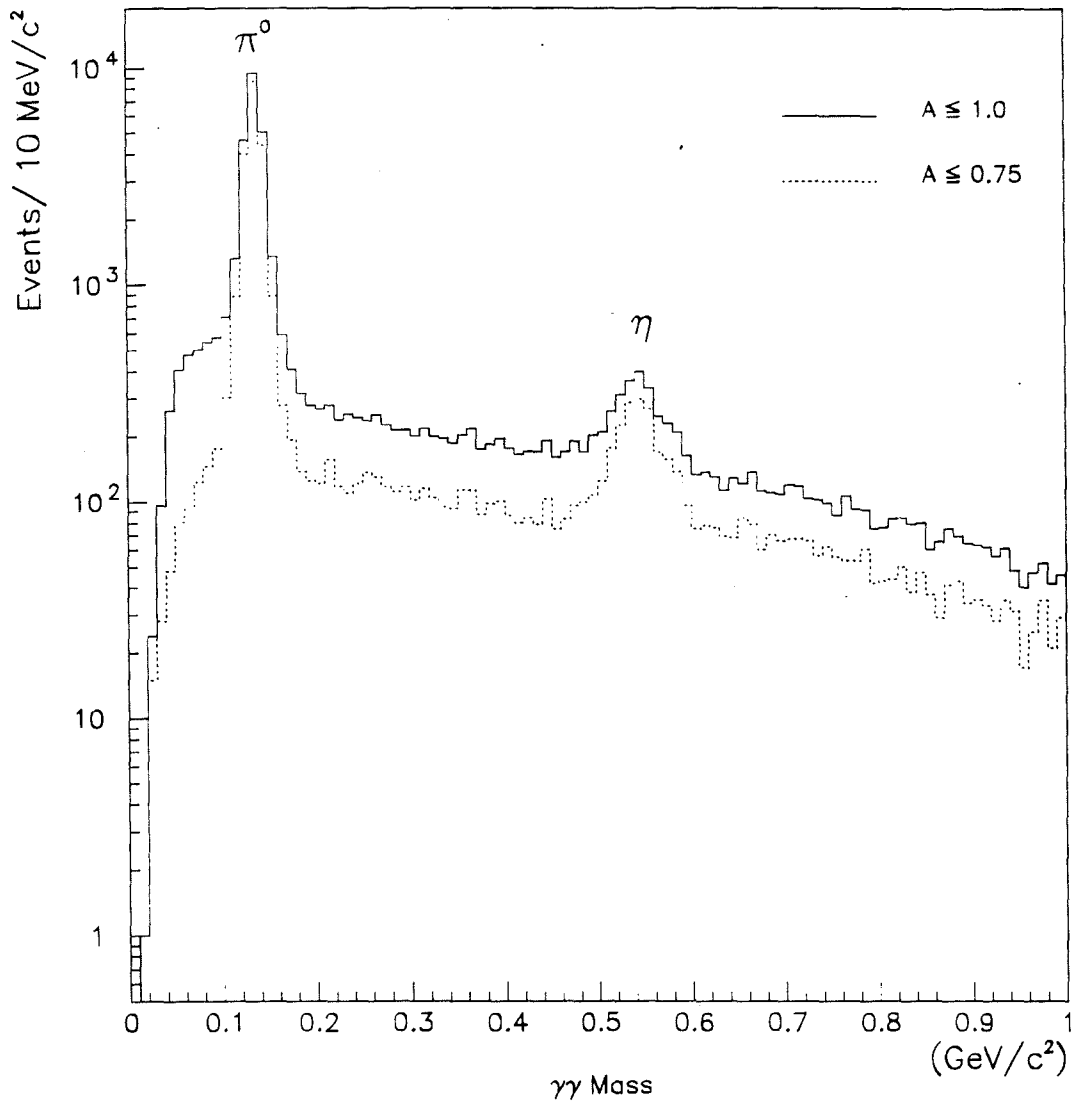


Figure 5.7:  $\gamma\gamma$  mass spectrum for photons which satisfy the cuts described in the text. Note the logarithmic scale.

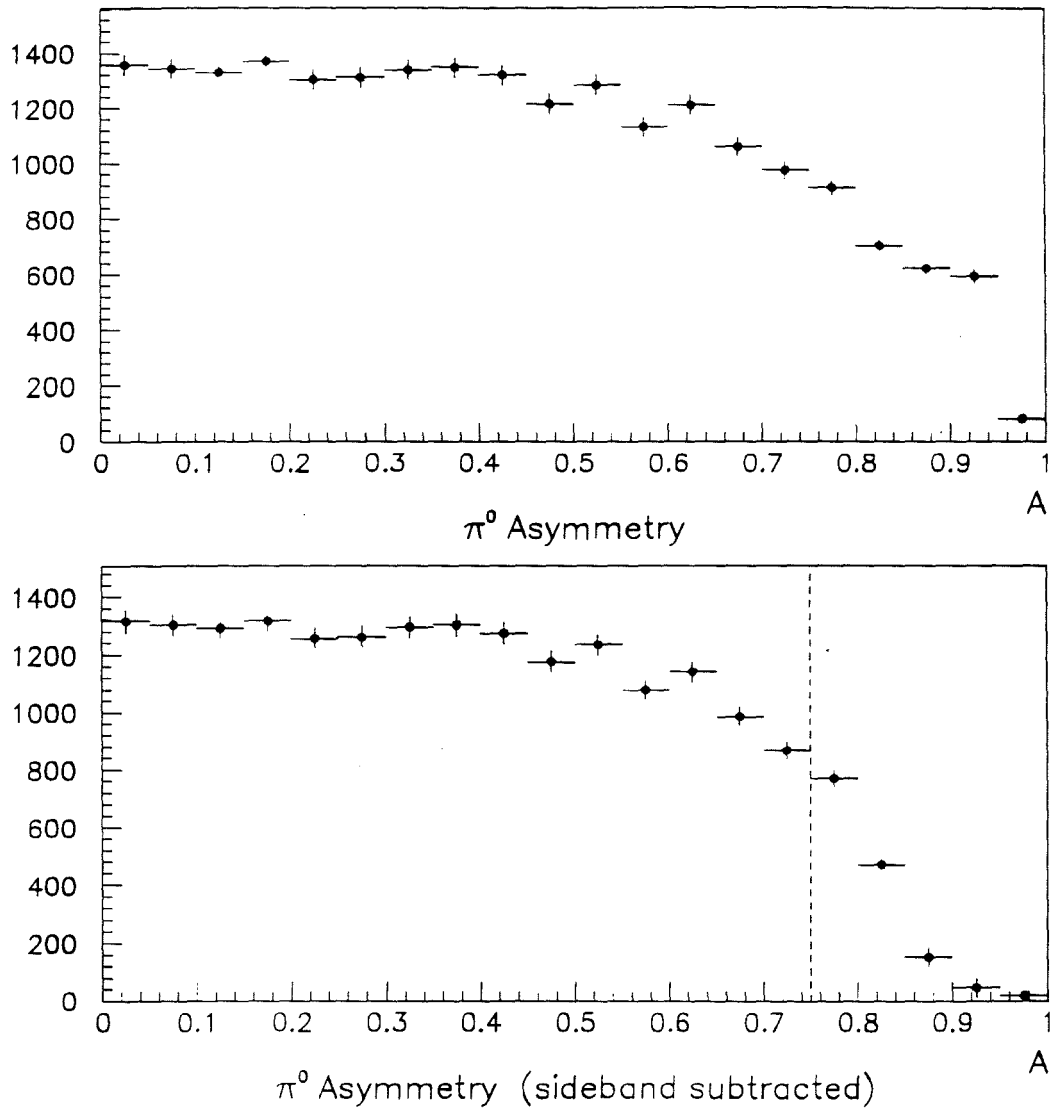


Figure 5.8:  $\pi^0$  energy asymmetry ( $A$ ) distribution (a) Unsubtracted and (b) sideband subtracted.

Table 5.2: Summary of the number of photons that survived the single photon selection cuts described in the text above.

Run Set	$P_T$ cut	Fiducial cut	Directionality cut	Track cut	$E_{Front}/E_{Total}$ cut	$\pi^0$ or $\eta$ cut
A	36,726	30,131	29,452	25,992	25,076	20,032
C	24,327	19,787	19,199	17,567	16,907	11,636
D	28,304	22,746	22,294	20,328	19,789	13,402
E	17,163	13,793	13,383	12,271	11,823	7,674

- candidate particles must be at least 1.75 radians ( $\sim 100^\circ$ ) away from the trigger particle, azimuthally.
- candidate photons must have an energy in the range  $5 \text{ GeV} \leq E \leq 250 \text{ GeV}$ .
- candidate photons have directionality  $< 0.4$ .
- candidate photons should not match with charged tracks. This is to eliminate double counting of charged hadrons and electrons.
- candidate charged tracks reconstructed in the PWC's have Y-view impact parameters  $< 1.5 \text{ cm}$  at the primary vertex.
- candidate charged tracks have a total momentum  $< 250 \text{ GeV}/c$  in the lab frame.
- candidate charge tracks have  $P_T < 10 \text{ GeV}/c$ .
- the *leading particle*<sup>1</sup> must have  $P_T > 500 \text{ MeV}/c$  with pseudorapidity  $< 1.75$ .

<sup>1</sup>The highest  $P_T$  particle in the opposite hemisphere of the trigger particle, which satisfy the particle selection cuts.

For an event to be considered for the *Jet Analysis*, there should at least be one particle that satisfies the above cuts. A detailed description of *Jet Reconstruction* is given in the next chapter.

### 5.3 Monte Carlo Calculation of Direct Photon Background

Measured direct photon cross sections have to be corrected for background due to single photons arising from mis-reconstructed  $\pi^0$ 's and  $\eta$ 's. The mis-reconstruction of the neutral mesons are mainly due to:

- failure to reconstruct low energy photons from highly asymmetric decays of  $\pi^0$ 's and  $\eta$ 's,
- geometrical losses due to the active fiducial regions and the finite acceptance of EMLAC, and
- coalescence of nearby photons from symmetric decays of high-energy  $\pi^0$ 's.

To estimate the magnitude of these backgrounds, a Monte Carlo simulation of the detector response to some specific physical event was performed. The spectrometer was simulated with GEANT3<sup>2</sup>, which was developed at CERN. For this particular study of single photon background, only the response of the EMLAC was modeled. A detail discussion of the simulation of the EMLAC response can be found in reference [42]. The  $\gamma$  and  $e^-$  (or  $e^+$ ) showers at the EMLAC were simulated with a parametrized shower shape, thus greatly reducing the CPU time involved in the event simulation[39].

The topology of the events of interest can be generated with various physics Monte Carlo programs available (such as ISAJET and PYTHIA), with a reasonable production spectrum similar to that observed in data. Due to the physics processes

---

<sup>2</sup>GEANT3 contain all the relevant physics processes that take place in the development of electromagnetic showers[41].

involved in the event generation, these Monte Carlo programs generate lots of events, that fall below the low threshold of the production spectrum, requiring large amount of computer time to generate a reasonably high statistics sample of interesting events. Hence an alternative technique was developed to select events from the DST's, based on the observed  $\pi^0$  spectrum, as the input events to GEANT3.

For input, the Monte Carlo used events<sup>3</sup> in which the highest  $P_T$  two-photon pair in the fiducial region of the triggering octant and had  $M_{\gamma\gamma} < 175 \text{ MeV}/c^2$  and  $P_T > 3.0 \text{ GeV}/c$ . For each such event, this  $\gamma\gamma$  pair was input to GEANT as a  $\pi^0$  with mass  $135.0 \text{ MeV}/c^2$  along with all the other observed photons in the same octant as the two-photon pair. The event was then processed through GEANT, allowing the  $\pi^0$  to decay randomly and isotropically in its rest frame. For each selected real event, five Monte Carlo events were generated by rotating the original momenta of all particles by a random azimuthal angle. To estimate the background to  $\gamma + jet$  signal, the charged tracks from the corresponding DST events were added to the already processed events (through GEANT), with appropriate azimuthal rotations. The direction cosines and the momentum components of these added physics tracks were recalculated to account for the azimuthal rotations.

Due to the low statistics on measured  $\eta$  and  $\omega$  signals, the observed  $\pi^0$  production spectrum was used to estimate the backgrounds due to the electromagnetic decays of these mesons. It was assumed that these mesons have production characteristics similar to that of a  $\pi^0$ . This assumption is consistent with the fact that the measured, relative  $\eta/\pi^0$  yield from data appears to be independent of  $P_T$ [39]. Therefore, the  $\pi^0$  was replaced by particles of appropriate mass, leaving the remainder of the event kinematics unchanged and the events were processed through GEANT, as for  $\pi^0$ 's. The resulting events were weighted by the  $\eta/\pi^0$  ratio of 0.45 and by the branching ratio for  $\eta \rightarrow \gamma\gamma$  of 0.39.

---

<sup>3</sup>These events satisfied all the previously described event level cuts.

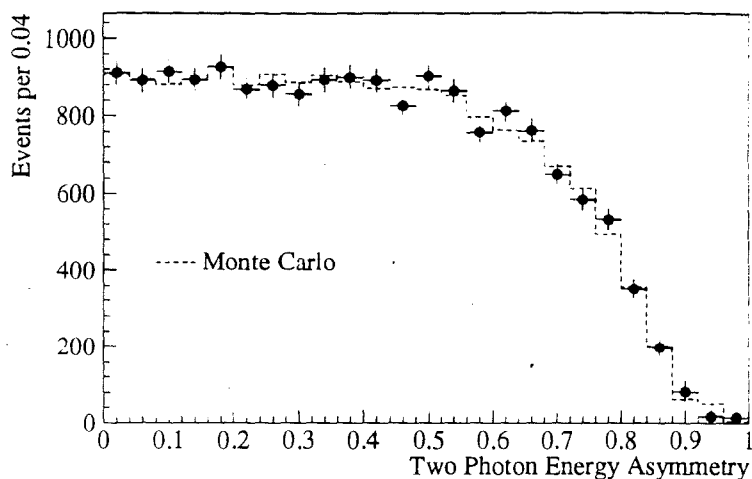


Figure 5.9: Comparison between data and Monte Carlo for  $\pi^0$  energy asymmetry.

These Monte Carlo simulated events were processed through the same event reconstruction code described in chapter 4, and the binary DST's were written out. These DSTs were then processed through the higher level analysis code to reconstruct  $\pi^0$ 's and single photons. Note that all reconstructed single photons in this Monte Carlo event sample are background to the direct photon signal from the decays of neutral mesons, since the Monte Carlo events had no direct photons in the event sample.

A detailed discussion on the comparison of data and Monte Carlo events can be found in references [39] and [42]. For the sake of completeness, the agreement between the data and Monte Carlo are shown for the  $\pi^0$  energy asymmetry distribution in figures 5.9. It should be noted that the relaxation of the mass and asymmetry cut on the  $\gamma\gamma$  pairs at the input event selection to Monte Carlo, allows one to reproduce the actual two- $\gamma$  mass spectrum and the the  $\pi^0$  asymmetry distribution.

## CHAPTER 6

### Jet Analysis

Within the (QCD) parton model, hard scattering of constituents from two colliding hadrons is expected to produce a characteristic four-jet structure[43]. Two of the jets contain fragments of the incoming hadrons and hence continue more or less in the forward direction. The two wide angle back-to-back jets<sup>1</sup>, emerging from the hard-scattered partons, contain particles with large  $P_T$ . Accompanying the large  $P_T$  particle ( $\pi^0$  or  $\gamma$ ) that triggered the event is a recoil jet resulting from the fragmentation of the recoiling parton.

Unlike the jet production cross sections and the jet axis angular distributions, the hadronization of partons emerging from the hard scatter is not well explained in terms of perturbative QCD, since it necessarily involves the long distance, non-perturbative properties of the theory[44, 45]. Due to the lack of such non-perturbative calculations, one must resort to phenomenological models to understand the hadronization of jets and their properties[46]. A detail description of jet fragmentation is given in the reference[44] and the references contained therein.

In this chapter, we will present the evidence for the existence of the recoil jet structure in our data, followed by a description of the recoil jet reconstruction algorithm and its performance. At the end of this chapter is a section devoted to a discussion of the properties of the recoil jets.

---

<sup>1</sup>In hadron-hadron collisions, the wide angle jets are not quite back-to-back due to different parton momentum fractions and the intrinsic  $k_T$  effects.

## 6.1 Experimental Evidence for Away-Side Jets

Observing jets at the collider energies is a straight forward matter. At collider energies, hadron jets appear distinct and well separated. But defining jets at energies available in fixed target experiments is a very difficult enterprise due to the available phase space and the complicated event structure. The experiments at ISR[47] and CERN SppS[15] have shown azimuthal and rapidity correlations as a signature for the existence of jets. We will show that similar correlations are observed in our data.

### 6.1.1 Azimuthal Correlation

Figure 6.1 shows the distribution of the azimuthal difference ( $\Delta\phi$ ) between the triggered  $\pi^0$  and the charged tracks in the event while figure 6.2 shows the same correlation between triggered  $\gamma$  and charged tracks.  $\Delta\phi = 0$  radians corresponds to the direction of the trigger particle while  $\Delta\phi = 3.14$  radians is in the azimuthally opposite direction of the trigger. Events were selected with trigger  $P_T > 4$  GeV/c and trigger pseudorapidity  $|\eta| < 0.7$ . The  $\Delta\phi$  plots for  $\pi^0$  events were made with four different track  $P_T$  cuts : figure 6.1 (a): Track  $P_T > 0.25$  GeV/c, figure 6.1 (b): Track  $P_T > 0.50$  GeV/c, figure 6.1 (c): Track  $P_T > 1.00$  GeV/c and figure 6.1 (d): Track  $P_T > 2.00$  GeV/c

All the four figures show a strong clustering of particles in the hemisphere opposite of the trigger  $\pi^0$  and some clustering of particles adjacent to the  $\pi^0$ . The clustering of particles opposite the triggered  $\pi^0$  is expected from the conservation of momentum constraint. Similar azimuthal correlations are shown in figure 6.2 (a)-(d), for events triggered by a single photon. A comparison of these  $\Delta\phi$  plots for  $\pi^0$  and  $\gamma$  show that the clustering of the particles adjacent to the  $\pi^0$  or  $\gamma$  diminish with increasing  $P_T$  of the charged tracks. This decrease in the particle density on the trigger side is much stronger for single photon triggered events. This observation is consistent

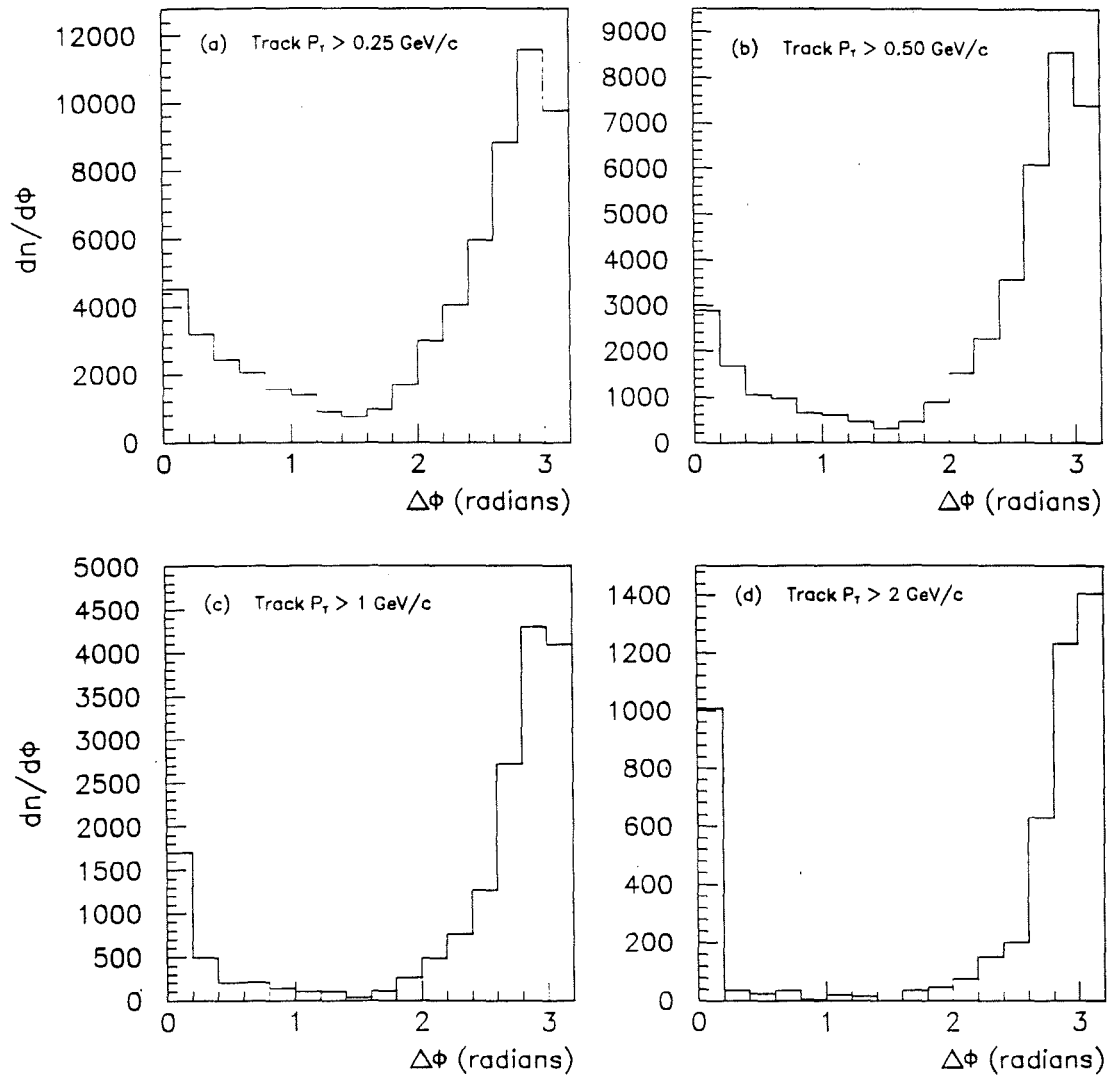


Figure 6.1:  $\phi_{Trigger} - \phi_{Track}(= \Delta\phi)$  distributions (with various track  $P_T$  cuts) for  $\pi^0$  triggered events. (a) track  $P_T > 0.25$  GeV/c, (b) track  $P_T > 0.50$  GeV/c, (c) track  $P_T > 1$  GeV/c and (d) track  $P_T > 2$  GeV/c.

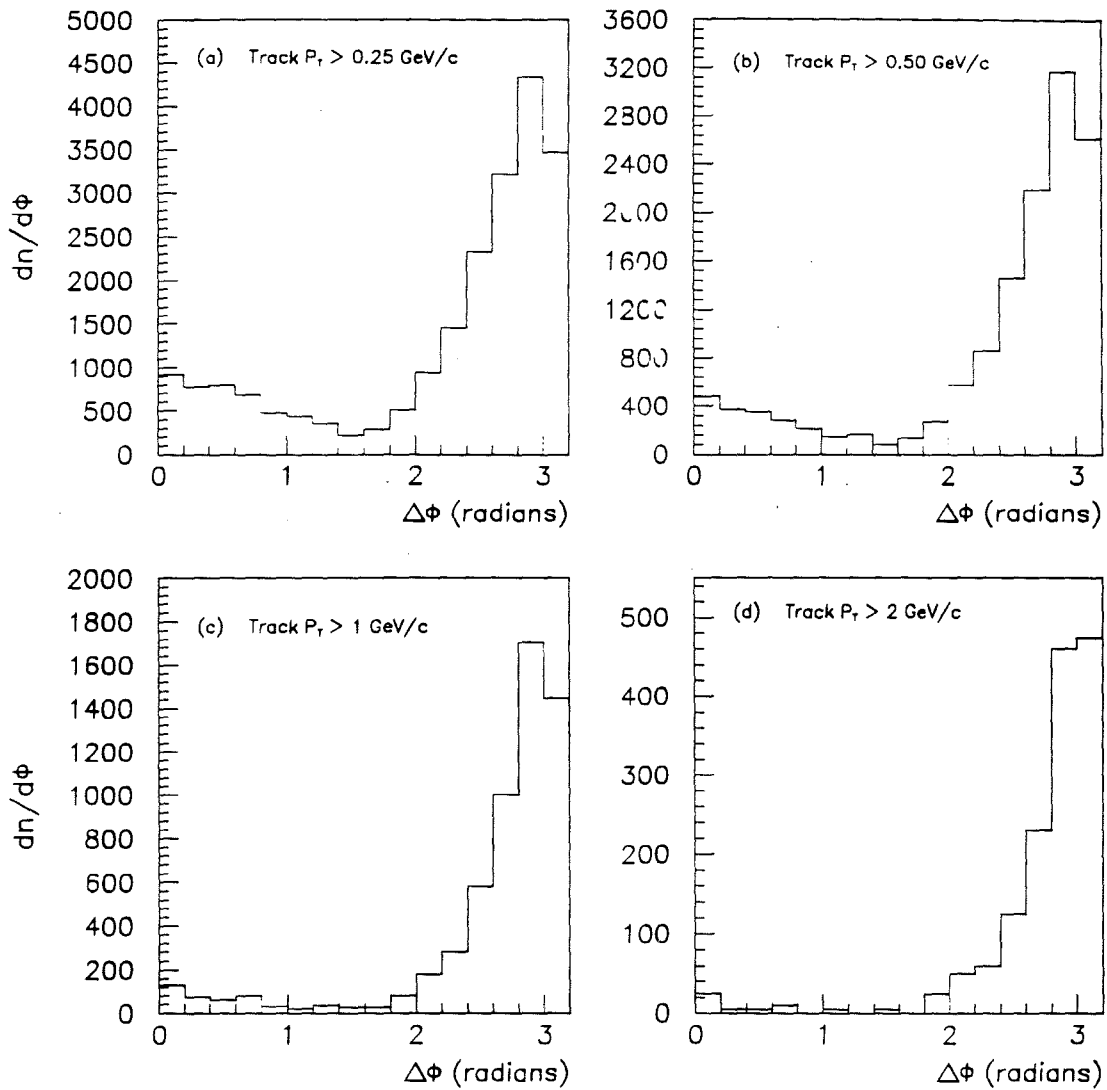


Figure 6.2:  $\phi_{Trigger} - \phi_{Track}(= \Delta\phi)$  distributions (with various track  $P_T$  cuts) for single photon triggered events. (a) track  $P_T > 0.25$  GeV/c, (b) track  $P_T > 0.50$  GeV/c, (c) track  $P_T > 1$  GeV/c and (d) track  $P_T > 2$  GeV/c.

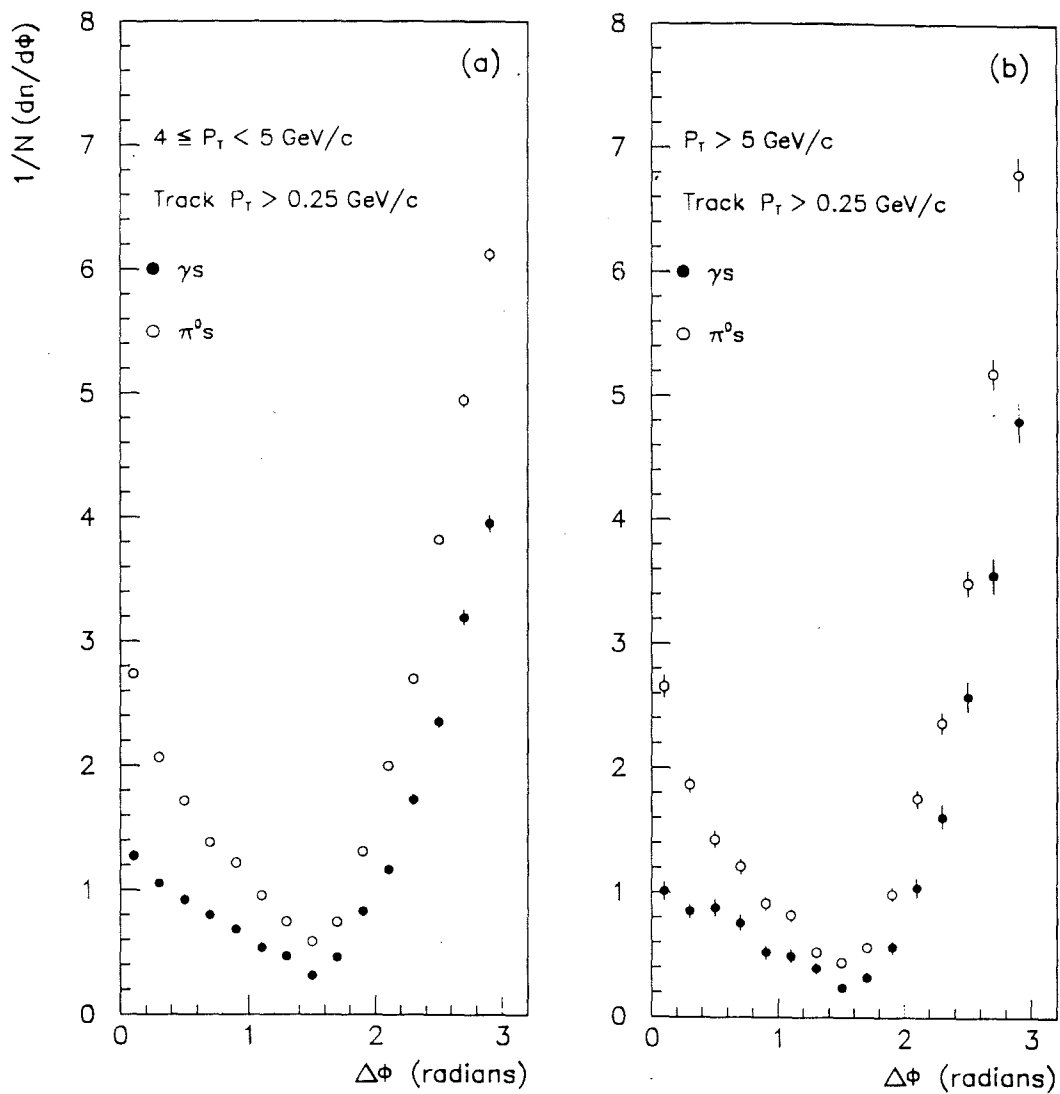


Figure 6.3:  $\Delta\phi$  distributions for  $\pi^0$  and  $\gamma$  triggered events. (a)  $4 \leq \text{Trigger } P_T < 5$  GeV/c, (b)  $\text{Trigger } P_T > 5$  GeV/c. Direct photon data are not corrected for the  $\pi^0$  background.

with QCD description of the jet production where a high transverse momentum  $\pi^0$  is produced from the fragmentation of a hard scattered parton, while the direct photons emanating from a hard scatter are isolated<sup>2</sup>. All the distributions shown in figures 6.1– 6.3 are not corrected for the background in the  $\pi^0$  or  $\gamma$  signal.

### 6.1.2 Rapidity Correlation

The clustering of particles opposite in azimuth to the trigger show that the recoil jet momentum is not carried by a single particle, but rather by a collection of particles. Hence, in addition to the existence of azimuthal correlation, one expects a dynamical correlation among the particles (opposite to the trigger), in the reaction plane defined by the trigger and the beam direction. To check for the jet-like structure on the away side, we will look at the rapidity difference ( $|\Delta Y|$ ) of the two highest  $P_T$  charged particles in the hemisphere opposite to the trigger within the same event. If these two particles are dynamically correlated, we should observe a peak near  $\Delta Y = 0$ . We indeed see such a peak in figure 6.4(a). The dotted line in figure 6.4(a) shows an uncorrelated  $\Delta Y$  distribution which is obtained by selecting leading and next-to-leading particles from different events.

To demonstrate that the observed correlation is not an artifact of energy and momentum conservation, a correlated and uncorrelated  $\Delta Y$  distribution is generated with a non-QCD phase space Monte Carlo calculation using the **GENBOD** routine in the CERN library package. Figure 6.4(b) shows a comparison of correlated and uncorrelated  $\Delta Y$  distributions generated from phase space calculation alone, and no correlation is observed above the accidental background. A detailed description of a such comparison appears in reference[48]. The existence of the correlated  $\Delta Y$  signal (figure 6.4(a)) above the accidental background provides a confirmation of the

---

<sup>2</sup>Single photons from Bremsstrahlung are produced with accompanying particles in the trigger side.

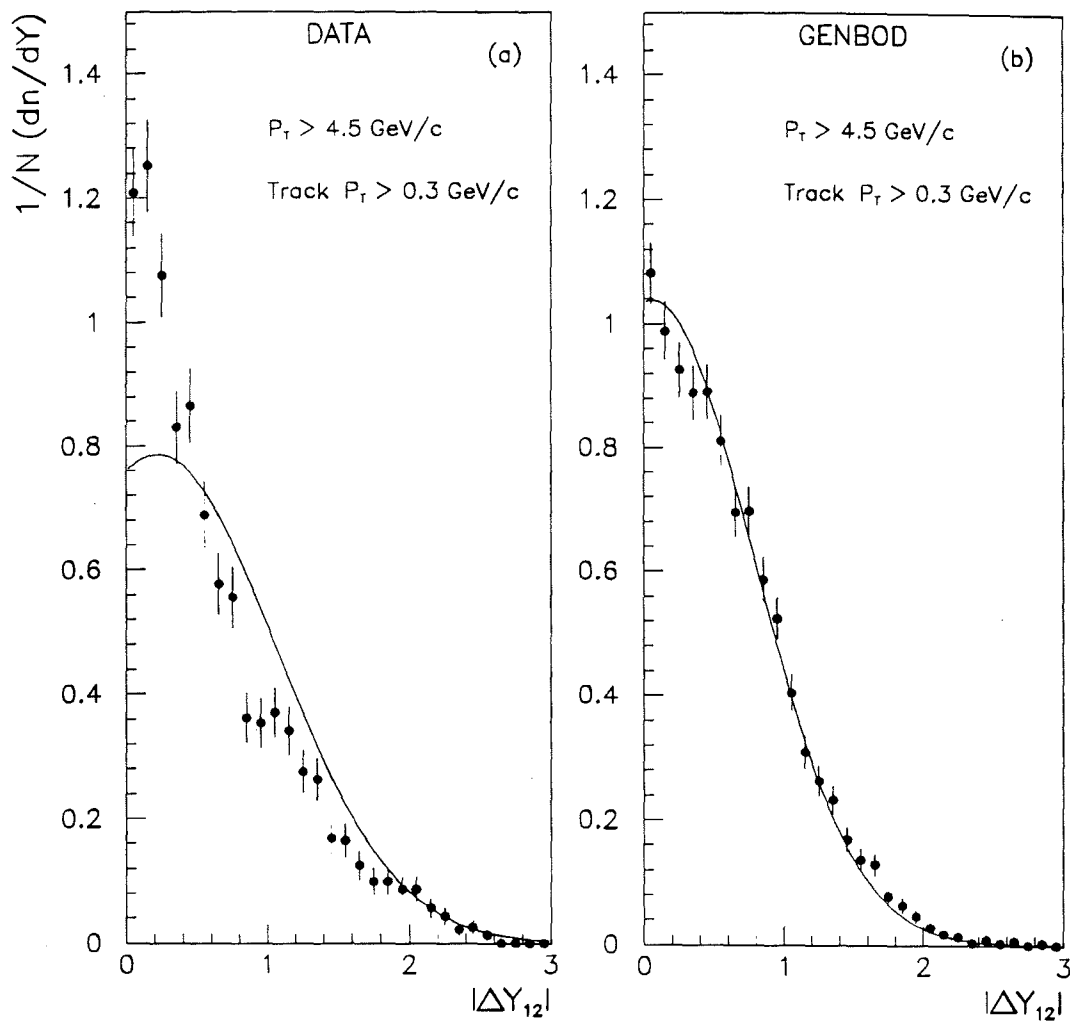


Figure 6.4: Rapidity Correlation ( $|\Delta Y_{12}|$ ) between the two highest  $P_T$  charged particles in the hemisphere opposite to the trigger. (a)  $\Delta Y$  distributions from data, and (b)  $\Delta Y$  distributions from GENBOD. Solid circles represent correlated  $\Delta Y$  and the solid line represents uncorrelated  $\Delta Y$ .

existence of recoil jets in our data.

## 6.2 Jet Reconstruction

The jet reconstruction algorithm employed in this analysis is quite similar to an algorithm used by the experiment WA70[15] at CERN. All of the charged tracks are assumed to be pions and all of the electromagnetic showers which are not associated with to charged tracks are assumed to be photons. The momenta of all the particles are transformed to the beam/target center-of-mass system. Figure 6.5 shows the quantities relevant to the recoil jet reconstruction. Those particles which failed to satisfy the cuts described in section 5.2 were removed from the candidate set of particles taken as input to the jet reconstruction algorithm. The jet reconstruction algorithm makes use of the fact that the particles properly assigned to the recoil jet subtend a smaller space angle ( $\theta_{i2}$ ) with the recoil *jet axis*, than towards either the trigger or beam momentum vectors.

The steps involved in the jet reconstruction algorithm are as follows:

1. Define the three *trial* jet axes; namely the trigger jet, recoil jet and the beam/target jet.
  - Trigger jet axis – The direction of the trigger particle momentum vector.
  - Recoil jet axis – The direction of the *leading particle* momentum vector. The *leading particle* is defined as the highest  $P_T$  charged or neutral particle in the opposite hemisphere of the trigger and has  $P_T > 500$  MeV/c with  $\eta < 1.75$ .
  - Beam/Target jet – The direction is always taken along the incident beam particle.

2. Each particle is assigned a weight ( $\omega$ ) and a probability (P), with respect to a given jet axis, where

$$\omega_{ik} = \cos(\theta_{ik}) \quad (6.1)$$

$$P_{ik} = \frac{\omega_{ik}}{\sum_{k=1}^3 \omega_{ik}} \quad (6.2)$$

with  $\theta_{ik}$  defined as the space angle between the  $i^{th}$  particle's momentum vector and the  $k^{th}$  trial jet direction ( $k=1,2$  and  $3$ ). See figure 6.5.  $P_{ik}$  is defined as the *probability* that the  $i^{th}$  particle belongs to  $k^{th}$  jet axis.

3. Particles are tentatively assigned to each trial jet axis, for which the "probability" is maximum. Particles for which the maximum  $P_{ik} < 0.34$  were excluded from the jet analysis.
4. Once the candidate particles are tentatively assigned to appropriate jet axes, the total momentum vector for the trigger and recoil jets were determined by taking the vector sum of the momentum vectors of the particles assigned to that jet. For the beam/target jet, the beam direction was taken to be the jet direction at all times.
5. The weights and probabilities are recalculated (as in step 2) using the new jet directions, determined in the previous step. Subsequently, the particles are re-assigned to respective jets as in step 3 and the trigger and recoil jet momenta are re-calculated with the newly assigned constituent particles.
6. Steps 4 and 5 are repeated for a third iteration. After the third iteration, candidate particles with maximum  $P_{ik} < 0.35$  are removed from that jet, and the trigger and recoil jet momenta are calculated. Those particles removed from any one of the jets are not assigned to any other jet. They are lost to the analysis.

7. Finally, the recoil jet is selected using the following criteria:

- At least one particle with a  $P_T > 250$  MeV/c is required in the hemisphere opposite to the trigger.
  - Even though the leading particle has  $P_T > 500$  MeV/c, some times the original leading particle is removed from the recoil jet during the iterative procedure, if it does not satisfy the probability cuts defined above. This happens when the original leading particle happens to be a fake one.
- The recoil jet  $P_T$  must be greater than 20% of the  $P_T$  of the trigger particle.
- The azimuthal angle between the recoil jet axis and the trigger particle must be greater than 1.75 radians.
- All recoil jets are restricted to a region  $|\eta_{jet}| < 0.9$ .

The value of the probability cut and the recoil jet pseudorapidity cut were determined from a Monte Carlo study of the jet analysis.

### 6.3 Monte Carlo Study of Jet Reconstruction

For the interpretation and correction of data, we used simulated events, generated by a QCD-based ISAJET V6.30 Monte Carlo program[49]. The aim was primarily to correct the data for the effects of detector acceptance and reconstruction inefficiencies, data selection and analysis method. These corrections strongly rely on a good representation of the data by an accurate simulation of the detector response. This was achieved by fine tuning of the model parameters in GEANT. A comparison of Monte Carlo events and real data for the charged particles<sup>3</sup> are shown on figures 6.6

---

<sup>3</sup>EMLAC acceptance and photon reconstruction efficiency have extensively been studied in the Monte Carlo calculation of the  $\pi^0$  background.

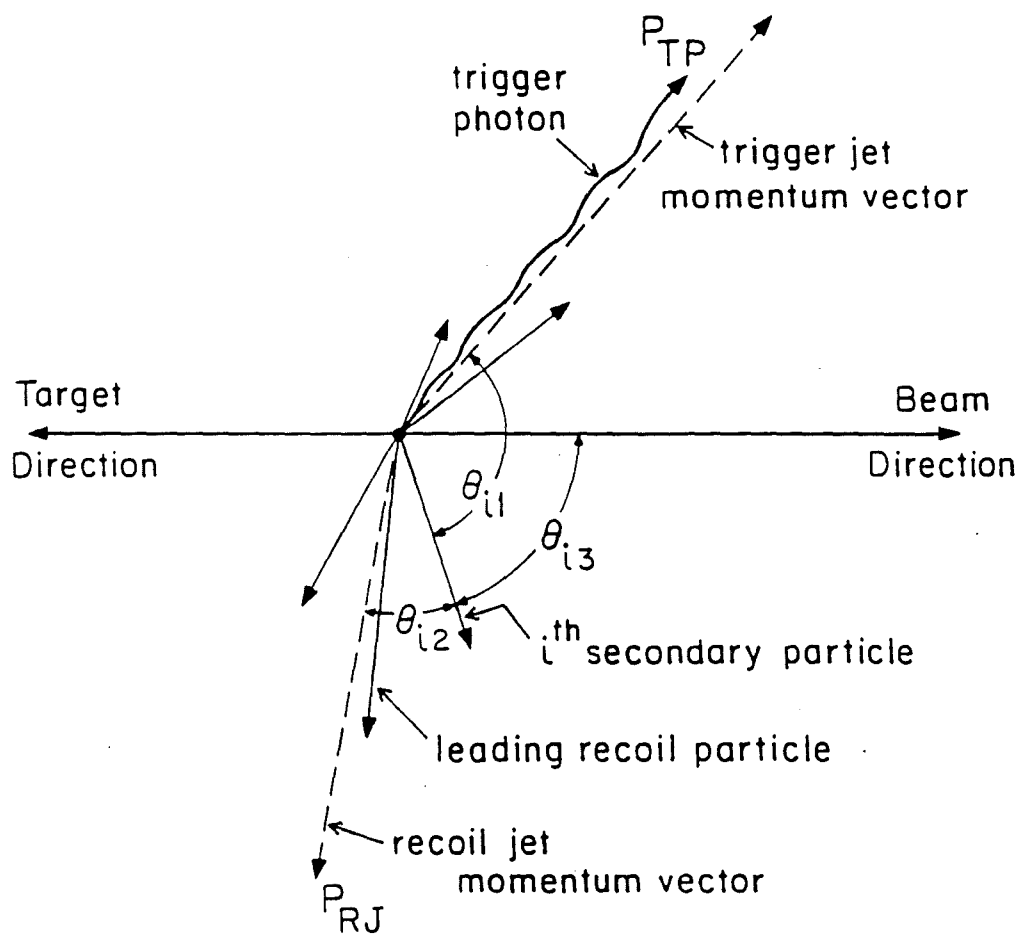


Figure 6.5: Quantities relevant to the reconstruction of recoil jets.

and 6.7. The dashed line superimposed in both figures are from Monte Carlo simulated events. The agreement between the data and Monte Carlo is reasonably good.

The quantities that are relevant to a Monte Carlo study of jet analysis are the misassignment of particles to the recoil jet, the jet reconstruction efficiency and the experimental resolution of jet direction (*ie.* pseudorapidity). Each of these subjects will be addressed in the next few sections.

### 6.3.1 Jet Monte Carlo Event Generation

The ISAJET event generator was used to generate direct photon plus away side jet events over the full  $P_T$  range observed in the real data. The ISAJET program generates high- $P_T$  photons which are emitted from partons which scatter according to lowest order perturbative QCD. For high- $P_T$  direct photon production the relevant processes are the Compton and annihilation subprocesses. The higher order corrections are not included. The scattered recoil partons evolve in to a cascade of quarks and gluons which finally fragment independently according to the Field-Feynman model[46]. The events were generated for each beam type (protons and  $\pi^-$ 's) incident on nucleon targets, using Duke and Owens structure functions with  $\Lambda_{QCD} = 0.2 \text{ GeV}$ [50].

To accommodate the effects of trigger bias in conjunction with an effective primordial  $k_T$  of the hard-scattering partons, a threshold of 3 GeV/c was imposed on the trigger particle  $P_T$  spectrum for the event generation and a 4 GeV/c  $P_T$  cut was applied at the event selection for the analysis. The  $k_T$  smearing was introduced by a random Lorentz boost in the parton-photon frame, assuming a Gaussian shape with  $\langle k_T^2 \rangle = 0.95 \text{ (GeV)}^2$ [49]. All the ISAJET parameters were left to their default values.

The ISAJET generated events were propagate through the GEANT simulation of the charged particle spectrometer and EMLAC and the output of the GEANT

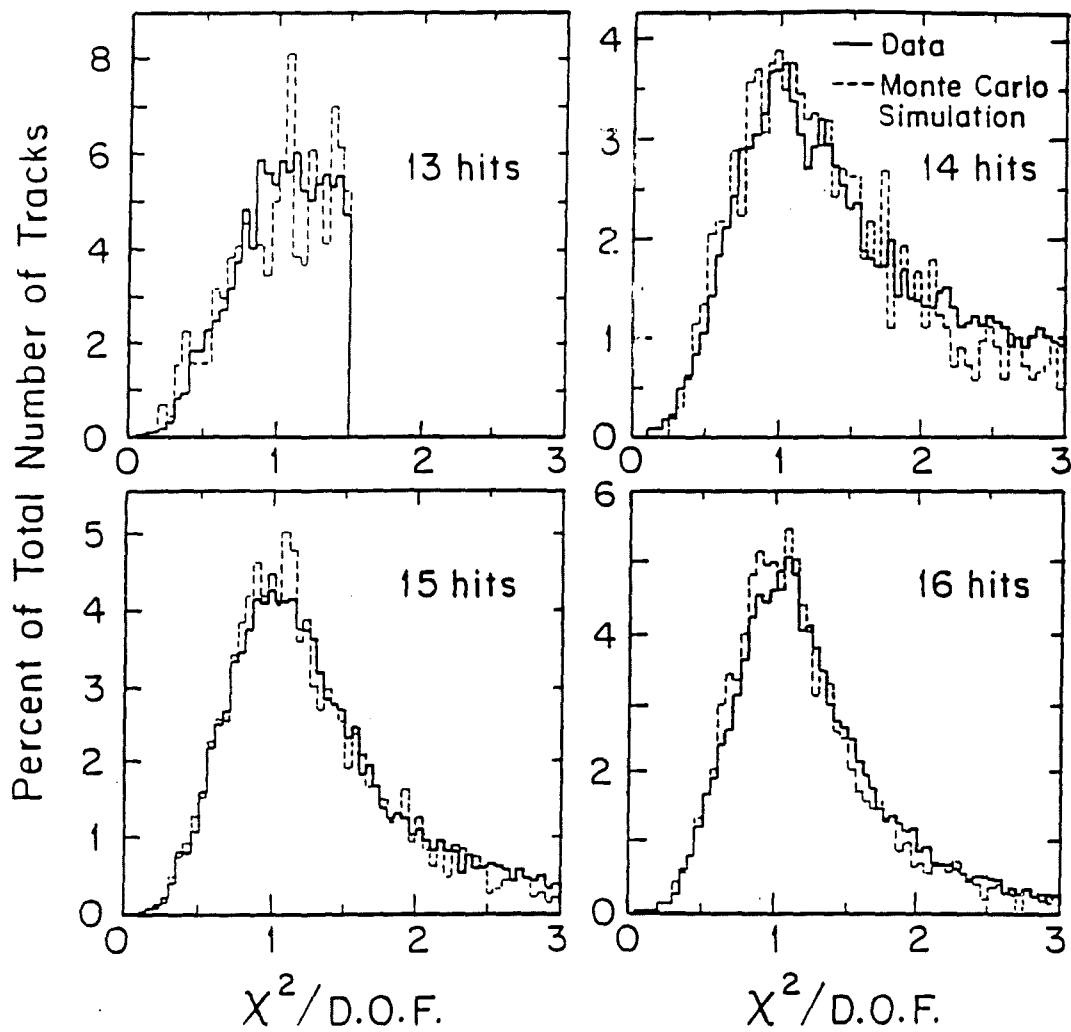


Figure 6.6: A comparison between data and Monte Carlo for the  $\chi^2$  per degree of freedom distributions for 13, 14, 15 and 16 hit PWC physics tracks. The solid line is for data and the dashed line is from Monte Carlo simulations.

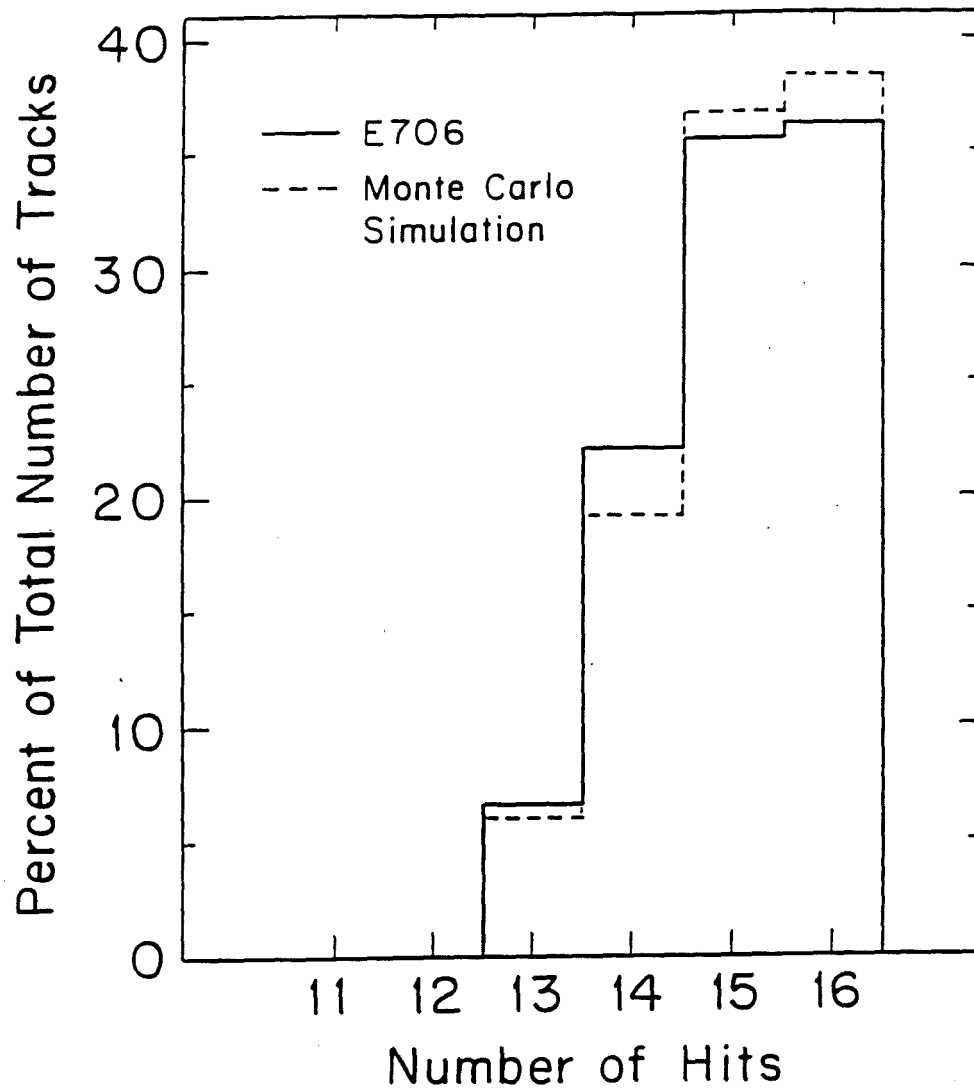


Figure 6.7: The relative percent of the number of hits per PWC track. The solid line is for data and the dashed line is for Monte Carlo simulation.

was processed through the reconstruction code and subsequently, the binary DST's were written out. These compressed DST's were then processed through the same jet analysis code that was used to analyze the real data. All the cuts that were applied to the real data in event selection and jet reconstruction have also been applied to the Monte Carlo data, to reproduce the systematics associated with the analysis.

### 6.3.2 Particle Misassignment

A basic problem encountered in the analysis of jet events in hadronic collisions at fixed target experiments arises from the attempt to distinguish between those particles belong to high- $P_T$  jets and those not directly associated with hard scattering. Because of the considerably smaller center-of-mass energy of a fixed target experiment, the fragments from the trigger, recoil, beam and target jets tend to overlap in space, complicating the reconstruction of trigger and recoil jets. We have studied extensively the misassignment of particles in the recoil jet, using the ISAJET Monte Carlo. The studies revealed that a significant fraction of beam/target jet particles are misassigned to the recoil jet. This is unavoidable due to the overlap of the beam/target jet and the recoil jet. Figure 6.8 show the pseudorapidity distributions of the charged particles in the center-of-mass frame. The solid line is for the particles assigned to a beam/target jet and the shaded area represent the pseudorapidity distribution of the particles assigned to a recoil jet, for both  $\pi^0$  and  $\gamma$  events. This shows that even in the central rapidity region ( $Y = 0.$ ), one would expect a non-negligible misassignment of beam/target jet particles to the recoil jet. Figure 6.9 shows the ratio of  $P_T(B \rightarrow R)$  and  $P_T(R \rightarrow R)$  as a function of the pseudorapidity of the *leading particle* in the recoil jet.  $P_T(B \rightarrow R)$  is the contribution to the recoil jet's  $P_T$  from the beam particles misassigned to the recoil jet and  $P_T(R \rightarrow R)$  is the total  $P_T$  from the correctly assigned recoil jet particles. Figure 6.9 shows that  $\sim 20$ - $25\%$  particles are misassigned to recoil jets at this center-of-mass energy.

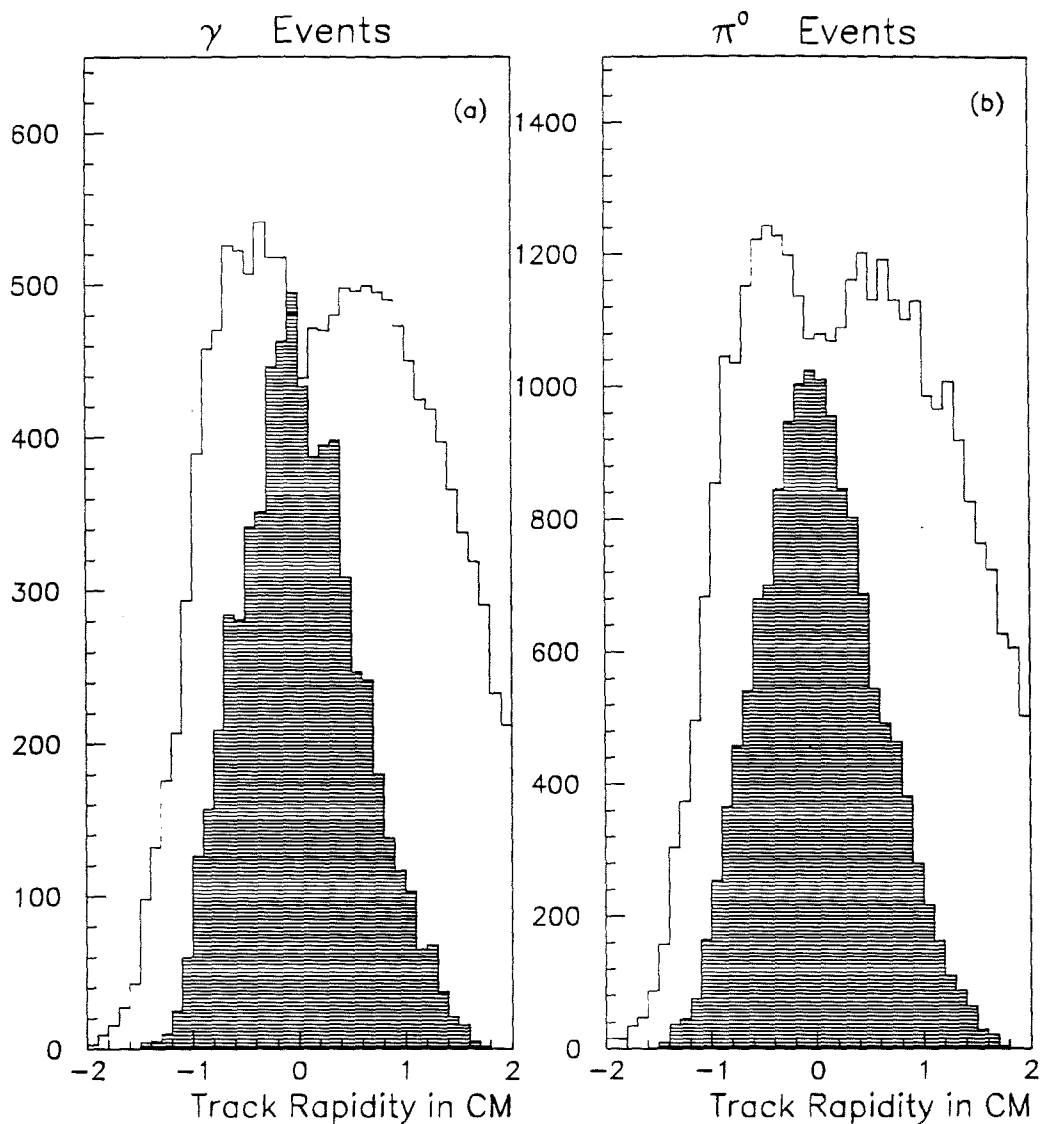


Figure 6.8: Pseudorapidity ( $Y$ ) distributions of charged tracks in CM frame. The shaded area represent the  $Y$  distributions of tracks assigned to a recoil jet. The solid line shows the  $Y$  distributions for tracks that are assigned to a beam/target jet. The  $\gamma$  and  $\pi^0$  events were selected from data by applying the cuts described in chapter 5.

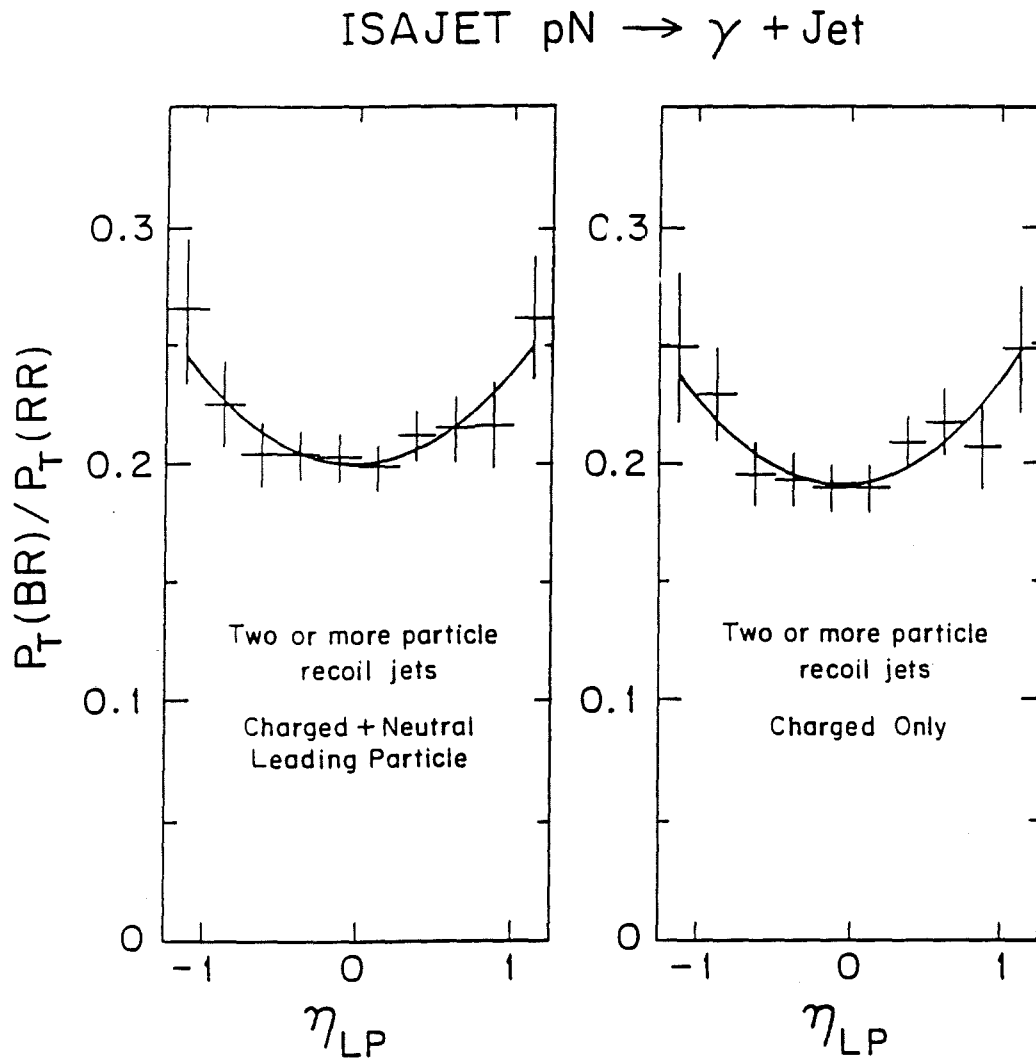


Figure 6.9:  $P_T(B \rightarrow R)/P_T(R \rightarrow R)$  as a function of the leading particle pseudorapidity. The plot on the left side shows the transverse momentum ratio for the jets reconstructed with either a charged or neutral leading particle while the one on the right side represents the jets reconstructed with a charged leading particle only.

The misassignment of the “soft” beam/target jet particles to the recoil jet does not alter the recoil jet direction significantly, hence there is no great impact on the cross section studies. Nevertheless it will have an impact on the measurements of the recoil jet fragmentation. We will address this issue in the discussion of the measurement of longitudinal fragmentation.

### 6.3.3 Jet Reconstruction Efficiency and Jet Axis Resolution

It is important to understand how accurately we determined the direction of the recoil jet axis, since it directly affects the calculation of the cross section as a function of recoil jet pseudorapidity. The jet axis resolution depends on the jet reconstruction algorithm as well as on the acceptance of the spectrometer. Jets are oftenly mis-reconstructed, if the true leading particle in the recoil jet is not correctly identified. This mis-reconstruction of jets can be viewed as a reconstruction inefficiency. One way to see the level of mis-reconstruction of recoil jets is to plot the reconstructed recoil jet pseudorapidity as a function of the generated jet pseudorapidity. In figure 6.10 we plot the reconstructed recoil jet pseudorapidity ( $\eta_{REC}$ ) for six different regions of the generated recoil jet pseudorapidity ( $\eta_{GEN}$ ). From these plots, we see that the recoil jets that fall near the edge of the detector acceptance are oftenly mis-reconstructed. This mis-reconstruction can largely be attributed to the loss of the leading particle in the jet. Since the positive and negative Monte Carlo data showed no relative difference in pseudorapidity smearing, we have combine the two sets of data to achieve high statistics. Figure 6.11(a) shows a similar behavior and further more, shows that the recoil jets with  $|\eta| > 1.0$  are not reliably reconstructed. Hence, we have imposed a pseudorapidity cut of  $|\eta| < 0.9$  on all the reconstructed recoil jets in the subsequent analysis. In order to correct for mis-reconstruction and the

loss of events in the recoil jet reconstruction, we calculate the quantity  $\eta_{REC}/\eta_{GEN}$  as function of  $\eta_{REC}$ . Figure 6.12 show this ratio for both positive and negative ISAJET data. The subject of reconstruction efficiency is addressed in more detail in chapter 7.

The quantity  $\Delta\eta = \eta_{GEN} - \eta_{REC}$ , shown in figure 6.11(b), is used here as a measure of the recoil jet axis resolution. The events shown are selected with a trigger  $P_T \geq 4$  GeV/c and trigger  $|\eta| < 0.7$ . The HWHM<sup>4</sup> of this plot (  $\sim 0.15$  units of pseudorapidity ) reflects the uncertainty inherent in the reconstruction of the recoil jet axis. In figure 6.13, we show a similar plot, where we reconstruct the recoil jets with and without the photons included in the jet. The shaded area corresponds to  $\Delta\eta$  with no photons included in the reconstructed recoil jet, except for those photons which are the leading particle in the recoil jet. We can immediately see that the width of the plots are not significantly different in the two cases. Thus one can conclude that, we can exclude the “soft” photons from the recoil jet reconstruction with out compromising the jet axis resolution. In the subsequent analysis, photons are excluded from this jet analysis except for those which proved to be the leading particle in the recoiling system.

## 6.4 Parton Momentum Fractions

The parton momentum fractions  $x_a$  and  $x_b$  for the  $\pi^0$  and  $\gamma$  events are shown in figure 6.14(a)-(d), for both the incident beam types. We have assumed that the  $P_T$  is balanced between the trigger and the recoil jet and have ignored the mass of the recoil jet in calculating parton momentum fractions. The validity of these two assumptions are addressed in the reference [48]. Both  $x_a$  and  $x_b$  distributions are peaked between 0.2 and 0.5, reflecting the  $x$  range of our experiment at  $\sqrt{s} = 30.1\text{GeV}$ . The difference

---

<sup>4</sup>Half Width at Half Maximum

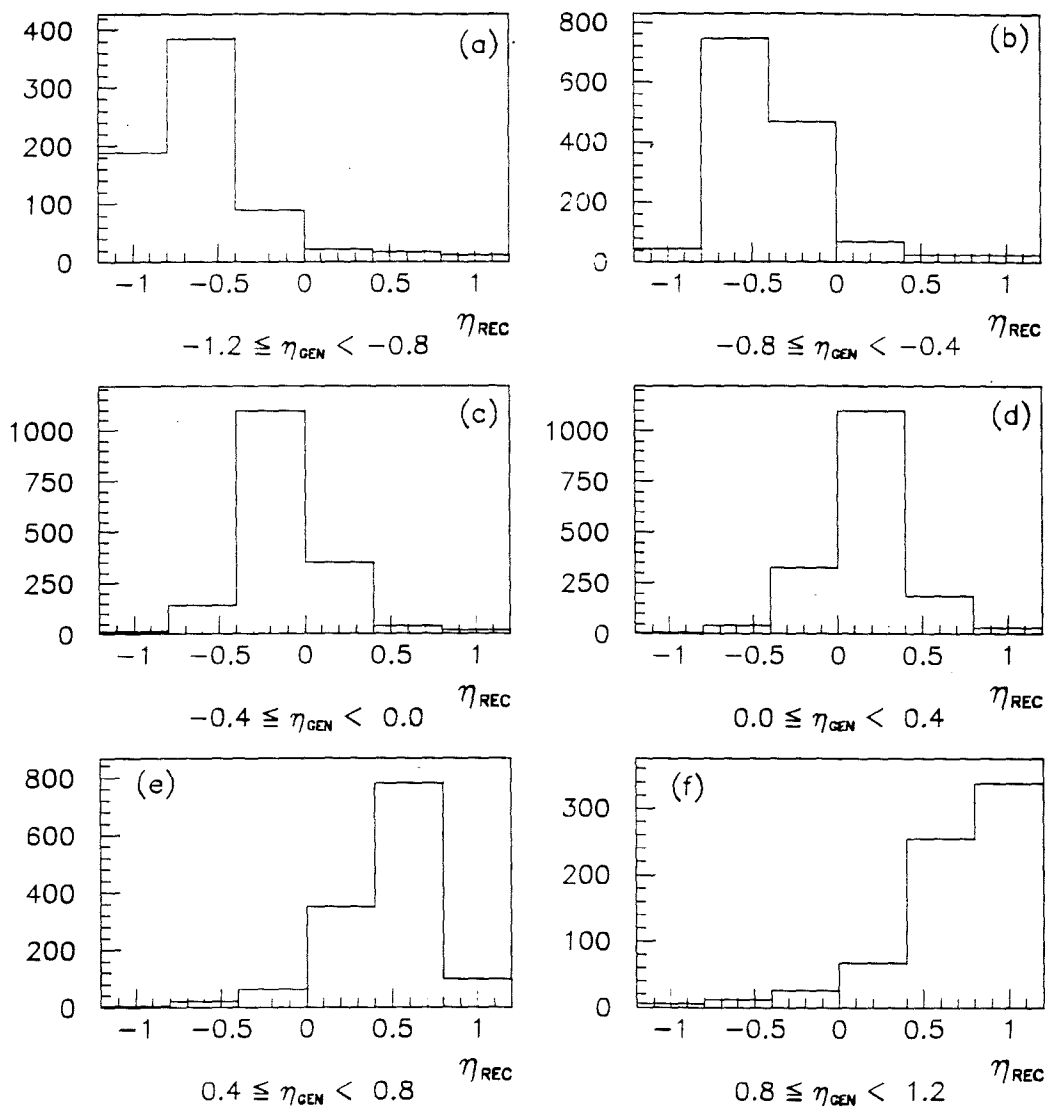


Figure 6.10: Pseudorapidity smearing of the reconstructed recoil jet for various pseudorapidity intervals of the generated recoil jet.

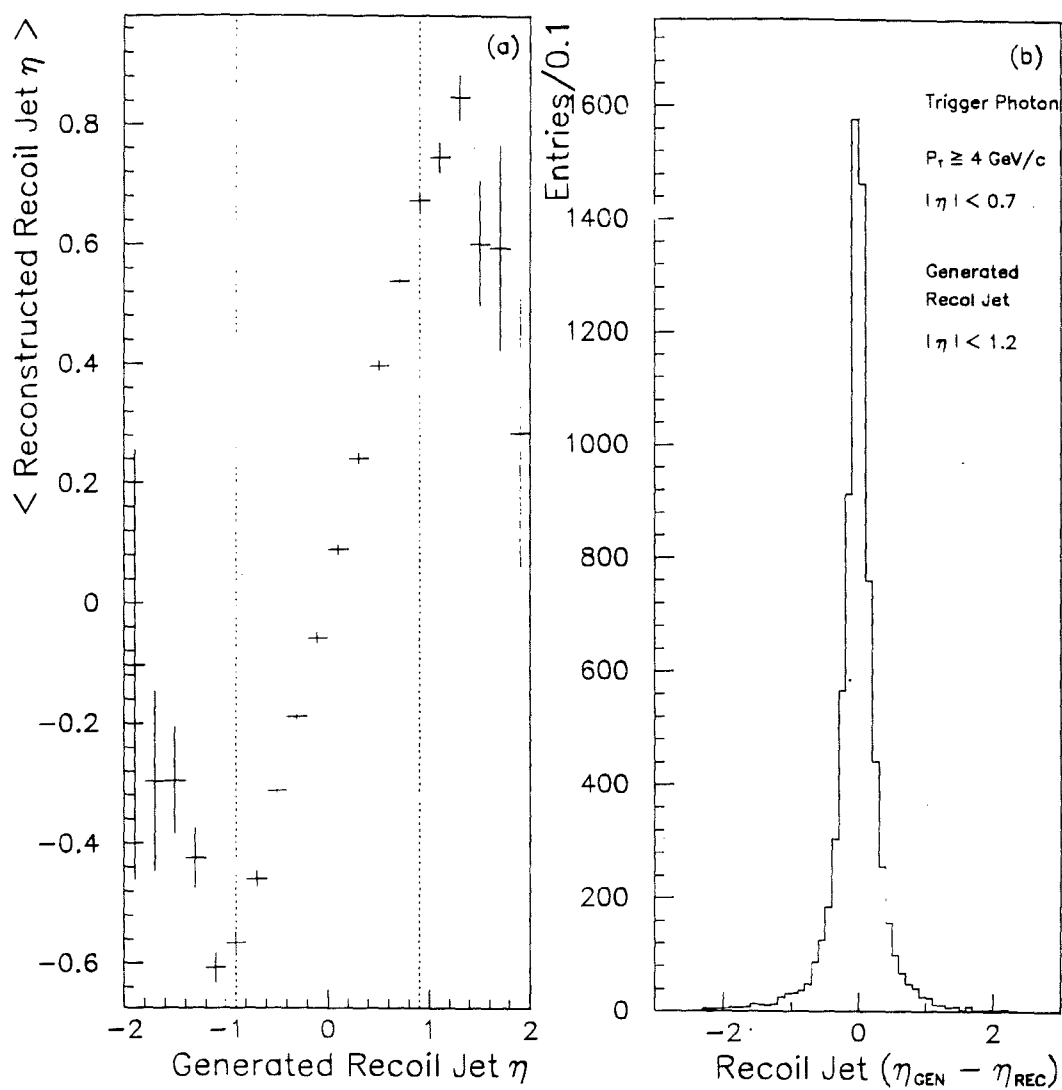


Figure 6.11: Recoil jet pseudorapidity smearing and jet axis resolution. (a) Average reconstructed recoil jet  $\eta$  as a function of the generated recoil jet  $\eta$  (b) Jet axis resolution,  $\Delta\eta = \eta_{\text{GEN}} - \eta_{\text{REC}}$ . The cuts applied are described in the text.

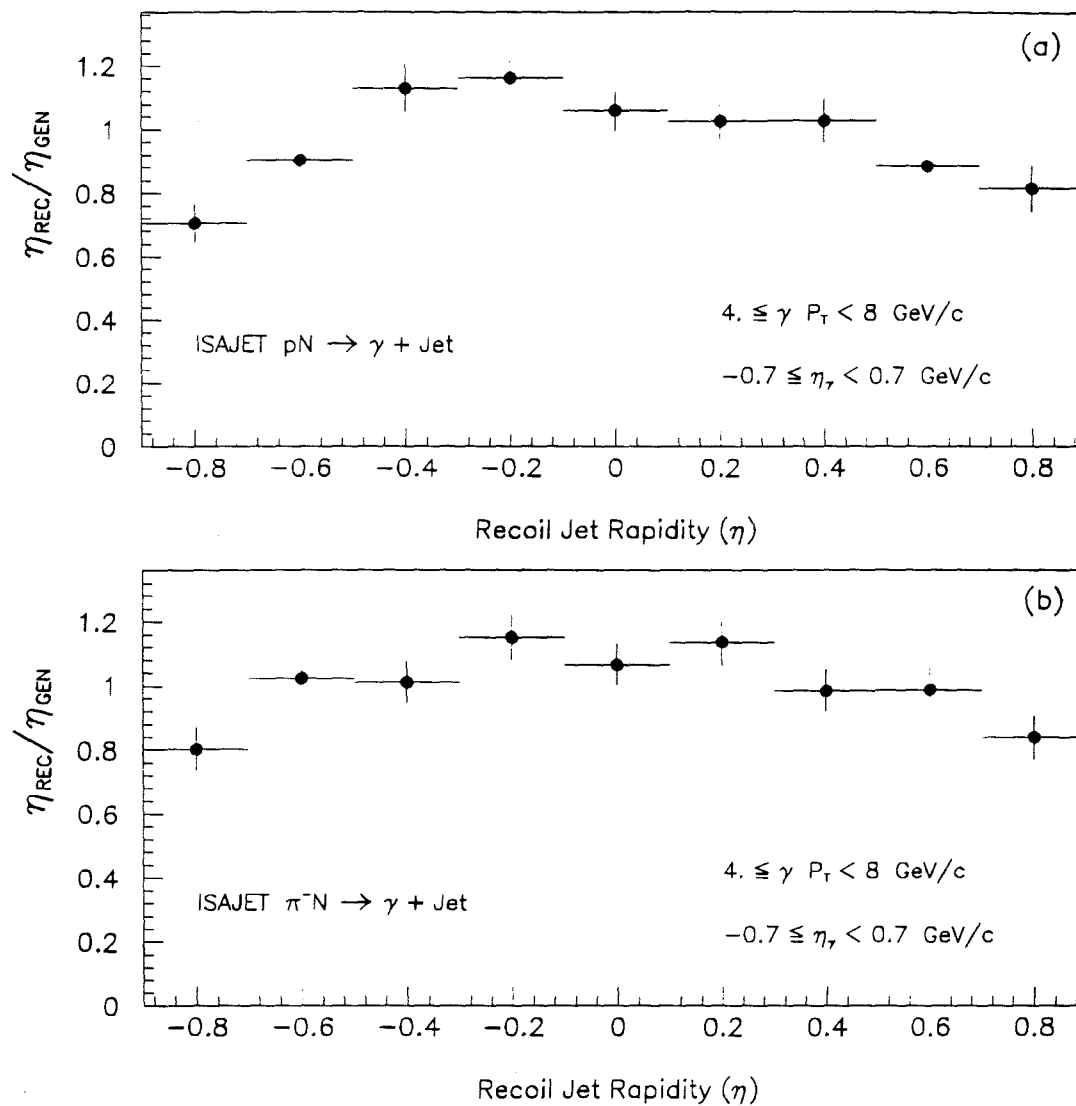


Figure 6.12: Recoil jet reconstruction efficiency ( $\eta_{REC}/\eta_{GEN}$ ). (a) ISAJET proton data, (b) ISAJET  $\pi^-$  data.

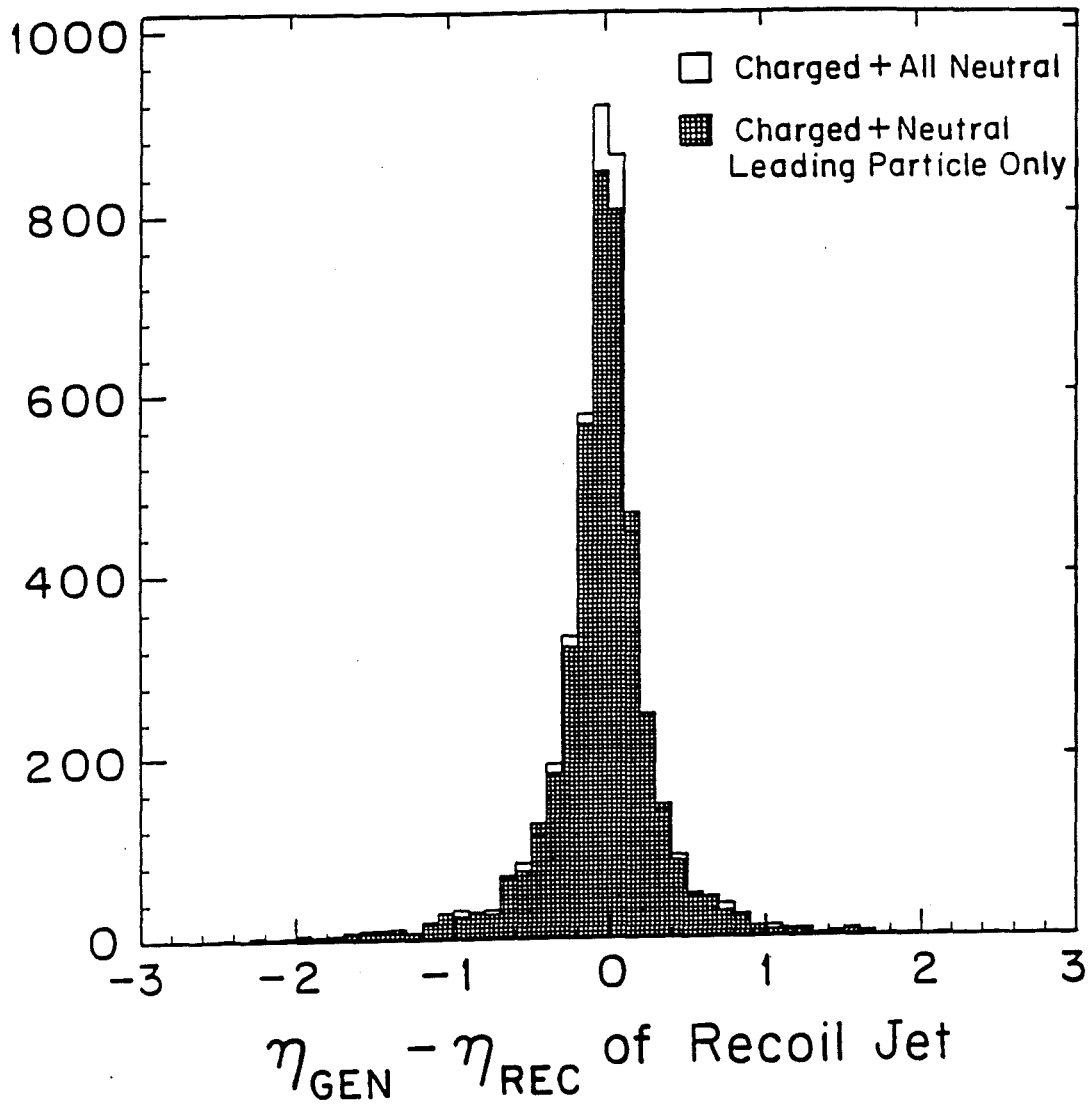


Figure 6.13: Recoil jet axis resolution ( $\eta_{GEN} - \eta_{REC}$ ). The shaded area represents the recoil jets reconstructed with no photons except the leading neutral particle in the recoil jet.

between  $x_a$  and  $x_b$  is shown in figure 6.15 for  $\gamma + jet$  and  $\pi^0 + jet$  events. The dashed curve (centered on zero) is for the positive data for  $\gamma + jet$  and  $\pi^0 + jet$  events.

## 6.5 Properties of Recoil Jets

As we have pointed out at the beginning of this chapter, the production of high- $P_T$  jets of hadrons is one of the most striking features of hard scattering processes in hadron collisions. The detection of a high- $P_T$  trigger particles plus their away side jets allow the study of the fragmentation of partons into observed jets as well as the study of jet properties.

In the following several subsections, we will present results on charged particle multiplicity, the transverse jet structure, and the longitudinal jet structure. Whenever applicable, the results are compared with ISAJET and PYTHIA Monte Carlo predictions and (or) QCD predictions.

### 6.5.1 Charged Multiplicity

Figure 6.16 (a) and (b) show the charged particle multiplicity distribution of recoil jets for the  $\pi^0$  and  $\gamma$  events, for both the  $pBe$  and  $\pi^-Be$  data. The average charged multiplicity ( $\langle N_{ch} \rangle$ ) is found to be  $\sim 3.8$  for jets recoiling from a  $\pi^0$  or  $\gamma$ . The dotted line superimposed in figure 6.16 is the ISAJET prediction<sup>5</sup> for  $N_{ch}$  using independent fragmentation model[46]. Although the ISAJET predictions seem to have a low  $\langle N_{ch} \rangle$ , there is nevertheless a reasonable agreement between these predictions and data.

Figure 6.16 (c) and (d) show the average charged multiplicity ( $\langle N_{ch} \rangle$ ) as a function of the total energy ( $W$ ) in the parton-parton center-of-mass frame. Once again we have ignored  $k_T$  of the colliding partons in calculating  $W$ . The dotted

---

<sup>5</sup>ISAJET predictions are for  $\gamma + jet$  events only.

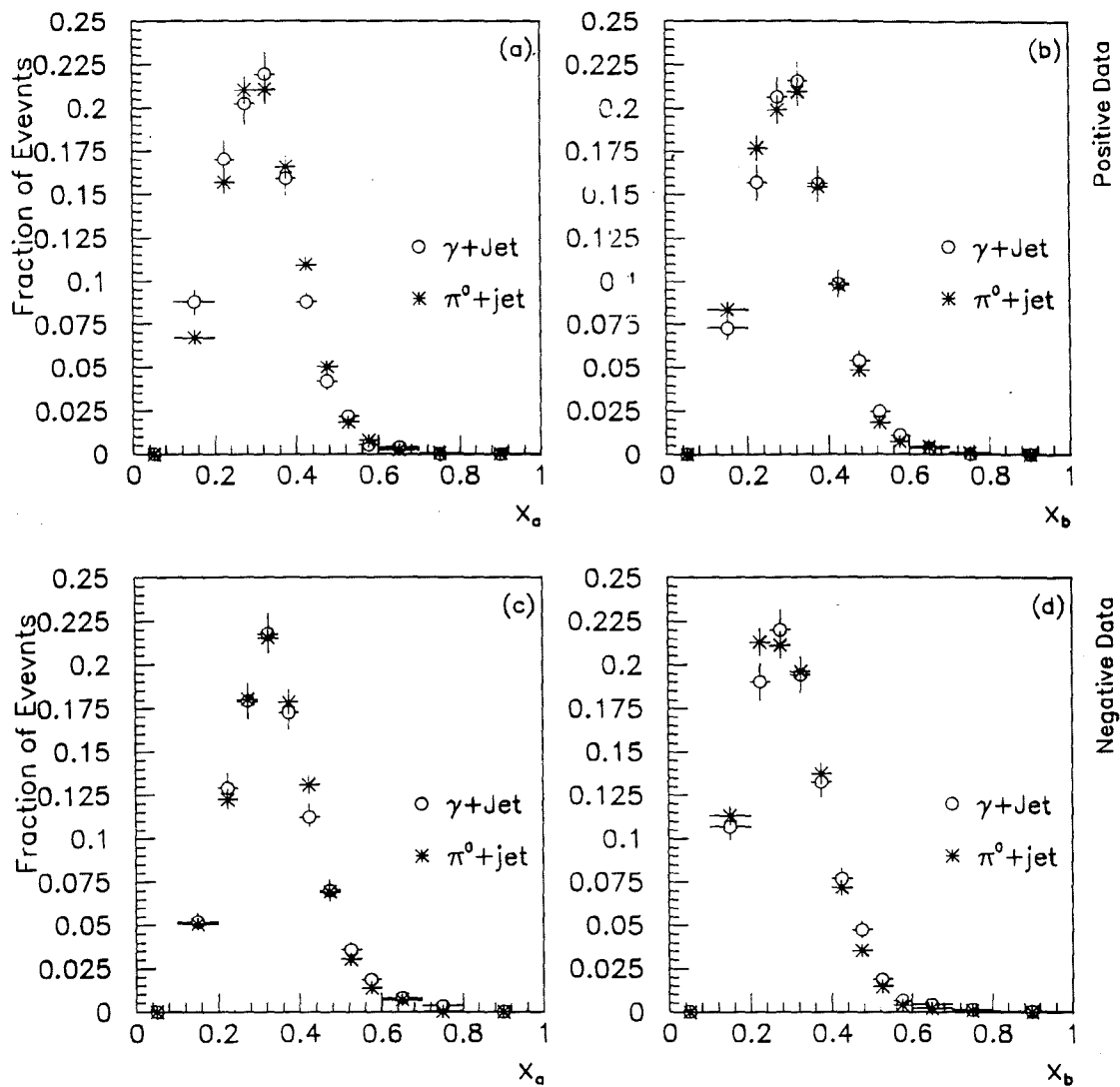


Figure 6.14: Parton momentum fractions  $x_a$  and  $x_b$  for  $\pi^0 + jet$  and  $\gamma + jet$  events in data. (a) and (b): positive data and (c) and (d): negative data.

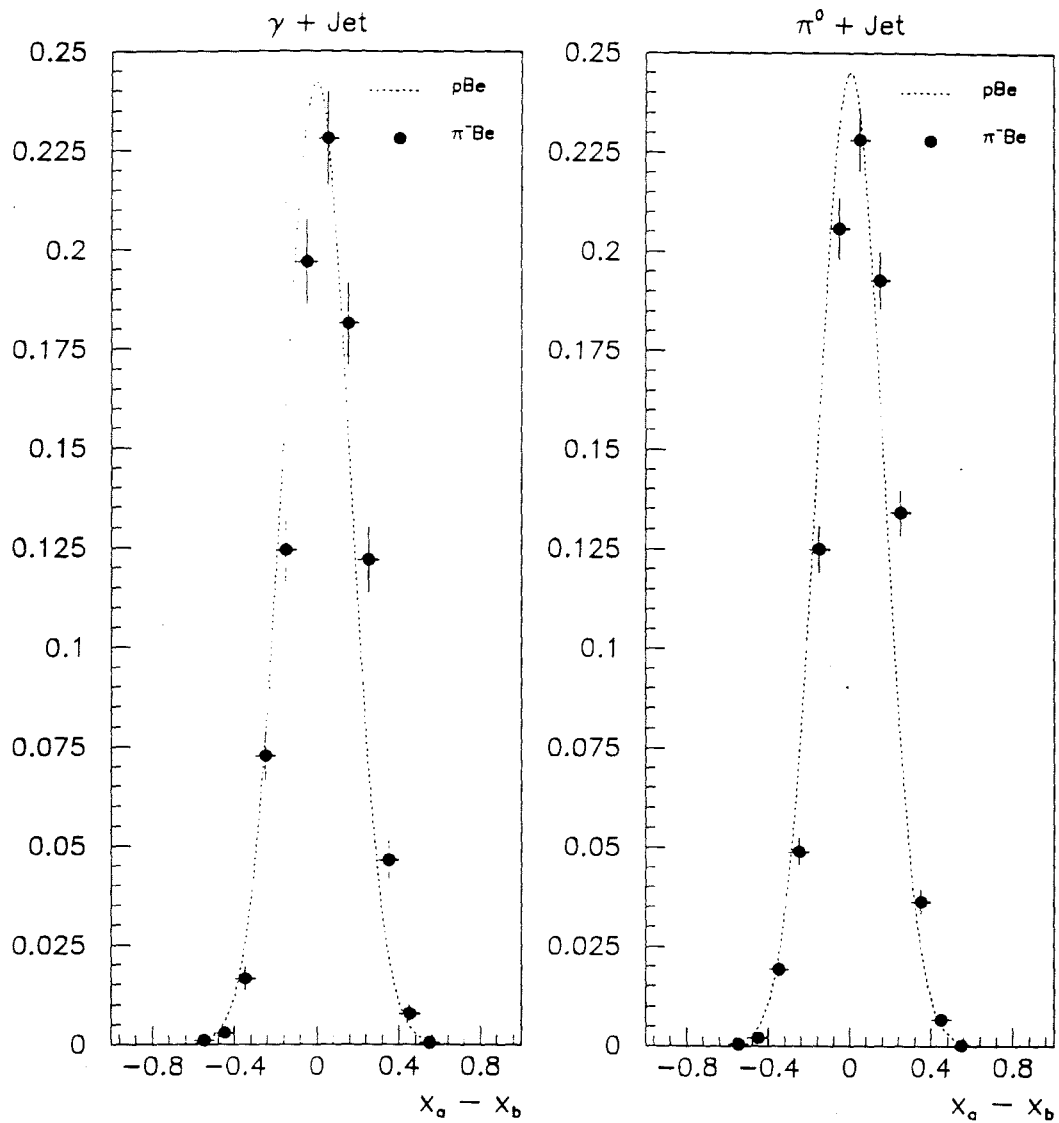


Figure 6.15:  $(x_a - x_b)$  distributions for  $\pi^0 + jet$  and  $\gamma + jet$  events in data. The dashed line is for the positive data and the solid circles are for the negative data.

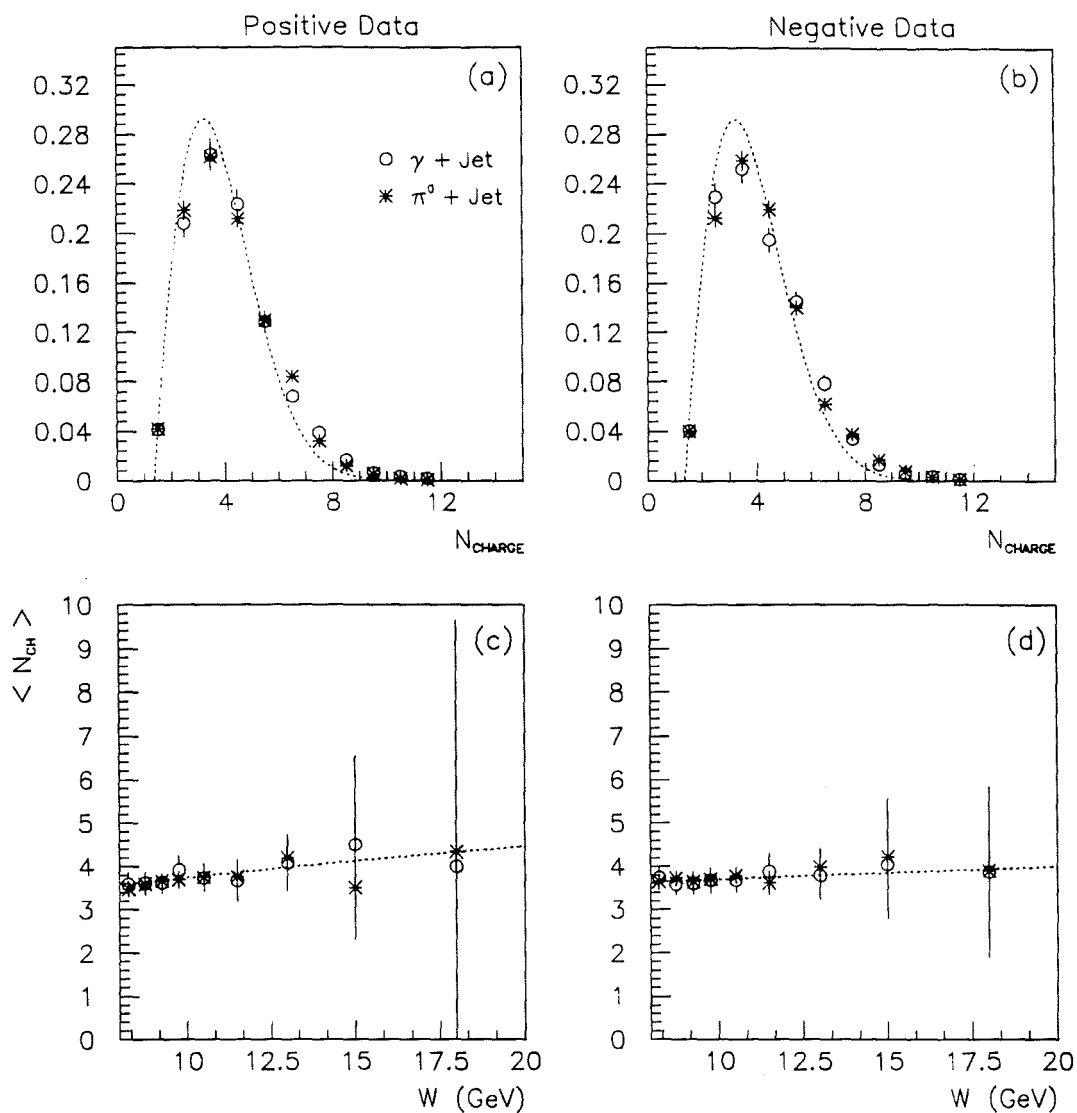


Figure 6.16: Distributions of charged particles in recoil jets.  $\circ$  represents  $\gamma + jet$  data while  $*$  represents  $\pi^0 + jet$  data.  $N_{ch}$  is the number of charged particles/recoil jet and  $W$  is the invariant mass of the  $\pi^0 + jet$  ( or  $\gamma + jet$  ) system. (a)  $N_{ch}$  : (+) data, (b)  $N_{ch}$  : (-) data, (c)  $\langle N_{ch} \rangle$  vs  $W$  : (+) data and (d)  $\langle N_{ch} \rangle$  vs  $W$  : (-) data. The dotted lines in (a) and (b) are the predictions of ISAJET while those in (c) and (d) are the fits of Eq. 6.3 to data.

line is the parametrization of QCD predictions for  $\langle N_{ch} \rangle$  in the leading log approximation[51, 52, 53]. The function

$$\langle N_{ch} \rangle = a + b \cdot \exp\{c\sqrt{\ln(s/Q_0^2)}\} \quad (6.3)$$

is fitted to data where  $\sqrt{s} = W$  and  $Q_0 = 1$  GeV.

For the negative data, the parameters in the fit to our data were found to be:  $a=3.24\pm 0.42$ ,  $b=0.014\pm 0.058$  and  $c=1.65\pm 0.78$  with  $\chi^2/DF = 0.7$  and for the positive data, they are:  $a=2.78\pm 0.47$ ,  $b=0.018\pm 0.018$  and  $c=1.54\pm 1.56$  with  $\chi^2/DF = 0.3$

## 6.5.2 Transverse Momentum and Jet Width

Often, the transverse jet structure is explained in terms of the variable  $q_T$ , the momentum component of charged particles transverse to the recoil jet axis. The average  $q_T$  provides a measurement of jet width. Figure 6.17 shows the  $\langle q_T \rangle$  as a function of the longitudinal fragmentation variable  $z$  (see section 6.5.3), for trigger  $P_T$  in the range 4–8 GeV/c. The dotted lines superimposed on figure 6.17(a) and (b), are from ISAJET predictions. There is a good agreement between data and ISAJET Monte Carlo, for both the positive and negative data. The agreement between data and Monte Carlo also reflects that we have an accurate model for the detector response in GEANT simulations. The results from the AFS[54] and WA70[15] have shown a similar  $z$ -dependence of  $\langle q_T \rangle$ . It should be stressed that the  $z$ -dependence of  $\langle q_T \rangle$  is very sensitive to the precision with which the recoil jet direction is determined. The average  $q_T$  is measured to be  $\sim 0.3$  GeV/c. Shown in figure 6.18 is the transverse fragmentation defined as

$$\frac{1}{N_{Jet}} \cdot \frac{dn_{ch}}{dq_T}$$

for  $\gamma$  and  $\pi^0$  triggered events in  $p\text{Be}$  and  $\pi^- \text{Be}$  interactions.

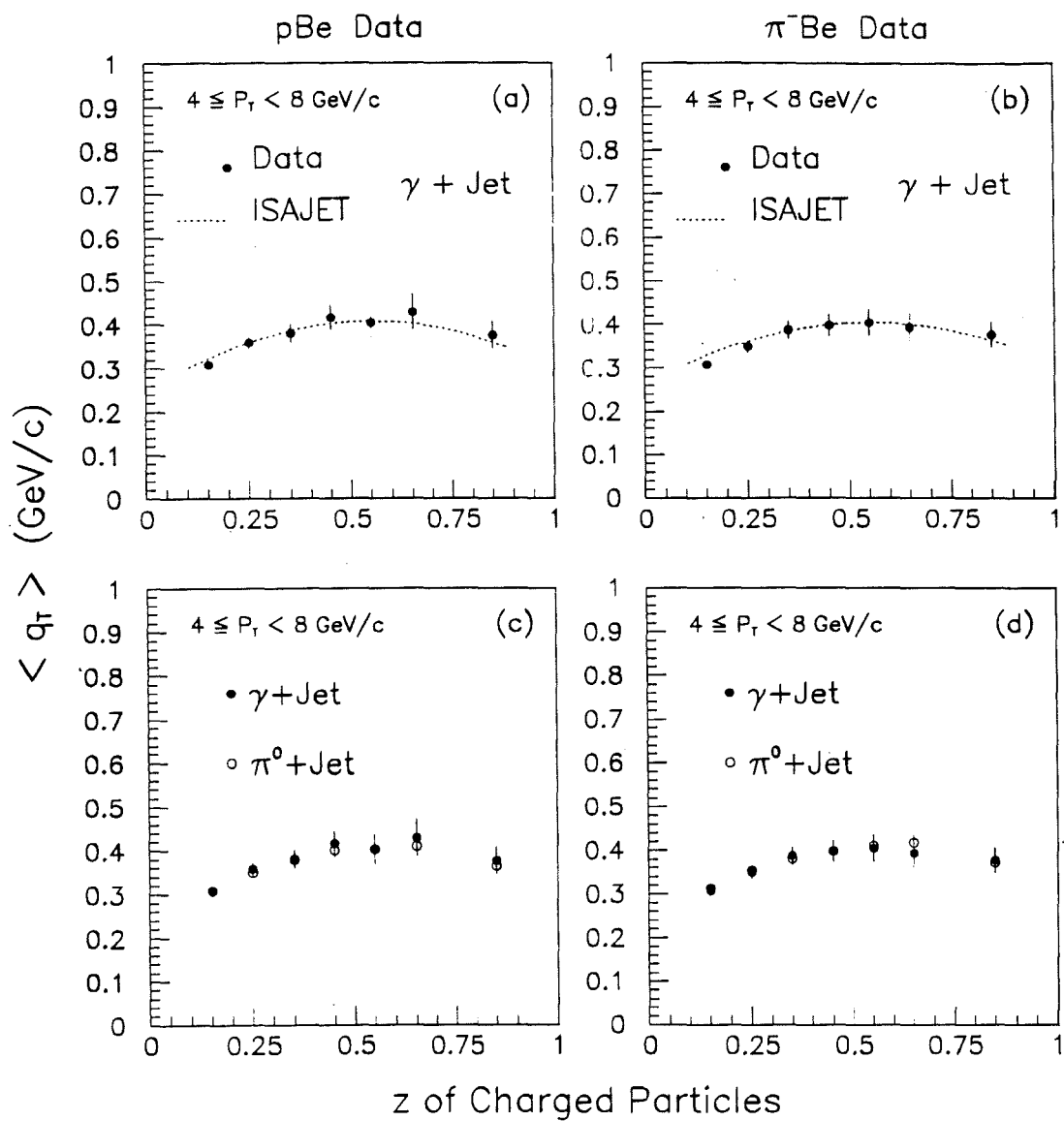


Figure 6.17: Average transverse momentum of recoil jet particles (relative to the recoil jet axis) as a function of the longitudinal fragmentation variable  $z$ .

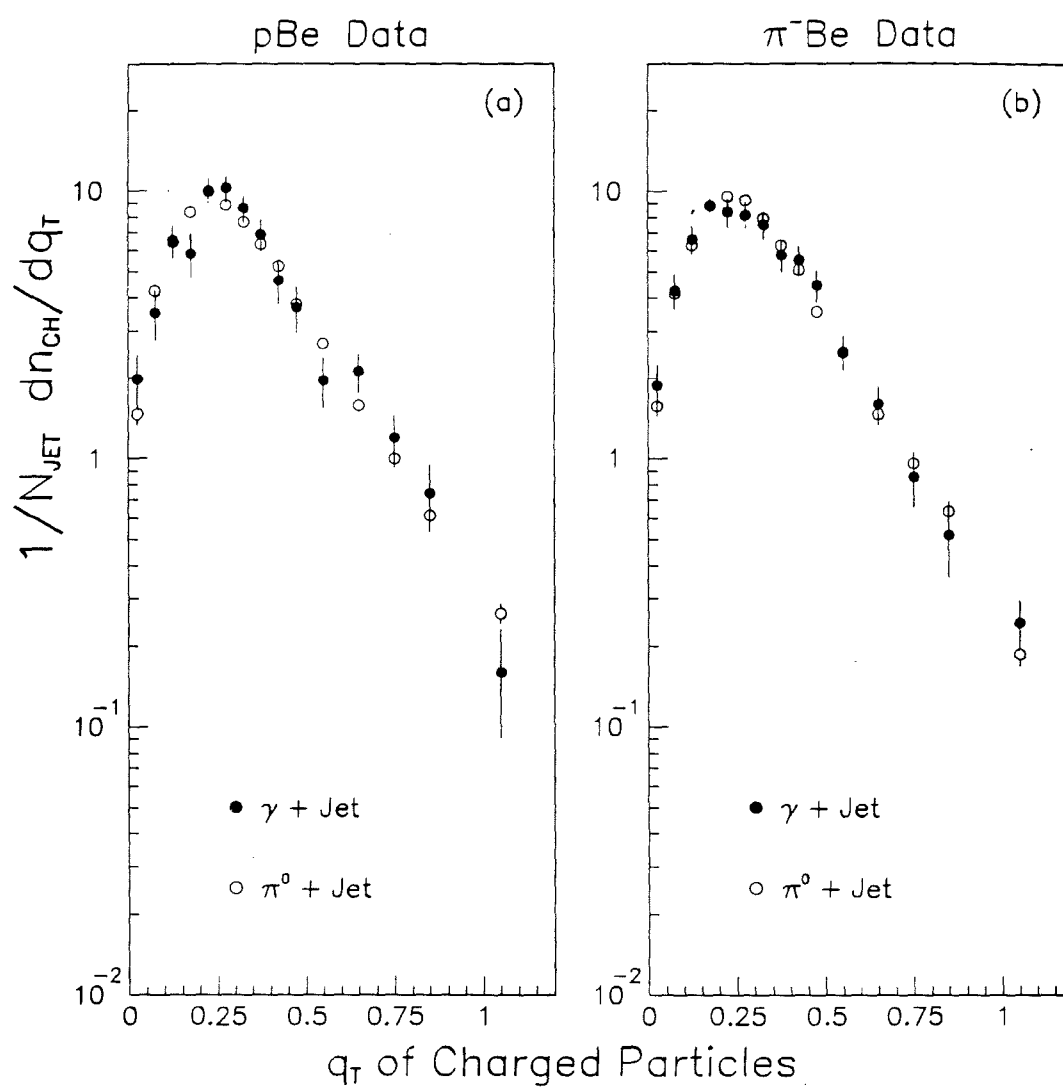


Figure 6.18: Transverse fragmentation distributions for recoil jets. (a) Positive data, and (b) Negative data.  $\gamma + jet$  and  $\pi^0 + jet$  fragmentation distributions are compared in each case.

The transverse fragmentation distributions for  $\gamma$  events are not corrected for the background to the direct photon signal.

### 6.5.3 Longitudinal Fragmentation

The longitudinal fragmentation of recoil jet into charged particles is described by  $D(z)_{ch}$ , where  $z$  defined as

$$z = \frac{p_L^{ch}}{|\vec{P}_{jet}|} \quad (6.4)$$

is the fractional momentum component of a charged particle along the recoil jet axis.  $|\vec{P}_{jet}|$  is the total recoil jet momentum and  $p_L^{ch}$  is the longitudinal momentum component of the particle along the jet axis. The fragmentation function for the recoil jet is presented as

$$D(z)_{ch} = \frac{1}{N_{Jet}} \cdot \frac{dn_{ch}}{dz} \quad (6.5)$$

where  $N_{Jet}$  is the total number of recoil jets and  $dn_{ch}$  is the number of charged particles in the interval  $dz$ . It is worthwhile to mention here, that the fragmentation variable  $z$  is determined with a scaled recoil jet momentum  $|\vec{P}_{jet}|$ . The magnitude of the recoil jet momentum is scaled such that  $P_T^{JET} = P_T^{Trigger}$  to account for any losses (neglecting  $k_T$ ) in the jet reconstruction. Momentum scaling only changes the magnitude of the jet momentum vector but not the jet direction. The effect of this scaling on the shape of the fragmentation function is discussed later in this section.

The measured fragmentation distributions for recoil jets associated with direct photon events have to be corrected for the background arising from the mis-identified neutral mesons. To subtract this background, which amounts to  $\sim 50\%$  for  $p\text{Be}$  data and  $\sim 60\%$  for  $\pi^- \text{Be}$  data, we have used the Monte Carlo simulated events for  $\pi^0$  background calculation described in section 5.3. The reconstruction of recoil jets from the Monte Carlo generated events was done in a fashion identical to the reconstruction of recoil jets from data, to produce background distributions as a function

of  $z$ . Figure 6.19 (a) and (b) show the unsubtracted fragmentation distributions  $dn_{ch}/dz$  for  $p\text{Be}$  and  $\pi^- \text{Be}$  data alone with the same distributions obtained from a data driven  $\pi^0$  Monte Carlo calculation. The fake direct photon contamination in the data, for each beam type, was determined and subtracted to get the corrected total number ( $N_\gamma^T$ ) of direct photon + jet events.  $N_\gamma^T$  was calculated in the following way:

$$N_\gamma^T = N_\gamma^{\text{exp}} - N_\gamma^{\text{fake}} \cdot \frac{N_{\pi^0}^{\text{exp}}}{N_{\pi^0}^{\text{MC}}} \quad (6.6)$$

where  $N_{\pi^0}^{\text{exp}}$  and  $N_{\pi^0}^{\text{MC}}$  are the total number of  $\pi^0 + \text{jet}$  events reconstructed from data and Monte Carlo, respectively.  $N_\gamma^{\text{exp}}$  is the total number of unsubtracted  $\gamma + \text{jet}$  events in the data and  $N_\gamma^{\text{fake}}$  is the total number of reconstructed fake  $\gamma + \text{jet}$  events in Monte Carlo.

By subtracting the fake distributions weighted by the ratio  $N_{\pi^0}^{\text{exp}}/N_{\pi^0}^{\text{MC}}$  from the data distributions, the corrected fragmentation distributions  $dn_{ch}/dz$  were determined. Finally the corrected fragmentation functions were obtained by normalizing these corrected  $dn_{ch}/dz$  to  $N_\gamma^T$ .

As mentioned in section 6.3.2, there are approximately  $\sim 20 - 25\%$  “soft” beam/target jet particles misassigned to the reconstructed recoil jet. Figure 6.20(a) shows the ratio of  $D(z)_{\text{MIS}}/D(z)_{\text{REC}}$  as a function of the longitudinal fragmentation variable  $z$ .  $D(z)_{\text{MIS}}$  is the contribution from the underlying event to the recoil jet fragmentation function and  $D(z)_{\text{REC}}$  is the total reconstructed longitudinal recoil jet fragmentation which includes the misassigned particles. As evident from figure 6.20(a), this background has a strong “ $z$ ” dependence, as one would expect. At low  $z$ , this background is about 22–24% and goes down to less than 4% for  $z > 0.35$ . This observation is consistent with what is observed in figure 6.9. All the measured fragmentation distributions have to be corrected for this contamination as well as for the acceptance of the detector and the inefficiencies due to the jet reconstruction algorithm.

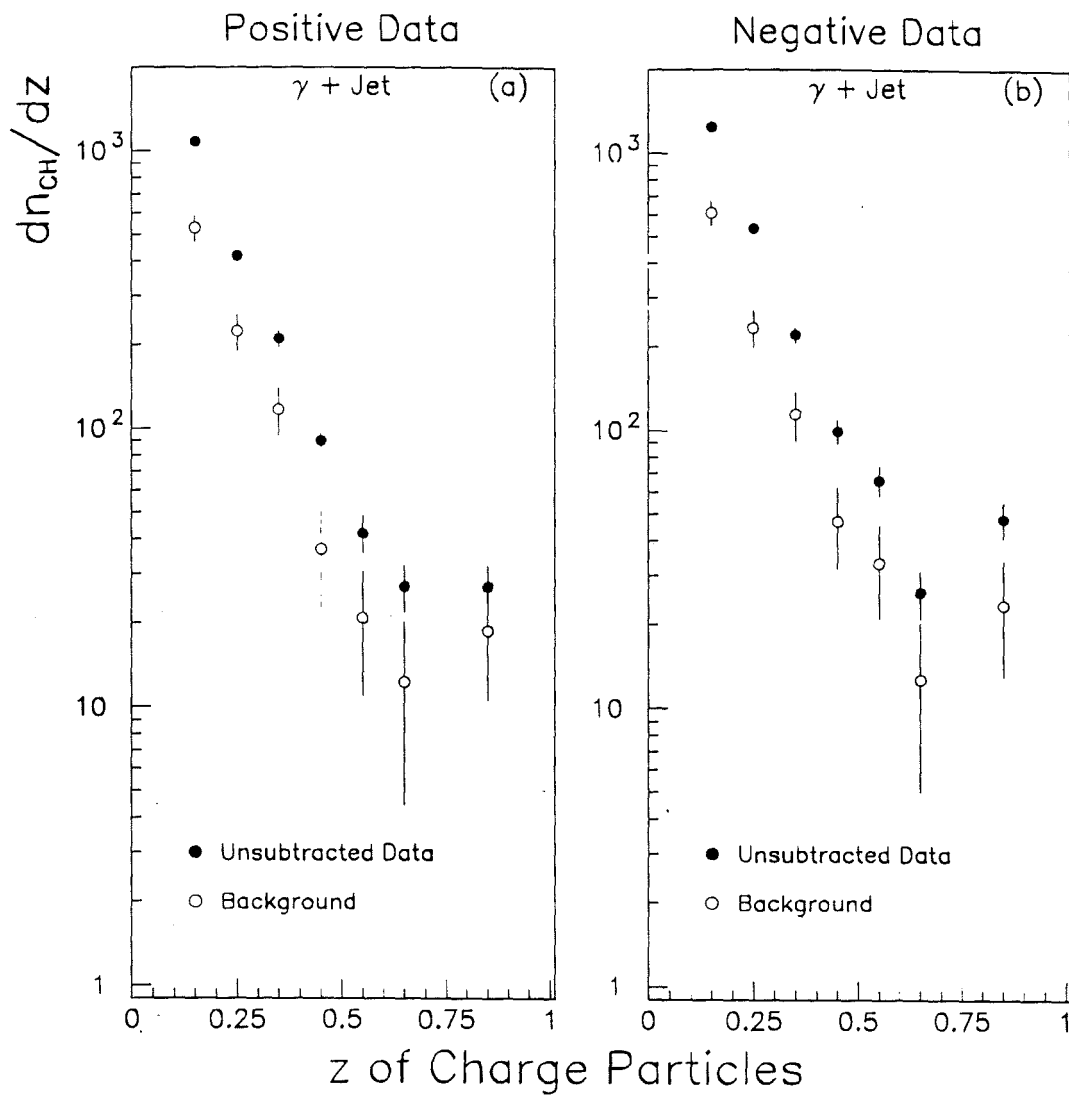


Figure 6.19: Unsubtracted  $dn_{ch}/dz$  distributions (solid circles) for  $\gamma + jet$  events, compared with the background (open circles).

Convoluting all these effects into a single  $z$  dependent number, the correction factor was calculated as the ratio:

$$\xi(z) = \frac{[D(z)]_{reconstructed}}{[D(z)]_{generated}} \quad (6.7)$$

where  $D(z)_{generated}$  is the generated fragmentation function and  $D(z)_{reconstructed}$  is the reconstructed fragmentation function. Figure 6.20(b) shows this ratio( $\xi(z)$ ) for the positive and negative data. The fact that this ratio is greater than one for  $z < 0.3$  is mainly due to effects of the detector simulation and the misassignment of beam particles to the recoil jets. For  $z > 0.3$ ,  $\xi$  drops below 1.0 and the effect could be interpreted as an inefficiency in detecting high  $z$  particles. But one should be careful in drawing such conclusions since the shape of the distribution in figure 6.20 is very sensitive to the method employed in determining the magnitude of the recoil jet momentum. For example, if we use the unscaled recoil jet momentum, we observe that  $\xi$  is greater than 1.0 for all the values of  $z$ . All the distributions in figures 6.21 6.22 are corrected for these inefficiencies and misassignment.

The fragmentation variable  $z$  used in figure 6.21 is calculated with an unscaled recoil jet momentum while those in figure 6.22 are determined with a scaled recoil jet momentum. The effect of scaling is to change the slope of the distributions, on average, by about 30%.

The corrected unscaled fragmentation functions for recoil jets associated with  $\gamma$  events are shown in figure 6.21(a) and (b) for  $p\text{Be}$  and  $\pi^- \text{Be}$  data, compared with ISAJET and PYTHIA Monte Carlo predictions. The overall agreement between data and the Monte Carlo prediction seems to be reasonable. In figure 6.21(a) ISAJET and PYTHIA Monte Carlo simulations predict a slightly harder fragmentation function than what observed in data. In figure 6.21(c) and (d), we compare the fragmentation functions for recoil jets associated with  $\pi^0$  and  $\gamma$  events for positive and negative data. We see no significant difference between the fragmentation functions for the recoil

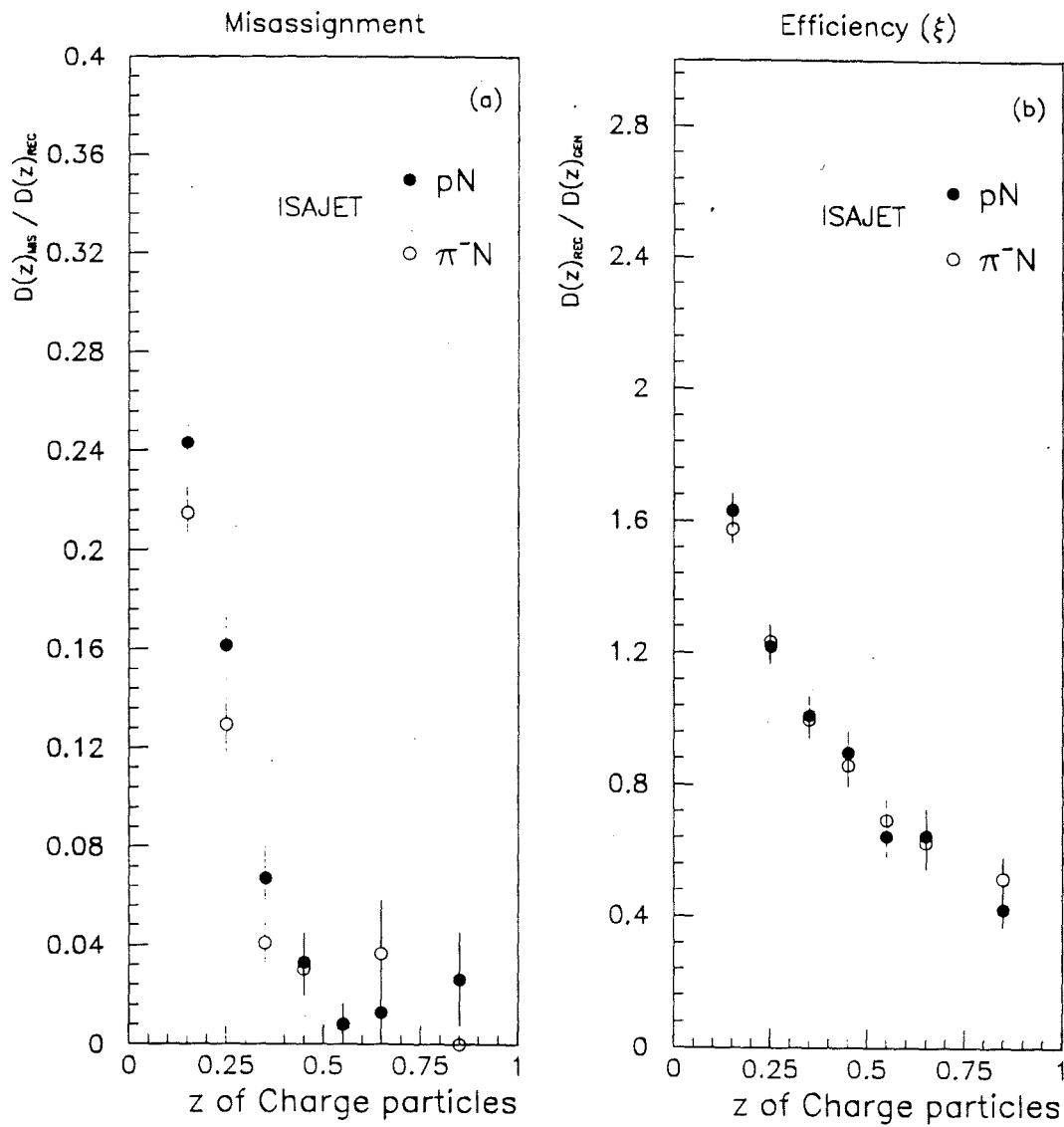


Figure 6.20: Misassignment and efficiency correction. (a) fraction of the misassigned particles in the recoil jet as a function of  $z$ , and (b)  $z$  dependent correction factor for the fragmentation function.

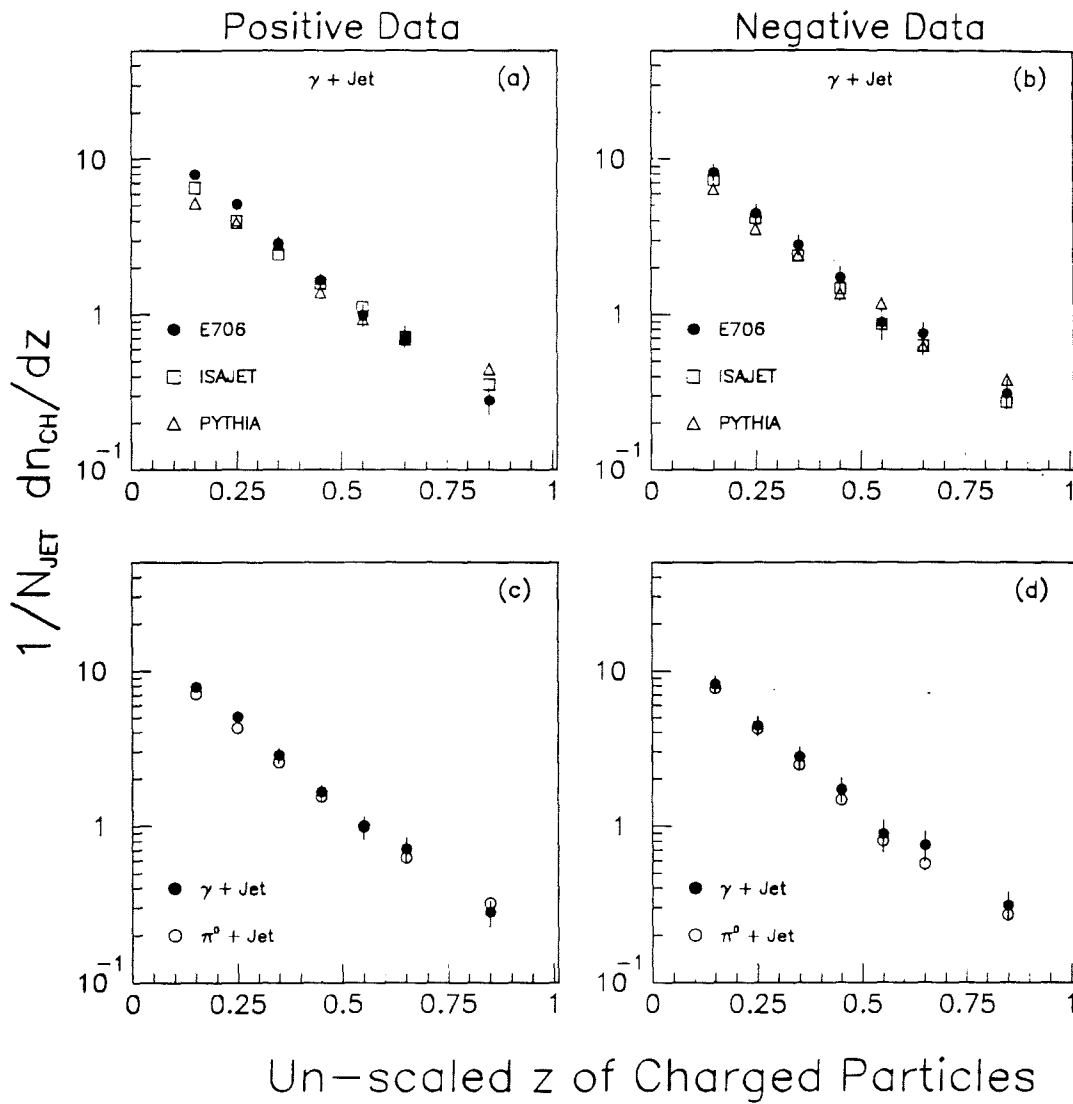


Figure 6.21: Unscaled fragmentation functions. (a) and (b)  $\gamma + jet$  fragmentation functions compared with the ISAJET and PYTHIA predictions, for positive and negative data. (c) and (d) Comparison between  $\pi^0 + jet$  and  $\gamma + jet$  fragmentation.

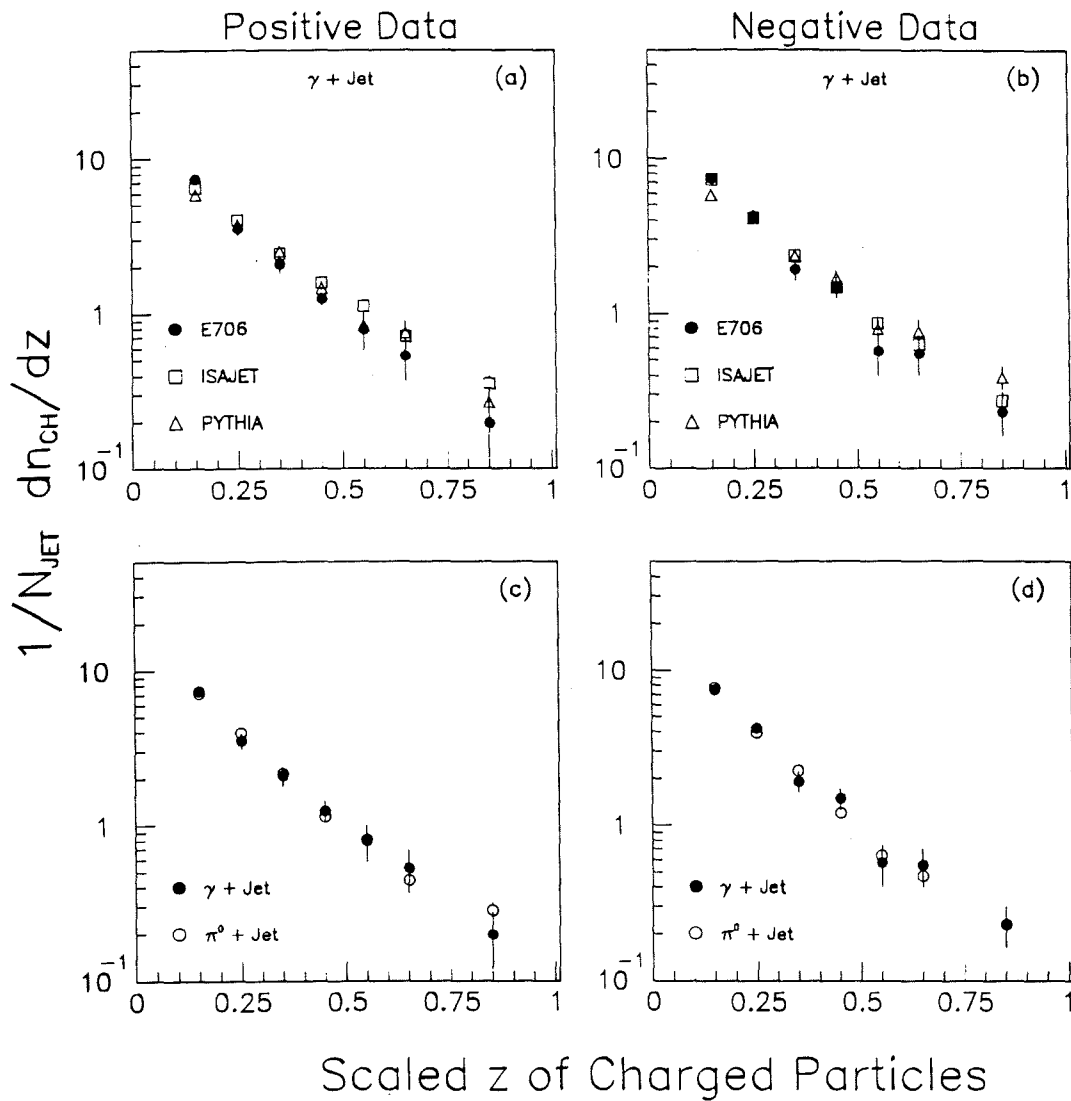


Figure 6.22: Scaled fragmentation functions. Recoil jet  $P_T$  is scaled to that of the trigger particle. (a) and (b)  $\gamma + \text{jet}$  fragmentation functions compared with the ISAJET and PYTHIA predictions, for positive and negative data. (c) and (d) Comparison between  $\pi^0 + \text{jet}$  and  $\gamma + \text{jet}$  fragmentation.

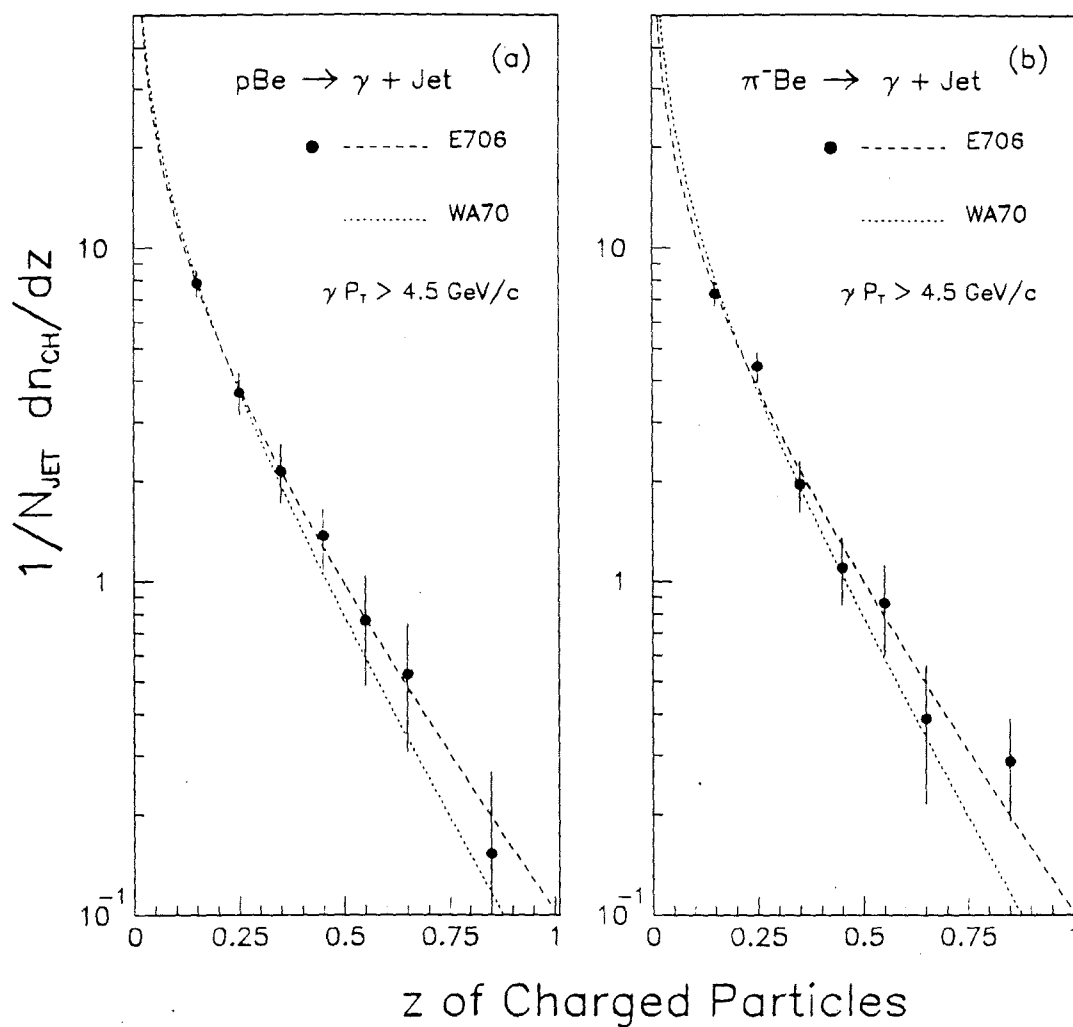


Figure 6.23: Fit to  $\gamma + jet$  fragmentation functions compared with WA70 parametrization for  $\langle W \rangle = 10 \text{ GeV}$ . The error bars represent only the statistical uncertainty. The solid circles represent E706 data while the the dashed lines represent the fits to our data and WA70 parametrization.

jets associated with  $\pi^0$  and  $\gamma$  triggers. This observation is consistent with results from WA70 experiment[15]. Similar agreements between data and Monte Carlo as well as between  $\pi^0 + jet$  and  $\gamma + jet$  events are observed in figure 6.22 as well.

Figure 6.23 show the measured fragmentation functions for  $\gamma + jet$  events with  $\gamma P_T > 4.5$  GeV/c for  $pBe$  and  $\pi^-Be$  interactions. The dashed line superimposed on figure 6.23 is a fit to our data in the interval  $0.1 < z < 1.0$ , using the form

$$D(z) = az^{-b}e^{-cz} \quad (6.8)$$

The parameters in the fit were found to be  $a=3.69\pm 3.67$ ,  $b=0.67\pm 0.44$  and  $c=3.58\pm 1.37$  with  $\chi^2 = 1.102$  for  $pBe$  interactions and  $a=4.38\pm 3.73$ ,  $b=0.58\pm 0.37$  and  $c=3.75\pm 1.18$  with  $\chi^2 = 1.106$  for  $\pi^-Be$  interactions. The dotted lines superimposed on figure 6.23 are the parametrization of the fragmentation functions measured in WA70 at  $\langle W \rangle = 10$  GeV (the average  $W$  for the E706 data presented in figure 6.23).

## CHAPTER 7

# Cross Sections

### 7.1 Overview

The calculation of the differential cross sections for the production of  $\pi^0 + jet$  events and  $\gamma + jet$  events is discussed in this chapter. In general the differential cross section per nucleon, as a function of trigger  $P_T$ , trigger pseudorapidity ( $\eta_1$ ) and recoil jet pseudorapidity ( $\eta_2$ ), is expressed as

$$\frac{d\sigma}{dP_T d\eta_1 d\eta_2} = \frac{1}{N_{scat} \times B_{in}} \cdot \frac{dN(P_T, \eta_1, \eta_2)}{dP_T d\eta_1 d\eta_2} \quad (7.1)$$

where  $dN(P_T, \eta_1, \eta_2)/dP_T d\eta_1 d\eta_2$  is the differential event distribution,  $B_{in}$  is the number of incident beam particles and  $N_{scat}$  is the number of target nucleons per unit cross sectional area. The latter is equal to  $\rho l N_A n_A / A$  where  $\rho$  is the density of the target in  $g/cm^3$ ,  $l$  is the length of the target in  $cm$ ,  $N_A$  is the Avogadro number,  $n_A$  is the number of nucleons per nucleus and  $A$  is the atomic number. The extraction of the cross section from data is a multi-step process involving a number of corrections applied to account for the inefficiencies in the selection of events. Each selected event was weighted to include these corrections. Application of these correction factors will be described in the actual calculation of the differential cross sections.

In the next several subsections, we will briefly describe certain considerations which are necessary to extract the cross section from data. They are, namely, the establishment of the energy scale, the EMLAC acceptance and photon reconstruction efficiency, the trigger corrections, correction for primary vertex reconstruction efficiency, corrections for the veto wall cut and the beam count.

### 7.1.1 Energy Scale

The determination of the absolute energy scale in the EMLAC is very important due to the steep  $P_T$  dependence of the differential cross sections. Because of this dependence, small variations in  $P_T$  can cause large variations in the cross section, when presented as a function of  $P_T$ . This dependence is less significant when the cross sections are plotted as a function of the recoil jet pseudorapidity since we are integrating over a  $P_T$  range.

The energy scale is established by using  $\pi^0$  events in which one photon coming from the decay of a  $\pi^0$  converts into an  $e^+e^-$  pair upstream of the dipole magnet. First the ratio of the electron (or positron) energy ( $E$ ) determined from the EMLAC to its momentum ( $P$ ) determined by the tracking system<sup>1</sup> was determined as a function of electron (positron) energy. Then an empirical correction to  $E$  (as a function of  $E$ ) was calculated by requiring the average  $E/P=1$  for all energies. Secondly, by comparing the loss of electron and photon energy upstream of the LAC, a formula was developed using Monte Carlo to correct the photon energy relative to the electron energy. This formula, in conjunction with the measured  $E/P$  dependence for electrons, was used to get the final energy correction for photons. Figure 7.1 shows the corrected  $E/P$  and figure 7.2 shows the average  $\pi^0$  mass (from the  $\gamma e^+ e^-$  system) as a function of photon energy. A detailed description of the determination of the EMLAC energy scale can be found in references [23, 39].

### 7.1.2 Reconstruction Efficiency and EMLAC Acceptance

The next quantities relevant to a measurement of cross sections are the corrections for geometrical acceptance of the EMLAC and the photon and  $\pi^0$  reconstruction efficiency.

---

<sup>1</sup>The momenta used here are properly calibrated as described in section 4.3

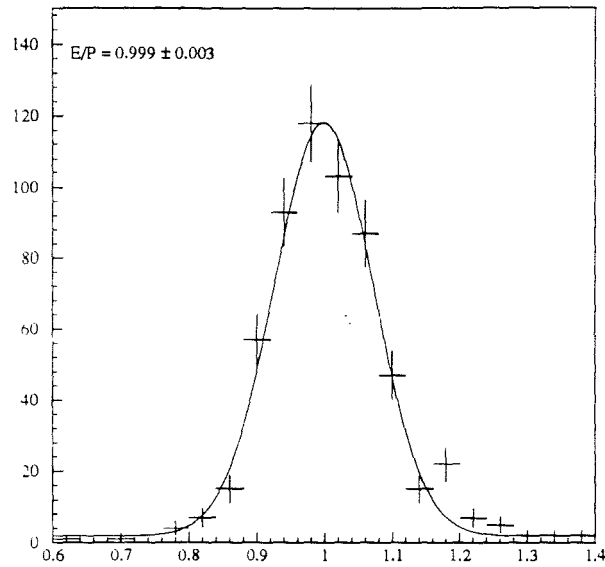


Figure 7.1: Corrected E/P ratio for electrons.

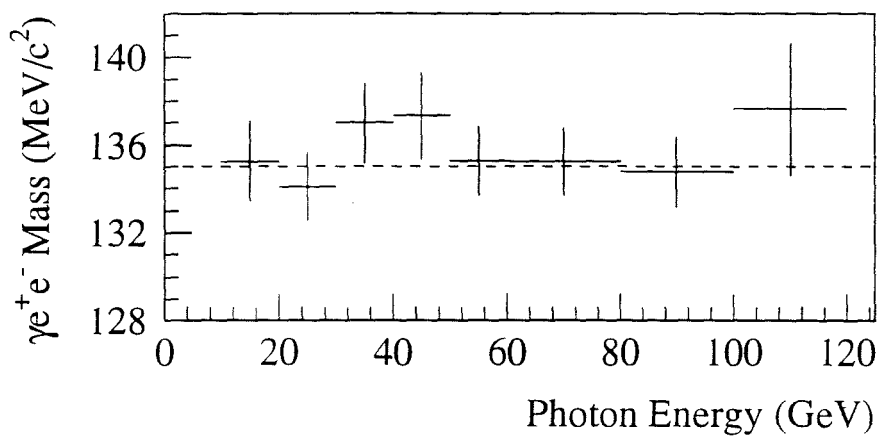


Figure 7.2:  $\gamma e^+ e^-$  invariant mass vs photon energy (E).

These were determined as a function of  $P_T$  and pseudorapidity ( $y_{cm}$ ) for both  $\pi^0$  and photons using Monte Carlo generated events described in section 5.3.

First, we determine the ratio of the number of reconstructed  $\pi^0$  's (or single photons) to the generated number of  $\pi^0$  's (or single photons) in the fiducial region of the EMLAC, as a function of  $P_T$  and  $y_{cm}$ , using a grid of 0.1 units for  $y_{cm}$  and 0.5 GeV/c units for  $P_T$ . To determine the geometrical acceptance for  $\pi^0$  's or for single photons at any given  $P_T$  (for  $P_T$  in the range 3 to 10 GeV/c) and  $y_{cm}$  (for  $y_{cm}$  in the range -0.8 to 0.8), a two-dimensional interpolation was performed on this  $(P_T, y_{cm})$  grid[32, 39]. Single photon and  $\pi^0$  reconstruction efficiencies were determined using a similar procedure.

### 7.1.3 Trigger Corrections

Corrections for the *Single-Local* trigger<sup>2</sup>, were calculated on an event by event basis using the measured trigger efficiency for different regions of EMLAC. To determine the corrections, the reconstructed R-view energy of all photons in the candidate direct photon or  $\pi^0$  octant was deposited into the corresponding EMLAC channels using the shower shape employed in photon reconstruction. Subsequently, the  $P_T$  sum of the channels was formed as was done for the online trigger[32]. Then the probability that the event satisfied the trigger was determined using the corresponding trigger efficiency curve. For a detailed discussion of the determination of the trigger corrections, the reader is referred to reference [39].

### 7.1.4 Correction for the Vertex Reconstruction Efficiency

As we have mentioned in section 4.4.3, a correction to the vertex reconstruction efficiency was determined as a function of the Z position of the primary vertex. This

---

<sup>2</sup>Recall that only the events with a *Single-Local* trigger were used in the analysis

correction was introduced to account for the inefficiency of the vertex reconstruction code that was used to determine the vertex location for the data used in the analysis in this thesis. We have reanalyzed a representative sample of data with an improved version of the vertex reconstruction code and have obtained a new distribution of the vertex- $Z$  location which includes the results from a visual scan of events. The correction factor is defined as the ratio of the new vertex- $Z$  distribution to that of the old distribution. The correction factor  $\omega_{vtx}$  was parametrized as a function of  $Z_{vertex}$  and is given by

$$\omega_{vtx} = 1.0019 - .0079 \times Z_{vertex} \quad (7.2)$$

### 7.1.5 Correction for the veto wall cut

An off-line veto wall cut was applied in the event selection as described in section 5.1 to remove the muon induced events from the data sample. The presence of an accidental hit in either veto wall corresponding to the triggering quadrant would satisfy this cut, resulting in a loss to the analysis of true events. In order to correct for this loss, the fraction of good  $\pi^0$  events rejected by this cut was measured[55]. The correction was parametrized as a function of the longitudinal coordinate  $Z$  and is given by

$$\omega_{veto} = 1.07 + 2.6 \times 10^{-4} e^{-0.46Z} \quad (7.3)$$

### 7.1.6 Beam Count

In order to determine the cross sections from the measured differential event distributions in Eq. 7.1, one would have to determine the total number of beam particles ( $B_{in}$ ) that could have produced an interaction in the experimental target.  $B_{in}$  is defined as

$$B_{in} = N_{LTB}(P_T) \times B_f \times \eta_{abs} \quad (7.4)$$

where  $N_{LTB}$  is referred to as the *Live Triggerable Beam* (LTB). LTB is defined as the total number of beam particles that hit the target when the experiment was ready to take data. This number depends on several things related to the data acquisition system and the experimental trigger[32].  $\eta_{abs}$  is the probability that a beam particle was not absorbed between the beam counters and the target of interest.  $B_f$  gives the fraction of beam particles which were not tagged as minority particles. The reaction dependent values of  $\eta_{abs}$  and  $B_f$  are given in table 7.1

Table 7.1: Process dependent corrections for the beam count.

	$\pi^-$ Be	$\pi^-$ Cu	$p$ Be	$p$ Cu
$\eta_{abs}$				
Be + Cu	0.949	0.986	0.934	0.981
Be only	0.957	-	0.943	-
$B_f$	0.986	0.986	0.942	0.942

$B_{in}$  is a  $P_T$  dependent quantity where the  $P_T$  dependence originated with having different  $P_T$  thresholds for different runs (see table 3.1). For a given  $P_T$  region, this value was only integrated over the runs for which that  $P_T$  was above the  $P_T$  threshold for that data set.

### 7.1.7 Recoil Jet Pseudorapidity Correction

In order to correct for the smearing effects of the reconstructed recoil jet pseudorapidity, separate correction factors were determined for  $p$ Be and  $\pi^-$ Be data using a sample of ISAJET Monte Carlo events. The correction factors were determined

as the ratio of the reconstructed recoil jet pseudorapidity distribution to that of the generated distribution. The generated events were weighted at the event level to force the reconstructed recoil jet pseudorapidity distribution to have the same shape as for the real data. The correction factors were parametrized as a function of the recoil jet pseudorapidity  $\eta_2$ , and are given by:

for  $p\text{Be}$  interactions:

$$\omega_{\eta_2} = 0.8623 + 0.1220\eta_2 + 0.5314\eta_2^2 \quad (7.5)$$

for  $\pi^- \text{Be}$  interactions:

$$\omega_{\eta_2} = 0.8982 - 0.0086\eta_2 + 0.4607\eta_2^2 \quad (7.6)$$

These correction factors were applied only to the background subtracted  $\gamma + jet$  cross sections.

## 7.2 $\pi^0 + Jet$ Cross Section

To select the events for the calculation of  $\pi^0 + jet$  cross sections, the event selection cuts described in chapter 5 were applied and later the cross sections were corrected for effects of these cuts.

The differential event distribution in Eq. 7.1 was calculated by taking a weighted sum of the event count for a selected  $P_T$  range and pseudorapidity regions of the  $\pi^0$  and the recoil jet. For the calculation of the differential cross section as a function of  $\pi^0 P_T$ , the weighted sum  $N_w(P_T)$  is defined as

$$N_w(P_T) \Big|_{P_T=P_T^{lo}}^{P_T^{hi}} = \frac{1}{\Delta P_T \Delta \eta_1 \Delta \eta_2} \sum_{i=1}^{N_1} \omega_i \quad (7.7)$$

where  $\Delta P_T = P_T^{hi} - P_T^{lo}$ ,  $\Delta \eta_1 = 1.4$  and  $\Delta \eta_2 = 1.8$  are the widths of the  $P_T$  and pseudorapidity bands and are the approximation of  $dP_T$ ,  $d\eta_1$  and  $d\eta_2$  in Eq. 7.1.  $N_1$  is the total number of  $\pi^0 + jet$  events with  $\pi^0 P_T$  in the selected  $P_T$  band and  $-0.7 \leq \eta_1 < 0.7$  and  $-0.9 \leq \eta_2 < 0.9$ .  $\omega_i$  is the event weight (see Eq. 7.9).

Similarly, to calculate the cross section as a function of the recoil jet pseudorapidity ( $\eta_2$ ), the weighted sum  $N_\omega(\eta_2)$  is defined as

$$N_\omega(\eta_2) \Big|_{\eta_2=\eta_2^{lo}}^{\eta_2^{hi}} = \frac{1}{\Delta P_T \Delta \eta_1 \Delta \eta_2} \sum_{i=1}^{N_2} \omega_i \quad (7.8)$$

where  $\Delta P_T = 4 \text{ GeV}/c$ ,  $\Delta \eta_1 = 1.4$  and  $\Delta \eta_2 = \eta_2^{hi} - \eta_2^{lo}$ .  $N_2$  is the total number  $\pi^0 + jet$  events with recoil jet pseudorapidity ( $\eta_2$ ) in the selected pseudorapidity band and  $4 \leq P_T < 8 \text{ GeV}/c$  and  $-0.7 \leq \eta_1 < 0.7$ .

In both cases, the event weight  $\omega_i$  is given by

$$\omega_i = \frac{\omega_{conv} \times \omega_{trig} \times \omega_{octa} \times \omega_{vrtx} \times \omega_{veto}}{\omega_{accp}} \quad (7.9)$$

where,

- $\omega_{conv}$  : Probability that neither photon converted in to an  $e^+e^-$  pair between the primary vertex and the dipole magnet.
- $\omega_{trig}$  : Trigger correction calculated on event-by-event basis.
- $\omega_{octa}$  : The correction for the malfunctioning EMLAC octants.
- $\omega_{vrtx}$  : The correction for vertex reconstruction efficiency.
- $\omega_{veto}$  : The correction for the off-line veto wall cut.
- $\omega_{accp}$  : The correction for the EMLAC acceptance and  $\pi^0$  reconstruction efficiency.

In order to correct for the accidentals in the  $\pi^0$  mass region, a similar weighted sum ( $N_\omega^{SB}$ ) was performed for the events falling in the  $\pi^0$  sideband regions. The sidebands subtracted event weight  $N_\omega^{CORR}(P_T)$  is given by

$$N_\omega^{CORR}(P_T) = N_\omega(P_T) - N_\omega^{SB}(P_T), \text{ and} \quad (7.10)$$

the sideband subtracted event weight  $N_{\omega}^{CORR}(\eta_2)$  is given by

$$N_{\omega}^{CORR}(\eta_2) = N_{\omega}(\eta_2) - N_{\omega}^{SB}(\eta_2). \quad (7.11)$$

The final differential cross section as a function of  $P_T$  is given by

$$\iint \frac{d\sigma}{dP_T d\eta_1 d\eta_2} d\eta_1 d\eta_2 = \frac{C_{\pi^0}}{N_{scat} \times B_{in}} \cdot N_{\omega}^{CORR}(P_T) \quad (7.12)$$

and the cross section as a function of recoil jet pseudorapidity is given by

$$\iint \frac{d\sigma}{dP_T d\eta_1 d\eta_2} dP_T d\eta_1 = \frac{C_{\pi^0}}{N_{scat} \times B_{in}} \cdot N_{\omega}^{CORR}(\eta_2) \quad (7.13)$$

The factor  $C_{\pi^0}$  appearing in Eqs. 7.12 and 7.13 is the product of the corrections for the cuts applied in the  $\pi^0$  event selection and the correction factors for the overall beam normalization. The breakdown of the factor  $C_{\pi^0}$  is given in table 7.2[39].

Figure 7.3(a) and (b) show the  $\pi^0 + jet$  cross section as a function of  $P_T$  for  $pBe$  and  $\pi^-Be$  interactions and figure 7.4(a) and (b) show the  $\pi^0 + jet$  cross section as a function of recoil jet pseudorapidity for  $pBe$  and  $\pi^-Be$  interactions.

### 7.3 $\gamma + Jet$ Cross Section

The calculation of the differential cross sections for  $\gamma + jet$  production is very similar to the calculation of  $\pi^0 + jet$  cross sections. In order to select the events, we have applied single photon selection cuts described in chapter 5, in addition to the event selection cuts. Here also we have corrected the measured cross sections for the effects of the these cuts.

In analogy with Eq. 7.7, to calculate the cross section as a function of  $P_T$ , a weighted sum  $N_{\omega}(P_T)$  is defined within a given  $P_T$  band, but here  $N_1$  is the total number of  $\gamma + jet$  events in that  $P_T$  band. Similarly, for the calculation of cross sections as a function of recoil jet pseudorapidity, a weighted sum  $N_{\omega}(\eta_2)$  was defined according to Eq. 7.8, where  $N_2$  is now the total number of  $\gamma + jet$  events within a given recoil jet pseudorapidity band.

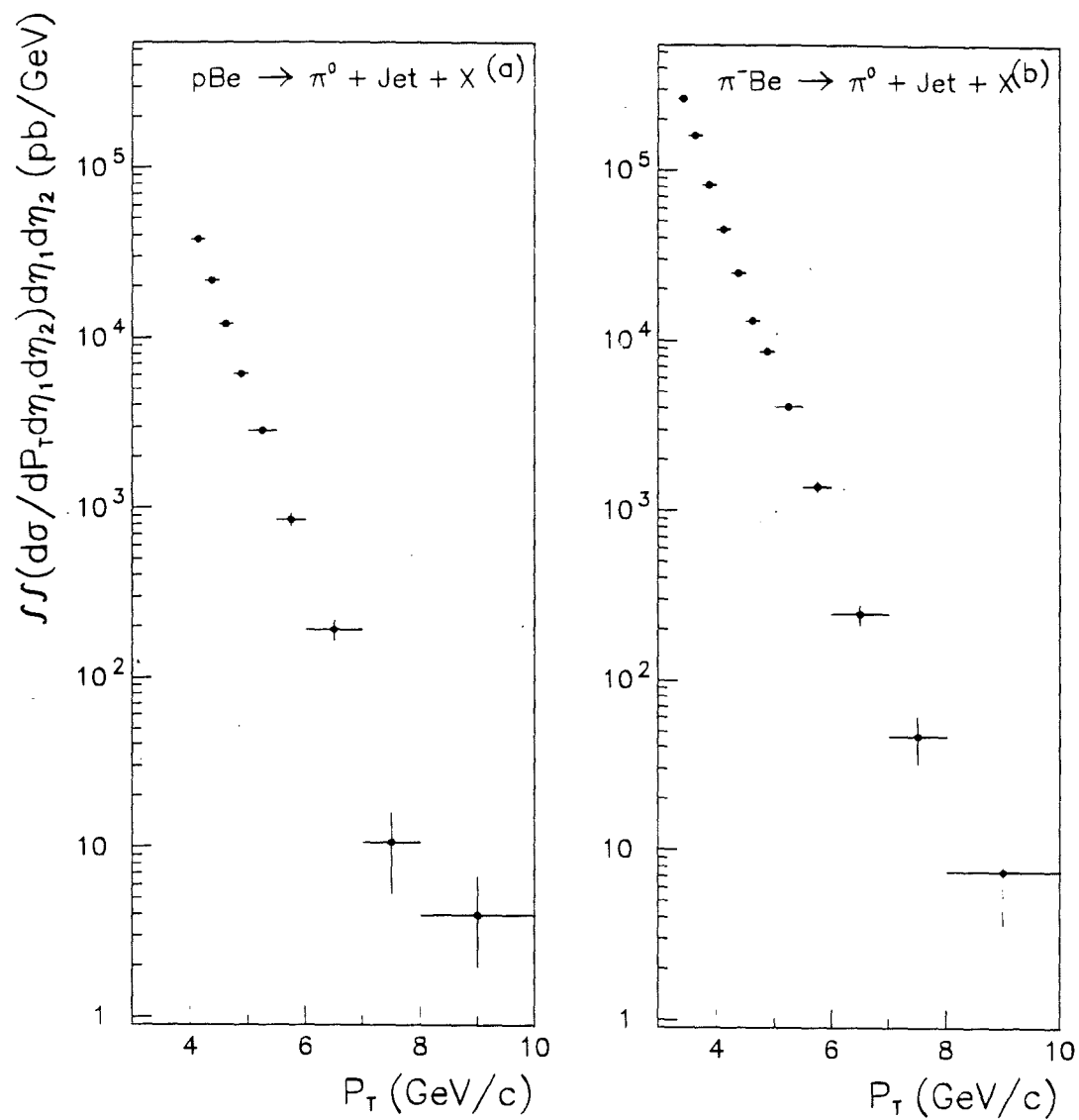


Figure 7.3: Sideband subtracted  $\pi^0 + jet$  cross section per nucleon as a function of  $P_T$  : (a)  $pBe$  collisions, and (b)  $\pi^-Be$  collisions.

Table 7.2: Averaged corrections for the cuts applied in  $\pi^0$  event selection as well as the corrections for the overall beam count.

	$\pi^- \text{Be} \rightarrow \pi^0 + jet + X$	$p\text{Be} \rightarrow \pi^0 + jet + X$
Double occupancy	0.980	0.980
Beam absorption	1.051	1.069
Veto wall back scatter	1.030	1.035
Uncorrelated energy cut	1.005	1.008
$P_T$ resolution	0.922	0.909
$\gamma$ conversion	1.148	1.147
Muon correction	1.010	1.000
Target correction	1.010	1.010
Asymmetry cut	1.330	1.330
Tail loss	1.040	1.040
$C_{\pi^0}$	1.592	1.592

The event weight  $\omega_i$  is defined in analogy with Eq. 7.9, where

$$\omega_i = \frac{\omega_{conv} \times \omega_{trig} \times \omega_{octa} \times \omega_{vrtx} \times \omega_{veto}}{\omega_{accp}} \quad (7.14)$$

where,

- $\omega_{conv}$  : Probability that photon did not convert between the primary vertex and the second PWC chamber.
- $\omega_{trig}$  : Trigger correction calculated on event-by-event basis.
- $\omega_{octa}$  : The correction for the malfunctioning EMLAC octants.

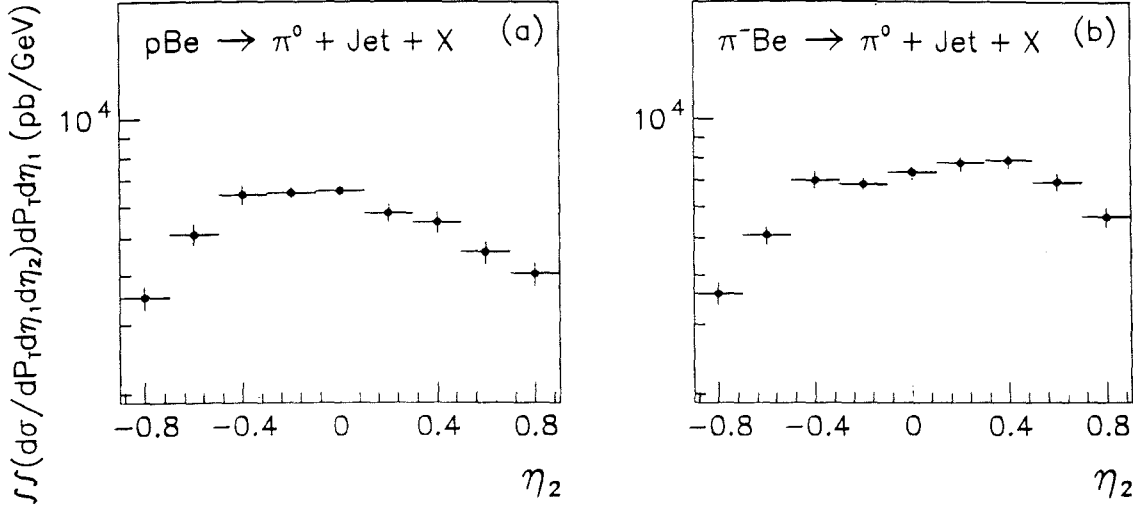


Figure 7.4:  $\pi^0 + jet$  cross section per nucleon as a function of recoil jet pseudorapidity  $\eta_2$ . (a)  $p\text{Be}$  collisions, and (b)  $\pi^- \text{Be}$  collisions.

- $\omega_{vrtx}$  : The correction for vertex reconstruction efficiency.
- $\omega_{veto}$  : The correction for the off-line veto wall cut.
- $\omega_{accp}$  : The correction for the EMLAC acceptance and photon reconstruction efficiency.

The uncorrected  $\gamma + jet$  cross sections as a function of  $P_T$  is given by

$$\iint \frac{d\sigma}{dP_T d\eta_1 d\eta_2} d\eta_1 d\eta_2 = \frac{C_\gamma}{N_{scat} \times B_{in}} \cdot N_\omega(P_T) \quad (7.15)$$

and the cross section as a function of recoil jet pseudorapidity is given by

$$\iint \frac{d\sigma}{dP_T d\eta_1 d\eta_2} dP_T d\eta_1 = \frac{C_\gamma}{N_{scat} \times B_{in}} \cdot N_\omega(\eta_2). \quad (7.16)$$

The factor  $C_\gamma$  appearing in Eqs. 7.15 and 7.16 is the product of the corrections for the cuts applied in the single photon events selection as well as the corrections for overall beam normalization. The breakdown of the factor  $C_\gamma$  is given in the table 7.3[39].

Figure 7.5(a) and (b) show the  $\gamma + jet$  cross section as a function of  $P_T$  for  $pBe$  and  $\pi^-Be$  interactions, respectively and figure 7.6(a) and (b) show the  $\gamma + jet$  cross section as a function of recoil jet pseudorapidity for  $pBe$  and  $\pi^-Be$  interactions, respectively.

Table 7.3: Averaged corrections for the cuts applied in direct photon event selection as well as the corrections for the overall beam count.

	$\pi^-Be \rightarrow \gamma + jet + X$	$pBe \rightarrow \gamma + jet + X$
Double occupancy	0.980	0.980
Beam absorption	1.051	1.069
Veto wall back scatter	1.030	1.035
Uncorrelated energy cut	1.005	1.008
$P_T$ resolution	0.971	0.943
$\gamma$ conversion	1.071	1.070
Muon correction	1.010	1.000
Target correction	1.010	1.010
Directionality cut	1.005	1.007
Timing cut	1.027	1.028
$E_F/E_T$ cut	1.015	1.015
Close track cut	1.006	1.006
Direct photons making $\pi^0$ or an $\eta$	1.101	1.105
$C_\gamma$	1.312	1.301

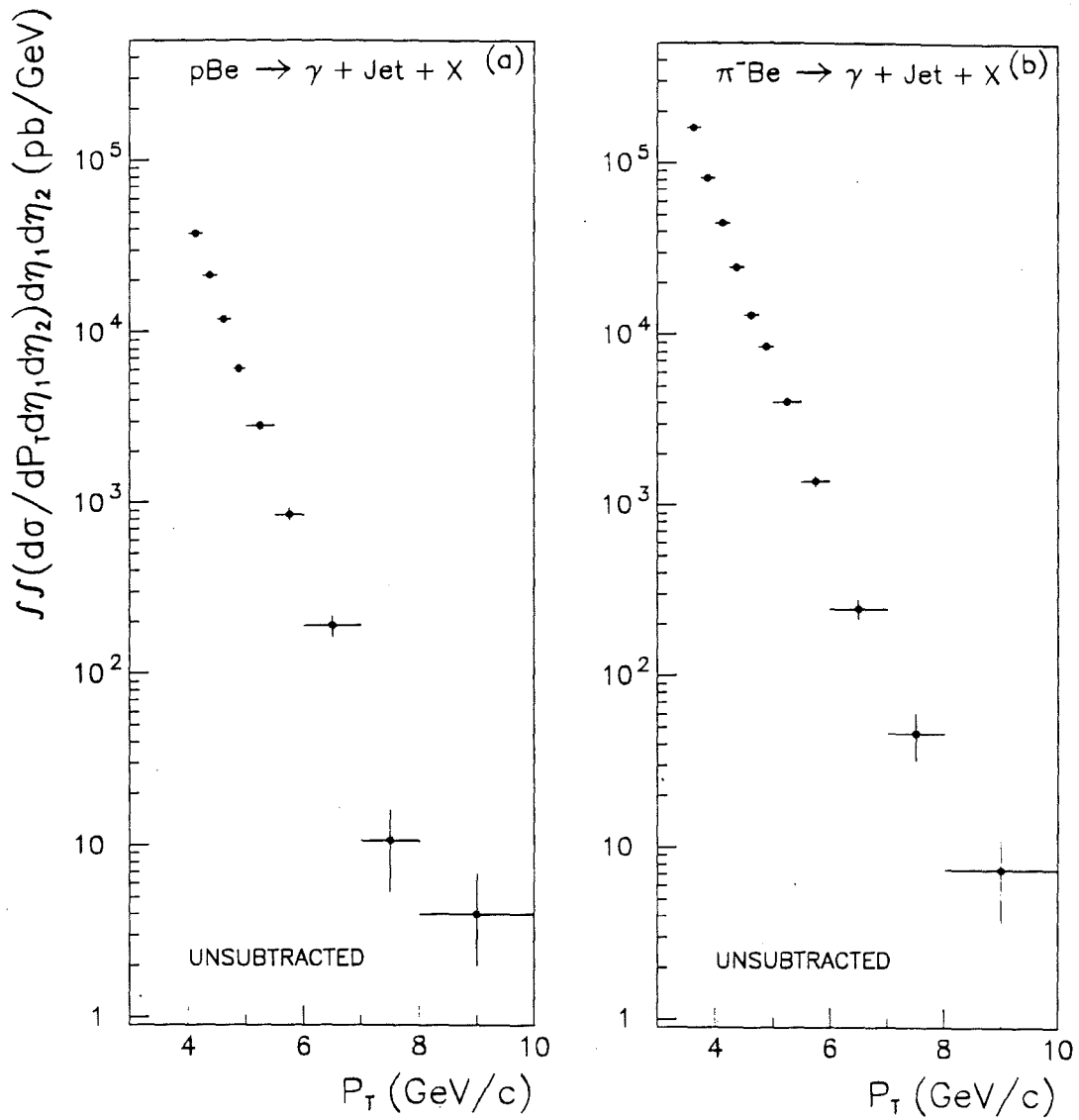


Figure 7.5:  $\gamma + jet$  cross section per nucleon as a function of  $P_T$  : (a)  $pBe$  collisions, and (b)  $\pi^- Be$  collisions.

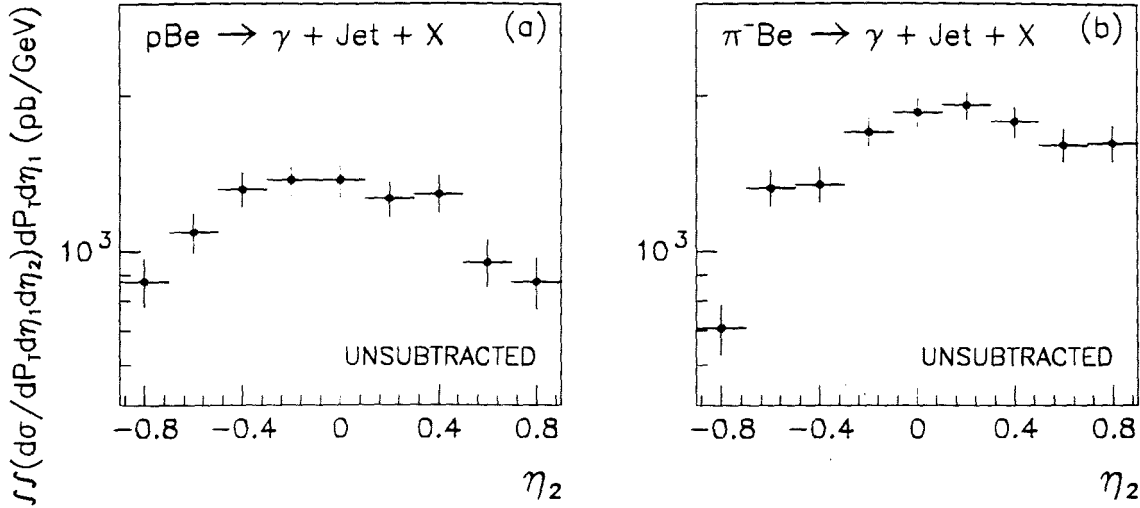


Figure 7.6:  $\gamma + jet$  cross section as a function of recoil jet pseudorapidity  $\eta_2$  : (a)  $p\text{Be}$  collisions, and (b)  $\pi^- \text{Be}$  collisions.

## 7.4 Background subtraction for the $\gamma + jet$ cross section

In order to calculate the background to the  $\gamma + jet$  cross section, we have used the Monte Carlo generated events described in section 5.3. The Monte Carlo events were processed using the same analysis code that was used to analyze the  $\gamma + jet$  events in the data. The Monte Carlo generated events are all  $\pi^0$  events and any event reconstructed to be a  $\gamma + jet$  event contributed to the direct photon background. The  $\gamma + jet$  background and the accepted  $\pi^0 + jet$  distributions were obtained as a function of  $P_T$  and as a function of recoil jet pseudorapidity. The ratio of  $\gamma + jet$  background to the accepted  $\pi^0 + jet$  was then calculated and parametrized as a function of  $P_T$  and  $\eta_2$  separately. This parametrized ratio  $(\gamma + jet / \pi^0 + jet)_{bck}$  was then multiplied by the  $\pi^0 + jet$  cross section obtained from the data and subtracted from the measured  $\gamma + jet$  cross sections to obtain the corrected  $\gamma + jet$  cross sections for the data. Figures 7.7(a) and (b) show the uncorrected  $\sigma_{\gamma+jet} / \sigma_{\pi^0+jet}$  as a function

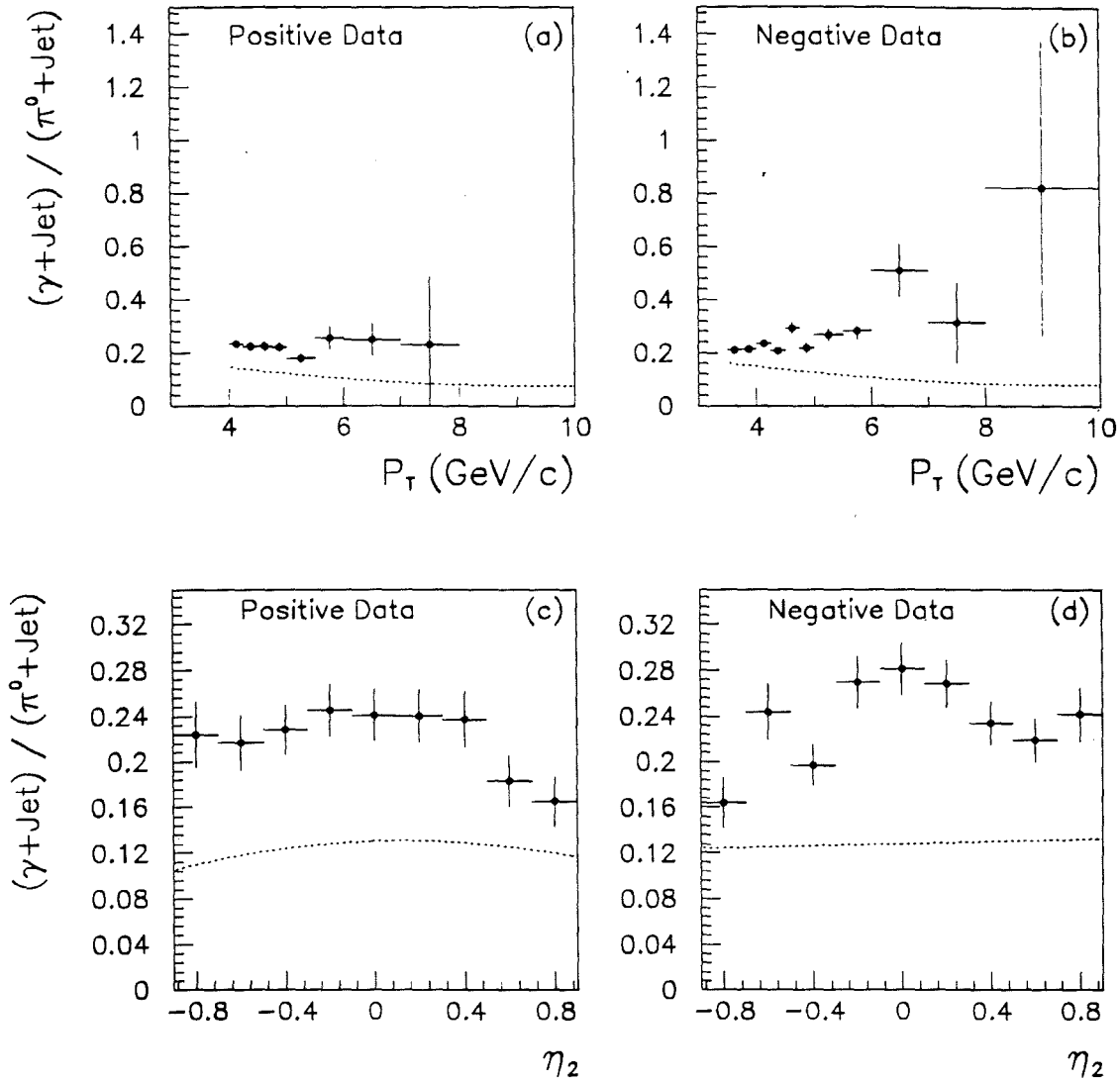


Figure 7.7: The ratios of  $(\gamma + jet)/(\pi^0 + jet)$  as a function of  $P_T$  (a)  $p$ Be data (b)  $\pi^-$ Be data, and as a function of recoil jet pseudorapidity  $\eta_2$  (c)  $p$ Be data (d)  $\pi^-$ Be data. The dotted lines represent the background to the direct photon signal as estimated from Monte Carlo.

of  $P_T$  and figures 7.7(c) and (d) show the uncorrected  $\sigma_{\gamma+jet}/\sigma_{\pi^0+jet}$  as a function of  $\eta_2$ . The dotted lines in all four figures represent the background to the direct photon signal as estimated from Monte Carlo.

## CHAPTER 8

### Results and Conclusions

The previous chapter dealt with the calculation of the differential cross section for the  $\pi^0 + jet$  and  $\gamma + jet$  production and the background subtraction to the direct photon + jet signal. In this chapter we present the background subtracted final results on cross sections for the  $\gamma + jet$  production in  $pBe$  and  $\pi^-Be$  collisions. The cross sections are presented as a function of direct photon  $P_T$  and as a function of the recoil jet pseudorapidity  $\eta_2$ . The beam dependence of the production cross sections are presented as a ratio of the cross sections for  $\pi^-Be$  interactions to that for  $pBe$  interactions. Finally the  $\gamma + jet$  cross sections are compared with the leading order and next-to-leading order QCD calculations.

#### 8.1 Direct Photon plus Away-Side Jet Cross Sections

Figure 8.1(a) shows the background subtracted cross section per nucleon for  $p + Be \rightarrow \gamma + jet + X$  as a function of the direct photon  $P_T$ . The cross sections are averaged over  $-0.7 \leq \eta_1 < 0.7$  and  $-0.9 \leq \eta_2 < 0.9$ . Figure 8.1(c) shows the  $\gamma + jet$  cross section per nucleon for the same interaction as a function of the recoil jet pseudorapidity. Here the cross section is averaged over  $4 \leq P_T < 8$  GeV/c and  $-0.7 \leq \eta_1 < 0.7$ .

Figures 8.1(b) and (d) show the cross section per nucleon for  $\pi^- + Be \rightarrow \gamma + jet + X$  as a function of  $P_T$  and as a function of the recoil jet pseudorapidity, respectively. The cross section in figure 8.1(b) is averaged over  $-0.7 \leq \eta_1 < 0.7$  and  $-0.9 \leq \eta_2 < 0.9$  and the cross section in figure 8.1(d) is averaged over

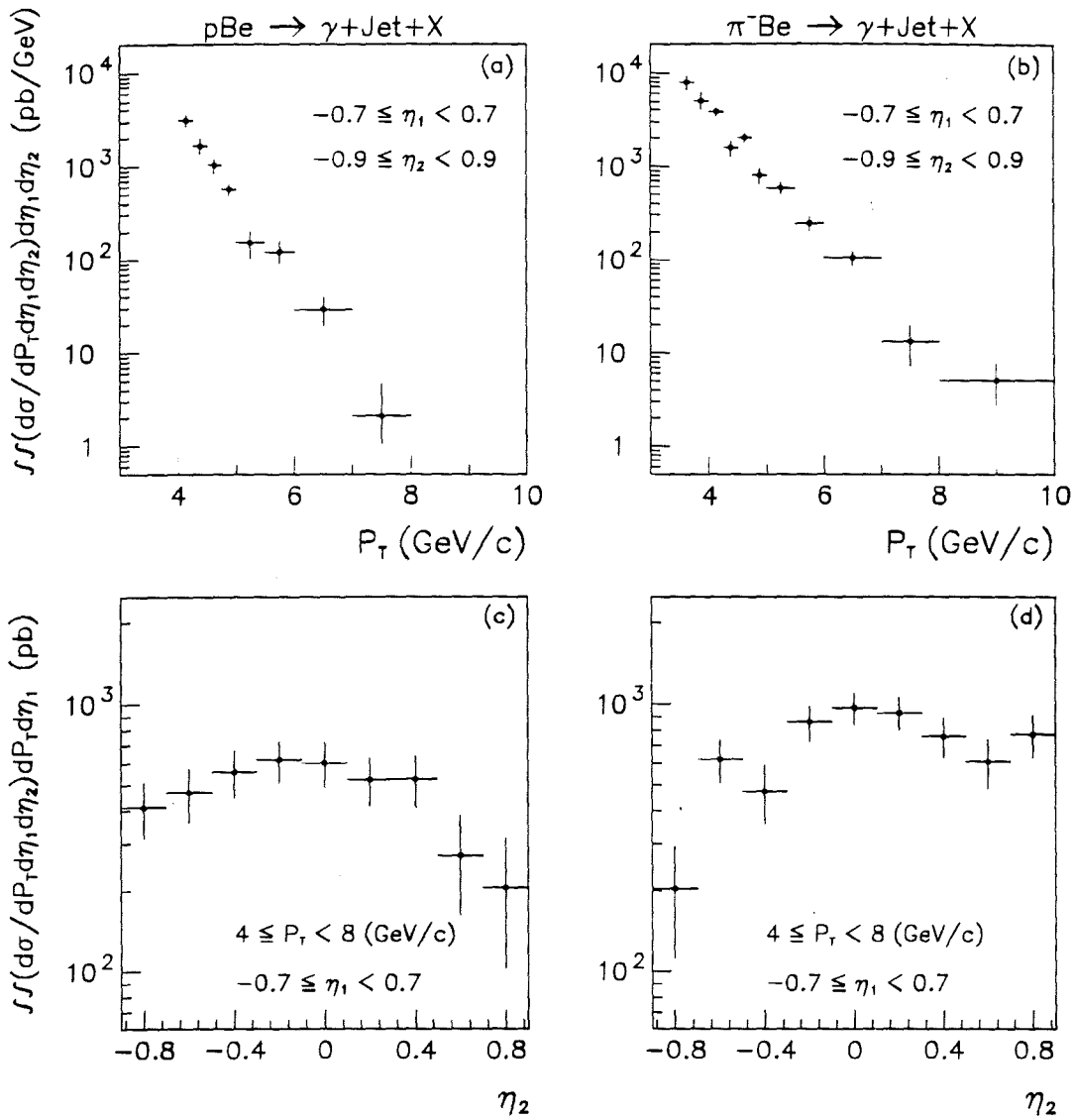


Figure 8.1: Background subtracted direct photon + jet cross sections. Cross sections per nucleon as a function of  $P_T$  for: (a)  $p + \text{Be} \rightarrow \gamma + \text{jet} + X$  (b)  $\pi^- + \text{Be} \rightarrow \gamma + \text{jet} + X$ . Cross sections per nucleon as a function of recoil jet pseudorapidity, for : (c)  $p + \text{Be} \rightarrow \gamma + \text{jet} + X$  (d)  $\pi^- + \text{Be} \rightarrow \gamma + \text{jet} + X$ .

$4 \leq P_T < 8$  GeV/c and  $-0.7 \leq \eta_1 < 0.7$ . The cross sections in 8.1(c) and (d) are corrected for the smearing in the reconstructed recoil jet pseudorapidity as described in the previous chapter. Tables A.1 and A.2 show the  $\gamma + jet$  differential cross sections per nucleon for the  $p$ Be interactions and  $\pi^-$ Be interactions.

The relative rise in the cross section in figure 8.1(d) for  $\pi^-$ Be interactions, in the forward pseudorapidity region can be attributed to the fact that the partons in  $\pi^-$  meson (beam) carry a higher momentum fraction than those in the target nucleons and hence, on average, the photon-jet system moves in the forward direction in the hadron-hadron CM frame.

Figures 8.2(a)–(d) show the  $\gamma/\pi^0$  ratio as a function of  $P_T$  and as a function of recoil jet pseudorapidity, for  $p$ Be and  $\pi^-$ Be interactions. The data are corrected for the background to the direct photon signal. The ratios in figures 8.2(a) and (b) seem to rise with increasing  $P_T$ . This can be attributed to that fact that the direct photons arise from the hard collision whereas the  $\pi^0$ s are produced as a fragment of a hard scattered parton and hence carry less  $P_T$ . The sharper rise in figure 8.2(b) is due to the dominant contribution of the annihilation term at higher  $P_T$  compared to the contribution from the Compton process. Tables A.3 and A.4 show the  $\gamma/\pi^0$  ratios as a function of  $P_T$  and as a function of recoil jet pseudorapidity for  $p$ Be and  $\pi^-$ Be interactions.

## 8.2 Beam Dependence of the Cross Sections

The beam dependence of the  $\gamma + jet$  cross sections are presented as a ratio of the cross sections for  $\pi^-$ Be interactions to that for  $p$ Be interactions. This ratio as a function of  $P_T$  is shown in figure 8.3 whereas figure 8.4 shows the ratio of the cross sections as a function of the recoil jet pseudorapidity. Figure 8.3 shows a monotonic increase in this ratio with  $P_T$  where the ratio is  $\sim 1$  at  $P_T = 4.25$  GeV/c and rising

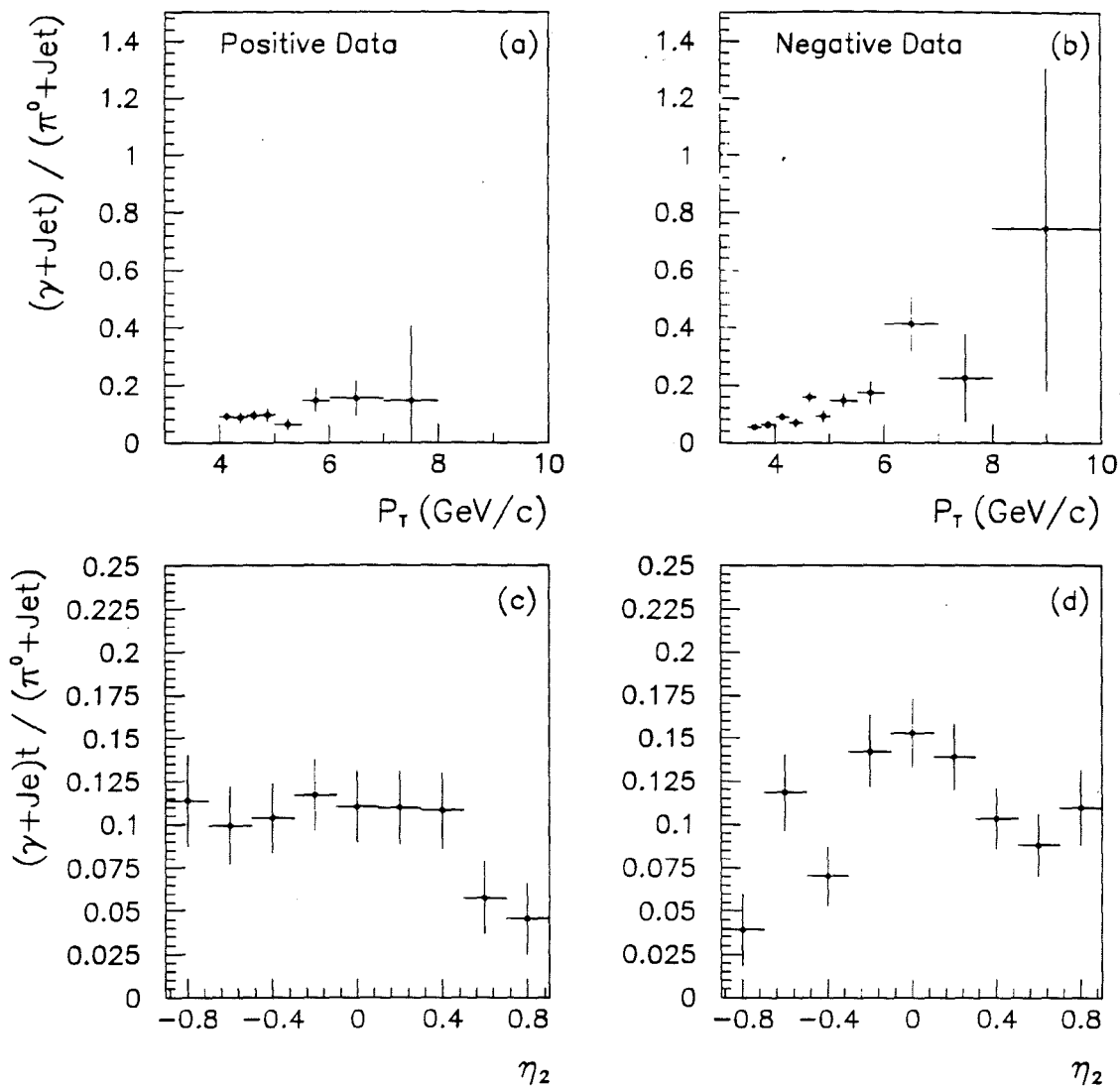


Figure 8.2: Background subtracted  $(\gamma + jet)/(\pi^0 + jet)$  ratios as a function of  $P_T$  for (a)  $p + \text{Be}$  (b)  $\pi^- + \text{Be}$  and as a function of recoil jet pseudorapidity, for (c)  $p + \text{Be}$  (d)  $\pi^- + \text{Be}$ .

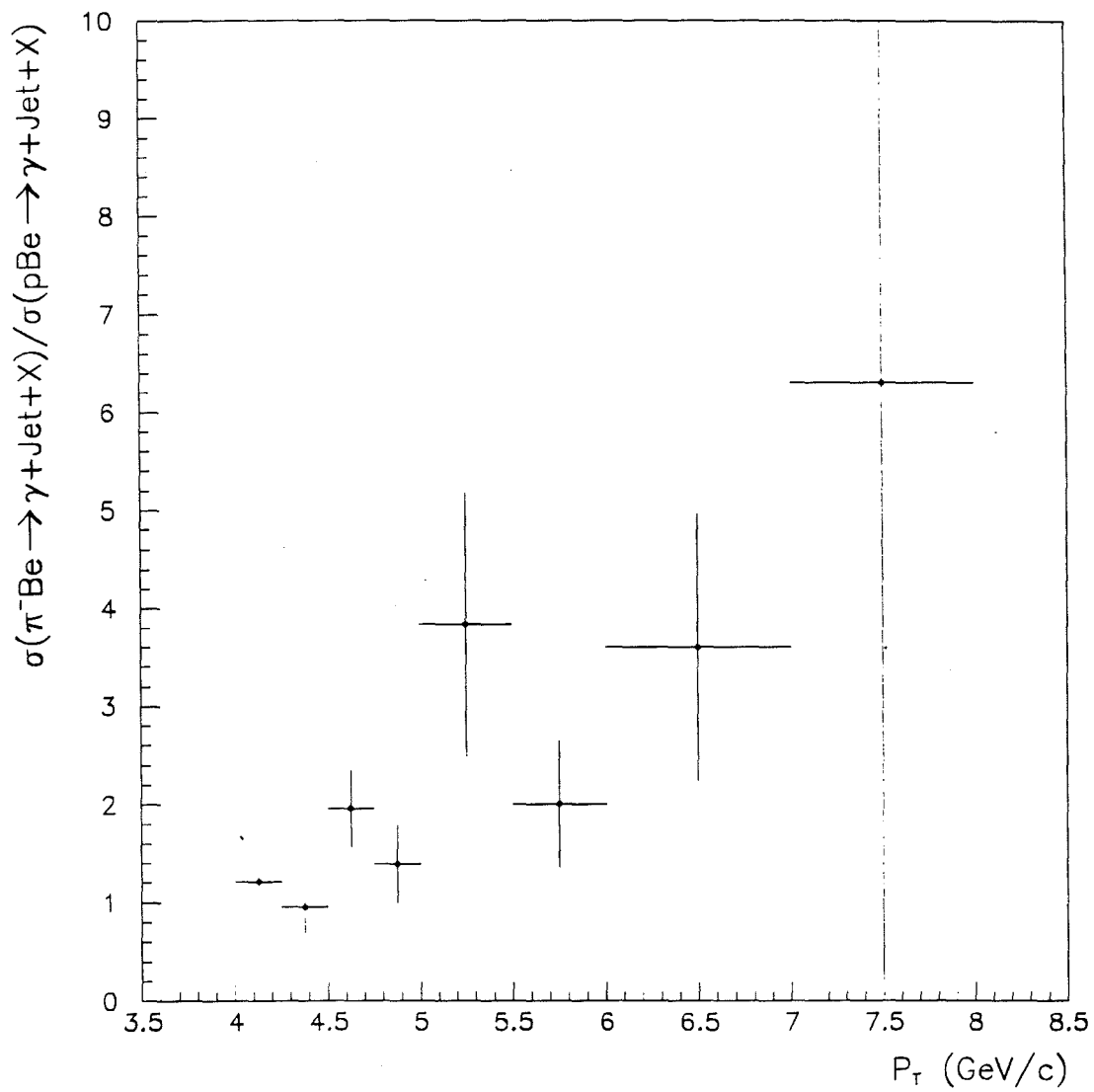


Figure 8.3:  $\sigma_{\pi^- \text{Be} \rightarrow \gamma + \text{jet} + X} / \sigma_{p \text{Be} \rightarrow \gamma + \text{jet} + X}$  as a function of  $P_T$ .

to  $\sim 6.5$  at  $P_T = 7.5$  GeV/c. One would expect such a trend based on the fact that the individual partons in the pion carry, on average, a larger fraction ( $x$ ) of the beam momentum than those of the proton at high  $P_T$ . Also the dominant contribution from the annihilation subprocess to the cross section for  $\pi^-$ Be collisions at large  $P_T$  results in an increase in the cross section compared to that for  $p$ Be collisions. A similar trend is observed in figure 8.4 where the ratio is presented as a function of recoil jet pseudorapidity. The rise in ratio in the forward pseudorapidity region can be attributed to the same effects that cause the ratio of the cross section to rise as a function of  $P_T$ . The results are summarized in tables A.5 and A.6.

### 8.3 Comparison with QCD Predictions

The comparison of data to the theoretical predictions are made with QCD calculations<sup>1</sup> involving leading log as well as next-to-leading log approximations. In either case one has to choose a suitable factorization scale and a renormalization scale to calculate the cross sections. As pointed out in chapter 1, in the leading log approximation, one could in principle ignore the distinction between the two scales at large  $P_T$  transfer[6] (*i.e.* large  $Q^2$ ). In the following discussion we have selected scales  $Q^2 = P_T^2/4$  and  $Q^2 = P_T^2$  for both the factorization and renormalization scales.

#### 8.3.1 Comparison with Leading Log QCD Predictions

Figures 8.5(a) and (b) show the  $\gamma + jet$  cross sections per nucleon for the  $p$ Be and  $\pi^-$ Be collisions, compared with the leading log QCD predictions. We have used  $Q^2 = P_T^2/4$  and Owens 1.1[56] structure functions for the nucleons and Duke and Owens structure functions[50] for the pions in the QCD calculations. Owens 1.1 structure functions were calculated in the leading log approximation with

---

<sup>1</sup>Leading log and next-to-leading log QCD calculations were performed using a program provided by J. F. Owens.

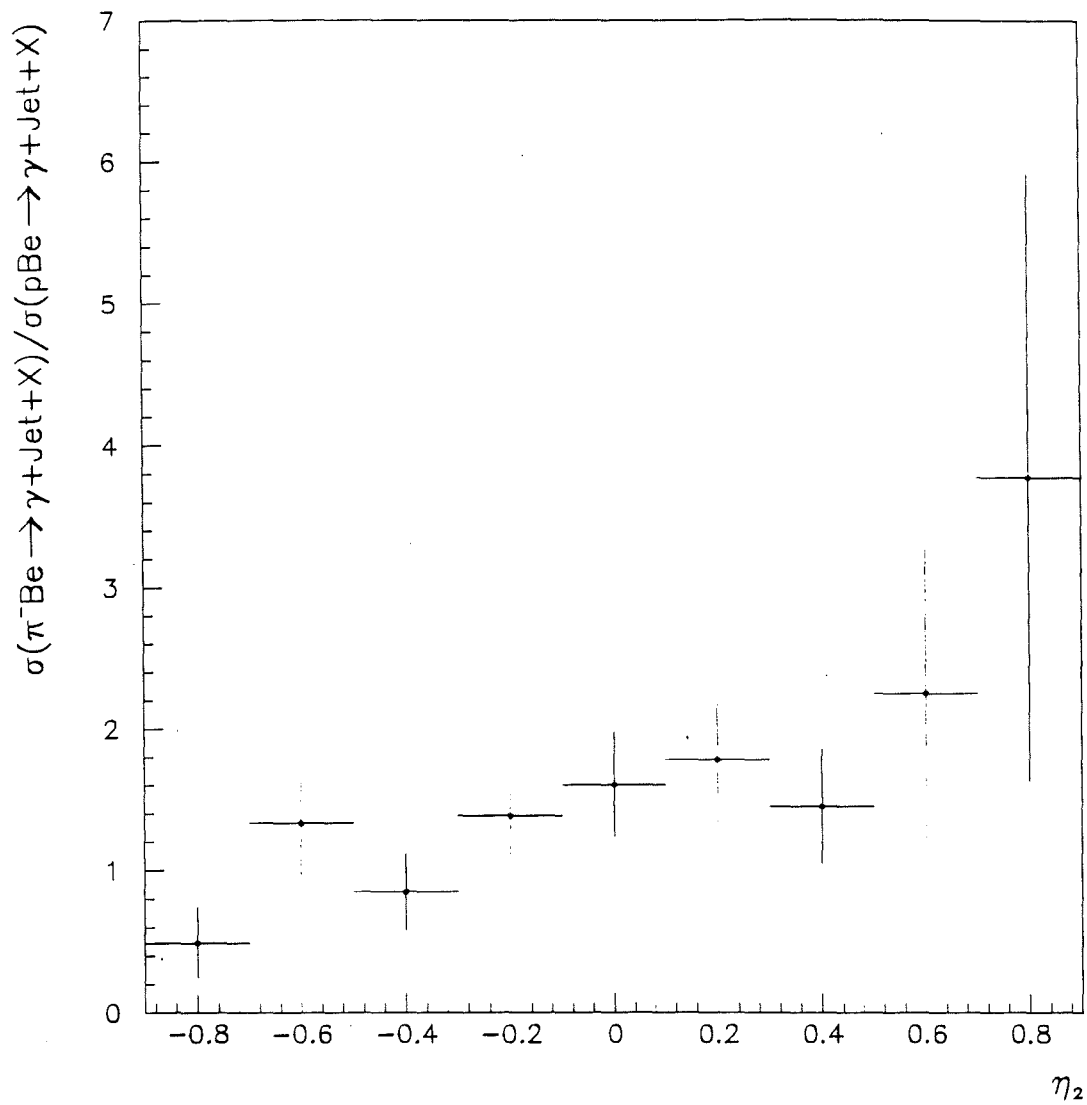


Figure 8.4:  $\sigma_{\pi^- \text{Be} \rightarrow \gamma + \text{jet} + X} / \sigma_{p \text{Be} \rightarrow \gamma + \text{jet} + X}$  as a function of recoil jet pseudorapidity.

$\Lambda_{QCD} = 177$  MeV and the gluon distribution in this set was parameterized as

$$xG(x, Q_0^2 = 4) = A_g x^a (1-x)^b (1 + \alpha x + \beta x^2 + \gamma x^3) \quad (8.1)$$

The cross sections are presented as a function of  $P_T$  and are averaged over  $-0.7 \leq \eta_1 < 0.7$  and  $-0.9 \leq \eta_2 < 0.9$ . The dashed line represents the QCD predictions with no intrinsic  $k_T$  in the calculations while the dotted line represents the QCD predictions with intrinsic  $k_T = 1$  GeV. The effect of a 1 GeV  $k_T$  is to raise the cross section, on average, by a factor of  $\sim 1.5$  for  $pN$  interactions<sup>2</sup>. But for the  $\pi^-N$  interactions, inclusion of 1 GeV  $k_T$  raise the cross section by a factor of  $\sim 1.4$  at  $P_T = 4$  GeV/c and by a factor of  $\sim 1.2$  at  $P_T = 8$  GeV/c.

For both the positive and negative data, the measured cross sections have a steeper  $P_T$  dependence than the QCD predictions. For the  $pBe$  interactions, the measured cross section at  $P_T = 4$  GeV/c is about a factor of 2 higher than the QCD predictions with  $k_T = 1$  GeV and is moderately consistent with QCD predictions in the high  $P_T$  region (for  $5 \leq P_T < 8$  GeV/c), within the statistical uncertainty. A similar observation can be made from the comparisons between data and theory for  $\pi^-Be$  interactions in figure 8.5(b). The normalization of the predicted cross sections strongly depends on the choice of the  $Q^2$  scale although the choice of the scale factor in the  $Q^2$  definition has very little effect on the slope of the predicted cross sections and hence is not shown in the figure 8.5.

### 8.3.2 Comparison with Next-to-Leading Log QCD Predictions

The discrepancy between data and the QCD predictions in the leading log approximation are probably due to the contributions from the higher order subprocesses and from the effects of the intrinsic  $k_T$  of the hard scattering partons. It has been

---

<sup>2</sup>Nucleon targets were used in the Monte Carlo calculation of QCD predictions.

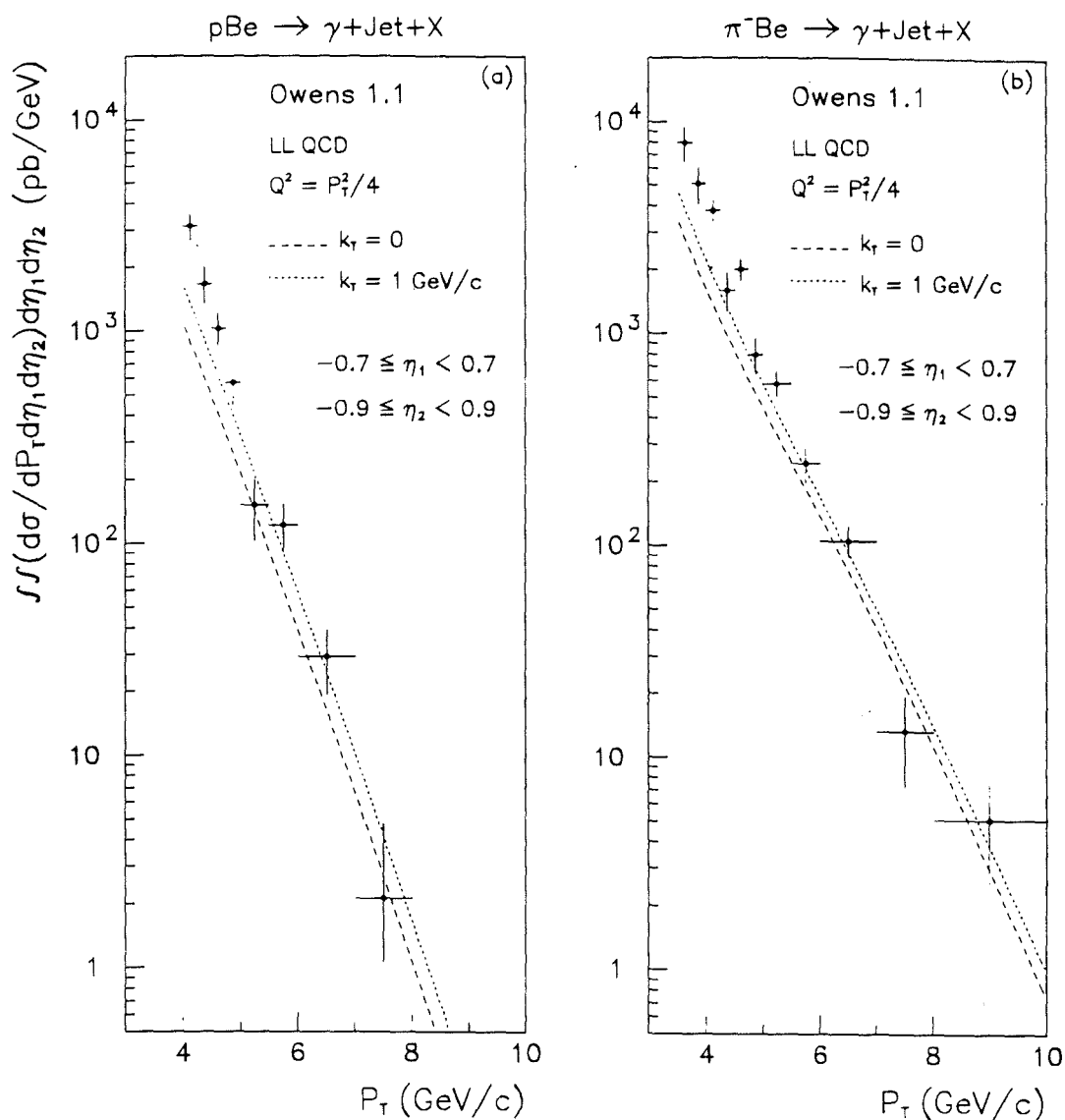


Figure 8.5:  $\gamma + jet$  cross sections as a function of  $P_T$  compared with the predictions of leading log QCD calculations with  $Q^2 = P_T^2/4$  and using Owens 1.1 structure functions from proton and Duke and Owens set-2 structure functions for pions. The dashed line is for the QCD calculations with no intrinsic  $k_T$  and the dotted line represents the QCD predictions with  $k_T = 1 \text{ GeV}$ . (a)  $p\text{Be}$  collisions, and (b)  $\pi^- \text{Be}$  collisions.

pointed out in reference [6] that the size of the  $k_T$  effect is decreased when higher order terms are included in the QCD calculations. Very recently such a calculation for  $\gamma + jet$  production was developed by Baer, Ohnemus and Owens[57] which includes both leading log and next-to-leading logarithm contributions. In this section we will compare the measured  $\gamma + jet$  cross sections to the QCD cross sections calculated in the next-to-leading log approximation.

Figure 8.6(a) and (b) show the  $\gamma + jet$  cross sections per nucleon for  $pBe$  and  $\pi^-Be$  interactions, compared with the next-to-leading QCD predictions. The cross sections are averaged over  $-0.7 \leq \eta_1 < 0.7$  and  $-0.9 \leq \eta_2 < 0.9$ . The curves represent the next-to-leading log QCD calculations of Owens using ABFOW[58] parton distributions for nucleons and ABFKW[59] parton distributions for pions, choosing scales  $Q^2 = P_T^2/4$  and  $Q^2 = P_T^2$ . These parton distribution functions have been evaluated at the next-to-leading log level with  $\Lambda_{QCD} = 230$  MeV and a gluon distribution parameterized as

$$xG(x, Q^2 = 2) = A_g(1 - x)^{\eta_g} \quad (8.2)$$

where  $\eta_g=3.9$  is generally referred to as the gluon density. As in the leading log approximation, a strong dependence of the QCD predictions on the choice of the scale is observed.

Figure 8.7 show the  $\gamma + jet$  cross section per nucleon for  $pBe$  and  $\pi^-Be$  interactions, compared with next-to-leading log QCD predictions. The cross sections are presented as a function of recoil jet pseudorapidity ( $\eta_2$ ), and are averaged over  $4 \leq P_T < 8$  GeV/c and  $-.7 \leq \eta_1 < .7$ . QCD calculations were performed with ABFOW/ABFKW parton distributions and for scales  $Q^2 = P_T^2/4$  and  $Q^2 = P_T^2$ . One observes that the QCD predictions are rather low compared to the data. This is due to the fact that the average  $P_T$  in each jet pseudorapidity bin is about 4.5 GeV/c (as shown in figure 8.8(a) and (b)) and at this  $P_T$  the theoretical predictions are lower by about a factor of 2 ( as shown in figure 8.8(c) and (d)). Once we

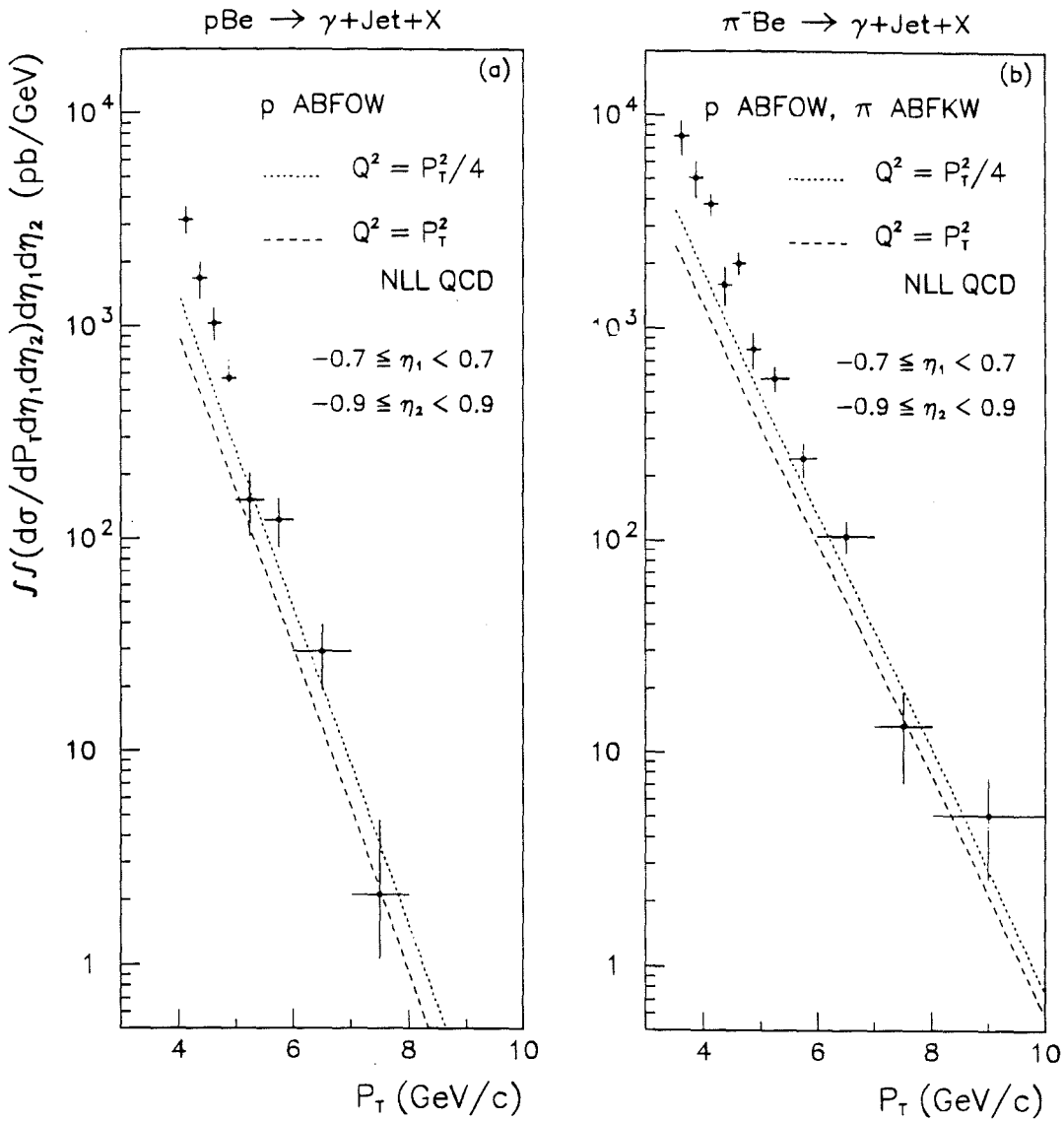


Figure 8.6:  $\gamma + \text{jet}$  cross section as a function of  $P_T$  compared with the predictions of next-to-leading log QCD calculations using ABFKW and ABFOW structure functions with  $Q^2 = P_T^2/4$  and  $Q^2 = P_T^2$  (a)  $p\text{Be}$  collisions, and (b)  $\pi^- \text{Be}$  collisions.

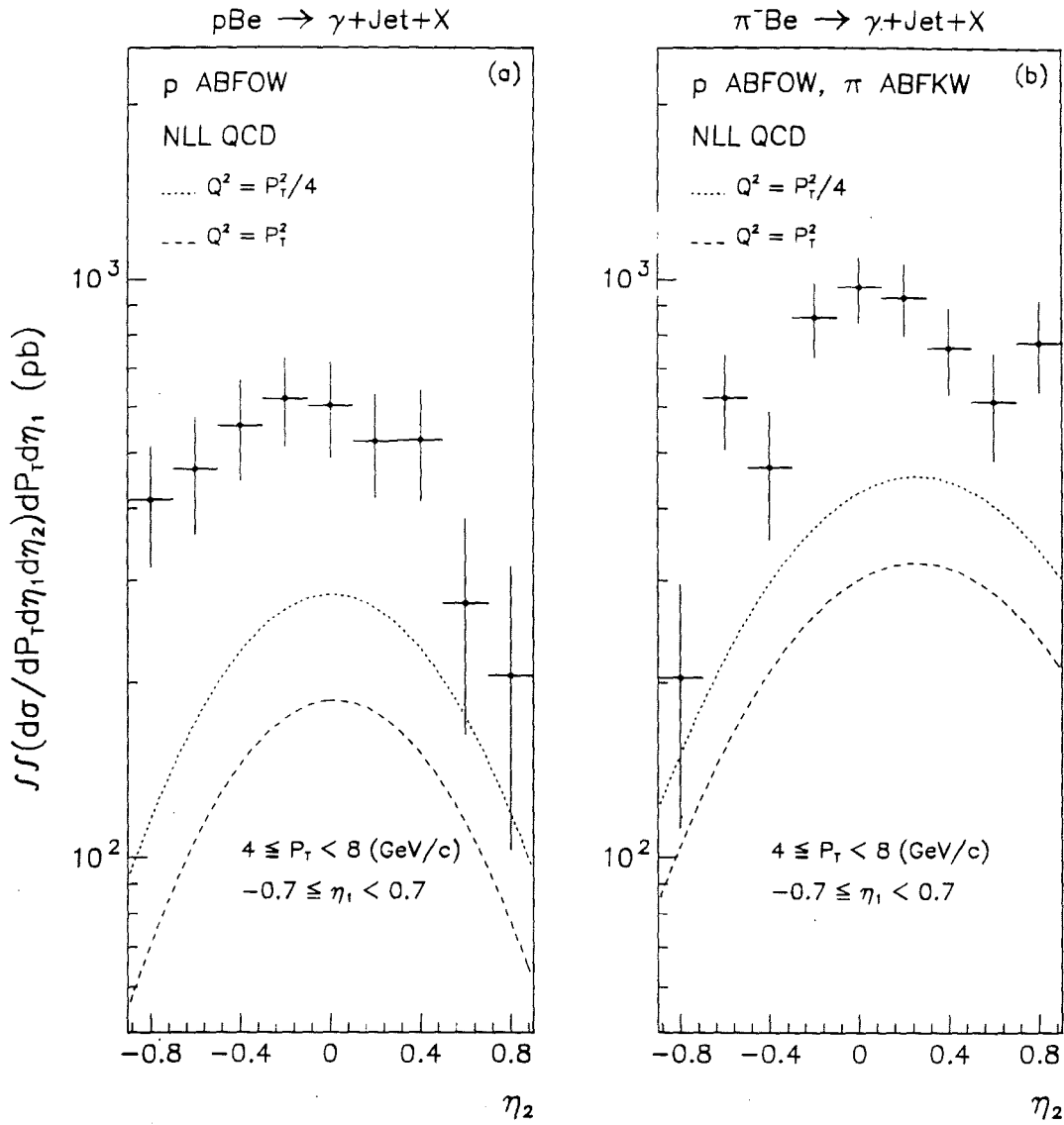


Figure 8.7:  $\gamma + jet$  cross section as a function of  $\eta_2$  compared with the predictions of next-to-leading log QCD calculations using ABFKW and ABFOW structure functions. Dotted line is for  $Q^2 = P_T^2/4$  and dashed line is for  $Q^2 = P_T^2$ . (a)  $p\text{Be}$  collisions, and (b)  $\pi^- \text{Be}$  collisions.

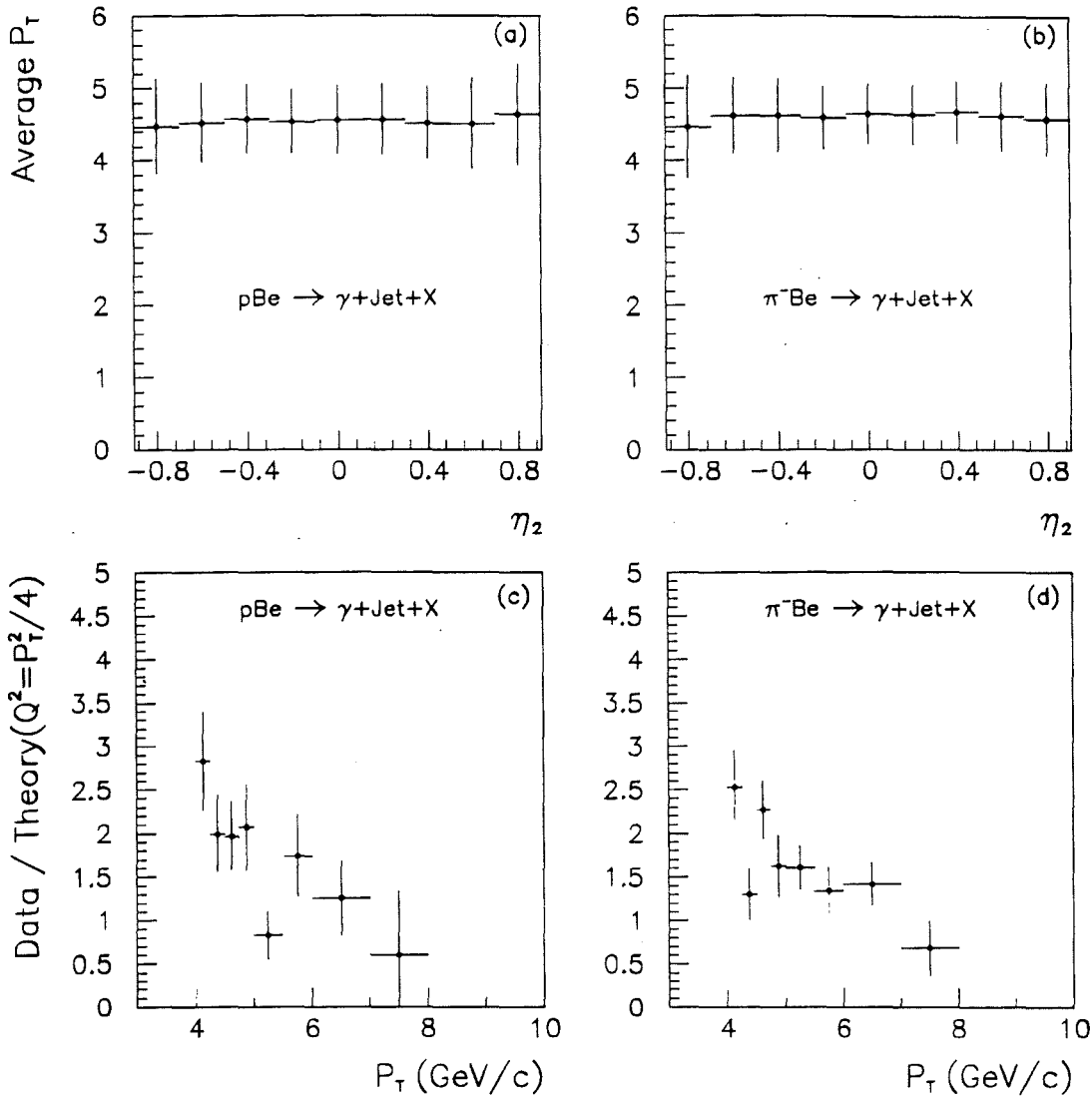


Figure 8.8: (a) and (b) show the average  $P_T$  as a function of  $\eta_2$  for  $p\text{Be}$  and  $\pi^- \text{Be}$  data and (c) and (d) show the ratio of the cross sections for data to that of next-to-leading log QCD predictions using ABFKW and ABFOW structure functions and  $Q^2 = P_T^2/4$ , for  $p\text{Be}$  and  $\pi^- \text{Be}$  interactions.

adjust the overall normalization by a constant factor for the QCD predictions and fit the shape of the predicted cross sections to data we get a reasonable agreement between data and theory. For the  $p\text{Be}$  collisions, the fit gives the constant factor =  $2.24 \pm 0.17$  with  $\chi^2=0.672$  and for the  $\pi^- \text{Be}$  collisions the constant factor =  $1.98 \pm 0.12$  with  $\chi^2=1.26$ . Once again, the shape of the cross sections are relatively independent of the choice for the  $Q^2$  scale and hence only the predictions for  $Q^2 = P_T^2/4$  is shown in figure 8.9.

Figure 8.10 show the ratio of cross sections for  $\pi^- \text{Be}$  to  $p\text{Be}$  as a function of  $P_T$ , compared with the QCD predictions. The advantage of studying the ratio of the cross sections is that it minimizes the ambiguities that may exist in the normalization of data and theory. The agreement between the data and theory is better than for the comparisons between the individual cross sections. Figure 8.11 show the ratio of cross sections as a function of recoil jet pseudorapidity  $\eta_2$ . Once again there is a reasonable agreement between data and theory.

## 8.4 Conclusions

We have presented results on a study of jets recoiling from large transverse momentum  $\pi^0$ 's and direct photons in 500 GeV/c hadron-nucleon interactions.

The *jet-like* structure of the recoiling system has been established by studying the azimuthal and pseudorapidity correlations of the charge particles in the away-side hemisphere of the trigger. Pseudorapidity correlations have shown that the coverage of the recoil jets ( $\sim 1$  unit of pseudorapidity) are well within the acceptance of the E706 spectrometer. The azimuthal correlations are consistent with the QCD predictions for hard scattering of  $2 \rightarrow 2$  subprocesses, in the lowest order in  $\alpha_s$ .  $\pi^0$  and  $\gamma$  events show a definite difference in particle density for the same-side jets, suggesting that high  $P_T$   $\pi^0$ 's are indeed produced as a fragment of outgoing hard

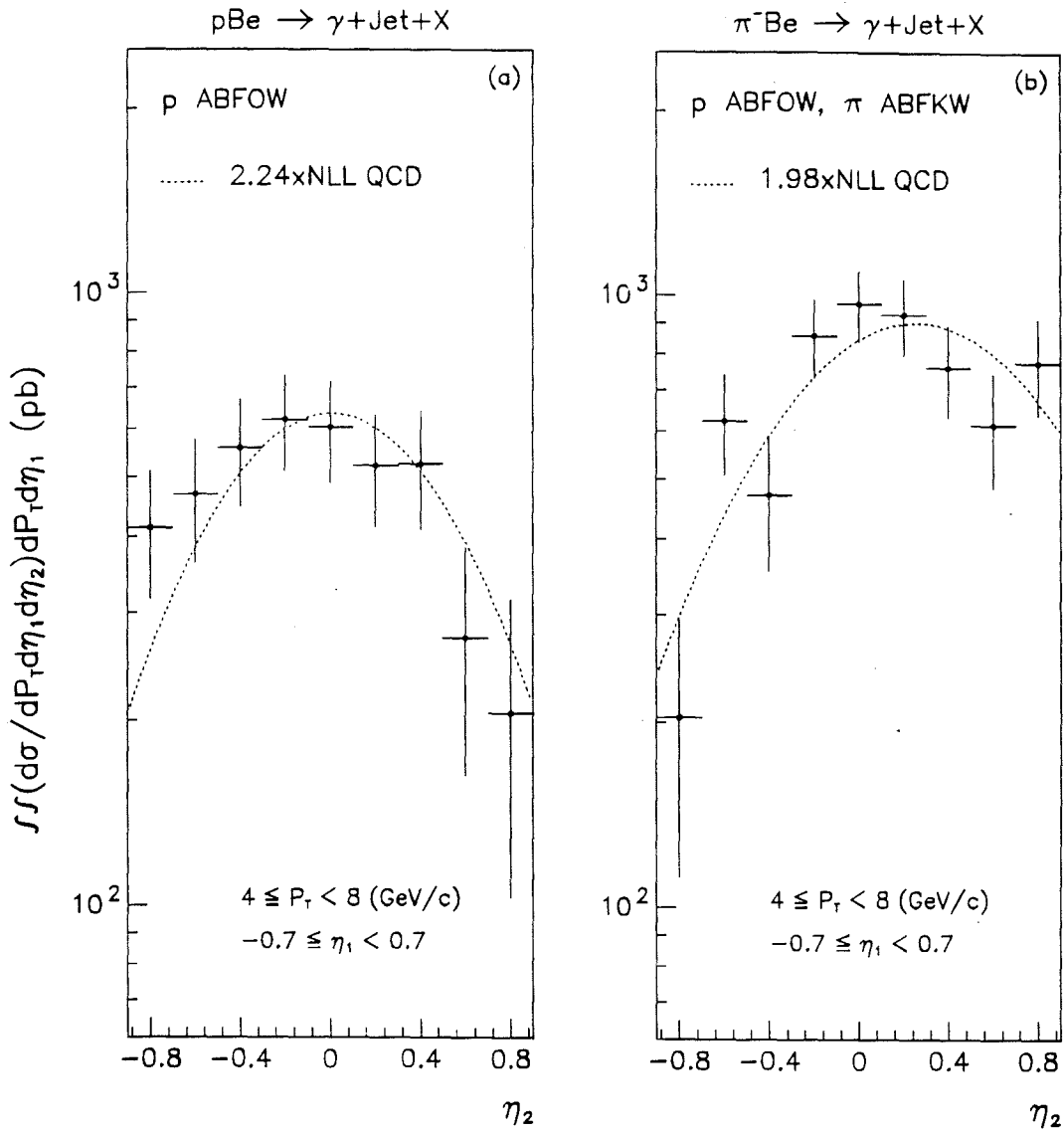


Figure 8.9:  $\gamma + jet$  cross section as a function of  $\eta_2$  compared with the predictions of next-to-leading leading log QCD calculations using ABFKW and ABFOW structure functions with  $Q^2 = P_T^2/4$ . QCD cross sections are normalized to data to compare the shapes of the cross sections. (a)  $p\text{Be}$  collisions, and (b)  $\pi^- \text{Be}$  collisions.

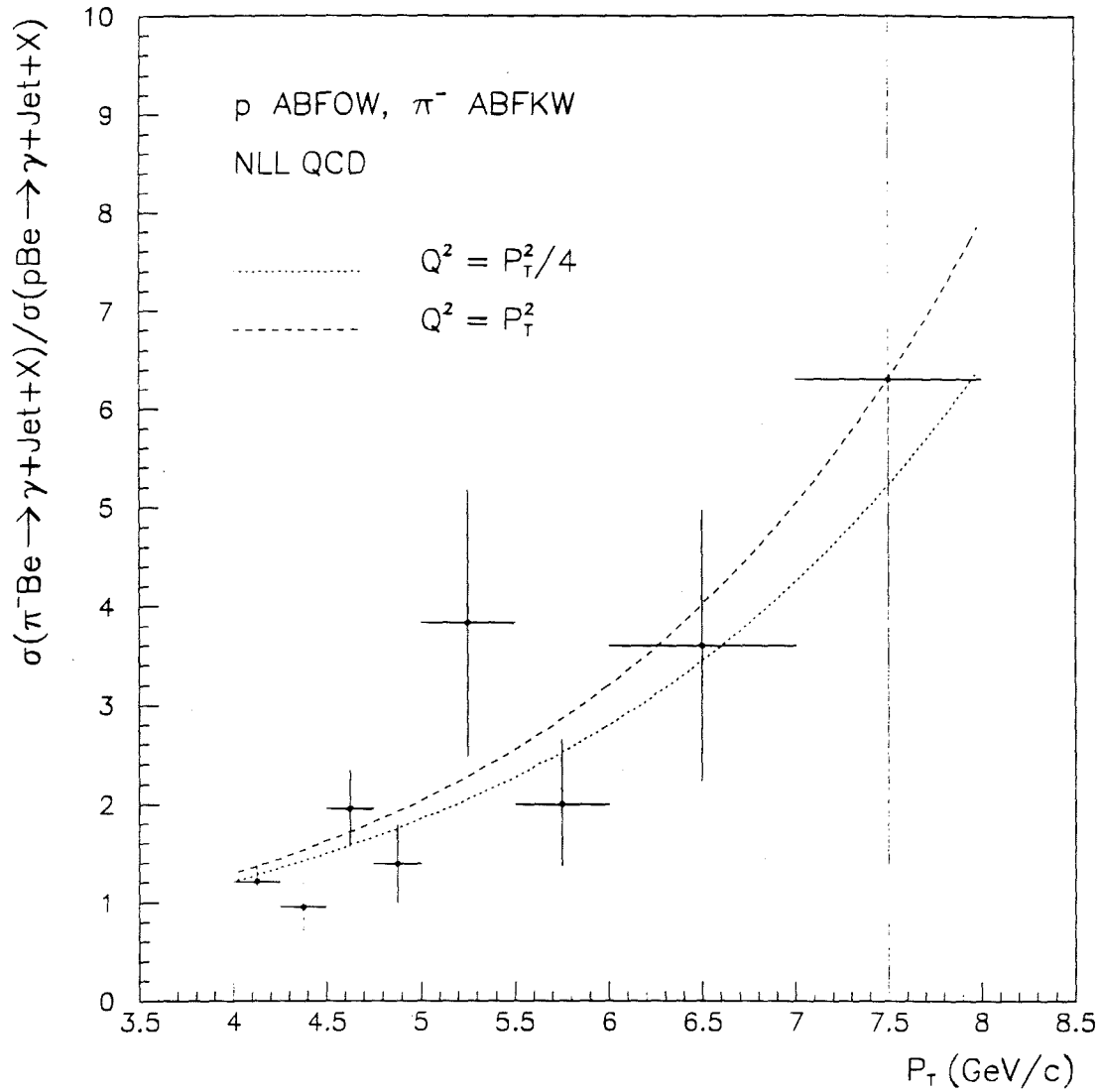


Figure 8.10:  $\sigma_{\pi^- Be \rightarrow \gamma + \text{jet} + X} / \sigma_{p Be \rightarrow \gamma + \text{jet} + X}$  as a function of  $P_T$  compared with next-to-leading log QCD predictions using ABFKW and ABFOW structure functions with  $Q^2 = P_T^2/4$  and  $Q^2 = P_T^2$ .

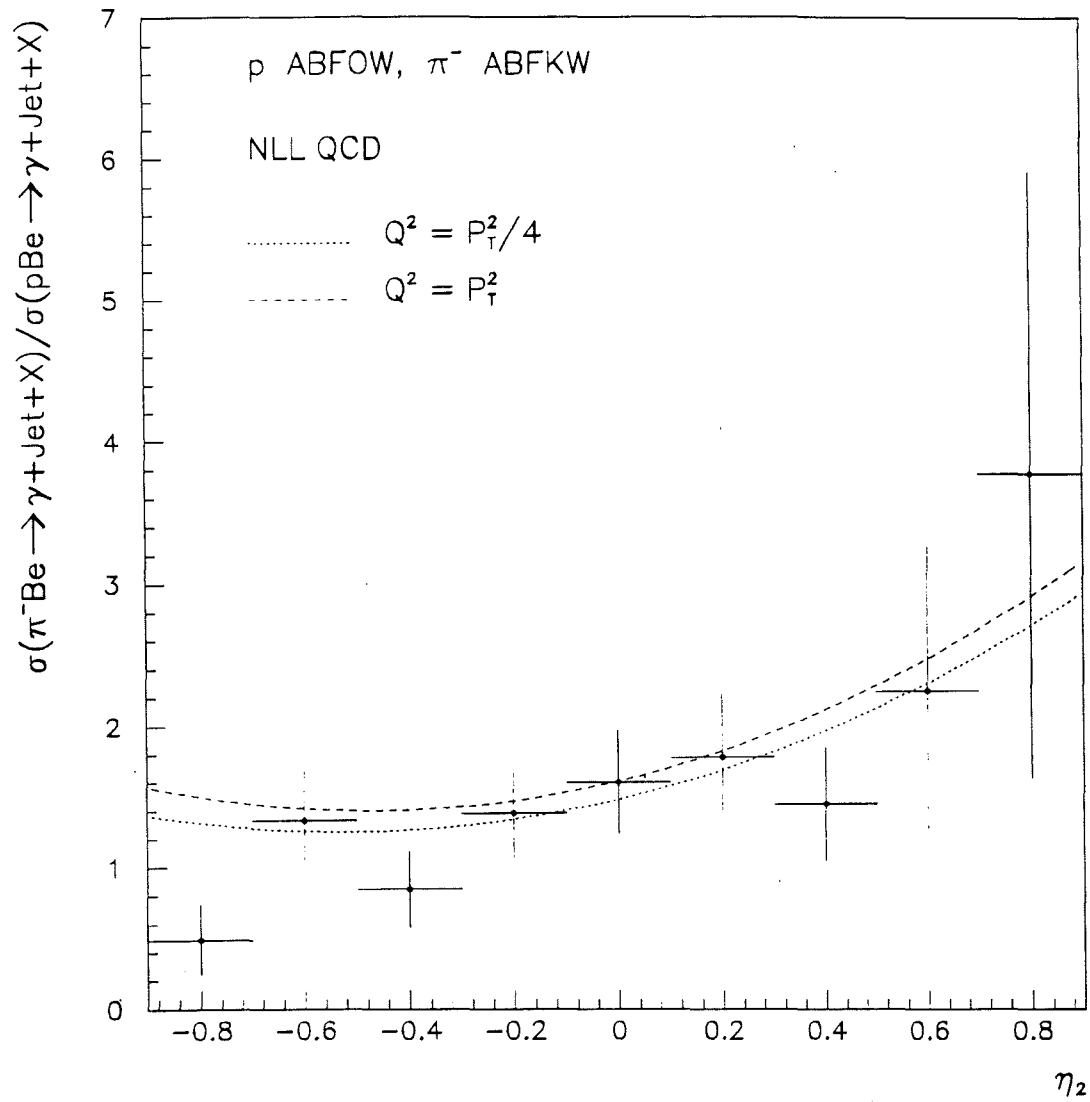


Figure 8.11:  $\sigma_{\pi^- Be \rightarrow \gamma + jet + X} / \sigma_{p Be \rightarrow \gamma + jet + X}$  as a function of  $\eta_2$  compared with next-to-leading log QCD predictions using ABFKW and ABFOW structure functions with  $Q^2 = P_T^2/4$  and  $Q^2 = P_T^2$ .

scattered partons while direct photons are directly produced from the hard scattering interaction.

A jet algorithm has been developed to reconstruct jets recoiling from large transverse momentum  $\pi^0$  or  $\gamma$ . Monte Carlo studies has successfully demonstrated the performance of the jet algorithm and the ability to reliably reconstruct recoil jets in our data. The longitudinal and transverse structure of the events containing a large transverse momentum  $\pi^0$  or  $\gamma$  has been investigated employing the above mentioned jet algorithm. We see no difference in the longitudinal and transverse fragmentation of the jets recoiling from a  $\pi^0$  or a direct photon produced in  $p\text{Be}$  and  $\pi^- \text{Be}$  interactions. The longitudinal fragmentation functions for the jets recoiling from a high  $P_T$  direct photon have been compared with the predictions of ISAJET and PYTHIA Monte Carlo simulations. The agreement is reasonably good. The measured fragmentation functions have been parameterized and compared with the results from the WA70 experiment. A reasonable agreement is observed.

Differential cross sections for  $\pi^0 + jet$  and  $\gamma + jet$  production have been measured for both  $p\text{Be}$  and  $\pi^- \text{Be}$  interactions. The cross sections were presented as a function of the trigger  $P_T$  as well as a function of the recoil jet pseudorapidity.  $\gamma + jet$  cross sections have been compared with the predictions of leading log and next-to-leading log QCD calculations. The data seem to have a steeper slope than the QCD predictions, when the cross sections are presented as a function of the trigger  $P_T$ . At low  $P_T$  the data are about factor 2 higher than the leading log QCD calculations with 1 GeV parton intrinsic transverse momentum. The agreement between data and QCD predictions at high  $P_T$  are moderate. A similar agreement exists between data and the predictions of next-to-leading log QCD calculations. Next-to-leading log QCD calculations reasonably predict the shapes of the differential cross sections when presented as a function of recoil jet pseudorapidity for both  $p\text{Be}$  and  $\pi^- \text{Be}$  interactions.

Finally the ratio of  $\gamma + jet$  cross sections for  $\pi^-Be$  to that for  $pBe$  were made and compared with the next-to-leading log QCD predictions. A better agreement is observed between data and QCD predictions in both trigger  $P_T$  and recoil jet pseudorapidity  $\eta_2$ .

In summary, we have studied the production of large transverse momentum  $\gamma+jet$  events in the context of the QCD parton model and have shown that the results are consistent with a QCD description of high  $P_T$  phenomenology.

## Appendix A

### Cross Section Results

Table A.1:  $\gamma + jet$  differential cross sections as a function of  $P_T$ . The cross sections are averaged over  $-0.7 \leq \eta_1 < 0.7$  and  $-0.9 \leq \eta_2 < 0.9$ .

$P_T$ (GeV/c)	$\iint \frac{d\sigma}{dP_T d\eta_1 d\eta_2} d\eta_1 d\eta_2$ (pb/GeV)	
	$p + Be \rightarrow \gamma + jet + X$	$\pi^- + Be \rightarrow \gamma + jet + X$
3.50 - 3.75	—	$7920 \pm 1440$
3.75 - 4.00	—	$5070 \pm 990$
4.00 - 4.25	$3140 \pm 450$	$3810 \pm 480$
4.25 - 4.50	$1670 \pm 320$	$1600 \pm 330$
4.50 - 4.75	$1030 \pm 170$	$2010 \pm 220$
4.75 - 5.00	$570 \pm 120$	$790 \pm 150$
5.00 - 5.50	$150 \pm 50$	$580 \pm 78$
5.50 - 6.00	$120 \pm 30$	$240 \pm 46$
6.00 - 7.00	$29 \pm 9$	$105 \pm 17$
7.00 - 8.00	$2.1 \pm 2.6$	$13 \pm 6$
8.00 - 10.00	—	$5.1 \pm 2.6$

Table A.2:  $\gamma + jet$  differential cross sections as a function of recoil jet pseudorapidity ( $\eta_2$ ). The cross sections are averaged over  $4 \leq P_T < 8$  GeV/c and  $-0.7 \leq \eta_1 < 0.7$ .

$\eta_2$	$\iint \frac{d\sigma}{dP_T d\eta_1 d\eta_2} dP_T d\eta_1$ (pb)	
	$p + Be \rightarrow \gamma + jet + X$	$\pi^- + Be \rightarrow \gamma + jet + X$
-0.9 - -0.7	$413 \pm 97$	$203 \pm 91$
-0.7 - -0.5	$468 \pm 107$	$622 \pm 116$
-0.5 - -0.3	$557 \pm 110$	$471 \pm 117$
-0.3 - -0.1	$620 \pm 109$	$856 \pm 124$
-0.1 - 0.1	$603 \pm 114$	$967 \pm 127$
0.1 - 0.3	$522 \pm 107$	$928 \pm 131$
0.3 - 0.5	$524 \pm 115$	$761 \pm 130$
0.5 - 0.7	$273 \pm 110$	$613 \pm 129$
0.7 - 0.9	$205 \pm 110$	$774 \pm 140$

Table A.3:  $\sigma_{\gamma+jet}/\sigma_{\pi^0+jet}$  as a function of  $P_T$ .

$P_T$ (GeV/c)	$\sigma_{\gamma+jet}/\sigma_{\pi^0+jet}$	
	Positive Data	Negative Data
3.50 - 3.75	—	$0.049 \pm 0.009$
3.75 - 4.00	—	$0.06 \pm 0.01$
4.00 - 4.25	$0.08 \pm 0.01$	$0.09 \pm 0.01$
4.25 - 4.50	$0.08 \pm 0.02$	$0.06 \pm 0.01$
4.50 - 4.75	$0.09 \pm 0.02$	$0.16 \pm 0.02$
4.75 - 5.00	$0.09 \pm 0.02$	$0.09 \pm 0.02$
5.00 - 5.50	$0.05 \pm 0.02$	$0.14 \pm 0.02$
5.50 - 6.00	$0.14 \pm 0.04$	$0.18 \pm 0.04$
6.00 - 7.00	$0.15 \pm 0.06$	$0.43 \pm 0.09$
7.00 - 8.00	$0.2 \pm 0.3$	$0.3 \pm 0.2$
8.00 - 10.00	—	$0.7 \pm 0.6$

Table A.4:  $\sigma_{\gamma+jet}/\sigma_{\pi^0+jet}$  as a function of recoil jet pseudorapidity ( $\eta_2$ ).

$\eta_2$	$\sigma_{\gamma+jet}/\sigma_{\pi^0+jet}$	
	Positive Data	Negative Data
-0.9 - -0.7	$0.11 \pm 0.03$	$0.05 \pm 0.02$
-0.7 - -0.5	$0.09 \pm 0.02$	$0.12 \pm 0.02$
-0.5 - -0.3	$0.10 \pm 0.02$	$0.07 \pm 0.02$
-0.3 - -0.1	$0.11 \pm 0.02$	$0.14 \pm 0.02$
-0.1 - 0.1	$0.11 \pm 0.02$	$0.15 \pm 0.02$
0.1 - 0.3	$0.10 \pm 0.02$	$0.13 \pm 0.02$
0.3 - 0.5	$0.10 \pm 0.02$	$0.10 \pm 0.02$
0.5 - 0.7	$0.05 \pm 0.02$	$0.08 \pm 0.02$
0.7 - 0.9	$0.04 \pm 0.02$	$0.12 \pm 0.02$

Table A.5:  $\sigma_{\pi^-Be \rightarrow \gamma + jet + X} / \sigma_{pBe \rightarrow \gamma + jet + X}$   
as a function of  $P_T$ .

$P_T$ (GeV/c)	$\frac{\sigma_{\pi^-Be \rightarrow \gamma + jet + X}}{\sigma_{pBe \rightarrow \gamma + jet + X}}$
4.00 - 4.25	$1.2 \pm 0.2$
4.25 - 4.50	$1.0 \pm 0.3$
4.50 - 4.75	$2.0 \pm 0.4$
4.75 - 5.00	$1.4 \pm 0.4$
5.00 - 5.50	$3.8 \pm 1.4$
5.50 - 6.00	$2.0 \pm 0.7$
6.00 - 7.00	$3.6 \pm 1.4$
7.00 - 8.00	$6.3 \pm 8.3$

Table A.6:  $\sigma_{\pi^-Be \rightarrow \gamma + jet + X} / \sigma_{pBe \rightarrow \gamma + jet + X}$   
as a function of recoil jet pseudorapidity  
( $\eta_2$ ).

$P_T$ (GeV/c)	$\frac{\sigma_{\pi^-Be \rightarrow \gamma + jet + X}}{\sigma_{pBe \rightarrow \gamma + jet + X}}$
-0.9 - -0.7	$0.5 \pm 0.3$
-0.7 - -0.5	$1.3 \pm 0.4$
-0.5 - -0.3	$0.9 \pm 0.3$
-0.3 - -0.1	$1.4 \pm 0.3$
-0.1 - 0.1	$1.6 \pm 0.4$
0.1 - 0.3	$1.8 \pm 0.5$
0.3 - 0.5	$1.5 \pm 0.4$
0.5 - 0.7	$2.3 \pm 1.0$
0.7 - 0.9	$3.8 \pm 2.1$

## REFERENCES

- [1] G. Miller, *et al.*, *Phys. Rev. D* **5** (1972) 528.
- [2] M. Gell-Mann, *Phys. Lett.* **8** (1964) 214.
- [3] D. J. Gross and F. Wilczek, *Phys. Rev. Lett.* **30** (1973) 1343.
- [4] H. D. Politzer, *Phys. Rev. Lett.* **30** (1973) 1346.
- [5] R. K. Ellis and W. J. Sterling, QCD and Collider Physics, FERMILAB-Conf-90/164-T.
- [6] J. F. Owens, *Rev. Mod. Phys.* **59** (1987) 465.
- [7] P. B. D. Collins and A. D. Martin, Hadron Interactions, Graduate Student Series in Physics, Adam Hilger Ltd. Bristol (1984).
- [8] R. K. Ellis *et al.*, *Phys. Lett.* **B78** (1978) 281.
- [9] R. K. Ellis *et al.*, *Nucl. Phys.* **B152** (1979) 285.
- [10] G. Altarelli and G. Parisi, *Nucl. Phys.* **B126** (1977) 298.
- [11] T. Ferbel and W. R. Molzon, *Rev. Mod. Phys.* **56** (1984) 181.
- [12] C. Albajar *et al.*, *Phys. Lett.* **B209** (1988) 385.
- [13] P. Aurenche *et al.*, *Phys. Lett.* **140B** (1984) 87, P. Aurenche *et al.*, *Nucl. Phys.* **B286** (1987) 509, P. Aurenche *et al.*, *Nucl. Phys.* **B297** (1988) 661.
- [14] L. Cornell and J. F. Owens, *Phys. Rev. D* **22** (1980) 1609.

- [15] M. Bonesini *et al.*, *Z. Phys. C44* (1989) 71.
- [16] I. Kourbanis, *unpublished*, Ph.D. Thesis, Northeastern University, Boston, Massachusetts (1990).
- [17] NATO series, Techniques and Concepts of High Energy Physics IV, edited by T. Ferbel, Plenum Press, New York (1987).
- [18] J. Kemmer, *NIM* **169** (1980) 499.
- [19] S. Mani, *unpublished*, Ph.D. Thesis, University of Pittsburgh, Pittsburgh, Pennsylvania (1986).
- [20] Nanometric Systems, Inc., *unpublished* Multi Wire Proportional Chamber Read-out System, Oak Park, Illinois.
- [21] E. Engels, Jr., *et al.*, *NIM A279* (1989) 272.
- [22] L. De Barbaro and F. Lobkowicz, E706 Note **E706-0167** (1988).
- [23] K. Hartman, *unpublished*, Ph.D. Thesis, Pennsylvania State University, University Park, Pennsylvania (1990).
- [24] ZIPTRACK manual, Fermilab Computing Department Note # PN267.
- [25] F. Lobkowicz, *et al.*, *NIM A235* (1985) 332.
- [26] W. E. DeSoi, *unpublished* Ph.D. Thesis, University of Rochester, Rochester, New York (1990).
- [27] J. P. Mansour, *unpublished*, Ph.D. Thesis, University of Rochester, Rochester, New York (1990).
- [28] E. Prebys, *unpublished*, Ph.D. Thesis, University of Rochester, Rochester, New York (1990).

- [29] D. Skow, *unpublished*, Ph.D. Thesis, University of Rochester, Rochester, New York (1990).
- [30] C. B. Lirakis, *unpublished* Ph.D. Thesis, Northeastern University, Boston, Massachusetts (1990).
- [31] R. Benson, *unpublished*, Ph.D. Thesis, University of Minnesota, Minneapolis, Minnesota (1989).
- [32] C. Yosef, *unpublished*, Ph.D. Thesis, Northeastern University, Boston, Massachusetts (1990).
- [33] V. White, *et al.*, 1985, *The VAXONLINE System at Fermilab*, Fermilab Computing Department note **PN318** and E. Berman, *et al.*, 1985, *VAXONLINE User's Guide*, Fermilab Computing Department note **PN252**, Fermilab, Batavia, Illinois.
- [34] G. O. Alverson and E. L. Pothier, E706 Note, **E706-0139** (1985).
- [35] H. J. Klein and J. Zoll, 1983, *PATCHY* reference manual, CERN Computer Center program library.
- [36] The Fermilab Advanced Computer Project consisted of a number of parallel processing hardware nodes with supporting software. E706 ran the reconstruction program MAGIC on an ACP multiprocessor systems with up to 68 nodes for three months. Details of this system may be found in the Fermilab Computing Department Notes #GA0001-GA0004.
- [37] R. Brun *et al.*, 1988, ZEBRA, A Fortran Based Dynamic Memory Management System, CERN write-up **Q100**, Geneva, Switzerland or Fermilab Software note **PU0046**, Fermilab, Batavia, Illinois.

- [38] S. Easo, *unpublished* Ph.D. Thesis, Pennsylvania State University, University Park, Pennsylvania (1989).
- [39] G. O. Alverson *et al.*, Production of Direct Photons and Neutral Mesons at Large Transverse Momenta by  $\pi^-$  and  $p$  beams at 500 GeV/c, *submitted to Phys. Rev. D*.
- [40] N. Varelas, Private Communication.
- [41] R. Brun, *et al.*, 1984, GEANT3 User's Guide, CERN DD/EE/84-1, Geneva, Switzerland, or Fermilab Software Note PM0062, Fermilab, Batavia, Illinois.
- [42] B. C. Choudhary, *unpublished* Ph.D. Thesis, University of Delhi, Delhi, India (1991).
- [43] S. M. Berman, J. D. Bjorken and J. B. Kogut *Phys. Rev. D* **4** (1971) 3388.
- [44] W. M. Geist *et al.*, *Phys. Rep.* **197** (1990) 263.
- [45] B. R. Webber, *Nucl. Phys.* **B238** (1984) 492.
- [46] R. D. Field and R. P. Feynman, *Nucl. Phys.* **B136** (1978) 1.
- [47] T. Åkesson *et al.*, *Z. Phys.* **C25** (1984) 13.
- [48] D. S. Brown, *unpublished* Ph.D. Thesis, Michigan State University, East Lansing, Michigan (1992).
- [49] F. E. Paige and S. D. Protopopescu, "A Monte Carlo event generator for p-p and  $\bar{p}$ -p reactions", *ISAJET V6.30* (1989).
- [50] D. W. Duke and J. F. Owens, *Phys. Rev. D* **30** (1984) 49.
- [51] A. Bassetto, M. Ciafaloni and G. Marchesini, *Phys. Lett.* **83B** (1978) 207.
- [52] K. Konishi, Rutherford Report RL 79-035 (1979).

- [53] W. Furmanski and S. Pokorski, *Nucl. Phys.* **155B** (1979) 253.
- [54] T. Åkesson *et al.*, *Z. Phys.* **C30** (1986) 27.
- [55] P. Gutierrez, Private Communication.
- [56] J. F. Owens, *Phys. Lett.* **B266** (1991) 126.
- [57] H. Baer, J. Ohnemus and J. F. Owens, *Phys. Rev.* **D42** (1990) 61, H. Baer, J. Ohnemus and J.F. Owens, *Phys. Lett.* **B234** (1990) 127.
- [58] P.Aurenche *et al.*, *Phys. Rev.* **D39** (1989) 3275.
- [59] P.Aurenche *et al.*, *Phys. Lett.* **B233** (1989) 517.

